Ultrafast Optical Control over Hot Electron Dynamics in Nanoplasmonic Systems

by

Jacob Pettine

B.S., University of Colorado Boulder, 2013

A thesis submitted to the
Faculty of the Graduate School of the
University of Colorado in partial fulfillment
of the requirements for the degree of
Doctor of Philosophy
Department of Physics
2020

Committee Members:
David Nesbitt, Chair
Markus Raschke
Margaret Murnane
Andreas Becker
Gordana Dukovic

Pettine, Jacob (Ph.D., Physics)

Ultrafast Optical Control over Hot Electron Dynamics in Nanoplasmonic Systems

Thesis directed by Prof. David Nesbitt

Nanoscale metal systems support strong light-matter interactions known as plasmons, which generate high densities of high-energy ("hot") electrons. These hot electrons can be harvested by surrounding molecules or semiconductors, or emitted into free space, with each possibility representing a broad set of applications, including next-generation solar energy conversion and storage, novel biological therapies, and ultrafast nanoscale electronics. The full realization and optimization of many of these applications, however, will require a detailed understanding of where hot electrons are excited, how fast and far they travel, and what directions they travel in—i.e. their spatial, temporal, and momentum distributions. In this thesis, new methods are introduced for measuring, modeling, and even optically controlling nanoplasmonic hot electron distributions on femtosecond timescales, using a unique single-particle, angle-resolved nonlinear photoemission spectroscopy technique with a highly-tunable ultrafast visible laser system. These experiments are both complemented and driven by the parallel development of a simple new theoretical framework for predictively modeling nanoplasmonic hot electron distributions and dynamics. A variety of nanoparticle geometries are investigated to reveal an equally wide variety of behaviors, from the simple directional photoemission properties of complex defects to the strikingly complex and often counter-intuitive photoemission properties of simple nanorods and spherical nanoparticles.

Dedication

To my wife, Janet, my parents, Holly, Chris, and Patty, and my grandparents, Bea, Al, and Helen, for the examples they all set with their strengths of character and for their unconditional support.

Acknowledgements

I would first like to thank my family and friends for their years of support, patience, and interest. One of the great joys of my PhD has been sharing the excitement and demystifying the experience of laboratory life with others. For directly shaping and sharing in that laboratory life, I would like to thank my friends and colleagues in the Nesbitt Lab, Tim, Mikhail, Hsuan-Lei, Andrea, Brian, David, Kirstin, Andy, Mia, Dan, Abhigyan, Ya-Chu, and Candice, with special thanks my adviser, David Nesbitt, for his insightful guidance and emphasis on the importance of community in science. I would also like to thank my undergraduate adviser, Dana Anderson, for his continued guidance. I'm very grateful to the phenomenal technical and administrative staff within JILA, including David, Mark, Corey, J.R., Jim, James, Carl, Terry, Hans, Kim, Todd, Beth, Julie, David, Kim, Agnieszka, Maryly, Cindy, Steven, Rebecca, Brian, Jennifer, Randall, Daniel, Karen, and Jason, as well as Garry in MCDB. I would further like to thank my collaborators, Catherine Murphy and Sean Meyer at the University of Illinois Urbana-Champaign, as well as Teri Odom and Priscilla Choo at Northwestern University. The opportunity to work with exceptional scientists both within and outside of the local CU Boulder community was a true highlight of my PhD. I also gratefully acknowledge the AFOSR, the NSF Physics Frontier Center, and the NSF Graduate Research Fellowship Program for funding this work. Finally, I would like to thank my wife, Janet, for reminding me to also live a full life outside of the lab.

Contents

Chapter

Appendix

Figures

Figure

Chapter 1

Introduction

Plasmonic science has experienced strong exponential growth in recent decades,[23] driven by applications such as surface-enhanced Raman scattering[71] (SERS) and sensing.[103] The dramatic increase in interest has been sustained by an increasing variety of precision synthetic[41, 113, 124] and fabrication[39, 206] methods, along with novel applications in areas such as solar energy harvesting,[30, 83] metamaterials,[132, 194] lasers,[194] quantum nanophotonics,[50] biological therapies,[157, 13] and ultrafast electron sources.[162, 126] Central to all of these applications is the simple concept of conduction electrons collectively "sloshing" back and forth in a nanoscale metal container (nanoparticle). For certain metals (e.g. Au, Ag, Cu, Al) this resonant oscillation can be very strong and can occur in the visible spectral range, with resonance properties tabulated for a variety of materials.[18] As charge carriers (electrons and holes) build up on the nanoscale surfaces of high and highly-varying curvature, they generate strong evanescent electric near-fields that may represent 10-fold or higher enhancements over the incident optical excitation fields. The strong plasmonic optic field density can subsequently excite high densities of hot charge carriers within the nanoscale volumes, which can be collected/emitted into the surrounding medium (e.g. molecules, semiconductors, or free space) or may decay into phonons to generate high thermal energy densities.[69] The resonance properties of nanoplasmonic particles/structures, the corresponding spatiotemporal energy (re)distribution in these systems, and their resonance positions depend strongly on the particle material, shape, and surrounding medium.[111]

The present work focuses both on photonic (plasmonic) and electronic (hot carrier) processes in nanoplasmonic systems, with a strong emphasis on the hot carrier dynamics that occur on tens of femtosecond timescales. These processes are central to hot carrier science and technology, which is a field in and of itself with important implications for next-generation solar photovoltaics,[30] chemical conversion and energy storage,[31, 6] photodetectors,[22] ultrafast electron imaging/diffraction,[127] x-ray laser sources,[138, 75] and terahertz nanoelectronics.[89, 173] All of these applications rely on the efficient generation and transfer/emission of hot carriers by shining coherent (laser) or incoherent (e.g. solar) light on nanoplasmonic structures. Ultimately, the efficacy of these technologies will clearly depend on how well the hot carrier excitation processes and subsequent dynamics are understood.

Much of the physics central to hot carrier science (particularly with semiconductor or vacuum collection media) has already been developed in the photoemission literature from the past century, with particularly strong progress in the 1960s [17] and the 1970s [114, 48] on the volume- and surface-mediated photoeletric effects,[189] as will be discussed in much greater detail in Section 1.4, Chapter 3, and subsequent chapters. However, even for macroscopic crystalline solids, the full (one-step) quantum theory of photoexcitation and emission is often intractable, forcing practitioners to rely on phenomenological (three-step) models,[78] to be discussed later. The uniquely strong, nanolocalized field enhancements and nanoscale curvatures of nanoplasmonic systems present further challenges for theoretically modeling electronic photoexcitation and emission. Moreover, visible plasmonic excitation frequencies ($\sim$1.5–2 eV) require multiphoton absorption to overcome the work function of plasmonic metals (e.g. $\phi_{\mathrm{Au}} \approx 5$ eV) and the band structure of gold, for instance, permits few to no direct/vertical/interband transitions above the vacuum level, instead promoting a variety of coherent vs. incoherent and volume vs. surface excitation pathways.

To understand nanoplasmonic hot carrier dynamics in detail—with the ultimate goals of predictive modeling, tailored particle/structure design, and optical control over hot electron emission dynamics—six–seven degrees of freedom must be experimentally resolved: two–three spatial degrees of freedom, three momentum degrees of freedom, and the temporal evolution of the hot carrier excitation and emission distributions. Spin or carrier charge can also become important in various applications (e.g. photocatalysis), although will likely be more readily encoded in any experimental/theory that captures many or all of the above six–seven degrees of freedom.[169] Thus, the most definitive experiments will include some combination of nanoscale spatial resolution, angle-resolved momentum resolution, and femto/attosecond temporal resolution. While a number of high-quality nanometer-femtosecond space-time-resolved photoemission studies are underway,[34] understanding of the essential momentum degrees of freedom is still nascent for nanoplasmonic hot electron science. The new experimental insights and theoretical models introduced here are therefore largely the result of building up a new technique for a better understanding of the momentum degrees of freedom of hot electrons emitted from single supported nanoparticles.

Following a general overview in the present chapter and detailed summaries of the experimental (Chapter 2) and theoretical (Chapter 3) methods utilized and developed for this work, this thesis will evolve chronologically from initial nanoplasmonic velocity mapping studies in Chapter 4, to capabilities for ultrafast photocurrent control via selective nanoshell and nanostar surface hot spot emission in Chapter 5, to fully distinguishing and modeling volume vs. surface photoexcitation/emission via gold nanorods in Chapter 6. Finally, Chapter 7 will address current efforts combining femtosecond pump-probe and 3D velocity mapping, with a look at future directions in Chapter 8.

Some initial notes on nomenclature that will be relevant throughout the thesis:

- The terms *photoemission* and *photocurrent* will be used interchangeably, although they normatively represent the difference between emission into the vacuum and emission into a surrounding collection material (e.g. a semiconductor). Such terms may also be applied to charge transfer to a molecular adsorbate. The essential features of the excitation and emission/transfer are largely the same, and it is primarily these features that are investigated herein.

- The terms *nanoparticle* vs. *nanostructure* typically denote synthetic particles vs. fabricated (nanolithographic) structures, respectively, although the distinction is neither fundamental nor particularly distinct for some hybrid methods (e.g. ablative nanoparticle generation or chemical nanostructure growth). Nanoparticles are typically synthesized in solution and thus tend to have stabilizing ligands, while nanostructures are typically fabricated via electron beam lithography or other nanolithography methods (e.g. nanosphere lithography) and are thus ligand-free. Nanoparticles are often (though not always) monocrystalline, while nanostructures are often polycrystalline. Only synthetic, ligand-stabilized nanoparticles are discussed here, but the supported nanoparticles and nanostructures are often treated interchangeably in the literature (and rightly so), so long as the particle geometry and relevant environmental effects (e.g. ligands, substrate) are accounted for accordingly. Both terms will thus be used to denote nanoplasmonic systems. It shall be shown that, barring damping effects over time due to conversion into an amorphous carbon layer,[183] ligands have negligible observable effect on the hot electron dynamics and the measured photoemission distributions.

1.1 Nanoplasmonics

Plasmonic nanoparticles are metal (e.g. Au, Ag, Cu, Al) nanoparticles hosting a collective conduction electron oscillation known as a localized surface plasmon resonance (SPR). Conduction electrons in metals are delocalized/itinerant, which in a ballistic picture means that they are free to move around with respect to the positive ion metal lattice. This system is therefore a plasma with mobile negative charge carriers (electrons) and a static positive ion background. In the free electron limit, such systems are known as Drude or free-electron metals, with plasma frequency (see discussion below)

$$\omega_{\mathrm{p}} = \sqrt{\frac{n_e e^2}{\epsilon_0 m_e}}, \tag{1.1}$$

while in other cases material dispersion can be accounted for via effective mass $m_e \rightarrow m_e^*$. The plasma frequency represents the fundamental optical response time of the metal. For an approximate toy model, taking a cubic volume element, V, and displacing the conduction electrons density n_e by a small amount δx leads to depolarization field between the two sheets of charge $E_{\mathrm{dep}} = en_e/\epsilon_0 \delta x$, neglecting fringe effects. Note that ϵ_0 is used instead of ϵ because the process under examination is the screening itself (with d-band screening effects neglected). Thus, the depolarization force on a displaced charge is

$$\begin{aligned} F_{\mathrm{dep}} &= -eE_{\mathrm{dep}} \\ &= -\frac{e^2 n_e}{\epsilon_0}\delta x \\ &= -m_e \omega_{\mathrm{p}}^2 \delta x, \end{aligned} \tag{1.2}$$

which is harmonic with plasma frequency given by Eq. 1.1.

The full optical response of the material is encoded in the complex dielectric function, which is isomorphic (contains the same information and bijectively maps onto) the complex refractive index, susceptibility, and polarizability. The optical response can be derived via the Lorentz oscillator model,[81]

$$m_e x''(t) + \gamma x'(t) + m_e \omega_0^2 x(t) = -eE(t) \tag{1.3}$$

with harmonic field $E(t) = E_0 e^{-i\omega t}$ and damping rate γ. For $x(t) = Ae^{-i\omega t}$, the dipole moment for N electrons is given by

$$\begin{aligned} \boldsymbol{p}(t) &= -Ne\boldsymbol{x}(t) \\ &= \frac{e^2}{m_e}\frac{1}{\omega_0^2 - \omega^2 - i\gamma\omega}\boldsymbol{E}. \end{aligned} \tag{1.4}$$

The dielectric function, $\epsilon/\epsilon_0 = 1 + \chi^{(1)}$ is therefore given by

$$\frac{\epsilon(\omega)}{\epsilon_0} = 1 + \frac{ne^2}{\epsilon_0 m_e}\sum_j \frac{f_j}{\omega_j^2 - \omega^2 - i\omega\gamma_j}, \tag{1.5}$$

where f_j is the oscillator strength for a resonance and $\sum_j f_j = 1$ (Thomas-Reiche-Kuhn sum rule). Approximating a free-electron metal or, correspondingly, taking the optical frequency ω to be much greater than the largest system resonance, $\omega_{j,\mathrm{max}}$, Eq. 1.5 reduces to the well-known Drude model,[81, 115]

$$\frac{\epsilon(\omega)}{\epsilon_0} = 1 - \frac{\omega_\mathrm{p}^2}{\omega^2 + i\gamma\omega}. \tag{1.6}$$

At this point, the phenomenological γ term is often modified for d-band effects or surface collisional effects via simple Mattheissen's rule summation over the relevant damping rates. For $\omega \gg \gamma$, Eq. 1.6 takes the simple form for the real part,

$$\frac{\epsilon_1(\omega)}{\epsilon_0} = 1 - \frac{\omega_\mathrm{p}^2}{\omega^2}, \tag{1.7}$$

and imaginary part,

$$\frac{\epsilon_2(\omega)}{\epsilon_0} = \frac{\omega_\mathrm{p}^2\gamma}{\omega^3}, \tag{1.8}$$

of the dielectric function. Neglecting the imaginary part, it is seen that that the metal is highly reflective with no propagating field for $\omega < \omega_\mathrm{p}$ (negative ϵ and thus purely imaginary refractive index, $n = \sqrt{\epsilon}$) and exponential/evanescent skin depth, with no absorption if $\epsilon_2 = 0$—i.e. strictly no damping and thus infinite conductivity. For $\omega > \omega_\mathrm{p}$, the metal becomes perfectly transmissive (positive ϵ and thus purely real refractive index). Non-negligible γ and thus ϵ_2 contributes to absorption and thus effectively blurs this transition. Thus, metals become highly transparent in the UV, while the ionosphere plasma frequency is around 10 MHz, for example.

Bulk plasmon resonances (along with traveling and localized surface plasmons to be discussed) are bosonic quasiparticle excitations of the conduction electron plasma (Fig. 1.1a). The bulk plasmons are longitudinal charge density oscillations, which therefore cannot be excited optically, but may be excited via electron beams (e.g. in energy loss spectroscopy) or via high-energy (often >5 eV) photoelectrons. The introduction of an interface to a bulk system leads to the possibility of surface-localized charge density oscillations coupled to optical fields, known as surface plasmon *polaritons* (Fig. 1.1b). As with bulk plasmons, these

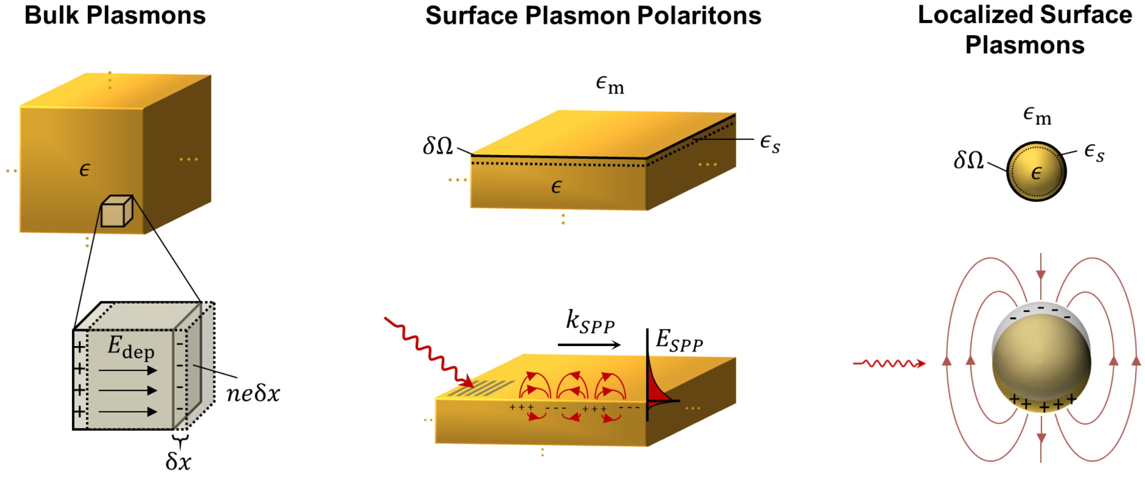

Figure 1.1: Plasmon resonance modes for bulk, surface, and nanolocalized systems. (a) Bulk material and corresponding bulk plasmon oscillation. (b) Surface interface with grating- (e.g.), roughness-, or prism-launched traveling surface plasmon polariton mode. (c) Nanoparticle with dipolar surface plasmon resonance shown.

traveling polaritons have well-defined momenta, which are greater than the corresponding electromagnetic field momenta. Thus, surface plasmon polariton excitation requires some additional mechanism for momentum conservation such as a higher-index (e.g. glass prism) coupler to launch a plasmon on the other side of a metal film, or a surface grating.[155] Finally, one can treat a flat film as the surface of an infinitely large sphere and then shrink down the sphere to the nanoscale. As the sphere shrinks down past the scale of the optical excitation wavelength, the traveling polariton mode resolves into a linear combination of multipolar oscillations and momentum is no longer a good quantum number. These multipolar oscillations are known as *localized surface plasmon resonances*, which will be abbreviated here simply as "SPRs". Most of the studies to be discussed will be in the dipolar/quasi-static regime ($R \ll \lambda$) (Fig. 1.1c), although quadrupolar resonances will occasionally be considered and the full multipolar Mie theory will be discussed in Section 3.1.2.

Localized SPRs dephase due to lifetime (T_1) and pure dephasing (T_2^*) contributions on ~10 fs timescales, with the total dephasing rate (T_2) given by Matthiessen's rule,

$$\frac{1}{T_2} = \frac{1}{2T_1} + \frac{1}{T_2^*}. \tag{1.9}$$

The factor of two difference is simply due to intensity (T_1) vs. field (T_2^*) dependence. Lifetime mechanisms include radiative damping into photonic modes and nonradiative damping into hot electron-hole excitations. Pure dephasing mechanisms include bulk electron-phonon and electron-surface scattering (particularly for small particles < 20 nm) during plasmon oscillations,[111] which serves as a ballistic interpretation for the essentially elastic energy redistribution that can take place during collective conduction electron motion. The homogeneously-broadened plasmon extinction linewidth is determined by T_2. For very small particles (< 100 nm) under visible excitation, the nonradiative energy pathways (σ_{abs}) are typically dominant over the radiative pathways (σ_{sca}). As an interesting consequence, many small particles with the same volume as one large particle can absorb energy more efficiently. When combined with the larger hot carrier escape efficiencies for the shorter path lengths, smaller particles are often ideal for hot carrier technologies. Such hot carrier excitation and subsequent dynamics will be discussed briefly in the next section and in detail in Chapter 3.

1.2 Dynamics in Nanoplasmonic Systems

Following plasmon decay into electron-hole excitations on ∼10 fs timescales, metallic screening eliminates the correlation between the opposite charges and yields free carriers on ∼1 fs timescales. Via the optical absorption at visible plasmonic frequencies (1–4 eV), the free carriers have energies much greater than kT (0.025 eV at room temperature), and are thus considered "hot" electrons and holes. Depending on the excitation energy (see Fermi Liquid Theory in Section 3.3.1), the hot electrons undergo both inelastic (hot-cold electron-electron) and essentially elastic (electron-phonon) collisions on ∼30 fs timescales. Electrons lose half of their energy on average to a single electron-electron collision[159] and a nascent hot electron probability distribution (following instantaneous excitation; i.e. the impulse response or Green's function) will thermalize relatively quickly within a few hundred femtoseconds.[69] By contrast, the elastic electron-phonon collisions incur minimal energy loss per collision (on the order of 10 meV[4]), which leads to longer, few-picosecond timescales for hot electron-lattice thermalization.[69] Since the temperature-dependent electron heat capacity is over an order of magnitude smaller than the lattice heat capacity, for instance, in gold (see Section 3.3.2), the peak hot electron temperatures are often an order of magnitude or so higher than peak lattice temperatures, which will have interesting implications for hot electron emission dynamics, as discussed in Section 3.4. In the nonradiative decay chain, therefore, the optical energy goes from plasmon excitations (∼10 fs) to nascent hot carriers (∼10–100 fs) to thermalized hot carriers (∼0.1–1 ps) to thermalized lattice phonons (∼1–100 ps) to environmental heating (>100 ps). Nascent hot electron distributions from intraband excitation (i.e. not d-band excitations just above the Fermi level[216]) contain the largest number of high-energy (> 1 eV) hot electrons, useful for many applications, which thus sets the relevant collection timescale around 10–100 fs following excitation.

Each step of this energy cascade has a broad set of corresponding applications. On the photonic timescale of the plasmon oscillation (∼10 fs), elastic photon scattering into dipolar or higher-order oscillation radiation patterns can be utilized for "optical antenna" applications, including phased arrays.[210] The strong plasmonic field enhancements can also be exploited for resonance-enhanced elastic or Raman scattering of nearby molecules.[71, 199] Additionally, the high nanoscale photon densities can also be used for light trapping in photovoltaic systems,[7] as well as sensing the environment via resonance shifts, scattering, or fluorescent signatures.[103] Electronic timescales of ∼10–100 fs will be the primary focus here, with applications in photocatalysis,[182, 214, 6, 55] photovoltaics/photodetection,[30, 23, 187] and photocathodes,[39, 127, 170, 99, 217] corresponding to electron transfer, injection, or emission into nearby molecules, semiconductor, or free space, respectively. These processes and applications will be discussed in greater detail in the next section. On picosecond and longer timescales, coherent acoustic modes can be utilized for nanoscale actuation,[195] while incoherent heating can be utilized for enhanced catalysis,[32] and targeted cancer ablation therapy.[157]

1.3 Hot Carrier Science and Applications

As mentioned in the previous section, plasmonic hot carriers are utilized for myriad applications and now represent a major emphasis of plasmonics research. While a few important applications such as photocatalysis, photovoltaics, and photocathodes will be described in further detail here, it should be recognized that the underlying physics for all of these systems is qualitatively similar. As will be discussed in Section 1.4 and Chapter 3, hot carriers can either be ballistically transferred following excitation *within* the nanoparticle into whichever collection medium is present, else they can be excited directly at the metal-medium interface. While different collection media (e.g. molecules, semiconductor, or vacuum) will influence the surface barrier and/or surface state properties and thus quantitatively affect the absolute and relative (surface vs. volume) cross-sections, many qualitative features of the semi-classical or quantum hot carrier dynamics remain the same across all processes.

1.3.1 Photocatalysis

Photocatalysis is perhaps the largest sector of nanoplasmonic hot carrier science, with important opportunities for enhanced catalytic efficiencies and bond selectivities compared with typical thermally-activated processes.[32, 6] While a wide variety of hot-carrier-driven catalytic processes have been studied, two areas of particular interest are H_2O[212, 201] and CO_2[198, 160] reduction for solar fuel production/storage and closure of the carbon cycle. The simple idea is that high densities of hot electrons and holes excited within individual nanoparticles can be transferred to surface molecules, with high overall interaction surface areas for nanoparticle colloids/ensembles. In some competition with the terminology from photoexcitation literature, charge transfer is categorized into "direct" excitation/transfer into a surface-hybridized admolecule/metal state or "indirect" excitation in the metal nanoparticle followed by ballistic transfer to the admolecule.[6] This qualitatively maps onto the distinction between surface vs. volume photoexcitation to be discussed in the Section 1.4. Direct excitation may have the advantage of additional energy specificity,[55] while indirect/ballistic transfer would be less discriminating with respect to adsorbed states due to the excited Fermi-Dirac hot carrier distributions. Various semiconductor (e.g. TiO_2) Schottky barrier energy "filters", however, can be employed both to promote charge separation and provide some control over the hot carrier energy distribution that participates in the chemical processes,[125, 123] e.g. by only collecting the highest-energy electrons and holes.

Indeed, a promising area for nanocatalysis includes nonuniform coatings of electron and hole "filter" materials, along with additional catalytic material coatings (e.g. Pt nanoparticles) such that invidual nanoparticles serve both as the anode and cathode with strong charge separation and sensitivities to both electron and hole reactions (also to ensure proper charge neutralizaton).[125, 201] In this direction, one also encounters opportunities for few-nanometer-scale site-selective catalysis, either via nanoparticle design[165] or by active optical control over the hot spot regions of highest hot carrier density and transfer efficiency.[31] This leads to intriguing new capabilities for optimization and ultrafast (possibly even coherent) control over chemical reactions. Such work, however, will require a thorough understanding of hot electron distributions and dynamics, toward which this thesis is directed.

1.3.2 Photodetection and Photovoltaics

Two other related areas of high interest in hot carrier science are next-generation photodetectors[95, 23] and photovoltaics,[30] both involving excited charge transfer to a surrounding semiconductor medium, such as TiO_2. So long as the carriers can be efficiently transferred over the Schottky barrier,[131] such applications can benefit from broadband plasmonic ensembles, heterostructures, or arrays that absorb nearly all of the incident radiation in the solar energy range. Both photodetectors and photovoltaics would benefit from enhanced broadband sensitivity, while photodetectors could also be designed with sensitivity to frequency and/or polarization (e.g. via spatially-varying nanostructure arrays[95]) for direct spectroscopic and polarimetric readout. Indirect vs. direct charge transfer pathways are also crucial to these systems.[202] A detailed understanding of volume and surface photoexcitation/injection pathways will allow for geometry-optimized nanostructures for the highest collection efficiencies within the short hot carrier lifetimes. In other words, designing metal nanostructures in which most hot carriers are either excited directly at the metal-semiconductor interface or are within an inelastic mean free path of the interface (with the appropriate directionality for efficient transfer) will require a detailed understanding of hot carrier excitation mechanisms, spatial distributions, momentum distributions, and temporal decay dynamics. While the results described herein are for multiphoton excitation/emission into the vacuum, the general insights apply equally to the single-photon regime, as well as to other surrounding media, such as semiconductors.

1.3.3 Photocathodes

The most direct set of applications of the present work are those involving ultrafast photocathodes,[99] i.e. the generation of spatially and temporally coherent electron pulses in free space for use in femtosecond transmission electron microscopy,[211, 49] point projection microscopy,[154, 127] diffraction,[211, 127, 66, 191] x-ray generation,[150, 75, 138] rectified optical signal detection,[152, 90, 206, 89, 219] lightwave electronics and attosecond streaking measurements.[99] Whereas conventional flat surface photocathodes have spatial coherence limited by the mesoscale focal spot of the triggering laser,[3] leading to corresponding limited focusability and image blurring, chemically-etched gold and tungsten nanotips have emerged[76, 162, 130] as a highly-coherent photocathode with point-like spatially emission for high beam coherence. Not only are tip dimensions typically smaller than a few tens of nanometers, but the effective source size of electrons emitted from a hemispherical tip can be smaller still.[43] State-of-the-art etched nanotips have indeed been shown to yield electron beams with spatial coherence only an order of magnitude above the quantum uncertainty limit, with femtosecond temporal coherence.[49] However, although the large shafts of etched nanotips lead to ready manipulation and positioning in many photocathode systems (including with respect to a surrounding electrodes for beam focusing and other manipulation) such systems are incompatible with nanoscale and/or on-chip configurations. Such nanoelectronic and on-chip electron beam probing applications are nascent, but will require carefully-controlled, fully nanoscale cathodes.

It will be shown in detail in Chapter 5 that gold nanostars with ultra-sharp (3.4 nm) tip radii serve as exceptional nanoscale counterparts to etched nanotips, with multiple tips and resonances for optically-controlled switching/steering of the directional emission and beam coherence properties approaching those of the etched nanotip beams. Such nanoparticles or comparable nanostructures could be readily integrated into existing on-chip nanoscale circuits, as demonstrated recently for THz nanoelectronics.[89, 219] Furthermore, the *per-*

turbative rather than strong-field emission properties are examined herein for these systems in order to achieve minimal energy spread (and thus optimal temporal coherence) as well as to mitigate heating.

1.4 Volume- and Surface-Mediated Photoelectric Effects

Following the work of Hertz, Einstein, and others around the turn of the twentieth century in explaining the photoelectric effect from an energy conservation standpoint, leading to a watershed in quantum mechanics, the question of momentum conservation was pending a more detailed development of the energy structure of solids. Despite the simplicity of Fowler theory and its success in predicting near-threshold photoemission efficiency curves,[52] the actual photoexcitation mechanisms were not addressed, although the theory invoked the notion that all of the excitation kinetic energy should go into the surface-normal velocity coordinate and thus implied a surface-mediated excitation mechanism. The surface vs. volume/bulk photoemission dichotomy for momentum conservation in photoexcitation/emission was introduced around the same time by Tamm and Schubin.[186] While the elucidation and theoretical treatments of various photoemission mechanisms has substantially evolved over the years, the fundamental volume vs. surface dichotomy has remained intact. These mechanisms will now be defined, with details of their corresponding spatial and momentum distributions in nanoplasmonic systems described in later chapters.

Volume excitation mechanisms are those that do not require the presence of a surface, in which momentum is conserved during photoexcitation via direct lattice-mediated or indirect phonon-, defect/impurity-, or electron-mediated excitations. The presence of a nearby surface is merely a practical necessity to observe subsequent photoemission. Volume emission contributions depend on $|E|$ and are related to the $A \cdot \nabla$ term in the light-matter interaction Hamiltonian (in the velocity gauge) in addition to third-body scattering terms. Such excitations are completely dominant, for instance, in studies of flat gold film excited via normally-incident laser light (thus the surface-normal field $|E_\perp| \approx 0$).[145] While understanding the precise volume excitation amplitudes for the various coherent (via virtual states) and incoherent (via intermediate state population) multiphoton excitation pathways remains a challenging problem, it has been argued that plasmon-mediated multiphoton excitation is typically a coherent process.[121, 63] Nonetheless, the absence of direct/interband excitations from the Fermi level to above the vacuum level for the current photon energy range (1.2–1.8 eV) indicates that at least one phonon or other indirect scattering event must take place during coherent multiphoton excitation to populate the final state. For instance, a coherent four-photon excitation above the vacuum level will require a final phonon scattering event.[145] Most of the presentation herein remains agnostic to the precise volume mechanism(s), as these do not meaningfully influence the analysis or conclusions but instead remain an interesting problem for further resolution on nanoplasmonic hot electron dynamics.

Surface excitation mechanisms, by contrast, are those that rely on momentum non-conservation due to translational symmetry breaking at the surface potential barrier, i.e. from strongly spatially-varying fields or wavefunctions. These contributions depend on $|E_\perp|$ and are related to both the $A \cdot \nabla$ term (e.g. due to evanescent external electron wavefunction or surface states) and $\nabla \cdot A$ (due to surface field variation) terms in the light-matter interaction Hamiltonian.[57] While the $\nabla \cdot A$ term is now often referred to as the "surface effect" in itself,[78] the original surface photoeffect theories only considered the $A \cdot \nabla$ term,[57] which should be considered for surface processes as well. Surface excitations are dominant, for instance, for gold nanostars with sharp tips and therefore extra-strong surface hot spots,[144] along with a variety of other systems in the multiphoton intensity regime.[180, 118] Surface-like tunneling emission is a given for strong field processes.[106] In the modeling to be presented in Chapter 3, coherent multiphoton surface-mediated excitation are considered,[144, 203] with the predominant excitation density occurring just outside the surface in the few-Å region of overlapping plasmonic field and external electron density.

Some ambiguity can begin to occur in very small (< 20 nm) nanosystems with geometric confinement becoming prominent,[117, 128] although such effects could still be treated within the surface vs. volume framework (i.e. treating it as diffuse volume-like excitation[117]). Some ambiguity may also exist with surface-phonon-mediated excitation or excitation from surface states. Taking surface states as an example: Surface states are clearly a surface-like feature, but they contribute some generic charge density within the volume that could be excited in a volume-like manner, i.e. depending on $|E|$ rather than $|E_\perp|$ with momentum conserved via volume-like phonon scattering. However, the intrinsic momentum non-conservation due to the highly-varying spatial fields along the surface direction can be expected to lead to much higher cross-sections for a direct surface-mediated excitation, i.e. depending on $|E_\perp|$ with momentum conserved via "surface scattering". Thus, in practice, surface states should lead to predominantly surface-mediated emission as defined above (although these are not expected to contribute appreciably in any of the present studies). This also highlights that the surface and volume processes are not defined by a particular length scale (e.g. electron scattering length or optical skin depth) but rather by the fundamental mechanisms for momentum conservation in the optical excitation matrix elements.

1.5 Angle-Resolved Photoemission Measurements

Even without angular resolution, photoemission spectroscopy of single plasmonic nanoparticles can provide a wide range of information on the plasmon resonances, multiphoton excitation processes, and total photoemission cross-sections.[171, 172, 65, 64, 62, 12] By varying the visible excitation laser intensity and measuring the total photoemission rate, one can determine the multiphoton process order via power-law fit ($n\text{PPE} \propto I^n$) or observe deviations from this behavior due to thermionic or strong-field emission.[75] By varying polarization and frequency, one can map out nanoparticle resonances in 2D optical parameter space,[144] which can be particularly rich for complex, multi-resonant geometries. The photoemission rate is extremely sensitive to the field enhancement, with $|E/E_0| = 10$ leading to a 10^6-fold increase in the photoemission rate for a 3-photon process. Far-field polarization-, frequency-, and intensity-dependent studies can therefore serve to map out the near-field plasmonic hot spots and some details of the hot electron dynamics/distributions, particularly when the nanoparticle geometry is subsequently correlated with electron microscopy and, perhaps, simulated via electromagnetic finite element or finite difference numerical methods.

The introduction of photoelectron velocity resolution provides substantial additional insight into the near-field hot electron dynamics. The implementation of velocity map imaging (VMI) to be introduced here for studying surfaces and supported nanoparticles is motivated by the enormously successful application of the technique in molecular spectroscopy and dynamics,[178, 197] while also drawing inspiration from angle-resolved photoemission spectroscopy (ARPES) on surfaces. A number of ARPES techniques have been established over the years, including what may be considered "conventional" ARPES using a hemispherical analyzer,[35, 196] more recent angle-resolved time-of-flight (AR-ToF) setups using a delay line detector for concurrent 3D detection,[196, 70, 36] and momentum imaging using a PEEM column and two hemispherical analyzers.[98] Time-, position-, and 1D energy-resolved PEEM also provides impressive capabilities for studying single-nanoparticle plasmonics and electron dynamics,[15, 161] and nanoARPES techniques are emerging for simultaneously high spatial and angular resolution.[163] All of these techniques offer different advantages, but only recently have two techniques been developed for angle-resolved, resonantly-excited single-nanoparticle photoemission spectroscopy studies at UV–visible–NIR frequencies: a time-of-flight momentum-resolving electron microscope (ToF k-PEEM)[106] and the scanning photoemission spectroscopy technique using VMI to be discussed herein.[145] With the latter technique, some of the most important experimental capabilities for comprehensive angle- and momentum-resolved photoelectron studies of single nanoparticles are demonstrated using the relatively simple, cost-effective, and versatile scanning photoemission microscopy/spectroscopy system. Some goals for these studies include (i) the measurement of low-energy (near threshold) photoelectrons produced via nonlinear emission following visible-photon plasmonic excitation, (ii) efficient and reproducible access to large numbers of addressable nanoparticles for correlated studies and statistics, and (iii) the ability to collect and characterize photoemission from the full 2π upper-half-space solid angle without sample manipulation (i.e., tilting). Also of crucial importance are high photoelectron collection efficiencies, such that nanoparticles may be investigated with low integrated pulse energies (which for femtosecond pulses may nevertheless correspond to high peak intensities) to minimize heating, melting, and ponderomotive forces, thereby permitting focus on photoemission processes relevant under truly perturbative laser intensity conditions. This technique is described in detail in Chapter 2.

1.6 Ultrafast Nanoscale Photocurrent Control

The primary goal of this research is to demonstrate new capabilities for measuring, predictively modeling, and ultimately optically controlling nanoscale photocurrents on ultrafast (i.e. femtosecond, approaching attosecond) timescales. Experimental angle-resolved photoelectron spectroscopy studies will prove essential for developing simple yet accurate models for femtosecond hot electron dynamics. These models can then be utilized to predict hot electron spatial and momentum distributions (and temporal dynamics) in arbitrarily complex nanoparticle geometries. In demonstrating these capabilities, a variety of optical photocurrent control mechanisms will be uncovered. In particular, control over hot carrier photocurrents can be achieved via (i) optically selecting plasmon resonance modes and their corresponding surface field distributions (hot spots) and volume field distributions, (ii) optical control over the surface vs. volume cross-sections, and (iii) with synthetically- or lithographically-controlled nanoparticle coatings. Methods (i) and (ii) will be addressed in detail for various nanoparticle and hot spot geometries, while upcoming results via method (iii) will be presented as well.

With applications in ultrafast information processing (preserving Moore's law by going faster as we approach fundamental size limtations), ultrafast nanoelectronics,[89, 173] femtosecond electron spectromicroscopy,[127] and coherent control over nanoscale chemistry[31, 55] in mind, detailed nanometer/femtosecond spatiotemporal photocurrent control is highly desireable. However, controlling photocurrents has remained surprisingly challenging, with the primary demonstrations thus far requiring specialized materials and/or strong, highly-tailored optical fields. Photocurrent polarity, for example, has been controlled via the circular photogalvanic effect in topological insulator systems,[119] carrier-envelope-phase sensitivity in dielectrics exposed to strong optical fields,[167] and perturbative[179] or strong-field quantum pathway interference in graphene.[73] Some level of angular control has also been demonstrated with etched nanotip (Au or W) emitters.[136, 204] By comparison, plasmonic nanodevices provide two essential benefits: (i) Versatility, with extensive angular control on few-femtosecond (or faster) timescales and few-nanometer spatial scales, along with (ii) simplicity, utilizing available nanofabrication/synthetic techniques and standard tabletop laser technologies for optical current control that can be readily integrated into a wide variety of existing nanocatalytic, photovoltaic, or nanoelectronic systems.

Chapter 2

Experimental Methods

The next generation of hot carrier devices, such as photocathodes, targeted drug delivery agents, photodetectors, and photocatalysts for solar fuel production, will require a higher level of design and control over the nanoscale, femtosecond hot carrier charge transfer and emission. Presently, most hot carrier applications simply take advantage of the high carrier densities excited within nanoplasmonic systems, with little regard for where the electrons are excited (spatially) and where they go from there (temporal dynamics and momentum distributions). Although a number of techniques have emerged to address these questions via nanoscale hot electron spatial mapping,[40, 165, 74] only recently have studies begun to directly address the critical momentum degrees of freedom.[106, 107] As a consequence, there remains a significant gap in understanding, optimizing, and actively controlling hot carrier excitation and emission dynamics.

Toward this end, a unique photoelectron spectroscopy system has been built up to study photoemission from individual nanoparticles as a function of input laser frequency, polarization, intensity, and femtosecond pump-probe time delay. Furthermore, using a simple three-electode electrostatic lens system in a velocity map imaging configuration[44] and a spatially-resolved electron detector, the photoelectrons are collected with 2D (v_x, v_y) angular resolution. With picosecond time-of-flight resolution, v_z can also be measured to acquire the full 3D photoelectron velocity distribution.[109] When correlated with scanning electron micrographs, finite element electrodynamics simulations, and 3D photoemission modeling, such measurements provide a wealth of information on the spatial and momentum distributions of hot electrons excited in various nanoplasmonic geometries. Recent studies have begun to elucidate these hot electron distributions and dynamics, but capabilities for the predictive theoretical modeling and design of next-generation nanoplasmonic systems will require more extensive experiment-theory comparisons. Theoretical methods are addressed in Chapter 3, while the present chapter provides a detailed description of our unique single-nanoparticle, angle-resolved photoelectron spectroscopy technique.

2.1 Scanning Photoelectron Imaging Microscopy

Scanning photoemission microscopy involves raster scanning a sample stage over a (diffraction-limited) laser spot and collecting the emitted photoelectrons as a function of position. In this way, individual nanoscale objects can be located and studied as a function of laser parameters such as polarization, frequency, and intensity. By combining such capabilities with velocity-resolved photoelectron detection, a substantial amount of information on near-field electron excitation and emission dynamics can be directly measured and/or reconstructed. We refer to this technique as scanning photoelectron imaging microscopy (SPIM), encompassing the scanning microscopy technique as well as the photoelectron velocity map imaging (VMI) collection scheme, discussed in detail below. By further correlating the SPIM measurements with scanning electron microscopy (SEM) or atomic force microscopy (AFM), along with correlated electromagnetic simulations, many details of the hot electron excitation/emission distributions and dynamics in nanoscale systems are revealed.

The SPIM system is illustrated in Fig. 2.1. While this unique and relatively simple configuration for photoelectron spectroscopy is primed for new insights into nanoscale systems, thin films, 2D materials, and perhaps eventually single molecules, the focus here is on the photoemission properties and hot electron dynamics of plasmonic nanoparticles. Due to their strong nanolocalized field enhancements, plasmonic metal nanoparticles that fill only a small fraction of the diffraction-limited laser spot can still dominate the photoemission by orders of magnitude over the conductive substrate (e.g. ITO) background. This is illustrated in the example SPIM scan of gold nanoshells in Fig. 2.1, which demonstrates the high signal-to-background, along with the spatial mapping resolution, which is actually sub-diffraction-limited due to the n-th order multiphoton excitation (with spot diameter $\lambda/(2\mathrm{NA}\sqrt{n})$).

2.2 Ultrafast Laser and Optics Systems

2.2.1 Laser System

The highly-tunable ultrafast laser system consists foremost of a modelocked Ti:sapphire oscillator (KMLabs Swift) running at 75 MHz and generating ∼40 fs pulses with up to ∼1.75 W of average output power. Modelocking is passively achieved via Kerr lensing in a "soft aperture" configuration (i.e. where the cavity loss for the continuous wave vs modelocked/pulsed mode is determined by the cavity optics rather than an additional hard aperture). The gain bandwidth of the Ti:sapphire crystal and the adjustable dispersion characteristics of the cavity allow for tuning between 675–980 nm. Four piezo-motor-controlled degrees of freedom are present for tuning the cavity dispersion: (i) dispersing prism insertion, (ii) collimation prism insertion, (iii) tuning slit position, and (iv) tuning slit width. By adjusting all four degrees of freedom, the oscillating mode can be tuned over the full range while maintaining similar pulse duration via appropriate bandwidth settings. A calibration file is generated manually and the values are interpolated for automated tuning over the full range. The cavity air is purged (primarily of water) via circulation through both desiccant and molecular sieve (Drierite), with regular replacement or desiccant regeneration multiple times a year required to maintain $< 1\%$ cavity humidity, particularly if the cavity is opened frequently for alignment. The humidity is monitored via a wireless sensor and low humidity is essential to stable operation at the furthest near-IR settings (> 925 nm). Even so, the cavity always remains highly unstable in the 930-950 nm range due to residual water vapor

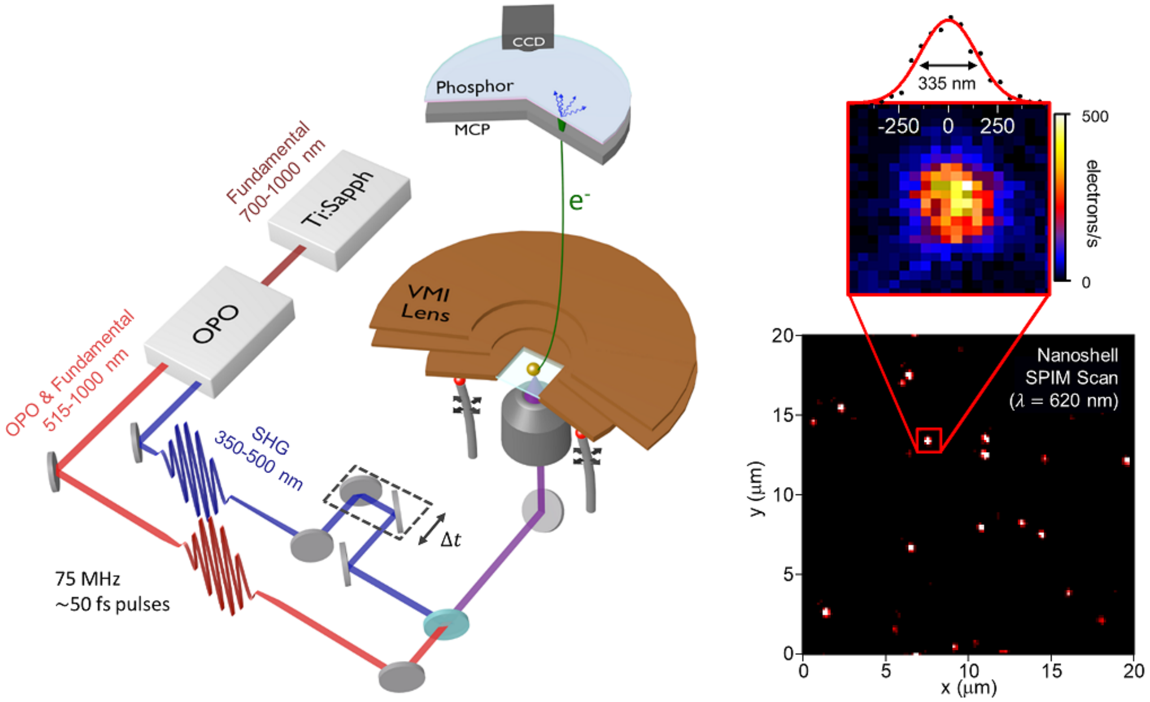

Figure 2.1: Overview of the SPIM apparatus and example SPIM scan. Photoelectron counts are collected as a function of sample position as the stage is raster scanned in the xy plane. While the illustration shows the pump-probe capabilities, the example scan and most studies presented herein are performed with single-color multiphoton excitation. Signal-integrated SPIM intensity maps allow for single-particle identification, as shown for gold nanoshells on ITO with excitation at $\hbar\omega = 2$ eV (620 nm). The 335(12) nm FWHM measured in the single-particle subscan agrees well with expectation of 340 nm, determined via convolution of the diffraction-limited laser spot size, 620 nm/2NA$\sqrt{3}$, with the 164 nm particle diameter, with a factor of $\sqrt{3}$ in the denominator to account for the three-photon photoemission process.

and strong absorption by a vibrational overtone or combination band thereof.

The Ti:sapphire cavity is operated with either a 10% or 20% output coupling (OC) mirror, which must be manually exchanged. The 10% OC leads to less loss and therefore greater tunability over the full cavity range, but with less overall output power ($<$ 1 W with 8–8.5 W pump power for stable operation). The 10% OC is therefore utilized when using the oscillator fundamental itself, i.e. when operating in the 675–980 nm tuning range. By contrast, the 20% OC leads to more cavity loss and less stability/tunability (typically $\sim$750–850 nm) but much higher output powers (up to $\sim$1.75 W with 9.5–10 W pump power) for subsequently pumping the second harmonic generation (SHG) and optical parametric oscillator (OPO).

Both SHG ($\chi^{(2)}(2\omega = \omega + \omega)$) and subsequent OPO (via difference frequency generation, $\chi^{(2)}(\omega_{\text{signal}} = \omega_{\text{pump}} - \omega_{\text{idler}})$) are generated with beta barium borate (BBO) crystals. Commensurate with the oscillator tuning range, the SHG is tunable between $\sim$350–490 nm, with typical conversion efficiency around 30% and peak powers greater than 650 mW achieved at 400 nm for 1.75 W fundamental power (20% OC). When pumped with $>$600 mW of SHG power at 400 nm, the OPO is tunable between 520–780 nm with output powers above 100 mW across much of the range. Thus, between the SHG, OPO, and fundamental outputs, the laser system is widely tunable across the entire visible range, while also reaching into the UV and near-IR.

2.2.2 Dispersion Compensation

Consider a narrow-band optical pulse traveling through a dispersive medium, with linewidth small enough that the wavevector ($k(\omega) = 2\pi n(\omega)/\lambda$ for real/dispersive refractive index component $n(\omega)$) can be reasonably expanded about some center frequency, ω_0:

$$\begin{aligned} k(\omega) &= k(\omega_0 + \delta\omega) \\ &\approx k(\omega_0) + k'(\omega)\Big|_{\omega_0} \delta\omega + \frac{1}{2} k''(\omega)\Big|_{\omega_0} \delta\omega^2 + \ldots, \end{aligned} \tag{2.1}$$

in which

$$\begin{aligned} k(\omega_0) &= \frac{\omega_0}{v_p(\omega_0)}, \\ k'(\omega)\Big|_{\omega_0} &= \frac{1}{v_g(\omega_0)}, \\ k''(\omega)\Big|_{\omega_0} &= \frac{v_g'(\omega)\Big|_{\omega_0}}{v_g(\omega_0)^2}, \end{aligned} \tag{2.2}$$

where $v_p = \omega/k = c/n$ is the phase velocity and $v_g = d\omega/dk$ is the group velocity. The zeroth-order term is therefore simply the overall phase lag due to traveling in a medium. The first-order term accounts for the group (pulse envelope) velocity through the medium, leading to a carrier-envelope offset phase. The second-order term accounts for the dispersion in group velocities for different carrier frequencies; i.e., if one imagines that the pulse is composed of many different sub-pulses with different carrier frequencies, these will spread out in a frequency-dependent dispersive medium (leading to pulse broadening and chirping). This is known as group velocity dispersion (GVD) and is the primary mechanism for femtosecond pulse broadening in materials. Higher-order terms will have additional pulse broadening and nonlinear chirping effects. Note that all of these effects are *linear* optical effects—i.e. depending on refractive index $n(\omega)$ (isomorphic with $\chi^{(1)}(\omega)$ when including the imaginary part) and independent of the field strength. Second- and higher-order dispersion are merely terms in the Taylor expansion of $n(\omega)$. This linearity is indeed crucial for pulse dispersion compensation, to be discussed.

The respective effects of each of these terms become clearer by writing out the electric field in terms of its Fourier transform:

$$\begin{aligned} E(t) &= \int \tilde{E}(\omega) e^{-i\omega t} d\omega \\ &= e^{-i\omega_0 t} \int |\tilde{E}| e^{ik(\omega_0+\delta\omega)z} e^{-i\delta\omega t} d(\delta\omega) \\ &= e^{i(k_0 z - \omega_0 t)} \int |\tilde{E}| e^{i(k'(\omega)|_{\omega_0}\delta\omega + \frac{1}{2}k''(\omega)|_{\omega_0}\delta\omega^2 + \ldots)z} e^{-i\delta\omega t} d\delta\omega, \end{aligned} \tag{2.3}$$

which has been separated into the carrier frequency (the exponential term out front) and the pulse envelope (the Fourier integral). The offset between the carrier (traveling at $v_p(\omega_0)$) and the envelope (traveling at $v_g(\omega_0)$) is known as the carrier-envelope offset (CEO) phase, described by the first-order dispersion term. This is seen more clearly by rearranging Eq. 2.3:

$$\begin{aligned} E(t) &= e^{i(k_0 z-\omega_0 t)} \int |\tilde{E}| e^{i(k'(\omega)|_{\omega_0}\delta\omega + \frac{1}{2}k''(\omega)|_{\omega_0}\delta\omega^2+\ldots)z} e^{-i\delta\omega t} d\delta\omega \\ &= e^{i(k_0 z-\omega_0 t)} \int |\tilde{E}| e^{i(\frac{1}{2}k''(\omega)|_{\omega_0}\delta\omega^2+\ldots)z} e^{-i\delta\omega(t-k'(\omega)|_{\omega_0}z)} d\delta\omega, \end{aligned} \tag{2.4}$$

such that $t \rightarrow t - k'(\omega)|_{\omega_0} z$, and

$$\phi_{\text{CEO}} = \omega_0 k'(\omega)|_{\omega_0} z. \tag{2.5}$$

The GVD of a material is an intrinsic physical property, typically reported in units of fs^2/mm, and for many glasses in the visible range is around 100 fs^2/mm. Group delay dispersion (GDD) is simply the GVD multiplied by the length of the material, and is therefore an extrinsic property with units of fs^2. Upon solving the inverse Fourier transform in Eq. 2.4, one finds that the pulse broadening effect is described (for a Gaussian, BW-limited pulse) by

$$\Delta t_{\text{f}} = \frac{\sqrt{\Delta t_{\text{i}}^2 + 16(\ln 2)^2 \text{GDD}^2}}{\Delta t_{\text{i}}}. \tag{2.6}$$

Higher-order terms such as third-order dispersion (TOD) lead to additional (asymmetric) pulse broadening, nonlinear pulse chirp, etc. These higher-order terms are typically determined via numerical pulse propagation modeling.

Except in regions of anomalous dispersion near a resonance, GVD in glass is positive; e.g. +45 fs/mm^2 in fused silica. Thus, to compensate for material GVD, some negative GVD elements must be introduced into the system, such as chirped mirrors, diffraction gratings, or prisms. Given that GVD is still a linear optical process, dispersion compensation can be performed anywhere in the system, including before or after the positive GVD elements, or anywhere between. Overshooting with too much negative GVD leads to the same detrimental effects on pulse durations as positive GVD, readily seen as Δt_f depends only on GDD^2 in Eq. 2.6. It is thus often necessary—particularly in systems with frequency-tunable pulses or variable material path lengths—to introduce a tunable negative GVD dispersion compensating element. This is achieved here using an ultrafast prism pair with a retro-mirror—i.e. a "prism compressor". In this configuration the laser pulse is dispersed by the first prism, collimated by the second prism, then returns via retroreflection to be focused by the second prism and re-collimated by the first prism. A slight downward angle is imposed so the return beam can be picked off by a half mirror. While positive GVD leads to a positive chirp with lower/redder frequencies at the front of the pulse, negative GVD of this prism system is achieved via configuring the prisms for longer total optical path length for longer wavelengths. While blue frequencies refract more from the first prism and ultimately travel longer distances in air, the red frequencies travel much longer distances within the second prism, leading to an overall longer optical path length ($\int n \mathrm{d}l$) for the redder frequencies and thus negative GDD.

2.2.3 Pulse Characterization

Pulse characterization is achieved by the typical means, including intensity autocorrelation and frequency-resolved optical gating (FROG),[188] which split the beam, vary the time delay between the two pulses, send them into a BBO crystal, and measure the output SHG power or power spectrum, respectively. While the intensity auto-correlation simply measures the symmetrized pulse intensity, FROG provides enough information to also retrieve the phase information and thereby reconstruct the electric field. As shown via the FROG trace in Fig. 2.2, the output pulses from the Ti:sapphire laser under typical operating conditions are measured to be ~50 fs, in reasonable agreement with the predicted bandwidth-limited pulse duration of ~40 fs.

More importantly, to characterize the pulses at the sample and optimize the relevant

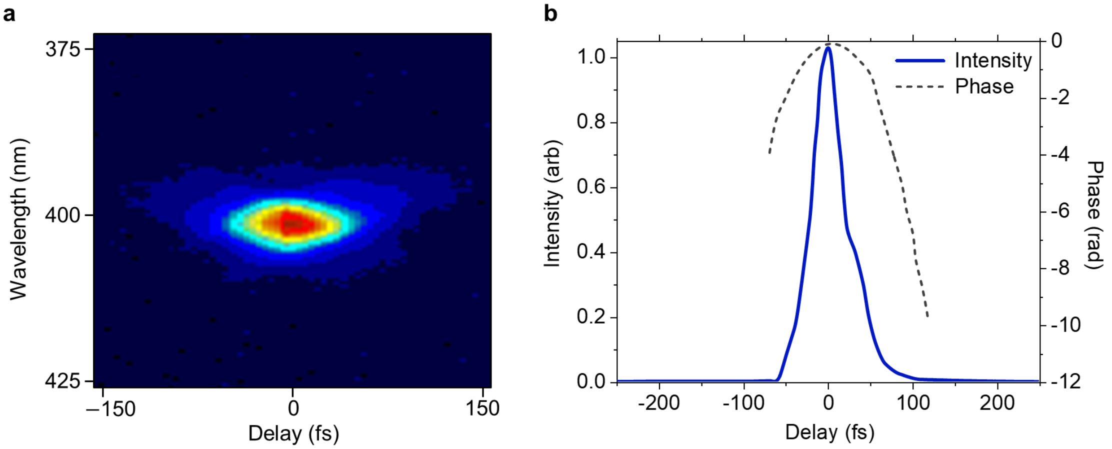

Figure 2.2: (a) FROG trace of a typical Ti:sapphire output pulse train. (b) Pulse intensity and phase retrieved from the FROG trace, with a Gaussian fit FWHM of 52 fs.

dispersion compensation, the built-in autocorrelation or cross-correlation capabilities of the nonlinear photoemission signals are exploited. As described in Section 2.9, an automated stepper motor translation stage in the SHG path is used to control the delay between pulses with ∼1 fs precision. First, the SHG pulse is split—one along the delay stage path and the other along a separate path—and recombined prior to the sample, i.e. in a Mach-Zehnder interferometer configuration. The $1 + 1$ pump-probe photoemission signal is measured as a function of delay time, thus yielding an intensity autocorrelation. Assuming an instantaneous response time for the sample, the pulse width is thus simply the autocorrelation FWHM/$\sqrt{2}$. The known SHG pulse duration is then used to measured the OPO or oscillator pulse durations via cross-correlation $1 + 1'$ pump-probe measurements. Note that the system is not suitably stable to resolve the interference fringes, and thus the auto- and cross-correlations are phase-averaged. However, with additional fine (piezo-actuated) stabilization, future phase-resolved interferogram measurements may be readily achieved.[143]

2.3 Vacuum System

The SPIM vacuum system is illustrated and shown schematically in Fig. 2.3. The system consists of a lower chamber (~90 L) which contains everything aside from the detector, including four unprotected flat silver mirrors redirecting the laser through the reflective microscope objective (Ealing 25-0548) onto the scanning sample stage, three quartered piezoelectric posts for fine positioning/scanning, the overall sample positioning block holding the stage and objective, three coarse positioning piezomotors (New Focus Picomotor 8302), the three VMI electrostatic lens electrodes, the μ-metal shield, and a nest of wiring. This lower chamber is pumped by two turbomolecular pumps (TI: Pfeiffer TMU 261, T2: Pfeiffer TMU 071 P) for a total pumping speed of 260 l/s, neglecting conductance limitations of the system geometry. Both of these turbos are backed by a single dual-stage rotary vane pump (Leybold D16A). The typical base pressure of the lower chamber, measured via ion gauge with the gate valve to the upper chamber closed, is 4×10^{-7} Torr. In case of power failure, the turbos turn off and remain off, while the rotary vane turns back on when power is restored. To prevent oil backstreaming from the rotary vane pump in case of power failure, a relay interlock is set to close a pneumatic auto-off safety valve (Kurt J. Lesker ASVQF25-120A), such that when the power returns to the rotary vane it will be pumping on ambient through a highly conductance-limited channel (thus limiting the gas load) rather than directly on the chamber without the turbos on. A zeolite molecular sieve further prevents any backstreamed oil from creeping into the foreline or system, which is occasionally baked and regenerated *in situ* with the rotary vane pump on and the foreline valve closed.

The upper chamber (~10 L) contains the microchannel plate (MCP) detector (Beam Imaging Solutions, BOS-75 with OPT01 (Chevron)), which is highly sensitive to oil and water vapor contamination and must be kept below 2×10^{-6} Torr during operation to prevent shorting and MCP damage. Prolonged storage below the room-temperature water vapor pressure (~ 15 Torr) is recommended, along with extended pumping and a slow voltage ramp-up cycle (see user manual) prior to subsequent operation. To maintain a high level of cleanliness in this chamber, a gate valve is situated between the lower and upper chambers that remains closed except when operating. The upper chamber has a dedicated turbo (T3: Hi-Pace 80, 67 l/s) with a dedicated oil-free diaphragm backing pump (Pfeiffer MVP 040-2). With the gate valve closed, typical upper chamber pressures are around 2×10^{-7} Torr and around 3×10^{-7} Torr with the gate valve open. These nominal pressures can be achieved within 2–3 hours of pumping down the system from ambient (e.g. after sample replacement), although minimum operating pressures $< 1\times10^{-6}$ Torr can usually be achieved within 1–1.5 hours of pumping down, so long as the chamber was only opened briefly for sample exchange. For a future improvement, it would be prudent to install an additional gate valve on the chamber-side of the upper turbo, thereby allowing for high-vacuum storage, currently limited by the few-Torr backing pressure of the diaphragm pump.

2.4 Sample Preparation

Samples for correlated photoelectron spectroscopy studies must be both (i) largely transparent across the visible excitation range and (ii) Ohmic with suitably low resistance for nanoparticle reneutralization between photoemission events. While glass coverslips with thin (~10 nm) metal films, such as Au or Pt, have been utilized successfully, similarly thin transparent conductive oxide films tend to have particularly high transmission (~90%) across the visible range and particularly low photoemission cross-sections for minimal background signal. Indium tin oxide (ITO) on glass is the most widely-manufactured substrate and is commonly utilized for supported photoemission studies.[64, 75, 106] Borosilicate coverslips (170 μm thick) with 10 nm ITO films are prepared commercially by Thin Film Devices, Inc. via sputtering deposition in a large (6×6 ft) chamber for optimal homogeneity, with an ultimate RMS area roughness < 1 nm, sheet resistance around 1 k$\Omega/\Box$, work function $\phi_{\text{ITO}} \approx 4.2$ eV, and background levels that are typically multiple orders of magnitude lower than plasmonic nanoparticle photoemission signals.[64]

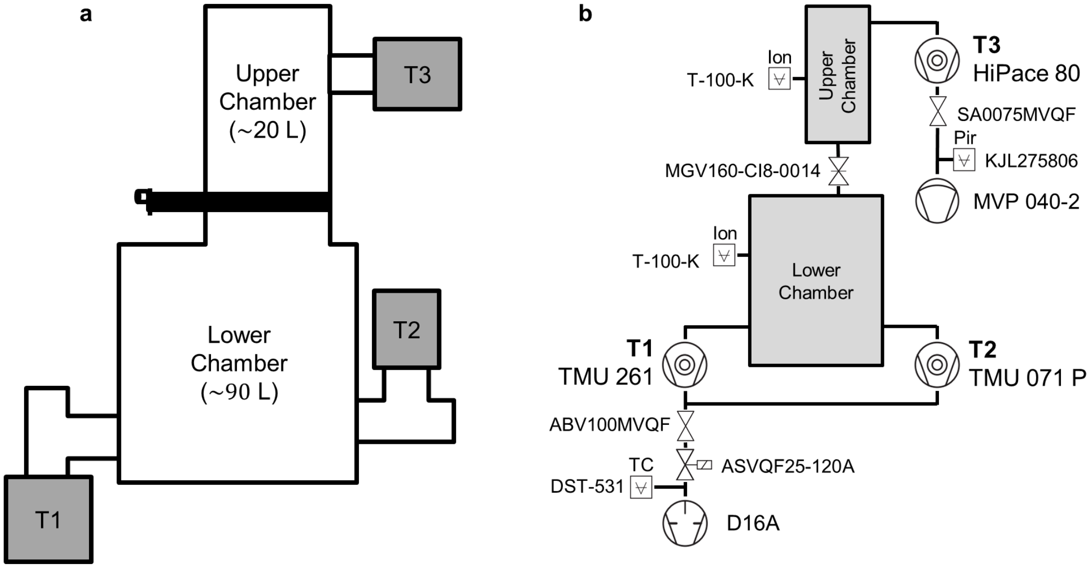

Figure 2.3: (a) Illustration of the vacuum system chambers and turbo pumps (T1-3). (b) Schematic version with all valve, gauge, and pump model numbers.

Correlated particle location ("registration") is achieved by depositing an alphanumeric Au grid on top of the ITO via negative photomask lithography. The grid is generated using negative UV photoresist with an uncoated copper TEM grid (LF-400) as the mask. A 5 nm Ti adhesion layer is deposited onto the exposed ITO regions prior to the 50 nm Au layer via e-beam evaporation. Following overnight resist removal via acetone soaking and gentle acetone-soaked cotton-tipped applicator removal of any lingering Au leaflets within the narrow grid regions, the ITO substrate sheet resistances and photoemission properties within SPIM remain unchanged from non-gridded samples. However, one or two instances occurred when using expired and perhaps over-baked resist in which the samples came out with ∼5-fold higher sheet resistances and ∼3-fold lower photoemissivities in SPIM, potentially due to residual resist.

Aqueous nanoparticle dispersions (synthesized commercially or via academic collaborators) are deposited onto registered ITO substrates via spin coating a 30–50 μL aliquot at 1500 rpm, following the appropriate dilution. With some variation due to nanoparticle size and stabilizing ligand effects (e.g. concentration-dependent micelle formation), concentrations of 3×10^{10} NP/mL (50 pM) are often optimal. These concentrations yield typical coverages of 0.05 nanoparticles/μm^2, or 20 particles in a 20 × 20 μm^2 scan area on average. Such coverages are ideal for efficient particle location and characterization via SPIM scans, while ensuring negligible probability of two particles overlapping within the same diffraction-limited excitation region. The full, typical deposition procedure is: 10 s vortex, 30 s sonication, 10 s vortex, dilute, 10 s vortex, dynamic 1500 rpm deposition onto a freshly UV-ozone-cleaned ITO substrate and drying via a 5 min spin. The UV-ozone cleaning of the ITO substrate for > 10 min (often > 30 min) up to deposition is essential for improving wetting by removing residual hydrocarbons. Dynamic spin coating is preferred to static drop casting as it prevents particle diffusion over the substrate, which can lead to aggregation during deposition.

For high-resolution TEM sample characterization, nanoparticle dispersions are dropcast onto carbon-coated TEM grids. Concentrations are adjusted for suitable coverages, but given the much broader range of acceptable coverages, full-concentration samples often yield suitable results with 5–10 min deposition times. A TEM-grid sample holder compatible with the VMI lens system has been implemented for correlated SPIM-TEM studies, but this is generally more challenging and the carbon substrate substantially damps the plasmon resonance. In most cases, nanoparticles cannot be resolved in SPIM above the background levels. New configurations such as ITO-coated SiN grids have been attempted, but grid damage during the coating process led to null results. Thus, capabilities for correlated TEM studies are limited to total count rate studies with no velocity resolution. However, opportunities exist in the future for very high-resolution (including potentially atomically-resolved TEM imaging) correlated angle-resolved photoelectron spectroscopy studies by finding a novel TEM grid configuration that is suitably robust.

2.5 Surface Cleaning

An important experimental "cleaning" protocol for achieving high-quality velocity maps is now briefly discussed. Essentially all nanoparticle velocity maps initially reveal a predominantly isotropic distribution peaking strongly at zero transverse momentum (see Section 5.1), which can be ascribed to inelastic scattering processes during photoemission. This occurs regardless of the cleaning method employed prior to loading the sample into the vacuum system (e.g. UV-ozone exposure, plasma cleaning, and/or solvent rinsing). Such effects are observed for all nanoparticles and most surfaces studied, and are attributed to brief (∼10 min) ambient air exposure between sample cleaning and loading into the vacuum chamber. However, as with similar demonstrations by the El-Sayed group with regard to Au-thiol ligand removal,[82] brief exposure of nanoparticle samples to second harmonic light (here ∼1 GW/cm^2 at 400 nm for ∼1 s, under high vacuum conditions) can serve to break surface bonds or remove surface adlayers, presumably due to hot electron transfer. In our VMI apparatus, this appears to eliminate the isotropically-scattered photoemission contribution near zero energy, thereby revealing the anisotropic photoemission distributions of primary fundamental interest, as demonstrated for gold nanoshells in Section 5.1. Most importantly, this procedure only eliminates the inelastically-scattered central peak near zero energy and has no observable effect on the underlying photoemission behavior, with the same directionality of the photoemission observed before and after 400 nm light exposure. Furthermore, this *in vacuo* laser cleaning is highly reproducible, yielding qualitatively identical results for every nanoshell studied and upon multiple venting/pumping cycles for the same nanoparticle. It can also be performed quickly and efficiently using the scanning stage to clean dozens of nanoshells in a target area prior to study.

While the precise scattering mechanisms remain unknown, the interaction appears to be primarily with an air (i.e., water) adlayer on the nanoparticle/ligand surface, evidenced by repeated cleaning → air exposure → cleaning studies of the sample nanoparticles. No additional changes are observed in the photoelectron momentum distributions for longer exposures or higher intensities, indicating that photoelectron scattering effects have been largely eliminated. Finally, this cleaning effect is only observed for ∼3.1 eV (400 nm) or higher-energy photons, with no significant effect evident even with higher intensities of the most energetic optical parametric oscillator output (∼2.3 eV photons). While further studies to explore the precise photoelectron-adlayer interactions would be warranted and interesting in themselves, here the cleaning remains a well-converged heuristic that eliminates unwanted post-emission inelastic scattering effects.

2.6 Scanning Sample Stage

While the tunable ultrafast excitation laser system and velocity-resolved detection system are essential to the work in this thesis, the custom scanning stage represents the heart of the SPIM system. The stage itself is custom-machined from copper with a removable central copper sample holder piece (Fig. 2.4), which can be selected for ITO-coated coverslips or TEM grids. ITO coverslips are positioned over the large hole in the stage for optical access and held down by a piece of copper shim with a large central hole for electron emission with minimal field distortion. The shim also establishes electrical contact between the sample stage and the sample ITO layer, and is held in place by a set of finger springs. With the TEM grid holder, the grid merely rests in a 3 mm alignment recess with no shim or other holder on top to prevent field distortion for velocity map imaging. A more conventional TEM grid holder arm that severely distorts the electrostatic lens field is also available and can be utilized for TEM-correlated non-velocity-resolved studies. In velocity map imaging studies, the entire sample stage acts as the repeller electrode and is held at large negative voltages (typically -4500 V).

The sample stage rests above the microscope objective on three ruby positioning balls held by three quartered piezoelectric posts for fine ± 20 μm xy scanning. The stage position is then controlled via applying voltages determined via the PID scanning software (see Section 2.10) through NI DAQ voltage output cards to be amplified via the piezo driver circuit (see Appendix) and applied to the appropriate post segments. Two small ($\sim$1 cm^2), electrically-isolated copper plates on the $+y$ and $-x$ sides of the sample stage couple to two nearby capacitive sensors ($\sim$1 mm gap at rest position) to read out the sample stage position for closed-loop positioning. The closed-loop scanning calibration is performed by imaging the photoemission from the C-flat substrate with a regular array of holes. Piezo calibration factors are adjusted to ensure the proper scan size, angle, and to eliminate distortion.

2.7 2D Velocity Map Imaging

Photoelectrons are mapped as a function of transverse (v_x, v_y) initial velocity onto transverse (x, y) final position on a spatially-resolved phosphor-MCP detection system. Velocity map imaging was originally introduced by Eppink and Parker in 1997[44] to overcome the limitations of grid electrodes in molecular photoionization studies.[27] In particular, electrodes with a wire grid/mesh were originally utilized to produce a nearly-uniform electric field, thereby mapping initial transverse velocity onto spatial detector position in a simple

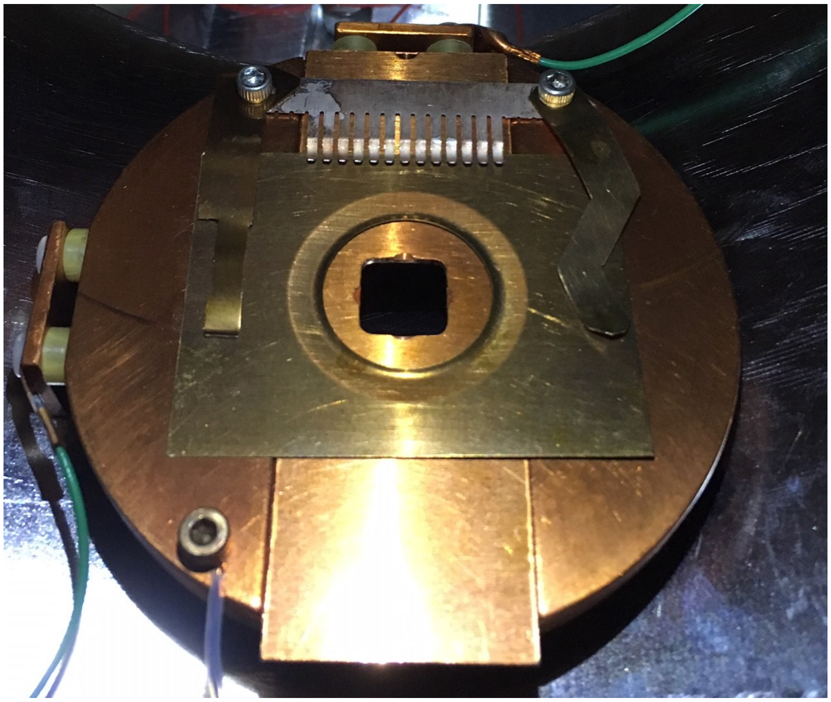

Figure 2.4: Copper sample stage with hole for optical access, shim to hold down and electrically contact ITO sample coverslip, and xy closed-loop positioning capacitive sensor plates.

manner. However, large excitation volumes (due to overlap of laser focal spot with molecular beam) in the tens of micron range or larger served to blur the final distributions. Furthermore, the grids led to charge collection and reduced collection efficiency, while also causing field distortions that led to further blurring of the final images. Eppink and Parker discovered that by instead using three electrodes (a repeller, extractor, and ground) with the extractor and ground electrodes having two central holes, enough degrees of freedom were present to generate a high-quality electrostatic lens for linear velocity-to-position mapping. Moreover, the lensing led to a novel property of the mapping being sensitive only to initial velocity rather than position, thereby reducing blurring due to the excitation volume, eliminating blurring due to mesh-related field distortion, and also eliminating photoion/photoelectron attenuation due to collection by the grid.

Here, the reduction in spatial blurring is not such an issue due to the nanoscale origin—however, it does allow for compensation of any offset from the electrostatic lens axis (i.e. imperfect laser-electrode alignment) that is bound to occur. The velocity map imaging electrostatic lens configuration is shown in Figs. 2.5 and 2.6, with the copper sample stage held at -4500 V serving as the repeller electrode, the copper extractor electrode ($\sim$1.8 cm hole diameter) placed 1 cm above the sample stage is held at -3700 V, and the ground electrode ($\sim$3.2 cm hole diameter) is placed 1 cm above that. Beginning just above the ground electrode, a μ-metal shield runs the length of the flight tube ($\sim$59 cm) to eliminate spatial drift due to the geomagnetic field. The voltages are applied via a single 5 kV power supply (SRS P350) and adjusted via a voltage divider between plates. The extractor-to-repeller voltage ratio of 0.82 is maintained for optimal focusing at the detector, while the overall voltage is adjusted to change the magnification. To prevent event overlap, counting-mode studies are often conducted at -500 V repeller voltage, for example. Distortions due to photoelectron proximity with the electrodes can occur for lower voltages (higher magnification) and must be treated with care if performing velocity mapping studies under these conditions.

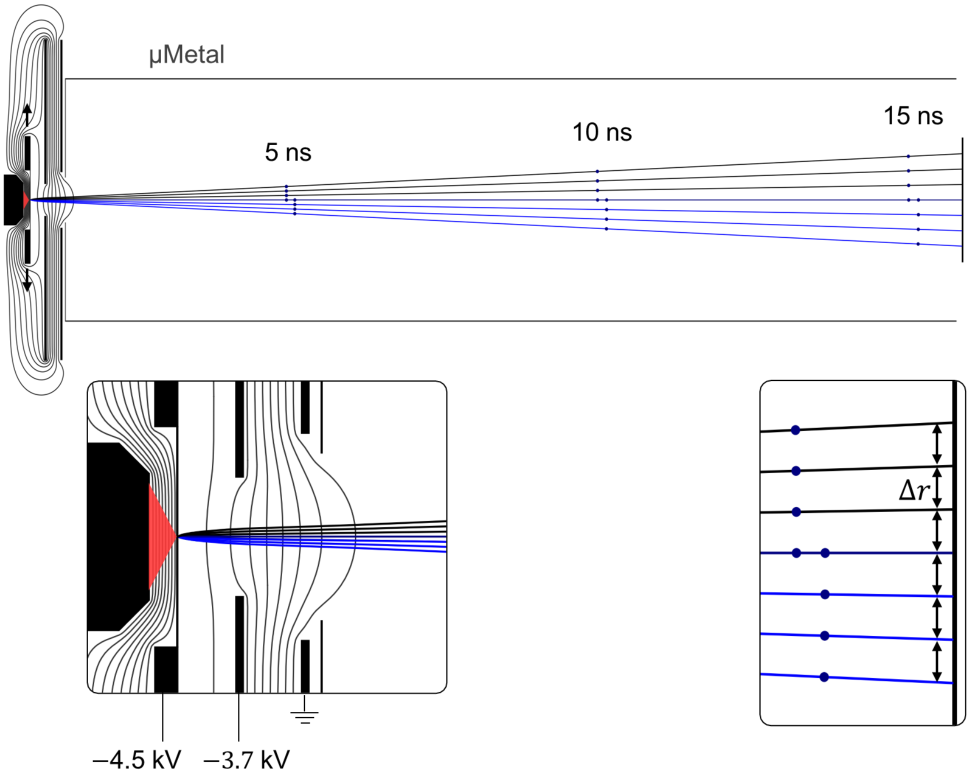

Figure 2.5: Simulation of electron trajectories and VMI equipotentials using *SIMION 8.0*, with equipotential lines displayed in 500 V increments and all distances to scale. A uniformly increasing transverse velocity $\Delta v_\rho = 0.44$ nm/fs, with outermost trajectories corresponding to $\frac{1}{2}m_e v_\rho^2 = 5.0$ eV) leads to a uniformly increasing radial displacement on the detector, increment $d = 8.82$ mm, which is constant within the 32 μm detector resolution limit (MCP pore pitch). This linear mapping is insensitive to v_z due to the strong immersive acceleration field at the sample ($\sim$1 kV/cm): the same linear mapping is achieved within instrument resolution for $\frac{1}{2}m_e v_z^2 = 0$ (black/left trajectories) and $\frac{1}{2}m_e v_z^2 = 10$ eV(blue/right trajectories).

The accelerated photoelectrons are focused onto a microchannel plate (MCP detector), where each 25 μm channel (32 μm pitch) acts as a continuous dynode electron multiplier. With a standard voltage of 0.9–1 kV applied across both of the two MCP plates arranged in a Chevron configuration (total 1.8–2 kV voltage differential), a single electron event is multiplied up to $\sim 10^7$ electrons with a log-normal distribution. Matched plates cut from the same die are utilized for optimal resistance (10 MΩ and 10.5 MΩ measured for the upper and lower plates, respectively) and gain matching. An external voltage divider can be utilized to control the plate biasing, but in this matched case the plates themselves serve as the voltage divider. A -40 V bias is applied to the front plate to reject slow electrons and thereby reduce background counts due to externally-generated events or backscattered events generated when photoelectrons impinge on the front plate area rather than in a pore. This noticeably reduces the background level by $\sim$50% while maintaining the same signal levels (a mere 40 V barrier will not block the 4.5 kV-accelerated photoelectrons). Due to the spatial correlation with the voltage connector wires, the primary source of such avoidable background counts appears to be electrons generated via field emission from hot spots on the bare connector wires.

The $\sim 10^7$ electrons leaving a single MCP pore (assuming good chevron pore alignment) are accelerated further onto the phosphor screen via a 3 kV differential between the phosphor and top MCP plate. This acceleration improves phosphorescence signal while preventing space-charge blooming of the electron clouds, to ensure the smallest spot sizes possible on the phosphor and thereby limiting event overlap on the camera. Spot sizes are measured to be around 500 μm, which indicates room for improvement compared with commercially-specified spot sizes of $\sim$200 μm. The 3+ keV electrons impinging on the P-47 (Y_2SiO_5:Ce^{3+}) phosphor plate (400 nm peak emission wavelength, 55 ns decay time, 0.06 photons/eV/electron quantum yields) generate photons that are collected by a CCD camera positioned outside of the vacuum system, imaging the phosphor screen through the phosphor-coated glass vacuum window (see Beam Imaging Solutions BOS-75 assembly). The events are centroided and coordinates compiled over tens of minutes to general 2D velocity maps with 10^5 counts or more. Pixel-to-velocity calibration is achieved via two methods: (i) fitting experimental Au film Fermi edges as a function of excitation photon energy, and (ii) *SIMION* electron trajectory simulations. *SIMION* was also employed to determine/verify the optimal extractor/repeller focusing conditions and is quite accurate for an accurate system model, as evidenced by agreement between the experimental and simulated calibration factors to better than 5% (Section 4.4).

2.8 3D Velocity Map Imaging

To extend the 2D velocity map imaging capabilities to full 3D angle-resolved photoelectron velocity mapping, the photoelectron time-of-flight can be measured. This is a significant challenge, however, due to the mere 200–300 ps time-of-flight spreads for a ∼ 1 eV electron beam kinetic energy spread, as timing resolution must be a few tens of picoseconds. This can be achieved via delay line detectors,[193] but Wen Li and coworkers have recently demonstrated simple methods for converting 2D VMI to 3D VMI systems by instead simply reading out the transient MCP currents and sampling the event pulses with an ultrafast (>2 GHz) digitizer.[104, 105, 109, 46, 45] While their methods utilize a regeneratively amplified (∼1 kHz) laser that triggers both the camera and digitizer collection, the 75 MHz collection rate utilized here requires a different method. The scheme is shown in Fig. 2.7, where the digitizer is instead triggered only when an event occurs via the MCP pulse, with another digitizer channel reading in the relevant laser pulse data. Both MCP and laser pulse peaks are fit down to the digitizer jitter level (a few tens of ps) to achieve ∼30 ps TOF timing. This is sufficient to resolve the v_z distribution.

Camera and digitizer events are correlated by their overall timestamps. For these studies, a faster 520 fps CMOS camera has been implemented to enable higher count rates. While multiple events in a single image can be correlated to the digitizer pulses via amplitude, for now the studies are performed in the regime with fewer than one event per frame on

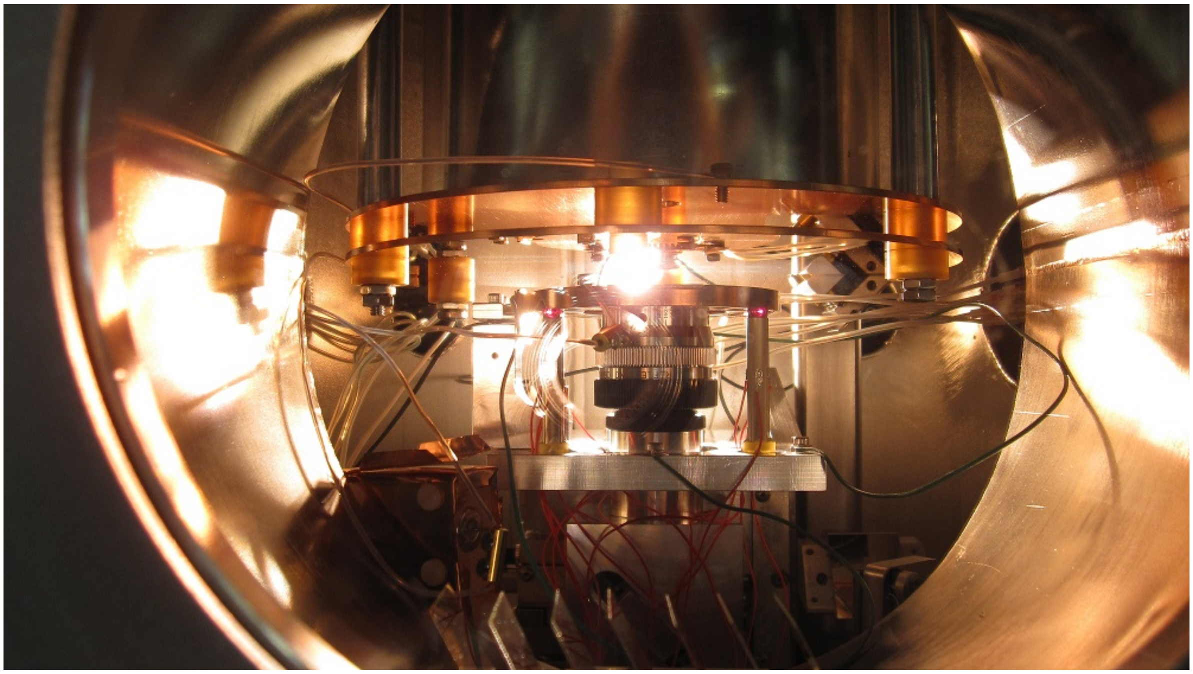

Figure 2.6: Velocity map imaging system, showing reflective microscope objective and scanning sample stage (repeller electrode).

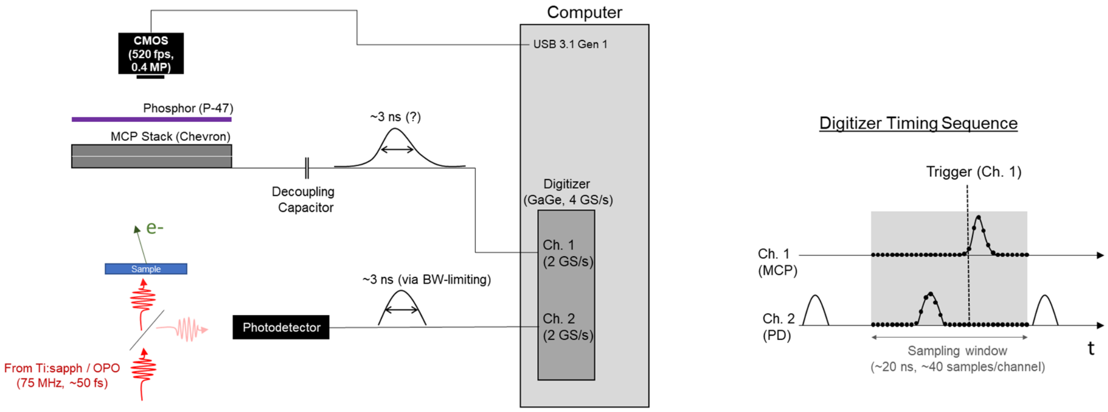

Figure 2.7: Scheme for 3D velocity map imaging data collection.

average to avoid ambiguity (i.e., incorrectly assigned camera-digitizer event correlation). Frame rates that are 25-fold higher thus help to compensate for these limited signal rates.

2.9 Femtosecond Pump-Probe Studies

Pump-probe studies to be discussed in Chapter 7 are achieved by placing a motorized linear delay stage (Newport UTS150CC, ESP301 Motion Controller) with a retro-mirror pair in the SHG beam path for ∼1 femtosecond timing accuracy. The position is not phase-stabilized via fast piezo-based PID interometry, so the pump-probe studies are all phase-integrated, i.e. only the intensity envelope is resolved with no/minimal interference fringes. Beam sample alignment is achieved approximately via markers on the back-reflection CCD television monitor, while careful alignment is achieved by particle location in SPIM scans at both colors. Relative pump-probe timing alignment is controlled via the automated and multiple manual delay stages in the beam paths, first using a fast photodiode to achieve coarse overlap, then running pump-probe delay scans to locate the signal peak. Further details will be described in Chapter 7.

2.10 System Control

The SPIM system is controlled by a software suite written in LabWindows/CVI, i.e. the National Instruments C Language integrated development environment with integrated graphical user interface functionality and ready implementation of the full national instruments hardware/software suite. The primary "SPIM.exe" program has purview over everything from the camera, digitizer, power supplies/voltages, and laser shutter, to the scanning/positioning functionality. This program is connected to the "PiezoPID.exe" positioning program via DataSocket Server, as well as the delay stage positioning software. All physical input/output (e.g. system control and data acquisitions) aside from commercial camera and digitizer hardware is handled by two NI DAQ cards, models PCI-6221 and PCI-6703, housed in BNC breakout boxes. The VMI detection camera is implemented in the control suite via the GenICam camera API standard, while the digitizer is run via its own custom C API. Both camera and digitizer are run on seperate threads, generated automatically via API event-driven callback functions.

Essentially all data analysis is performed in a MATLAB AppDesigner-generated program, “VMI Aanlysis Suite”, which includes VMI visualization, angular and radial distribution analysis, time series analysis, 3D visualization and routines, as well as all simulation routines for Monte Carlo and quantum photoemission calculations. The simulation routines simply take data exported directly from *COMSOL Multiphysics* as inputs.

The KMLabs laser system is controlled on a seperate, dedicated computer by commercial “KMCtrl.exe” software package for adjusting prism and slit positions (along with calibration, spectrometer readout, etc.). The OPO control software has been customized for ready tunability and PID-driven wavelength locking.

Chapter 3

Theoretical Methods

A significant element in this thesis is the development and implementation of simple theoretical methods for calculating nanoplasmonic 3D photoelectron distributions. A fair amount of real estate will therefore be devoted in this chapter to expounding on these methods.

3.1 Analytic Electrodynamics

Analyticity in electrodynamics simulations requires a high degree of nanoparticle symmetry. Most plasmonic field distributions will be calculated numerically, which can be done for arbitrary nanoparticle geometries. However, some simple analytic geometries will first be examined to understand some essential features of the plasmon modes. Detailed derivations for spheres, ellipsoids, and Mie theory are presented in Bohren and Huffman,[20] while some essential features will be highlighted here.

3.1.1 Sphere and Ellipsoid Electrostatics

Nanoparticles much smaller than the wavelength of an applied optical field can be treated as if exposed to a constant electric field. This is known as the quasi-static or dipole approximation. The harmonic time dependence is then readily included as the sum or integral over harmonic modes, so long as the fastest frequency component remains in the quasi-static regime. This is a good approximation for nanoparticles with $<$ 100 nm dimensions under resonant visible and near-IR excitation (400–1000 nm wavelength). The electrostatics of spheres and ellipsoids are presented in detail in various textbooks,[20, 177] but some key features of the derivations and results will be discussed here. These features will provide important context in which to understand the plasmonic behaviors of various spherical (e.g. nanospheres and nanoshells) and prolate (e.g. nanorods and nanostar arms) geometries to be discussed later on.

The electric field inside of an uncharged metal nanosphere immersed in a uniform background field, $\boldsymbol{E_0} = E_0\hat{x}$, can be determined by solving the Laplace equation in spherical coordinates subject to the appropriate boundary conditions.[81] The result is a constant internal field,

$$\boldsymbol{E}_{\text{in}} = \frac{3\epsilon_0}{\epsilon(\omega) + 2\epsilon_0} E_0\hat{x}, \tag{3.1}$$

and a dipolar external field at the nanosphere surface,

$$\boldsymbol{E}_{\text{out}} = E_0\hat{x} + \frac{\epsilon(\omega) - 2\epsilon_0}{\epsilon(\omega) + 2\epsilon_0}(3E_0\hat{n} - E_0\hat{x}), \tag{3.2}$$

where $\hat{n}$ is the surface normal. Evidently, there is a resonance at $\epsilon(\omega) = -2\epsilon_0$, which is known as the Fröhlich condition. Since $\epsilon(\omega) = \epsilon_1(\omega) + i\epsilon_2(\omega)$ is a complex quantity, the imaginary component must be small for strong resonance. For noble metals such as gold, silver, the resonance has a high Q factor and occurs in the visible spectral range, as described in the "periodic table of plasmonics".[18] One often approximates $\epsilon_2 \approx 0$ and ϵ_1 via the Drude model[81] as

$$\epsilon_1(\omega)/\epsilon_0 = 1 - \omega_p^2/\omega^2, \tag{3.3}$$

where $\omega_{\text{p}} = (ne^2/\epsilon_0 m_e)^{1/2}$ is the bulk plasma frequency, n being the electron number density. Plugging this into Eq. 3.1, one finds that the Fröhlich condition is satisfied at localized SPR frequency

$$\omega_{\text{SPR}} = \frac{\omega_{\text{p}}}{\sqrt{3}}. \tag{3.4}$$

For gold nanospheres, Eq. 3.4 yields a resonance around 5.2 eV. The actual resonance occurs around 2.4 eV (520 nm), which is significantly different than the Drude model due to

d-band contributions to the dielectric function, where the gold $5d$-band lies approximately 2 eV below the Fermi level.

It will be of particular interest to determine surface- versus volume-mediated photoemission contributions, which will depend on the ratio of surface to volume fields. From Eqs. 3.1 and 3.2, this ratio is given for the surface point along the polarization axis ($\hat{n} = \hat{x}$) by

$$\left|\frac{E_{\text{in}}}{E_{\text{out}}}\right| = \left|\frac{\epsilon(\omega)}{\epsilon_0}\right|. \tag{3.5}$$

This could also be determined immediately by considering the boundary condition for the normal component of the displacement field, which must be continuous across an interface with no free charge,

$$\boldsymbol{D}_{\text{in}} \cdot \hat{n} = \boldsymbol{D}_{\text{out}} \cdot \hat{n}. \tag{3.6}$$

At the "tip" along the laser polarization axis, where both internal and external fields are normal to the surface, this leads immediately to Eq. 3.5. It can be seen that the plasmon resonance, $\propto (\epsilon(\omega) + 2\epsilon_0)^{-1}$ drops out of Eq. 3.5, such that the ratio of surface to volume fields only depends upon the material dielectric function for spheres and more generally for ellipsoids, which also have uniform internal fields and corresponding dipolar surface charge/field distributions.

The derivation here in the quasi-static regime suggests that the SPR does not depend upon the size of the sphere. As will be shown in the next section, deviations begin to occur for larger particles ($>$ 100 nm), with additional dipolar dynamic depolarization contributions and higher-order multipolar contributions. For particles much smaller than the elastic (phonon scattering) mean free path of $\sim$30 nm in Au,[4] an additional surface scattering contribution becomes prominent in influencing the plasmon dephasing time (Section 1.1). In general, the SPR frequency depends upon the nanoparticle size, geometry, material (via $\epsilon(\omega)$), and the surrounding medium ($\epsilon_0 \rightarrow \epsilon_m(\omega)$).

Understanding the effects of nanoparticle geometry on plasmonic field distributions and corresponding photoemission distributions will be the primary objective of this thesis.

The geometry influences the manner in which charges build up on nanoscale curved surfaces and their Coulombic interactions. Many such effects can be illustrated by the behaviors of ellipsoidal nanoparticles, which can also be treated analytically. The discussion here shall again be restricted to ellipsoids with all dimensions much smaller than the optical wavelength, thus permitting the quasi-static approximation. In this case, the Laplace equation must be solved in ellipsoidal coordinates with the scalar potential expanded in ellipsoidal harmonics. This problem has been solved in detail in a number of textbooks, including Bohren and Huffman[20] and Stratton.[177] For a general ellipsoid (principal semi-axes $a > b > c$), the internal electric field is given by

$$E_{\text{in},i} = \frac{1}{1 + L_i(\epsilon - \epsilon_m)} E_{0,i}, \tag{3.7}$$

where L_i is the "depolarization factor" along one of the principal semi-axes, $i = a, b, c$,

$$L_i = \frac{abc}{2\epsilon_m} \int_0^\infty \frac{ds}{(s + i^2)((s + a^2)(s + b^2)(s + c^2))^{1/2}}. \tag{3.8}$$

Now specializing a bit to the particularly relevant case of a prolate spheroid (ellipsoid of revolution with $a > b = c$), the tip field due to $E_0 = E_a$ polarized along principal axis a is readily determined by the boundary condition on the surface-normal component of the displacement field (Eq. 3.6) to be

$$E_{\text{tip}} = \frac{\epsilon}{\epsilon_m} \frac{1}{1 + L_a(\epsilon - \epsilon_m)} E_0. \tag{3.9}$$

Thus the external-to-internal tip ratio is the same as Eq. 3.5, as it must be by boundary conditions.

More interesting is the absolute tip field enhancement, which is given from Eq. 3.9 by E_{tip}/E_0. As described by Liao and Wokaun,[108] the result can be written as the sum of the relative ellipsoid field and E_0 as

$$E_{\text{tip}} = \frac{(1 - \epsilon_m L_a)(\epsilon - \epsilon_m)}{1 + L_a(\epsilon - \epsilon_m)} E_0 + E_0. \tag{3.10}$$

This can be further rewritten as

$$E_{\text{tip}} = \gamma E_{\text{dip}} + E_0, \tag{3.11}$$

into a resonant dipolar field that encodes the plasmonic contribution,

$$E_{\text{dip}} = 2\frac{\mu}{a^3} = \frac{2}{3}\frac{b^2}{a^2}\frac{\epsilon - \epsilon_m}{1 - L_a(\epsilon - \epsilon_m)}E_0 \tag{3.12}$$

and a purely geometrical enhancement factor,

$$\gamma = \frac{3}{2}\frac{a^2}{b^2}(1 - \epsilon_m L_a). \tag{3.13}$$

This geometric enhancement compared with the dipolar field is known as the "lightning rod effect", with $\gamma > 1$ along the a axis of a prolate spheroid, and $\gamma = 1$ for a sphere. For a 3:1 prolate spheroid, for instance (similar to nanorod geometries to be studied), $\gamma = 12$ is already a whopping geometrical tip field enhancement, *on top of* the plasmonic field enhancement. The simple physical picture behind this lightning rod enhancement is that more electrons can pack into regions with higher curvature due to the asymmetric forces on the charges from the material vs. environment directions (e.g. charge A in the medium can move closer to charge B at a nanotip because no charges lie beyond charge B in the vacuum to push back), as is well known in electrostatics. Such strongly electric-field-enhanced "hot spots" at sharp nanoparticle tips are an important feature for many nanoplasmonic applications—particularly nonlinear applications such as surface-enhanced Raman scattering (SERS), with signal $\propto |E/E_0|^4$, and multiphoton photoemission studies, with signal $\propto |E/E_0|^8$ being common (i.e., in the 4-photon photoemission regime).

3.1.2 Mie Theory

For larger nanoparticles (> 100 nm) approaching a significant fraction of the visible excitation wavelength scale, the dipolar approximation of a uniform electric field across the particle is no longer adequate and higher-order multipolar oscillation modes become significant. From the other direction, taking an extended metal surface and shrinking it down to the nanoscale, one finds that traveling surface plasmon polariton modes with well-defined momentum begin to resolve into multipolar oscillation modes for which momentum is no longer a good quantum number, i.e. "localized" surface plasmon oscillations. The solution to Maxwell's equations for light scattering off of large metal spheres was first treated by Gustav Mie in 1908. The derivation, based upon expansion in vector spherical harmonics, is reproduced in detail in various texts, including Bohren and Huffman.[20] While quadrupolar modes become relevant in some of the studies to be discussed, another important result of Mie theory is the expansion of the dipolar term with respect to the size parameter, $x = ka$ where k is the optical wavenumber and a is the sphere radius. As shown in Meier[120] and summarized by Maier[115] (not to be confused), the dipolar polarizability begins to display substantial contributions from radiative damping and an effect known as *dynamic depolarization*—i.e. the retardation of the polarization field due to the finite speed of light. These terms lead to plasmon broadening and red-shifting, independent of interactions with higher-order multipolar oscillations.

3.1.3 Hybridization Theory

When multiple plasmon modes interact strongly due to Coulomb interactions between the surface charges, it may become necessary to rediagonalize into a more appropriate basis. This "strong coupling" effect must be accounted for in studies of gold nanoshells (with interacting core/shell modes) and gold nanostars (with interacting arm modes), for instance. The typical approach to describing such effects in plasmonic systems is by *hybridization theory*, which was developed by Prodan, Nordlander, and coworkers in the early 2000s[151] in a treatment that directly parallels molecular orbital theory. For example, the dipolar oscillations of the gold nanoshell outer sphere (radius R_2, resonance at $\omega_\mathrm{p}/\sqrt{3}$) and inner core void (radius R_1, resonance at $\sqrt{2/3}\omega_\mathrm{p}$) couple to generate nanoshell dipolar modes at frequencies[151]

$$\omega_{\pm}^2 = \frac{\omega_{\mathrm{p}}^2}{2}\left[1 \pm \frac{1}{3}\sqrt{1 + 8\left(\frac{R_1}{R_2}\right)^3}\right]. \tag{3.14}$$

The lower-energy ω_- "bonding" mode corresponds to inner and outer oscillations being in-phase, whereas for the higher-energy ω_+ "anti-bonding" mode they are π out of phase. The ω_- mode has a large dipolar moment and is thus "bright", while the ω_+ mode is "dark" and has a very small optical excitation cross-section. Similar considerations exist for higher-order multipolar moments and other nanoplasmonic geometries, although both hybridized modes may maintain a non-negligible optical excitation cross-section.

3.2 Finite Element Electrodynamics Simulation

Even barring substrate effects, most nanoparticle geometries are too complicated (i.e. have insufficient symmetry) to be treated analytically. A variety of numerical methods for solving Maxwell's equations, including the discrete dipole approximation (DDA),[205] the boundary element method (BEM), the finite difference time domain (FDTD) method, and the finite element method (FEM).[85] Here, FEM is employed to capitalize on a number of advantages discussed below (along with the simple, pragmatic advantage of software license availability).

3.2.1 Finite Element Method

The finite element method (FEM) is a numerical technique for solving differential equations, particularly useful for complicated domain geometries and inhomogeneous media. Although finite element, finite difference, and other methods are commonly and effectively used to simulate nanoplasmonic electromagnetic fields, the main difference is that FEM takes advantage of the weak formalism (see below) for solving partial differential equations (i.e., weighted integral with one derivative shifted over to the weighting function), which decreases the differential order and relaxes the continuity requirements on the approximate solutions.

Finite difference methods (e.g. FDTD), on the other hand, solve the differential equations directly in their strong form and are thus generally not as versatile with complex geometries and physical boundary systems. This is often evidenced by strong noisy spikes in FDTD solutions around nanoparticle surface boundaries. Such effects may be overcome or excused when investigating linear processes, but are intolerable when simulating surface-mediated multiphoton photoemission (to be discussed in Section 3.5.2), which is proportional to the surface field to the $2n$ power (e.g. E^8 for 4-photon photoemission) and thus greatly amplifies any numerical noise. *COMSOL Multiphysics* (a portmanteau of COMputational-SOLver) is the popular finite element analysis software package utilized for all electromagnetic field simulations in this thesis. *Multiphysics* refers to the ability to simultaneously solve multiple coupled sets of PDEs, including for stress/strain, electromagnetics, fluid mechanics, and heat flow.

To understand the weak form of a PDE, begin with a generic (just linear, for now) differential equation in domain Ω (boundary $\delta\Omega$):

$$\hat{L}^{(n)}u(x) - f(x) = 0, \tag{3.15}$$

where $\hat{L}^{(n)}$ is some n^{th}-order differential operator and $u(x)$ is the desired solution. The appropriate number of boundary conditions is assumed. Eq. 3.15 is known as the *strong form* of the differential equation as the n^{th}-order derivative must exist (i.e. the function must be continuous to the $(n-1)^{th}$-order). Taking the weighted integral with arbitrary weight function, $\omega_i(x)$, leads to the weighted-integral form of the differential equation:

$$\int_\Omega \omega_i(\hat{L}^{(n)}u(x) - f(x))dx = 0. \tag{3.16}$$

Now integration by parts relieves $u(x)$ of one differential order and places it on the weight function:

$$\omega_i(\hat{L}^{(n-1)}u(x))\Big|_{\delta\Omega} - \int_\Omega \partial_x\omega_i(\hat{L}^{(n-1)}u(x))dx - \int_\Omega \omega_i f(x)dx = 0. \tag{3.17}$$

(This is playing somewhat fast and loose with the nature of the differential operator; if it has a zeroth-order term, this must be separated out explicitly.) This is known as the *weak form* of the PDE. The weight function, ω_i can be readily chosen to be continuous to first order, and to have a simple derivative, which we'll ultimately use to solve the integrals directly and obtain a linear algebraic set of equations. As it stands, Eq. 3.17 still represents an exact formulation of the problem, for arbitrary weight function.

To make the problem tractable and numerically soluble, the domain is discretized into a set of N nodes. The function is then expanded in a basis set,

$$u(x) \approx \sum_{N} c_j \phi_j(x). \tag{3.18}$$

The basis functions $\phi_j(x)$ are typically chosen to be hat/triangle/tent functions centered on node i and going to zero at the nearest-neighbor nodes. The approximation indicated in Eq. 3.18 is due to the incompleteness of the basis functions. Since the weak form holds for any weighting function, a convenient choice is $\omega_i = \phi_i$ (Galerkin method). The integrals in Eq. 3.17 can then be solved in a relatively straightforward fashion for each i and j, and are only nonzero for $j = i, i \pm 1$. The net result is a set of linear algebraic equations which can be summarize in matrix form as

$$\mathrm{A}\mathbf{c} = \mathbf{b}, \tag{3.19}$$

in which A is known as the "stiffness matrix" and is a sparse, tridiagonal matrix. Inverting A via efficient algorithms for sparse matrices and solving for the c_i's leads to an approximate solution (Eq. 3.18) to the differential equation. At each step of the iterative matrix solver, the error of the i-th step is determined via

$$\mathrm{Error}^{(i)} = \frac{|\mathbf{b} - \mathrm{A}\mathbf{x}^{(i)}|}{|\mathbf{b}|}, \tag{3.20}$$

where $\mathbf{b}$ and A are already known. The goal of the iterative solver is to iterate until this error is below some tolerance, e.g. 10^{-3}. The actual discretization process generates an n-dimensional mesh, which may consist of triangular/quadrilateral or analogous higher-order elements. The preferred element type and meshing method (e.g., structured, unstructured, or hybrid) depends on the problem geometry and parameters.

A final important consideration for electrodynamics simulations is to truncate the domain using absorbing boundary conditions. To avoid spurious reflections at the domain boundaries, perfectly matched layers (PMLs)are often implemented.[16] This is achieved by analytic continuation of the relevant propagation coordinate into the complex plane, $x \to x + \frac{i}{\omega} f(x)$ for some chosen decay function $f(x)$, such that the plane waves are damped as

$$e^{ikx} \to e^{ikx} e^{-\frac{k}{\omega} f(x)}, \tag{3.21}$$

which yields frequency-independent attenuation (for dispersionless $k = n\omega/c$) that has been shown to be reflectionless for normal-incidence waves[16] and still minimal reflection at all but the steepest off-normal angles.

3.2.2 Cross-Sections

Scattering, absorption, and extinction are calculated in multiple non-redundant ways, including via heat dissipation, incident/scattered flux, the optical theorem, and linear combinations thereof. All of the results are within a few percent, verifying the accuracy of the calculations. While methods exist for calculating the scattering cross-sections of supported nanoparticles, scattering is only considered here for nanoparticles embedded in homogeneous media as the absorption cross-section and corresponding heating is the primary quantity of interest for photoemission studies. In the following equations, $\boldsymbol{E} = \boldsymbol{E}_0 + \boldsymbol{E}_{\text{rel}}$, where $\boldsymbol{E}$ is the total electric field, $\boldsymbol{E}_0$ is the incident electric field, and $\boldsymbol{E}_{\text{rel}}$ is the relative field due to interactions with the nanoparticle, which is equal to the scattered field in the far-field domain ($r \gg \lambda \gg D$ for particle dimension D).

The absorption cross-section is given by the total power dissipation over the nanoparticle volume, V,

$$\sigma_{\text{abs}} = \frac{1}{I_0} \int_V P_{\text{loss}} dV, \tag{3.22}$$

where, by Ohm's law, $P_{\text{loss}} = \boldsymbol{J} \cdot \boldsymbol{E}$. Alternatively, the absorption is given by the net inward

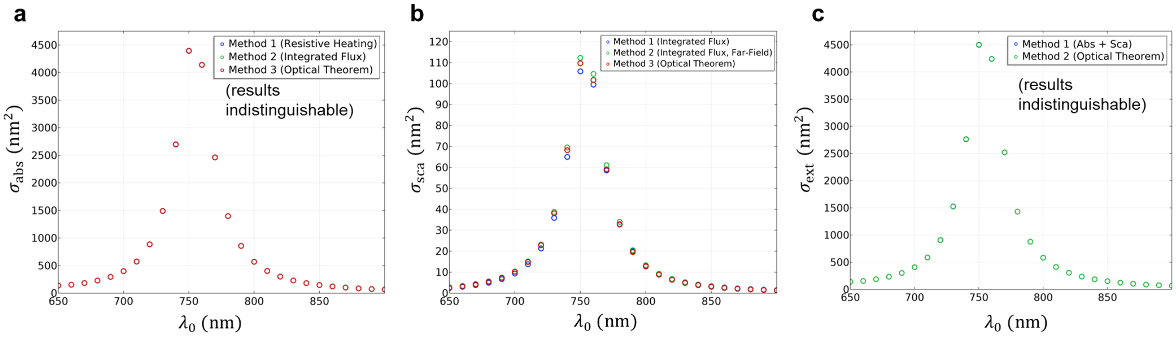

Figure 3.1: Cross-sections calculated via FEM field solutions in *COMSOL* for a 9×31 nm gold nanorod in water. (a) Absorption, (b) scattering, and (c) extinction cross-sections calculated via the different methods described in the text, all displaying either perfect or strong agreement.

flux across a boundary surface surrounding the nanoparticle, $\delta\Omega$,

$$\sigma_{\mathrm{abs}} = -\frac{1}{I_0}\int_{\delta\Omega} \boldsymbol{E}\times\boldsymbol{H}\cdot dS, \tag{3.23}$$

or by

$$\sigma_{\mathrm{abs}} = \sigma_{\mathrm{ext}} - \sigma_{\mathrm{scat}}, \tag{3.24}$$

For the example of a nanorod in water, all three methods are found to yield identical results Fig. 3.1a. The scattering cross-section is given by the net far-field scattered flux across a surrounding boundary surface,

$$\sigma_{\mathrm{scat}} = \frac{1}{I_0}\int_{\delta\Omega_{\mathrm{FF}}} \boldsymbol{E}_{\mathrm{rel}}\times\boldsymbol{H}_{\mathrm{rel}}\cdot dS_{\mathrm{FF}}, \tag{3.25}$$

or via Eq. 3.24 if the other two quantities are known. In *COMSOL*, the far-field fields can be realized either with a large domain and far-away boundary surface, or by implementing the Stratton-Chu far-field formulation. All three methods for determining the scattering cross-section agree to within a few percent Fig. 3.1b. Finally, the extinction cross-section is determined either by Eq. 3.24 or by the optical theorem, which relates the imaginary part of the forward scattering amplitude $f(0)$ to the total extinction via

$$\sigma_{\mathrm{ext}} = \frac{4\pi}{k}\mathrm{Im}\{f(0)\} \tag{3.26}$$

Both methods for determining σ_{ext} agree to within negligible error Fig. 3.1c.

3.3 Thermalization Kinetics

Localized plasmon modes are bosonic quasiparticle excitations with dephasing times typically < 10 fs, partially due to lifetime decay into electron-hole excitations (note that due to metallic screening, such electron-hole pair excitations decorrelate within a few femtoseconds, leading to individual/uncorrelated hot carriers). These hot carriers thermalize via scattering with cold (Fermi sea) carriers on tens of femtosecond timescales, which subsequently thermalize with the lattice phonon bath on few picosecond timescales.[69] Depending upon the timescale and physical quantities of interest, such thermalization kinetics may be modeled by different means, including isolating the femtosecond electron-electron thermalization and considering energy-depending in/out-filling effects (particularly via Fermi liquid theory).

3.3.1 Femtosecond Electron Thermalization

Electron-phonon scattering mean free paths in gold of ∼30 nm around the Fermi level correspond to ∼30 fs scattering times, but due to the nearly elastic ∼10 meV energy loss per collision it takes many collisions for the electrons to effectively transfer energy into the lattice. Thus, on the few-hundred femtosecond timescales or faster, the electron kinetics can be modeled independent from the lattice. The energy deposited into the electron bath by a femtosecond laser pulse with intensity profile $I_0(t)$ is given by

$$C_e(T_e)\frac{dT_e}{dt} = I_0(t)\sigma_{\text{abs}}. \tag{3.27}$$

The temperature-dependent electron heat capacity is given via the Sommerfeld model[4] as

$$C_e(T_e) = \frac{\pi^2 k_B^2 T_e n_e}{2E_F}V \approx 1.5 \times 10^{-19}\text{J/K}, \tag{3.28}$$

for nanoparticle volume $V = 10^4$ nm^3, gold electron density $n_e \approx 5.9 \times 10^{28}$ m^{-3}, Fermi energy $E_F = 5.53$ eV, and using $T_e = 300$ K for the estimated value. Integrating Eq. 3.27 leads to

$$T_e(t) = \sqrt{T_0^2 + \frac{4E_F\sigma_{\text{abs}}}{\pi^2 k_B^2 n_e V}\int_{-\infty}^{t} I_0(t')dt'}, \tag{3.29}$$

where taking $t \to \infty$ yields an expression for the max electron temperature reached in terms of the total pulse fluence. A typical electron temperature evolution for a 100 fs pulse, peak $I_0 = 10^8$ W/cm^2, $\sigma_{\text{abs}} = 10^4$ nm^2, and $V = 10^4$ nm^3 is shown in Fig. 3.2, leading to a pulse-averaged temperature of 1000 K at the laser pulse peak and a peak temperature of 1500 K, with a much more modest peak lattice temperature of 350 K. These short timescale kinetics are particularly important when determining an effective, pulse-averaged temperature in photoemission spectra (approximately the temperature at the pulse peak) and when considering possibilities for thermionic emission from a highly heated electron gas—see Section 3.4.1 for further details.

The model in Eq. 3.27 assumes that the pulse energy is immediately transferred into a thermalized excited electron distribution. However, it is clear that electrons will first be excited to a nascent non-thermal distribution (essentially a small fraction of the ground-state Fermi-Dirac distribution excited up to $E_F + \hbar\omega$) which then internally thermalizes via hot-cold electron-electron scattering on tens of femtosecond timescales. These dynamics effectively delay the temperature increase by a few tens of femtoseconds and are accounted for via Fermi liquid theory. The term "Fermi liquid theory" actually refers to a broader framework for analyzing metal conduction excitations as quasiparticles, but in this context it is specifically used in reference to the $\tau_{e-e} \propto (E - E_F)^2$ hot electron (quasiparticle) lifetimes.[111] This is a simple result of Fermi's Golden Rule when assuming a uniform joint density of states and excitation matrix elements around the Fermi level—i.e. hot electrons in collision with cold electrons have a phase space proportional to $(E - E_F)$ to decay *into*, while cold electrons have the same phase space factor they can be excited *from*, such that the hot electron decay rate goes as the square of the excitation energy. This well-known result can be encoded into the dynamics by modifying Eq. 3.27 as follows:

$$C_e(T_e)\frac{dT_e}{dt} = \int_0^{\hbar\omega} \frac{f_{\mathrm{na}}(t,\delta E)\delta E}{\tau_{\mathrm{FLT}}(\delta E)} d(\delta E), \tag{3.30}$$

where $\delta E = (E - E_F)^2$ and $\tau_{\mathrm{FLT}}(\delta E) = a(\delta E/E_F)^2$ with a determined experimentally. The nascent excited distribution, f_{na}, only loses population and can thus be solved for independently via

$$\frac{df_{\mathrm{na}}(t,\delta E)}{dt} = -\frac{1}{\tau_{\mathrm{FLT}}(\delta E)} f_{\mathrm{na}}(t,\delta E) + \frac{I_0(t)\sigma_{\mathrm{abs}}}{\hbar\omega} f_{\mathrm{na}}(0,\delta E). \tag{3.31}$$

3.3.2 Picosecond Lattice Thermalization

On tens of picosecond timescales after most of the absorbed pulse energy has been transferred to the lattice, but before energy is transferred to the environment on 100 ps to nanosecond timescales, the peak lattice temperature can be simply approximated via

$$T_l = \frac{F_{\text{pulse}}\sigma_{\text{abs}}}{C_l} \tag{3.32}$$

for total pulse fluence F_{pulse} and lattice heat capacity

$$C_l = c_l \rho V \approx 2.5 \times 10^{-17} \text{J/K}. \tag{3.33}$$

In Eq. 3.33, for gold, the specific heat capacity $c_l = 129$ JK^{-1}kg^{-1}, mass density $\rho = 19.32$ kg/m^3, and nanoparticle volume $V = 10^4$ is utilized for the approximate heat capacity. Since the lattice heat capacity (Eq. 3.33) is over two orders of magnitude larger than the room-temperature electron heat capacity (Eq. 3.28), the peak lattice temperature (on tends of picosecond timescales) is much greater than the peak electron temperature (on hundreds of femtosecond timescales), as seen in Fig. 3.2. Note that this does not scale proportionately with the relative heat capacities due to the T_e dependence of $C_e(T_e)$—i.e. the T_e increase is about an order of magnitude greater than T_l rather than two order of magnitude since C_e itself increases by about an order of magnitude during electron heating. These simple calculations of peak lattice temperature are important for determining nanoparticle melting thresholds for pulsed laser excitation.

3.3.3 Two-Temperature Model

Finally, to fully model the electron and lattice temperature evolution, including intermediate (few picosecond) timescales, the two-temperature model is utilized.[69] The kinetic equations become

$$C_e(T_e)\frac{dT_e}{dt} = -g(T_e - T_l) + I_0(t)\sigma_{\text{abs}} \tag{3.34}$$

$$C_l\frac{dT_l}{dt} = g(T_e - T_l), \tag{3.35}$$

where $g \approx 2 \times 10^{-7}$ W/K is the electron-phonon coupling constant.[69, 47] The full electron and lattice temperature evolution for the same parameter set as above is shown in Fig. 3.2. Eq. 3.34 could additionally be modified to account for Fermi liquid theory dynamics as described above.

3.4 Electron Emission Mechanisms

Electron emission from metals is often separated into three primary categories: thermionic emission due to heating of the conduction electron gas, perturbative multiphoton photoemission (MPPE), and strong-field optical field emission (OFE). Note that MPPE includes single-photon emission—i.e. the conventional photoelectric effect. The distinction between these three processes is not so clear-cut, however, as MPPE and OFE are limiting cases of the same surface photoemission physics[203] and thermionic emission is the zeroth-order term in the multiphoton perturbative expansion. In practice, many processes are categorized as thermally-enhanced MPPE or OFE (e.g. W or LaB_6 electron microscopy emitter tips)—particularly when the effect is significant enough for a given MPPE application to lower the process order by one—or photofield emission, in which multiphoton absorption promotes electrons to higher energies with a smaller subsequent tunnel barrier. While we emphasize emission into vacuum, analogous processes can occur for other collection media, including semiconductors or molecular layers.

3.4.1 Thermionic Emission

Thermionic emission occurs for metals above absolute zero due to the thermal tail of the Fermi-Dirac conduction electron distribution. Assuming the metal is held at a constant temperature, the thermionic current per area is given by the Richardson-Dushman equation[4]

$$J = cAT^2 e^{-\frac{\phi}{k_B T}}, \tag{3.36}$$

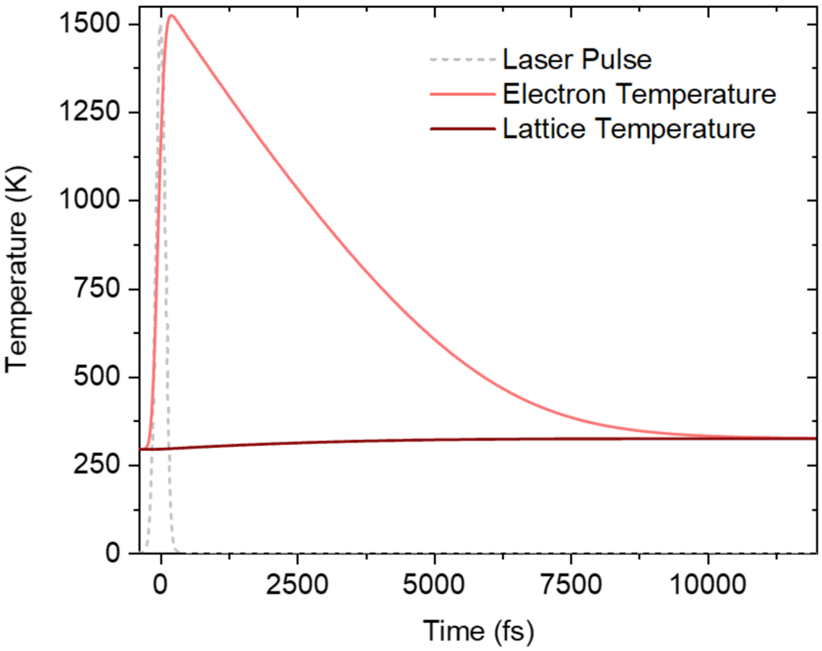

Figure 3.2: Two-temperature model evolution of the electron and lattice temperatures for a 20 nm diameter, 60 nm length gold nanorod for a 100 fs pulse, peak $I_0 = 10^8$ W/cm^2, $\sigma_{\text{abs}} = 10^4$ nm^2, and $V = 10^4$ nm^3.

in which ϕ is the work function and where the Richardson constant,

$$A = \frac{4\pi e m_e k_B^2}{h^3} = 1.2 \times 10^6 \mathrm{Am}^{-2}\mathrm{K}^{-2}, \tag{3.37}$$

is modified by some constant $c \approx 0.5$ that depends on surface reflections and other details of the surface and emission. Setting aside such details, Eq. 3.36 is readily derived by integrating over the fraction of the Fermi-Dirac conduction electron velocity distribution with sufficient surface-directed kinetic energy to overcome the work function. While this current is only strictly zero at absolute zero temperature, it remains quite negligible in photoemission experiments for electron gas temperatures less than a few thousand kelvin.

3.4.2 Multiphoton Photoemission (MPPE)

Excluding the zeroth-order thermionic term, the multiphoton photoemission expansion determined via time-dependent perturbation theory can be written in general form as

$$\mathrm{MPPE} = \sum_{n=1}^{\infty} \sigma_{n\mathrm{PPE}} I_0^n, \tag{3.38}$$

in which the dependence on the laser polarization and frequency is left implicit. While I_0 is merely the input field intensity at the local surface or volume region of interest and is therefore often known, the $\sigma_{n\mathrm{PPE}}$ are quite complicated and encode all of the relevant plasmonic field enhancement effects, surface vs. volume effects, laser parameter dependencies (i.e. polarization and frequency), coherent vs. incoherent excitation pathways, etc. The primary objective of this thesis, therefore, is to determine these nonlinear coefficients both experimentally and theoretically with as much generality as possible. Some of the relevant theoretical considerations will be addressed in Section3.5, with combined experimental and theoretical insights in the remaining chapters. While all of the experimental investigations are necessarily in 2PPE or higher regimes to overcome the 4–5 eV metal work functions with visible photon energies, the physics will be made as general as possible and therefore apply to the linear regime as well (most relevant to photovoltaic and photocatalytic collection via semiconductors and molecules, respectively).

3.4.3 Optical Field Emission (OFE)

For strong optical fields approaching the surface atomic fields of ∼10 V/nm, conduction electrons can tunnel through the triangular barrier either directly from the ground state (OFE), with thermal assistance ("thermally-assisted" OFE), or following below-threshold multiphoton absorption ("photofield" emission). Considering only typical OFE, tunneling emission occurs in the strong-field, low-frequency limit where the optical phase is longer than the electron "tunneling time". By contrast, MPPE occurs in the weak-field, high-frequency perturbative regime. These regimes are commonly and conveniently distinguished by a single, dimensionless quantity known as the Keldysh parameter,[91]

$$\begin{aligned}\gamma &= \frac{\omega}{\omega_t} \\ &= \sqrt{\frac{\phi}{2U_\mathrm{p}}},\end{aligned} \tag{3.39}$$

where ω is the optical frequency, $\omega_t = eE/\sqrt{2m_e\phi}$ is the tunneling frequency under surface electric field E (including plasmonic enhancement), ϕ is the work function, and

$$U_\mathrm{p} = \frac{e^2E^2}{4m_e\omega^2} \tag{3.40}$$

is the ponderomotive energy. Conditions for which $\gamma \geqslant 2$ lead to MPPE, while $\gamma \leqslant 1$ lead to OFE. In particular, the transition is found to occur within the $1 < \gamma < 2$ range.[75] Even in the MPPE and transitional regimes, post-emission classical dynamics due to ponderomotive acceleration in strongly spatially varying and decaying plasmonic fields can be important and may be accounted for by simulating the classical trajectories via the simpleman model.[39]

While OFE requires strong optical intensities around $\sim 10^{13}$ W/cm^2 (corresponding to electric fields of ∼10 V/nm), typical nanoparticle surface plasmonic field enhancement factors of 10–30 significantly reduce the laser intensity requirements, leading to OFE for more readily achievable input intensities in the range of a tens of GW/cm^2.[75, 106] The large currents and narrow angular emission distributions from nanoplasmonic tips and other systems make the OFE regime appealing for a variety of nascent applications, including optical phase detection,[164, 152] x-ray free electron laser (XFEL) sources,[150, 75] and electron imaging and diffraction.[127, 66, 126] However, the intensity must be managed carefully in such systems to balance strong OFE with space-charge effects, along with strong heating and possible melting. Such effects are negligible in MPPE applications. Furthermore, the photoelectron kinetic energy spread in MPPE is typically < 1–2 eV and can be made quite narrow near threshold,[3] compared with > 10 eV spreads typical in OFE.[39] For high-resolution diffraction and other applications, therefore, MPPE (with possible post-emission acceleration) may be more appealing. All studies described herein are performed within the MPPE regime.

3.5 Multiphoton Photoemission Theory

Photoelectric effect experiments and theory in the late 19th century and early 20th century heralded the quantum revolution. Such progress was related only to the energy conservation aspect of the photoelectric effect, however, as the nascent quantum theory wasn't sufficiently sophisticated to understand features relevant for momentum conservation. It wasn't until the work of Bloch, Sommerfeld, and others in the 1920s in developing an understanding of the quantum electronic structure of solids that notions of momentum conservation arose.[186]

Due to the negligible linear momenta of the incoming photons compared with the outgoing electrons in the visible-frequency photoelectric effect, momentum conservation demands electron scattering with a massive third body during photoexcitation and emission. Photoemission via volume excitation is dominated by scattering with the periodic lattice potential when the transition is energetically allowed, but visible plasmonic excitation is often below the relevant interband threshold and instead involves interactions with phonons, defects, impurities, or other electrons. By contrast, surface photoexcitation and emission pathways arise due to the translational symmetry breaking at an interface and thus involve scattering with the surface potential barrier, including contributions from the electromagnetic field variation, localized surface states, and the evanescent external decay of internally-delocalized Bloch wavefunctions.[57] For nanoscale systems with $\lesssim 20$ nm dimensions, intraband excitation mediated by geometrical confinement can also become significant.[117, 24, 128]

3.5.1 Volume Monte Carlo Modeling

Volume (multiphoton) photoemission is modeled within the phenomenological, ballistic three-step framework developed by Berglund and Spicer in 1964.[17] Although phenomenological, the three-step model was placed on firm theoretical footing by Feibelman and Eastman,[48] and others (see, e.g., Hufner[78]) via comparison with a formal one-step Fermi's Golden Rule treatment. In the three-step framework, electrons (i) are optically excited into a higher-energy eigenstate of the material, (ii) travel ballistically to the surface with an exponential survival probability due to inelastic scattering ($\lambda_{\text{inel}} \approx 5$ nm at $E_{\text{F}}+ 5$ eV in gold[88, 102]) along the way, and (iii) transmitted into the vacuum (or other surrounding collection medium, such as semiconductor or surface adsorbate layer) with finite probability if they have sufficient normal momentum to overcome the surface potential barrier. For a step potential barrier, the transmission function increases gradually above threshold and is given by[56]

$$T_{\text{step}}(k_z) = \frac{4\hbar k_z p_z}{\hbar k_z + p_z}, \tag{3.41}$$

where $\hbar k_z$ is the internal surface-normal momentum and p_z is the external surface-normal momentum, related via energy conservation by

$$\frac{\hbar^2 k_z^2}{2m_e} = \frac{p_z^2}{2m_e} + E_{\text{F}} + \phi, \tag{3.42}$$

for surface barrier height $E_F + \phi$. By contrast, the transmission function for a smooth barrier due, for instance, to an unscreened image force, is approximately a unit step function[56]

$$\begin{aligned} T_{\text{smooth}}(k_z) &\approx \theta\left(\frac{\hbar^2 k_z^2}{2m_e} - E_{\text{F}} - \phi\right)\theta(k_z) \\ &= \theta(p_z). \end{aligned} \tag{3.43}$$

To account for all hot electron trajectories over a nanoparticle volume within the three-step photoemission framework, a Monte Carlo numerical integration routine is implemented. Whereas direct integration is computationally intensive, wasteful for highly spatially-nonuniform nonlinear excitation, and also requires care with the internal-to-external phase space Jacobian transformation, the Monte Carlo method is efficient and encodes all Jacobian effects automatically. Varying degrees of sophistication have been implemented in previous Monte Carlo hot electron transport/emission calculations, including emphasis on surface-scattering[19] or on volume scattering determined via *ab initio* theory.[31, 84] None of these previous calculations have emphasized full momentum resolution, however, only total incident counts or internal quantum efficiencies. Here, the elements that are most important for full 3D velocity resolution and nonuniform spatial excitation (i.e. utilizing near-fields determined via finite element simulation) with inelastic mean free paths smaller than particle dimensions (thus neglecting minor surface scattering effects) are implemented. Approximations of constant joint density of states and constant excitation matrix elements are made for the coherent nonlinear excitations, such that the ground state Fermi-Dirac distribution is preserved for the nascently-excited hot electrons. Furthermore, the approximation is made that the hot electrons are excited isotropically, which is realistic for phonon-mediated multiphoton excitation that effectively randomizes the final hot electron momenta.

The Monte Carlo routine is represented in Fig. 3.3. A weighted random selection of a nanoparticle volume point is performed with nonlinear field enhancement weight factor $|E/E_0|^{2n}$ determined via finite element simulation. To avoid volume discretization error, we then perform a random displacement (Δr) within the volume associated with each mesh vertex. An angle is then selected at random and the momentum is randomly selected, weighted by the excited Fermi-Dirac distribution. Next, the surface vertex closest in angle is determined and the corresponding distance and surface normal ($\hat{n}_{\text{surf}}$) are used to determine scattering and transmission probabilities, respectively. Given the small amount of excess kinetic energy (~1 eV) relative to the work function (~4.25 eV), hot electrons that un-

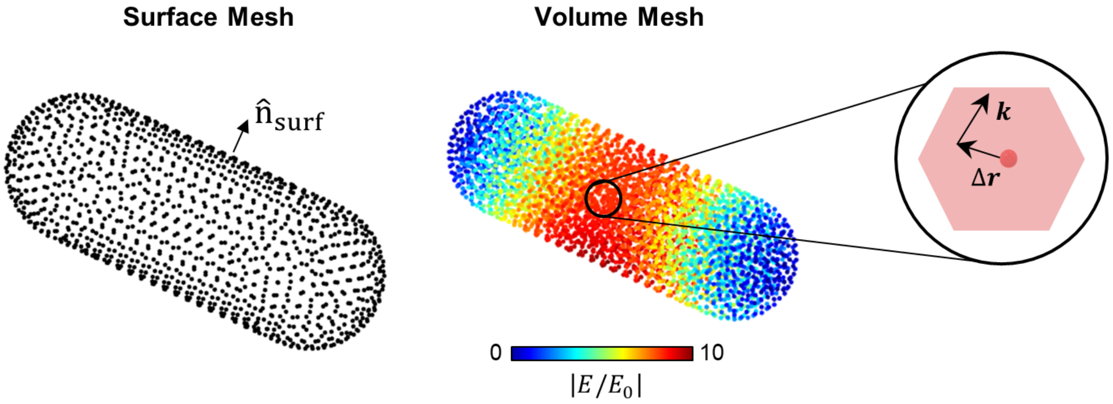

Figure 3.3: Depiction of the surface and volume mesh vertices utilized in the Monte Carlo modeling. Each surface vertex corresponds to a ∼1 nm^2 area with nearly constant surface normal ($\hat{n}_{\mathrm{surf}}$). Each volume vertex corresponds to a ∼1 nm^3 volume with an electric field enhancement determined via finite element modeling. To avoid any discretization effects, the excitation coordinates are randomly perturbed by Δr within the volume associated with a randomly-selected (nonlinear field-weighted) mesh vertex.

dergo even a single inelastic scattering event with a cold electron lose half of their energy on average[159] and are therefore typically unable to escape and may be neglected. The possibility of surviving a single scattering event via the triangular final energy distributions of electrons determined by Ritchie and Ashley[159] is accounted for, including exchange effects, but the emission contribution of these scattered electrons is negligible. The mean free path for elastic scattering (∼30 nm) is much larger than the inelastic mean free path (∼5 nm) and therefore safely neglected as well. In cases where it is deemed necessary-—i.e. for lower-energy excitations escaping over a low-energy Schottky barrier-—the effects of inelastic and elastic scattering can be readily included in this simple Monte Carlo algorithm. This method can also be modified to allow for geometries with concave features (and therefore self-intersecting trajectories), but the simple convex modeling covers many essential geometries, including spheres, rods, cubes, triangles, etc.

3.5.2 Surface Photoemission Theory

While a number of photoemission theories exist for metal surfaces,[116, 114, 208, 203, 135] the recent Green's function perturbation theory analysis by Yalunin and coworkers[203] provides a particularly versatile framework for multiphoton photoemission, along with ponderomotive effects and the extension into the OFE regime. Furthermore, the theory accounts for essential backscattering effects and quantum amplitude interference between the direct and backscattered outgoing waves. This theory is therefore selected and implemented to model surface-mediated multiphoton photoemission velocity distributions for coherent excitation at a metal-vacuum interface, modified into a two-step process to account for the high-gradient evanescent surface plasmonic fields. In the first step, free-electron initial states are excited into field-dressed final states (Volkov states) with the ponderomotive quiver energy appearing in the energy conservation equation,

$$\frac{\hbar^2 k^2}{2m_e} + n\hbar\omega = \frac{p^2}{2m_e} + U_{\mathrm{p}} + E_F + \phi \tag{3.44}$$

in which $\hbar k$ is the initial state momentum and p is the final state drift momentum. In the second step, as the electron leaves the evanescent surface plasmon field region, the ponderomotive energy is fully converted into kinetic energy corresponding to the surface-normal momentum. The differential multiphoton photocurrent is given by

$$\frac{d^3 J_{\mathrm{MPPE}}}{dk_x dk_y dk_z} = \frac{2\hbar}{(2\pi)^3 m_e} \sum_{n \geqslant n_{\min}} \frac{k_z}{e^{(\hbar^2 k^2/2m_e - E_F)/k_B T} + 1} P_n(k_z) \tag{3.45}$$

which is the collision rate of Fermi sea electrons on the surface potential barrier, scaled by the dimensionless excitation and emission probability, $P_n(k_z)$, and summed over all allowed multiphoton process orders as determined by energy conservation.

The photoemission rate can be written in terms of external momentum via the coordinate transformation

$$\begin{aligned} \hbar k_x &= p_x, \\ \hbar k_y &= p_y, \\ \frac{\hbar^2 k_z^2}{2m_e} + n\hbar\omega &= \frac{p_z^2}{2m_e} + U_{\mathrm{p}} + E_F + \phi. \end{aligned} \tag{3.46}$$

The Jacobian determinant is $|d^3k/d^3p| = p_z\,(\hbar^4 k_z)$ and the photoemission probability is thus given in external momentum coordinates by

$$\frac{d^3 J_{\mathrm{MPPE}}}{dp_x dp_y dp_z} = \frac{2}{h^3 m_e} \sum_{n} \frac{p_z}{e^{(p^2/2m_e + U_{\mathrm{p}} + \phi - n\hbar\omega)/kT} + 1} P_n(k_z(p_z)), \tag{3.47}$$

in which all process orders may contribute to a final momentum state at finite temperature due to the exponential Fermi-Dirac tail, though most processes are negligible at room temperature except the dominant multiphoton order dictated by energy conservation. For completeness, the photoemission probability derived by Yalunin and coworkers via Green's function solution to the time-dependent Schrödinger equation[203] is given here in terms of external coordinates as

$$
\begin{aligned}
P_n(k_z(p_z)) &= \frac{\hbar^2\sqrt{\frac{p_z^2}{2m_e}+U_\mathrm{p}+\phi+E_F-n\hbar\omega}}{\sqrt{2m_e}(EF+\phi)p_z}\left|I_n(p_z)+R_n^{(1)}R_n^{(2)}I_n(-p_z)\right|^2, \\
I_n(p_z) &= \frac{2m_e}{h}\int_0^{2\pi}\left(\sqrt{\hbar\omega-U_\mathrm{p}-\frac{p_z^2}{2m_e}}+\frac{p_z}{\sqrt{2m_e}}-\sqrt{2U_\mathrm{p}}\right)e^{iS(q)}dq, \\
S(q) &= nq+2\frac{p_z}{\hbar\omega}\sqrt{\frac{U_p}{m_e}}\cos(q)-\frac{U_\mathrm{p}}{2\hbar\omega}\sin(2q), \qquad (3.48) \\
R_n^{(1)} &= -\frac{\sqrt{\frac{p_z^2}{2m_e}+U_\mathrm{p}+E_F+\phi}-\frac{p_z}{\sqrt{2m_e}}}{\sqrt{\frac{p_z^2}{2m_e}+U_\mathrm{p}+E_F+\phi}+\frac{p_z}{\sqrt{2m_e}}}, \\
R_n^{(2)} &= J_0\left(-4\frac{p_z}{\hbar\omega}\sqrt{\frac{U_\mathrm{p}}{m_e}}\right).
\end{aligned}
$$

The integral terms $I_n(\pm p_z)$ represent the outward- and backward-moving excited waves outside of the medium. The reflection coefficients on the backward-moving wave account for rescattering on the surface potential barrier, where $R_n^{(1)}$ is the reflection coefficient for a step-down potential (height $E_F+\phi$) and $R_n^{(2)}$ accounts for the effect of the oscillating triangular barrier in the applied optical field. Interference between the direct and rescattered waves can have significant effects on the final emission amplitude, as discussed in detail by Yalunin and coworkers.[203] Finally, we include the ponderomotive energy transfer in the present case of an evanescent plasmonic field via the coordinate transformation $p_z^2/2m_e \rightarrow p_z^2/2m_e - U_p$.

To calculate the full 3D photoelectron velocity distribution for a given nanoparticle, the photoemission contributions from each surface area element are calculated using the surface field enhancements determined via finite element simulation. The photoemission distribution is calculated with respect to each surface normal ($\hat{p}_{z,\mathrm{rel}}$) and rotated into the global frame ($\hat{p}_z$) via Cartesian rotation matrices. Only a single rotation about axis $\hat{p}_z \times \hat{p}_{z,\mathrm{rel}}$ is required for azimuthally-isotropic distributions. A sample uniform surface mesh and nonlinear surface-normal field enhancement distribution is shown in Fig. 3.4. It should finally be noted that geometries with concave surface regions may allow for the intersection of emitted electrons with other surfaces of the emitter geometry. These effects are not presently accounted for, although they should be negligible for the tip-like emission described in the present work.

3.6 3D Reconstruction

While time-of-flight photoelectron resolution is being implemented for direct 3D photoelectron velocity mapping, all measurements shown herein are 2D (v_x, v_y), v_z-integrated velocity maps. Many features of interest will be directly evident in these distributions, although in some cases it will be beneficial or necessary to reconstruct the full 3D distributions. There are essentially two routes to such reconstruction: (1) When the functional form of the 3D distribution is known (e.g. $\sim \cos(\theta)$ surface photoemission), the 2D velocity map can be fit to the projection of this distribution. (2) If some minimal symmetry condition is present in the photoelectron velocity distribution, such symmtery can compensate for the information lost in the projection and numerical reconstruction methods can be applied (Sections 3.6.1 and 3.6.2). The minimal symmetry condition in the velocity map imaging configuration is for the photoelectron velocity distribution to have an axis of cylindrical symmetry *parallel* to the detection plane, i.e. perpendicular to the v_z projection axis. While method (1) will be discussed in Chapter 4 in the context of thin film photoemission, some methods of type (2) will be addressed here.

3.6.1 BASEX Algorithm

The v_z projection (forward Abel transform) in velocity map imaging (VMI) experiments is given by

$$P(v_x, v_y) = \int_{-\infty}^{\infty} f(v_x, v_y, v_z) dv_z, \tag{3.49}$$

for an initial 3D distribution $f(v_x, v_y, v_z)$. This projection/transform can be reversed for 3D distributions with cylindrical symmetry along an axis parallel to the detector—i.e. $f(v_x, v_y, v_z) = \tilde{f}(v_r, v_x)$ for x-axis cylindrical symmetry—using various inverse Abel transform methods. Here the basis set expansion (BASEX) algorithm of Dribinski *et al.*[42] is

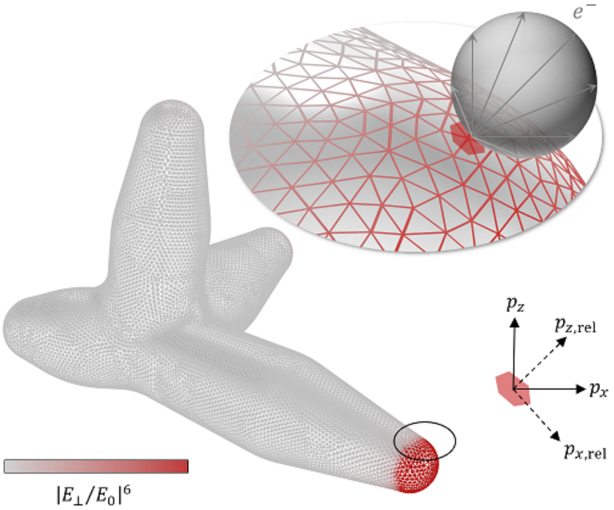

Figure 3.4: Surface photoemission simulation geometry. Example nanostar surface mesh and nonlinear field enhancement distribution utilized in theoretical 3D photoemission calculations. Multiphoton photoemission distributions are calculated with respect to the surface normal for each nanostar surface area element (e.g. shaded patch), corresponding to each triangular mesh vertex at which the surface field enhancements are calculated.

implemented, using the nearly-Gaussian basis set from the original paper with $\sigma = 1$ px and a regularization parameter value of q =10. The transform is carried out efficiently via matrix inversion and multiplication in *MATLAB*, yielding the original 3D photoelectron velocity distribution so long as the cylindrical symmetry assumption is valid, otherwise yielding an approximation to the original distribution.

The essential idea of the method is to fit the projected distribution ($\boldsymbol{P}$) to the projections of Gaussian-like basis functions to reconstruct the original cylindrically-symmetric image space distribution. By cylindrical symmetry, $Im(x, y) = Im(x, \rho)$ for radial vector ρ in cylindrical coordinates. The data matrix form of $Im(x, y)$ is thus denoted as $\boldsymbol{Im}$. The fit in this analytic treatment corresponds to a linear operation (using the notation of Dribinski *et al.*[42] unless otherwise specified),

$$\begin{aligned} \boldsymbol{Im} &= \boldsymbol{Z}^T \boldsymbol{C} \boldsymbol{Z}, \\ \boldsymbol{C} &= (\boldsymbol{X}\boldsymbol{X}^T + q^2\boldsymbol{I})^{-1}\boldsymbol{X}\boldsymbol{P}\boldsymbol{Z}^T(\boldsymbol{Z}\boldsymbol{Z}^T)^{-1}, \end{aligned} \tag{3.50}$$

where $\boldsymbol{C}$ is the fit coefficient matrix for the projected Gaussian basis functions, $\boldsymbol{X}$ is the projection-space basis, $\boldsymbol{Z}$ is the image-space basis, q is the regularization parameter to prevent over-fitting to noise, and $\boldsymbol{I}$ is the identity matrix. Eq. 3.50 reduces to

$$\boldsymbol{Im} = \boldsymbol{Z}^T(\boldsymbol{X}\boldsymbol{X}^T + q^2\boldsymbol{I})^{-1}\boldsymbol{X}\boldsymbol{P}, \tag{3.51}$$

such that the transform matrix is $\boldsymbol{Z}^T(\boldsymbol{X}\boldsymbol{X}^T + q^2\boldsymbol{I})^{-1}\boldsymbol{X}$. The basis matrices $\boldsymbol{Z}$ and $\boldsymbol{X}$ depend only on the image size and Gaussian width parameter, σ, and are thus calculated once and utilized for all calculations. For further details, the reader is referred to the original work of Dribinski and coworkers.[42]

3.6.2 Other Methods

Other methods for reconstruction include the Hankel transform method and polar onion peeling methods.[197] While the brute-force Hankel method can lead to noisy results in the presence of noisy inputs and problems with divergences,[197] the polar onion peeling method presents an interesting alternative for metal film photoemission. The method effectively deconvolves the v_z degree of freedom by progressively peeling away radial projections of the 3D distribution. For $\sim \cos(\theta)$ surface photoemission, the projection is a constant value out to the Fermi level, which leads to particularly straightforward implementations (e.g. for Au film), as shown by Ye and Küpper.[207] This serves as a particularly nice alternative method to the direct fitting method presented in Section 4.1 for reconstruction of film photoemission distributions.

Chapter 4

Volume Photoemission from Thin Gold Film

Before examining the photoemission behaviors of nanoscale particles, some general features of multiphoton photoemission from a typical plasmonic metal (gold) are investigated, while simultaneously calibrating the velocity mapping system. In particular, flat gold films are prepared commercially (PHASIS) via sputter deposition of 10 nm polycrystalline Au film on a 2 nm Ti adhesion layer on a borosilicate coverslip. The adhesion layer and careful sputtering procedure ensure flat gold films ($<$ 1 nm RMS surface roughness) without the island formation commonly observed for $<$ 100 nm Au films deposited directly on glass. The samples are stored in N_2-purged containers prior to usage and the the sample area is refreshed for each experimental measurement to prevent any laser-induced adlayer buildup from affecting the velocity distributions. For example, a central inelastic scattering peak can "grow in" under typical exposure to peak intensities of $\sim$0.1 GW/cm^2 over the course of 10–20 minutes, although the precise cause of this remains unknown. The majority of this chapter is taken from recent work on Au film.[145]

4.1 Three-Step Photoemission Modeling

The majority of VMI applications take advantage of the high level of spatial symmetry offered by atomic and molecular photoelectron/photoion velocity distributions in the gas phase, specifically perfect cylindrical symmetry with respect to an axis parallel to the plane of detection. Under these conditions, the full 3D photoelectron/photoion velocity distributions can be efficiently recovered from the 2D VMI projections using inverse Abel transform algorithms.[197, 5] Unfortunately, photoemission from surfaces and supported nanoparticles may not exhibit the requisite spatial symmetry necessary to infer the v_z projections directly (although this shall be examined in subsequent chapters). The ultimate solution has been to implement fast timing on the electron arrivals and thereby measure the full 3D velocity distributions directly (Section 2.8).[109] However, provided one has a sufficiently accurate and physically justified model (*vide infra*), it is also possible to directly fit the 2D photoelectron projections and thereby infer the full 3D velocity distributions. A simple photoemission model below, with the fitting method demonstrated for Au films.

It should first be clarified that PES methods in the low-energy (visible) regime essential for studying nanoplasmonic phenomena provide qualitatively different insights compared with UV or x-ray PES studies. For example, the band structure of gold[156] makes evident that the visible OPO photons ($\hbar\omega < 2.4$ eV) employed herein have insufficient energy to promote direct/vertical transitions (in which total momentum is conserved modulo the reciprocal lattice vector) from below the Fermi level to states above the vacuum level ($E_{\mathrm{vac}} - E_{\mathrm{F}} \approx 5$ eV). To achieve momentum conservation in an indirect/nonvertical photoexcitation process within the volume of the material (bulk-mediated photoemission), an electron must necessarily undergo a collision with a third body such as a photon, lattice defect, or impurity center.[94] Alternatively, the necessary momentum during photoexcitation can be provided by a collision with the surface potential barrier (surface-mediated photoemission). In this case, the photoemission signal depends only upon the surface-normal component of the electric field due to the well-defined direction of the surface potential gradient (∇V) contributing to the transition matrix element.[114] Such surface contributions are expected to be quite minimal for the smooth Au films studied here (∼1 nm RMS surface roughness, characterized via AFM), since the surface-normal electric field component is small for light excitation at normal incidence. In contrast, such surface-mediated photoemission effects will be shown to play a more important role for nanoplasmonic geometries such as nanostars

(Chapter 5), with strong and sharp tip hot spots, with plasmon-enhanced optical fields that are both concentrated at the surface and pointed primarily along the surface normal.

To model photoemission following bulk-mediated excitation in the Au film and Au nanoshells, we treat the emission process within the framework of a ballistic three-step picture (see Fig. 4.1),[17] in which the electrons (i) are excited within the volume of the material, (ii) travel ballistically to the interface with the possibility of scattering along the way, and (iii) escape ("refract") into the vacuum if there is sufficient momentum normal to the surface to overcome the work function barrier. Such a three-step model has been the most commonly used method for predicting and interpreting photoemission spectra since its development in 1964 by Berglund and Spicer.[17] This three-step model is phenomenologically simple by nature but nonetheless can provide important physical insight into the photoemission process due to the same underlying Fermi golden rule formalism with the rigorous (but often intractable) quantum-mechanical one-step model.[48, 78] Most importantly, since the result is independent of the specific excitation mechanism, the same model can be applicable to a large variety of processes, such as linear photoemission, multiphoton photoemission, and thermionic emission.

The final velocity distribution of the ejected photoelectrons ($f_{\mathrm{out}}(v)$) can be predicted from the velocity distribution inside the metal ($f_{\mathrm{in}}(v')$), based on the knowledge of the inelastic scattering probability, $S(v')$, the surface barrier transmission function, $T(v')$, and the Jacobian transformation between the internal (primed) and external (unprimed) coordinates that accounts for the momentum loss and corresponding refraction at the surface barrier. Conservation of particle number for electrons with sufficient perpendicular velocity to escape, $dN_{\mathrm{out}}(v) = S(v')T(v')dN_{\mathrm{in}}(v')$, leads to a direct relation between the internal (f_{in}) and external (f_{out}) velocity distributions

$$f_{\mathrm{out}}(\boldsymbol{v})v^2\sin(\theta)dvd\theta d\phi = S(\boldsymbol{v}')T(\boldsymbol{v}')f_{\mathrm{in}}(\boldsymbol{v}')v'^2\sin(\theta')\left(\left|\frac{\partial(v',\theta',\phi'))}{\partial(v,\theta,\phi)}\right|dvd\theta d\phi\right), \tag{4.1}$$

where $|\partial(v',\theta',\phi'))/\partial(v,\theta,\phi)|$ is the determinant of the Jacobian matrix.

For a surface normal in the $\hat{z}$ direction, the photoelectron transmission function is given by

$$T(\boldsymbol{v}') = T(v', \theta') = \Theta\left(\frac{1}{2}m_e^* v'^2 \cos^2(\theta')/\Phi - 1\right) \tag{4.2}$$

in which Θ is the Heaviside step function, m_e^* is the electron effective mass, and Φ is the surface potential barrier measured with respect to the bottom of the conduction band, as shown in Fig. 4.1. This form of the transmission function simply assumes that the electrons will escape with unity probability if they have sufficient kinetic energy associated with the perpendicular momentum component to overcome the surface barrier ($\frac{1}{2}m_e^* v' \cos(\theta') \geqslant \Phi$) or will otherwise be reflected. The effective mass accounts for the fact that the excited electrons are actually quasiparticle excitations in a strongly interacting (Coulombic) many-body system, which may be regarded as a free particle with an adjusted mass. Henceforth, however, it will be approximated that $m_e^* \approx m_e$ for the nearly free electrons in the gold conduction band. The velocity-dependent inelastic scattering probability is determined by integrating the velocity and depth-dependent scattering probability,

$$\tilde{S}(\boldsymbol{v}', z') = \frac{1}{\tau} e^{-\frac{z'/\cos(\theta')}{\lambda_{\text{inel}}}}, \tag{4.3}$$

over all $z' = [0, \tau]$, where τ is the gold thickness (10 nm for the Au film), and $\lambda_{\text{inel}} \approx 5$ nm is the inelastic mean free path for hot electrons near the photoemission threshold ($\sim$5 eV).[88, 102] For $\lambda_{\text{inel}} \ll \tau$, the depth-averaged inelastic scattering probability takes on the limiting form, $S(\boldsymbol{v}') = S(\theta') \approx \lambda_{\text{inel}} \cos(\theta')/\tau$.

Finally, the Jacobian transformation requires a well-defined relationship between the internal and external variables. Energy conservation yields the relation, $\frac{1}{2}m_e v^2 = \frac{1}{2}m_e v'^2 - \Phi$, while conservation of parallel momentum requires that $v \sin(\theta) = v' \sin(\theta')$ and $\phi = \phi'$ since there is no azimuthal dependence to the transmission through a smooth surface barrier. These results can be combined to rewrite Re. 4.1 explicitly as

$$f_{\text{out}}(\boldsymbol{v}) \approx \frac{\lambda_{\text{inel}}}{\tau}\left(\frac{m_e}{e\Phi}\right)^{1/2} f_{\text{in}}(\boldsymbol{v}'(\boldsymbol{v})) v \cos(\theta), \tag{4.4}$$

where λ_{inel} is taken as a constant over the narrow energy range of near-threshold electrons, and the transmission step function limits the applicable domain of Eq. 4.4 to the upper-half space, $\theta \leqslant \pi/2$. Note that if the internal distribution is isotropic (i.e., $f_{\text{in}}(\boldsymbol{v}') = f_{\text{in}}(v')$), the external distribution for near-threshold photoemission is predicted to vary with the typical $\cos(\theta)$ angular distribution, with an additional $\sin(\theta)$ term from the spherical Jacobian factor. From detailed balance conditions, this would be consistent with angle-independent, unity sticking coefficients for electrons impinging on the Au surface from the vacuum. It is noted for later analysis of curved nanoparticle surfaces that the angle θ in Eq. 4.4 is defined with respect to the surface normal of each emitting area element. Using the simple relationship between f_{in} and f_{out} in Eq. 4.4, the details of the internal excited electron distributions in various systems can now be explored via velocity map imaging experiments. This will be demonstrated next for Au film, the results from which will then provide a useful context for nanoparticle VMI investigations.

4.2 Au Film Velocity Mapping

A representative sample of 5 velocity map images (VMIs) measured on Au film is displayed in Fig. 4.2a, taken from 16 total measurements at different OPO photon energies between 1.63 and 2.25 eV. These VMIs represent v_z-integrated projections of the full 3D photoelectron velocity distributions, where the initial transverse speed ($v_\rho = (v_x^2 + v_y^2)^{1/2}$) is linearly mapped onto the corresponding radial position on the detector. Several features of the velocity distributions are immediately evident in the log-scale VMIs, such as the sharp circular edges corresponding to photoemission of electrons from the Fermi level in the metal, clearly extending outward with increasing photon energy (1.80, 1.90, 2.00, 2.10 eV) due to the increasing energy above the vacuum level. Note, however, that this smooth trend is broken by a dramatic contraction that occurs between 2.1 and 2.25 eV photon energy, which corresponds to the sharp transition between the 3PPE and 2PPE regimes, also identified in the intensity-dependence studies in Fig. 4.3. For these normalized VMIs (10^5 electrons

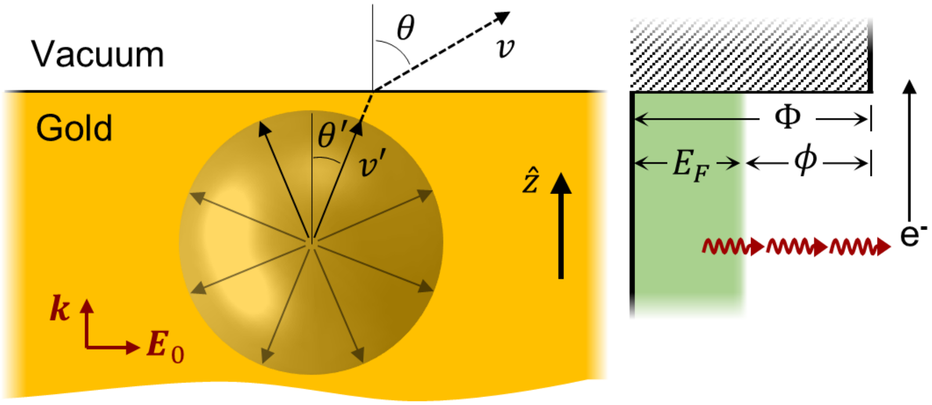

Figure 4.1: Illustration of the ballistic photoemission process. Internal variables are denoted with primes, and the external variables are unprimed (see text for details of the three-step model).

per image), this contraction occurs when $2\hbar\omega$ becomes comparable to the work function and near-threshold (and thus lower velocity) 2PPE electrons become the dominant source of signal.

Another striking aspect of the VMI data for Au film in Fig. 4.2a is the high degree of azimuthal symmetry in the ejected electrons, which from Eq. 4.4 would be consistent, for example, with a spherically-symmetric photoelectron distribution excited within the Au film. It is worth noting that this is not an obvious result, since for transitions with linearly polarized light, anisotropy in the momenta might have been expected due to the polarization dependence of the transition matrix elements $M_{\mathrm{i,f}} \propto \langle f \left| \boldsymbol{A} \cdot \boldsymbol{p} \right| i \rangle$, where $\boldsymbol{A}$ is the electromagnetic vector potential, and $\boldsymbol{p} = i\hbar\boldsymbol{\nabla}$ is the momentum operator.[78] However, the band structure of gold requires transitions at visible frequencies to be nonvertical/indirect (even for two- or three-photon excitation), in which case the requisite scattering with phonons or lattice impurities randomizes the electron velocity vectors during excitation. It is therefore reasonable to approximate the hot electron internal excited velocity distributions as isotropic, as strongly corroborated by the azimuthal symmetry in the Au film VMI data. This provides additional symmetry constraints and simplifies the inversion procedure to determine the scalar electron speed distributions by analyzing the radial dependence of the velocity map images.

Angularly averaged VMI radial distributions are presented in Fig. 4.2b, where angular averaging involves summing all electron events that fall within a certain radial bin (bin width = 1 pixel) and dividing by the corresponding cylindrical phase space factor, $2\pi v_\rho$. Thus, the distributions in Fig. 4.2b must be multiplied by $2\pi v_\rho$ to obtain the total count rate at a particular v_ρ. Based on the three-step photoemission model (Eq. 4.4), least-squares fits to the radial distributions in Fig. 4.2b can be used to determine the emitted photoelectron speed distribution and the corresponding internal hot electron speed distributions inside the Au film. To reproduce the experimental loss of v_z information due to the projection onto the detector, the full 3D photoelectron velocity distribution described by Eq. 4.4 is transformed

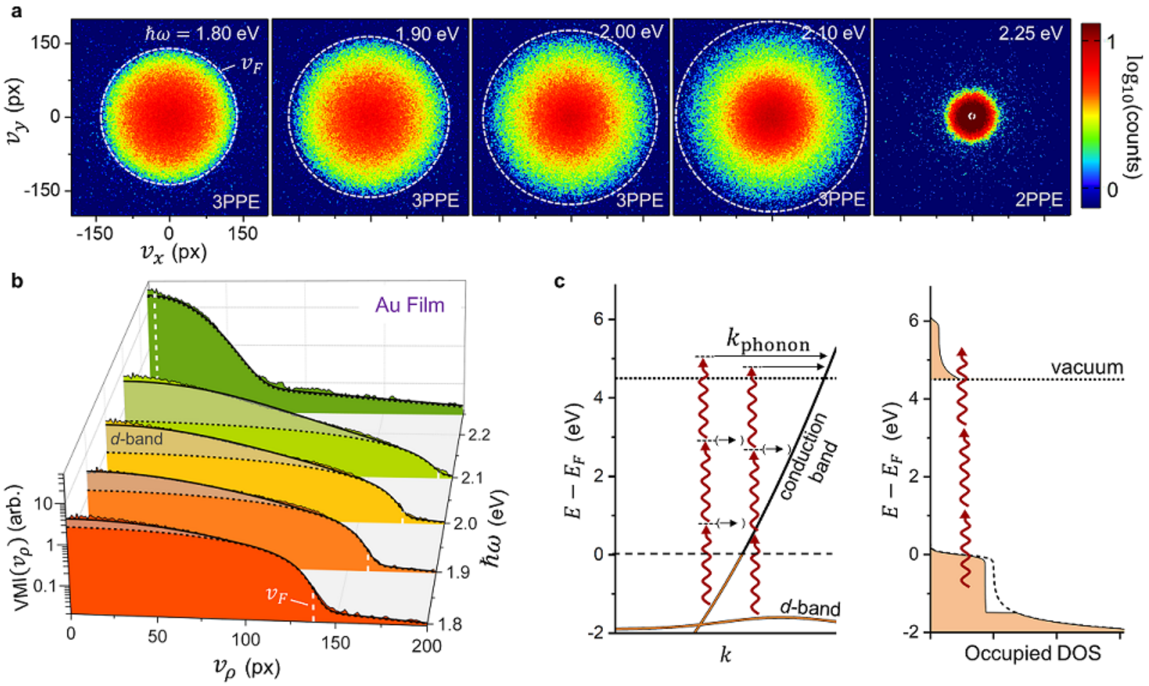

Figure 4.2: (a) Log-scale velocity map images measured on gold film for a series of photon energies and linear polarization, count-normalized to 10^5 electrons per image, with the speed corresponding to electrons emitted from the Fermi level (v_{F}) indicated with a dashed line based on fits. (b) Angularly averaged radial distributions, shown with fits to the three-step photoemission model (solid black lines). The dashed black lines are the fits with the d-band contribution subtracted out, and the shaded areas therefore correspond to the d-band contribution at each photon energy. The noise floor is characterized with the laser blocked and is included in the fits. (c) Depiction of the possible routes for multiphoton excitation, with a simplified band structure for the purpose of demonstration, along with the corresponding density of states distributions. Arrows in parentheses indicate possible phonon-mediated transitions necessary to conserve momentum.

into cylindrical coordinates and integrated over v_z,

$$\mathrm{VMI}(v_\rho) = A \int_0^\infty f_{\mathrm{out}}(v_\rho, v_z) dv_z, \tag{4.5}$$

in which $f_{\mathrm{out}}(v_\rho, v_z)$ is the emitted photoelectron distribution function in cylindrical coordinates, with the z axis orthogonal to the substrate and detection planes. Since $f_{\mathrm{out}}(v) \propto f_{\mathrm{in}}(v'(v))v_z$ (Eq. 4.4), the observed radial VMI distributions can then be least-squares fit to a sufficiently physically motivated and parametrized expression for f_{in} via Eq. 4.5.

4.3 Interband vs. Intraband Photoexcitation

The internal distribution of hot electrons (f_{in}) is generated by the promotion of the Fermi-Dirac conduction electron distribution to energies above the vacuum level via multiphoton absorption, as depicted in Fig. 4.2c. Any energy dependence of the Au joint density of states (JDOS) and transition matrix elements between the initial and final states will alter the excited distributions relative to the initial distributions, but these quantities can be approximated as constant in gold over the narrow range of photon energies studied here. For indirect (e.g. phonon-assisted) volume excitation mechanisms, MPPE may proceed via a single phonon-assisted multiphoton absorption step coupled through virtual intermediate states or multiple phonon-assisted absorption steps with hot electron population also generated in intermediate eigenstates of the system below the vacuum level. As an additional consideration for photon energies approaching 2 eV, direct $5d$-$6sp$ interband transitions also become possible.[156] Due to the weak interatomic overlap between tightly bound $5d$ orbitals, these $5d$ bands in gold have relatively flat dispersion curves compared with that of the $6sp$ conduction band, leading to a large additional DOS at energies $\geqslant$ 2 eV below the Fermi level. These interband transitions are quite strong, as evidenced by the strong yellow color of gold.[153] Following direct one-photon absorption from a $5d$-band state to a $6sp$-band state above the Fermi level, the electrons can then be indirectly excited above the vacuum level via subsequent multiphoton absorption (Fig. 4.2c), which again requires a collision

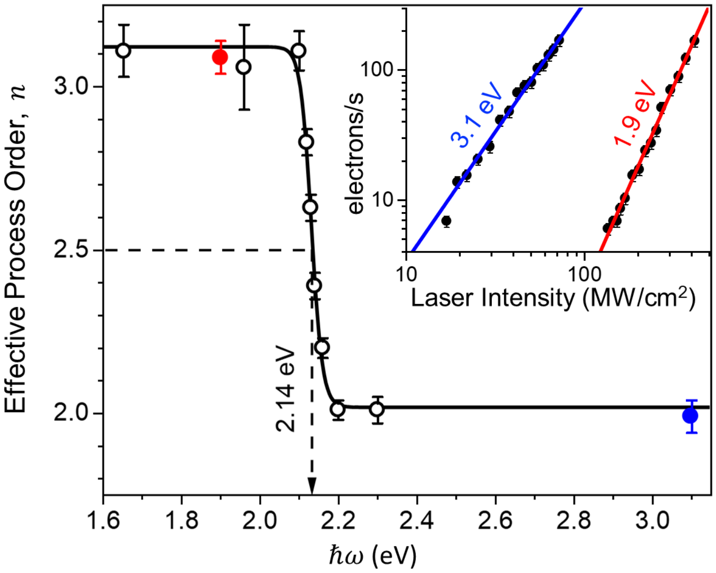

Figure 4.3: Multiphoton photoemission process orders are determined for gold film by measuring the photoemission signal as a function of peak laser intensity for a series of photon energies. The process order is the number of photons an electron must absorb to overcome the work function, where "effective" non-integer process orders are due to contributions from both the two-photon (I^2) and three-photon (I^3) processes. Examples of the intensity-dependent plots are provided in the figure insets for photon energies at 1.9 eV (3PPE, solid red) and 3.1 eV (2PPE, solid blue).

with a phonon or lattice impurity for momentum conservation.

The combination of intraband and interband multiphoton excitation pathways can be modeled via a sum of (i) a pure Fermi-Dirac term for electrons originating in the conduction band ($f_{\mathrm{in}}^{(\mathrm{FD})}$) and (ii) an exponentially decaying term that approximates the d-band contribution to the JDOS ($f_{\mathrm{in}}^{(d)}$). This approximation appears to be justified by previous XPS measurements of the conduction and 5d-band DOS of gold.[175] Within the three-step model, energy redistribution due to inelastic scattering is calculated to be negligible for the near-threshold electrons studied herein (free electron kinetic energies $\leqslant$1 eV), since very few electrons are able to escape after even a single inelastic collision.[17] The net speed distribution for electrons excited in the Au film is therefore

$$\begin{aligned} f_{\mathrm{in}}(v') &= f_{\mathrm{in}}^{(\mathrm{FD})}(v') + A_d f_{\mathrm{in}}^{(d)}(v'), \\ f_{\mathrm{in}}^{(\mathrm{FD})}(v') &= (e^{(\frac{1}{2}m_e(v'^2 - v_{\mathrm{F}}^2) - n\hbar\omega)/kT_e} + 1)^{-1}, \\ f_{\mathrm{in}}^{(d)}(v') &= e^{-\beta_d(\frac{1}{2}m_e(v'^2 - v_{\mathrm{F}}^2) - n\hbar\omega)}, \end{aligned} \tag{4.6}$$

where the internal electron velocity in the gold (v') is related to the external velocity in the vacuum (v) by conservation of energy: $\frac{1}{2}m_e v'^2 = \frac{1}{2}m_e(v^2 + v_{\mathrm{F}}^2) + \phi_{\mathrm{Au}}$. By Eq. 4.6, Eq. 4.5, and Eq. 4.4, the angularly-averaged velocity distributions determined from the VMIs can then be fit with parameters A (total amplitude), A_d (relative d-band contribution), β_d (effective exponential decay constant for d-band DOS), kT_e (conduction electron Fermi-Dirac temperature), and v_{F} (Fermi velocity). To minimize parameter correlation, A_d, β_d, and kT_e are globally constrained across the speed distribution fits for the 16 different excitation photon energies. The dominant process order, n, is known and held fixed for each photon energy. The resulting fits are shown in Fig. 4.2b, which clearly capture both the independent and global behaviors of the distributions quite well. Note, in particular, the increasing importance of the d-band contributions for higher photon energies, particularly > 1.8 eV, as well as the dramatic contraction of the Fermi edge due to the onset of 2-photon photoemission channel above 2.1 eV.

As a brief interlude, it should be noted that the measured velocity distributions are actually in camera pixel units, which must therefore be calibrated. This is simultaneously achieved via these fit distributions, as addressed in the next section, resulting in a calibration factor that is utilized for the remainder of this section. The globally-fit Fermi-Dirac electron temperature is found to be $T_e = 450 \pm 50$ K ($\pm$ standard error). This fairly modest increase above room temperature can be attributed to electron heating that occurs during a laser pulse, with equal or higher electron temperatures $>$500 K demonstrated previously for 30 nm thick Au film and similar absorbed pulse fluences ($\sim$200 μJ/cm^2).[47] The relative d-band amplitude fits globally to $A_d = 0.06 \pm 0.01$, and the exponential constant approximating the d-band DOS is globally fit to $\beta_d = 4.2 \pm 0.2$ eV^{-1}, which nicely reproduces the approximate DOS of gold determined via XPS experiments.[175]

For an even clearer parsing of the 3PPE, d-band 3PPE, and 2PPE contributions to Au thin film photoemission, the overall signals have been measured as a function of OPO photon energy, as reported in Fig. 4.4. On a logarithmic scale, the total MPPE spectrum shows a dramatic increase in the photoemission rate (over four orders of magnitude) with increasing photon energy between 1.63 and 2.33 eV, at constant intensity. This, in turn, reflects the increasing electron DOS that can be excited above the vacuum level with increasing photon energy, especially once $n\hbar\omega$ is large enough to promote 3PPE from the d-band states and 2PPE from the occupied conduction band states. The MPPE curve in Fig. 4.4 is fit by integrating the ejected photoelectron distribution over all velocities and employing the parameters determined in the VMI fits. The fits reproduce the behavior well with only the 2PPE and 3PPE amplitude parameters floated, for which the steep onset of 2PPE between 2.1 and 2.2 eV photon energies is in excellent agreement with the abrupt transition in power-law slopes demonstrated in Fig. 4.3. The fit amplitude of the 2PPE term is nearly four orders of magnitude greater than that of the 3PPE term, which illustrates how lower-order processes in the perturbative MPPE expansion become dominant once energetically above threshold. It is clear that the 2PPE signals (once energetically accessible) should eventually become stronger than the *d*-band contributions with increasing OPO photon energy, as the *d*-band emission is still a 3-photon (interband absorption + intraband 2PPE) process and therefore involves an additional transition matrix element with respect to any 2-photon process. As expected, however, the *d*-band signal (i.e., the difference between the solid and dashed lines in Fig. 4.4) does become much stronger than 3PPE from the conduction band for photon energies $\geqslant$1.9 eV. Despite a few approximations, the excellent agreement between least-squares fits and photoemission data for both the VMIs at many different photon energies (Fig. 4.2a) and the integrated distribution (Fig. 4.4) indicates that the ballistic three-step model with *d*-band contributions captures much of the essential physics underlying MPPE from thin Au films.

4.4 VMI Calibration

Velocity map images are read out as counts per camera pixel. The origin and the velocity calibration factor must therefore be determined in order to analyze these distributions. The origin is simply determined via Gaussian center fit of the highly-centralized photoemission distribution from a nearby spot on the ITO at 400 nm (2-photon) excitation. The calibration factor is more challenging, and would ideally be determined by measuring photoelectron emission from discrete energy lines in a molecular system.[178] While a noble gas flow source may be implemented in future with the laser focal spot shifted just above the ITO sample coverslip to stimulate gas-phase emission, this is currently not available. Instead, all electrons are photoemitted from solids with no discrete energy lines (note also that no surface states are probed given the surface-parallel polarization). Instead, therefore, the Fermi edge represents the most dramatic feature in the photoemission distributions, whch may therefore be fit as a function of photon energy to calibrate the system. The photoelectron kinetic energies corresponding to the Fermi level in the material ($\propto v_{\mathrm{F}}^2$) have been plotted as a function of multiphoton excitation energy in Fig. 4.5. Note the strong linear proportionality, confirming simple expectations from the photoelectric effect that the maximum kinetic

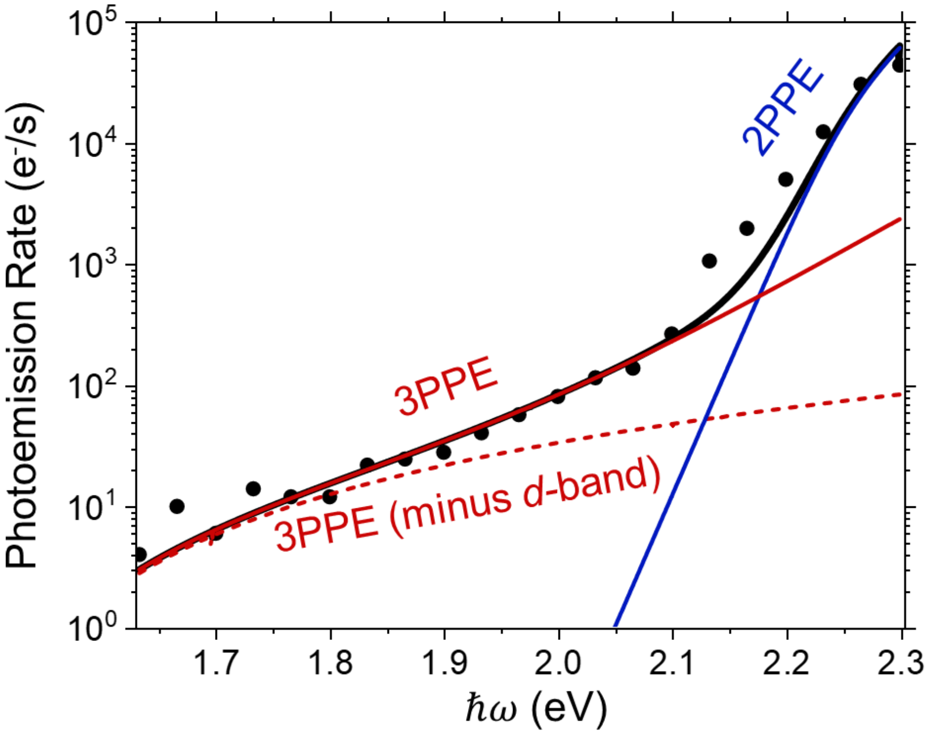

Figure 4.4: Gold film MPPE spectrum measured with a constant effective (i.e., pulse-width-corrected) input intensity at each OPO photon energy. The spectrum is fit using the ballistic photoemission model integrated over all photoelectron velocities. To achieve the 5 orders of magnitude in dynamic range without event overlap on the CCD and corresponding event loss at high count rates, the intensity is decreased for photon energies $\geqslant$2.2 eV, and the measured signal scaled back up accordingly. While changing the intensity will affect the relative amplitude between the 2PPE and 3PPE contributions, care is taken to avoid any effects on the spectrum by performing this operation far enough away from the transition region (2PPE is already dominant at 2.2 eV).

energies increase with total photon energy, with the intercept yielding the work function, $\phi_{\mathrm{Au}} = 4.46 \pm 0.05$ eV. This value is lower than observed for atomically clean, single-crystal gold surfaces[122] ($\sim$ 5.1 eV) but consistent with measurements of polycrystalline gold surfaces exposed to ambient air/water vapor.[51] This decrease in work function with ambient exposure arises from a molecular adlayer (e.g. water), which can suppress the inherent dipole layer at the metal surface and decrease the corresponding potential barrier.[87] The slope in Fig. 4.5 provides an important experimental calibration, yielding a pixel-to-speed conversion factor of $\gamma = 4150 \pm 40$ m/s/px, which is within 5% of the value simulated using *SIMION* (4240 m/s/px). This value will is utilized for all subsequent studies.

4.5 Discussion

Sensitive detection and analysis of multiphoton photoelectrons as a function of angle and speed has been demonstrated using the SPIM technique on smooth, extended Au thin films. The 2D transverse velocity map data has been fit in the framework of a ballistic, three-step photoemission model to recover the v_z information and thereby the full 3D photoelectron velocity distribution. This analysis strongly suggests that the hot electron distribution in the Au film is excited isotropically as well as that the electrons are excited with sufficient perpendicular momentum to overcome the surface potential barrier and leave the surface in a $\cos(\theta)$ external angular distribution, due to the loss of momentum normal to the surface and the corresponding Jacobian transformation between internal and external coordinates. Furthermore, the final electron speed distributions are reproduced well by a simple sum of (i) a Fermi-Dirac distribution for the conduction electrons and (ii) an exponential decay in DOS for the *d*-band electrons. Along with insights into the electronic properties of thin Au films, which provide an essential context for subsequent Au nanoparticle studies, two important observations about the SPIM surface VMI technique are summarized below.

First of all, multiphoton PES in the visible-photon energy range provides fundamentally different information than single-photon UV or x-ray PES, which are commonly used

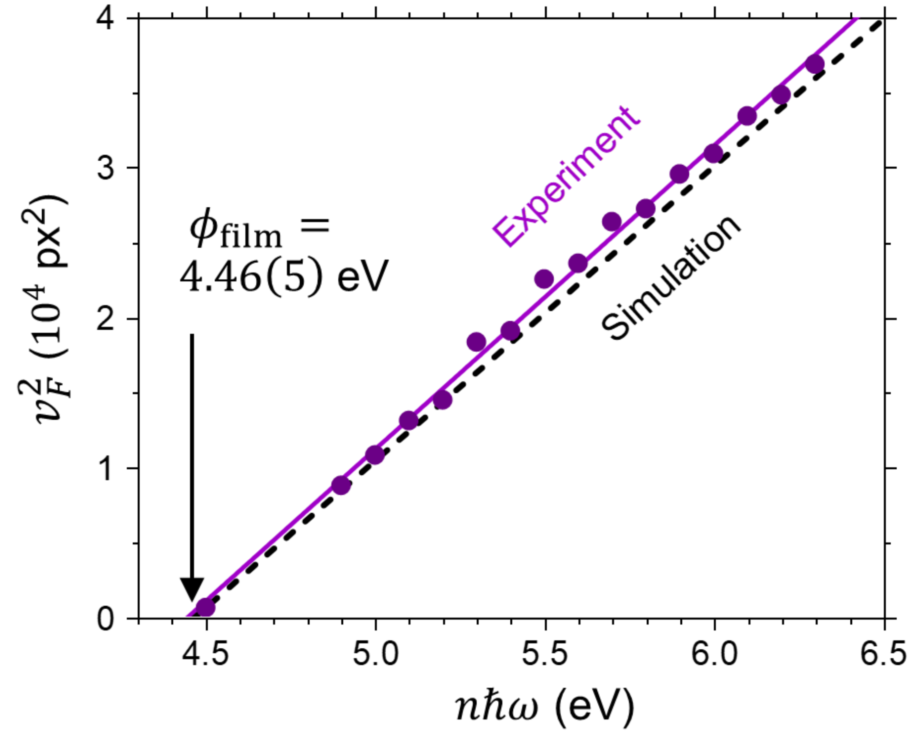

Figure 4.5: Summary of fit results for gold film VMIs, showing the kinetic energy for electrons originating at the Fermi level ($\propto v_{\mathrm{F}}^2$) versus the total energy for an n-photon process. The intercept yields a work function of 4.46(5) eV, and the slope, 20,400(350) px^2/eV, corresponds to a velocity calibration factor $\gamma = 4150(40)$ m/s/px . The simulation (dashed line) is from *SIMION*-calculated trajectories and the slope is within 5% of the experimental value.

for measuring valence band structure and core/valence DOS, respectively. This is because visible excitations above the vacuum level in noble metals involve nonvertical/indirect transitions and therefore require collisions with a phonon, lattice defect, impurity center, or the surface during excitation to conserve momentum. Implications of this indirect excitation mechanism have been demonstrated by the Au film studies, Fig. 4.2, including isotropic excitation and the strong, vertical interband excitation of *d*-band electrons compared with the weaker, nonvertical intraband excitation of conduction electrons. Furthermore, in multiphoton excitation processes, electrons must couple through real or virtual intermediate states before escaping. Multiphoton techniques (e.g., time-resolved 2PPE) can therefore provide information on the unoccupied states below the vacuum level and are particularly useful for measuring hot electron dynamics in femtosecond pump-probe studies.[14, 143, 218] Properties such as the lifetimes and decay pathways of excited electron distributions in these intermediate states are especially important for plasmonic applications that rely on hot electron extraction, such as photodetection,[22] photocatalysis,[110] and solar energy conversion.[30]

Second, determination of the work function to within ∼50 meV is possible even in the absence of any narrow spectral features due to the steepness of the Fermi edge, which is preserved by the high-quality linear VMI mapping of transverse velocity onto radial detector position. This ∼50 meV precision approaches that of common photoemission and Kelvin probe work function measurements, which have typical uncertainties ranging from 10 to 50 meV,[38] although the accuracy has not been characterized here via other work function measurements. While this aspect of the experimental technique still has room for optimization, the fundamental instrument energy resolution is calculated to be better than 10 meV at 1 eV photoelectron kinetic energy (or 1%) for the voltages/magnification utilized, limited primarily by the MCP pore spacing and ultrashort pulse bandwidth. This could in principle be further improved for low-energy electrons by increasing the magnification and/or MCP size or decreasing the pore size/pitch. It should finally be emphasized that these SPIM studies benefit significantly from continuous OPO tunability over the full visible spectrum, which provides a crucial additional spectral dimension and the ability to characterize photoelectron velocity distributions as a function of photon energy.

Chapter 5

Optical Photocurrent Control with Nanoshells and Nanostars

Now that the performance of the SPIM system and studies of thin gold film on flat glass have been studied in detail, a natural step into the nanoscale domain is to study thin gold film on nanoscale curved glass—i.e. gold/silica nanoshells. It will be shown that many nanoshells display crevice defect hot spots that lead to highly-spatially-localized and thus highly-directional photoemission. This provides an opportunity to demonstrate polarization-controlled hot spot selectivity and photoemission angular control for nanoshells with multiple defects. However, the precise near-field photoemission mechanisms from concave, uncontrolled hot spots are not so clear. For further clarity and control, we thus study gold nanostars and demonstrate both polarization- and frequency-controlled emission from well-controlled, sharp convex tip hot spots. The nanostars behave as multi-tip photocathodes and provide an unprecedented level of optical control for current generation, switching/modulation, and even pseudo-continuous beam steering. These results and associated theoretical methods for simulating surface-mediated photoemission from arbitrary gold nanoparticles provide crucial insights for similar light-matter transducers to be incorporated in THz nanoelectronics and novel on-chip electron beam sources, circuits, and novel quantum probe modalities. The majority of this chapter is taken from recent work on Au nanostars[144] and Au nanoshells.[145, 146]

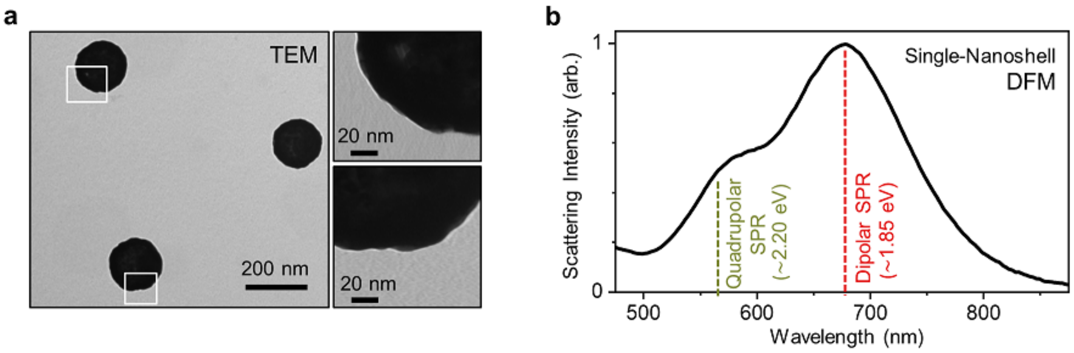

Figure 5.1: (a) Transmission electron micrograph of three nanoshells supported on a carbon film, with high-magnification images demonstrating various gold shell surface roughness features. (b) Representative single nanoshell scattering spectrum measured via dark-field microscopy (DFM), for a nanoshell supported on an ITO/glass substrate.

5.1 Gold Nanoshells

For the present experiments, commercially available Au shell/silica core nanoparticles with lipoic acid ligands (nanoComposix Inc., $R_{\text{core}} = 60$ nm and $R_{\text{total}} = 82$ nm) are spin-coated onto a 10 nm ITO-coated glass coverslip with an Au registration grid for correlated studies. High-resolution TEM micrographs of nanoshells deposited on a carbon film are shown in Fig. 5.1a. Although the geometric cross section of a single nanoshell represents only a relatively small fraction of the laser focal illumination area (10% at 650 nm), the combination of strong plasmonic near-field enhancements and the $|E|^{2n}$ photoemission sensitivity result in nanoshell emission rates several orders of magnitude higher than the ITO background, as previously demonstrated for Au nanoshells[62] and nanorods.[65, 64] Since the localized surface plasmon resonance (LSPR) plays such a dominant role in the photoemission dynamics for these nanoparticles, it is worth first presenting a brief characterization of the plasmonic properties of the nanoshells via both optical and photoemission measurements (along with theoretical expectations) and comparing these with Au film.

Dipolar and quadrupolar nanoshell scattering properties are characterized via dark-field microscopy (DFM), with a single-nanoshell scattering spectrum shown in Fig. 5.1b. As described elsewhere,[64] the DFM setup is separate from the SPIM system and consists of white light from a tungsten/halogen lamp focused onto the sample via a dark-field condenser lens. Scattered light is collected via a microscope objective on the opposite side of the sample and imaged onto an electron-multiplying CCD (Princeton Instruments Cascade II) via a spectrometer (Acton SpectraPro 150, 150 grooves/mm grating). The spectrographs from individual nanoparticles are background-corrected and scaled to correct for spectral nonuniformity of the light source, the system transmission function, and the camera sensitivity curve. Unless otherwise indicated, nanoshells in these SPIM experiments are excited with 100–200 fs pulsed light at $\hbar\omega = 1.9$ eV (650 nm), which is strongly coupled to the dipolar SPR.

Experimental UV-vis extinction data for an ensemble aqueous nanoshell solution are compared with the COMSOL finite element method (FEM) and Mie theory calculations[140] for isolated (non-aggregated, uncoupled) nanoshells in water (Fig. 5.1a). The dominant low-energy extinction peak can be readily identified in Mie and finite element method (FEM) calculations as the dipolar SPR scattering component, while the smaller peak to the blue is quadrupolar SPR absorption. These calculations are based on the measured core radius of 60(6) nm (1σ standard deviation) and an outer radius of 82(12) nm, as characterized via TEM of 100 nanoshells. Radii are calculated from the particle areas after thresholding TEM images, thereby averaging over any bumps on the shell surfaces. The shell layer is modeled using the bulk dielectric function of Au,[86] with the silica and water refractive indices set to 1.45 and 1.33, respectively. The Mie and FEM theoretical results in Fig. 5.1a are in excellent agreement with one another, but clearly blue-shifted by $\sim$0.1 eV with respect to the UV-vis measurements. Due to the strong sensitivity of the nanoshell SPR to shell thickness, there are a number of factors that could be contributing to this disagreement, such as surface roughness, nonconcentric core offsets,[134, 80] or the environment effect of surface ligands. Similar offsets observed previously for gold nanoshells were attributed to $\sim$4 nm surface roughness on both the interior and exterior surfaces of the Au shell layer.[133]

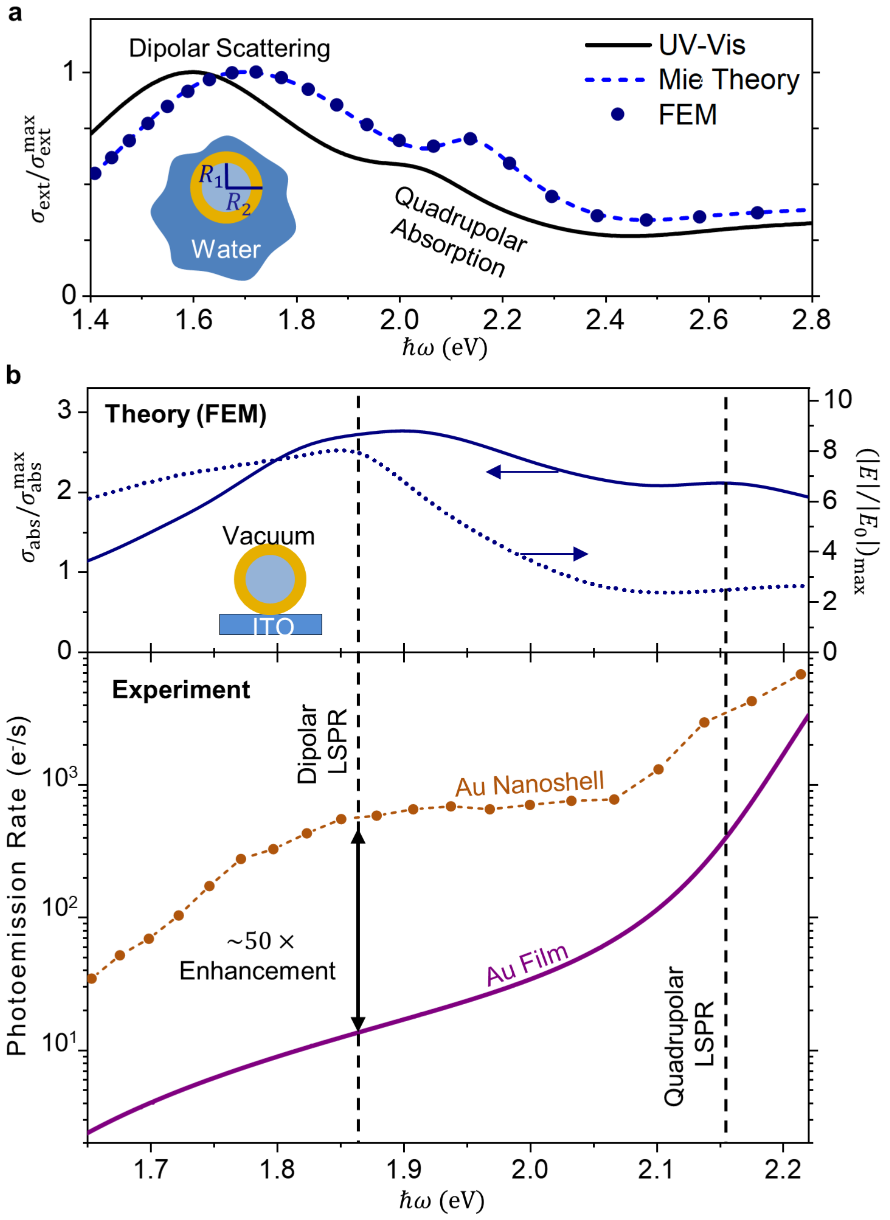

Figure 5.2: (a) UV-vis data compared with FEM and Mie theory calculations, all normalized to the dipolar scattering peak. The calculations use the average core radius $R_1 = 60(6)$ nm and average outer radius $R_2 = 82(12)$ nm. (b) Linear absorption cross section and near-field enhancement calculated via FEM (top) and experimental MPPE spectrum for a representative gold nanoshell with the gold film spectrum shown for comparison (bottom).

Mie theory is applicable for spherical particles but is not readily extended to supported nanoparticles. However, FEM calculations are highly versatile with respect to complex geometries[85] and are therefore used to calculate the absorption cross section and near-field enhancement spectrum for a supported nanoshell, as shown in Fig. 5.2b. The supported nanoshell dipolar LSPR is predicted to be blue-shifted from the aqueous value (1.65 → 1.85 eV) due to the smaller effective refractive index of the vacuum/substrate environment.[92] The electronic band structure properties of the Au shell layers are expected to be much the same as Au film, and the photoemission proceeds via MPPE with the crossover from 3PPE to 2PPE occurring around $\hbar\omega \approx 2.15$ eV for both systems (Figs. 4.3 and 5.3). This strongly suggests that nanoscale curvature and corresponding plasmonic near-field enhancement effects have the most significant influence on the photoemission properties of Au nanoshells relative to Au thin film. Simply stated, the plasmon resonance enhances the absorption and photoemission but also emphasizes any surface effects due to charge localization and the resulting electric-field enhancements at the nanoshell surface. To confirm these expectations, the integrated MPPE spectrum is shown for a single Au nanoshell in Fig. 5.2b, where a photoemission enhancement of ∼50 compared with the Au thin film signals represents an unmistakable signature of the dipolar plasmon resonance around 1.85 eV. A sharp kink due to the onset of 2PPE is also observed around 2.1 eV, in good agreement with the intensity-dependence results in Fig. 5.3. The nanoshell MPPE spectrum can thus be thought of as a scaled version of the Au thin film spectrum, enhanced by over an order of magnitude by the dipolar and quadrupolar plasmon resonances.

Turning now to investigations utilizing the SPIM velocity mapping capabilities, a series of VMIs collected at different photon energies is summarized in Fig. 5.4a for a single, representative nanoshell, prior to any cleaning (see Section 2.5). The transition from 3PPE to 2PPE behavior is again clearly evidenced in the velocity distributions by the corresponding dramatic contraction in the Fermi edge that occurs between 2.00 and 2.15 eV, in excellent agreement with both the intensity-dependence results in Fig. 5.3 and the 2PPE

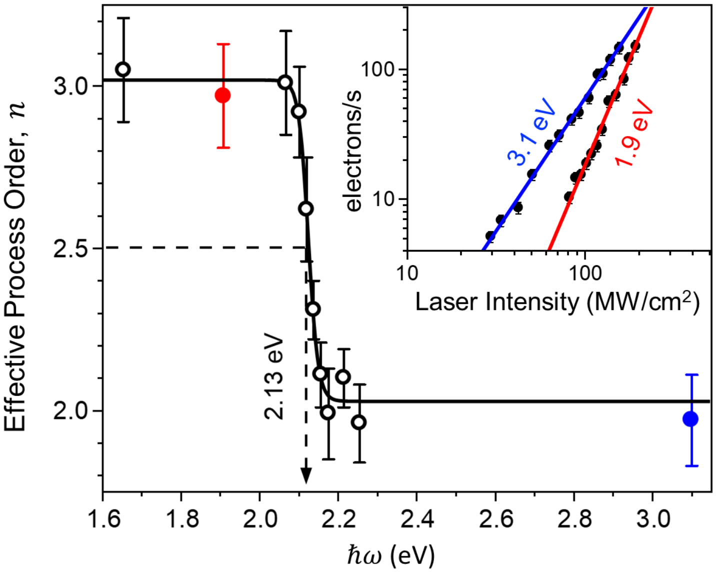

Figure 5.3: Multiphoton photoemission process orders are determined for a representative gold nanoshell by measuring the photoemission signal as a function of peak laser intensity for a series of photon energies. The process order is the number of photons an electron must absorb to overcome the work function, where "effective" non-integer process orders are due to contributions from both the two-photon (I^2) and three-photon (I^3) processes. Examples of the intensity-dependent plots are provided in the figure insets for photon energies at 1.9 eV (3PPE, solid red) and 3.1 eV (2PPE, solid blue).

onset observed in Fig. 5.2b. A surprising characteristic of these nanoshell VMIs is the high degree of azimuthal isotropy, despite linearly polarized excitation light coupling to the dipolar and quadrupolar SPR modes and the strong anisotropy of the corresponding near-field enhancements.[134] This will turn out to be due to post-emission photoelectron inelastic scattering with some air (i.e. water) adlayer on nanoshells that have not yet been cleaned via high-energy photon (3.1 eV SHG beam) exposure. The inelastic scattering effectively randomizes the emitted electron directions. However, as a first attempt at modeling this scattered behavior, it is assumed that the electrons are emitted uniformly from the nanoshell surface. The three-step photoemission model is again utilized but now with the $\cos(\theta)$ factor in Eq. 4.4 eliminated to account for uniform emission from the overall spherical nanoshell geometry. The presence of the substrate can be approximately taken into account by assuming that all downward-moving electrons are collected by the ITO, which uniformly scales the photoemission distribution by an overall factor of 0.5. With these additional assumptions, the radial VMI distributions in Fig. 5.4b are least-squares fit using the *d*-band parameters determined from the Au film studies. Although the Fermi edges are fit reasonably well with a globally fit Fermi temperature of 430(50) K, it is now clear that the fits do not even qualitatively capture all of the behavior in the photoemission distributions. In particular, the large excess signals near zero velocity that constitute as much as 30% of the total photoemission count rates are not correctly predicted by the three-step photoemission model, which does not account for post-emission inelastic scattering. Even so, the work function of 4.33(10) eV can still be determined with high accuracy as it depends primarily upon the sharp Fermi edges. This is close to the 4.46(5) eV work function measured on Au film but lowered by additional considerations such as the spherical particle geometry (when electrically grounded),[200] ligand surface dipole effects,[87] and the contact potential with the ITO substrate.[215]

When one takes into account the linear laser polarization and strong anisotropy of the dipolar and quadrupolar LSPR electric near-field distributions, the nearly complete

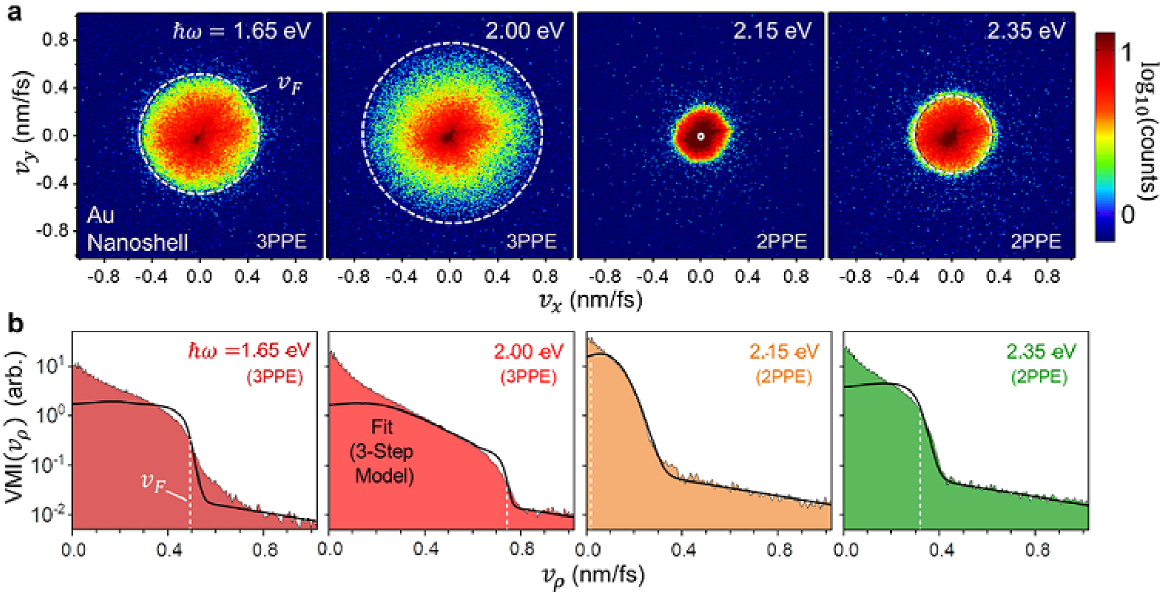

Figure 5.4: (a) Log-scale VMIs measured on a representative gold nanoshell for a series of photon energies and linear polarization, count-normalized at 10^5 electrons per image, with the speed corresponding to electrons emitted from the Fermi level (v_{F}) indicated with a dashed line based on fits. The axes are now in physical velocity units, using the calibration factor determined via gold film measurements. (b) Angularly averaged VMI radial distributions are displayed on a logarithmic vertical scale, shown with fits to the three-step model (black) assuming uniform photoemission from all surface areas on the nanoshell.

azimuthal symmetry observed in the nanoshell VMI distributions is initially rather surprising. For example, considering just the dipolar SPR, the near-field enhancements are predicted to be strongest along the plasmon axis defined by the laser polarization, with maximum enhancements of $|E/E_0| \approx 8$ determined via FEM calculations at the nanoshell surface ($\hbar\omega =$ 1.9 eV—see Fig. 5.2b), compared with $|E|/|E_0|$ near unity at the surfaces perpendicular to the plasmon axis. It shall be shown in Section 6.6 that volume-like emission is dominant for defect-free nanoshell dipolar excitations, but the simple, initial intuition of excitation in the surface-enhanced regions is first examined here. Most electrons will be excited in the plasmon-enhanced-field regions near the surface of the Au shell, only traveling ~5 nm in the gold film before either escaping from the surface or decaying below the vacuum level via electron-electron scattering.[24, 102] Since these short inelastic mean free paths are very small compared with the nanoshell dimensions (~160 nm diameter), photoemission will effectively be localized to the regions of greatest excitation. The $\cos(\theta)$ distribution of the emitted electrons is peaked in the direction normal to each surface area element from which the electrons escape, such that any anisotropy in the position-space emission distribution should produce a corresponding anisotropy in velocity space. In the case of dipolar nanoshell surface emission (which again, turns out not to be the correct explanation, let alone post-emission scattering effects), one would expect emission peaking along the dipolar plasmon axis. Very much contrary to these expectations, there is little anisotropy evident in Au nanoshell VMI distributions in Fig. 5.4a. Furthermore, neither the process order (2PPE/3PPE), nor the coupling to different SPR modes (dipolar/quadrupolar) at different photon energies appears to affect the VMI distribution. Only a change in the energy cutoff corresponding to the Fermi level inside the metal is evident with increasing photon energy, as clearly displayed in Fig. 5.4b.

The possibility that scattering is occurring with the surface ligands (lipoic acid) and/or an additional molecular adlayer (i.e. due to brief exposure to ambient conditions in sample preparation) during the photoemission process—effectively randomizing the photoelectron velocity directions—will now be explored. As described in Section 2.5, repeated air exposure → cleaning cycles demonstrate that it is not ligands, but rather some reversible adlayer (e.g. water) that develops upon air exposure. Such an adlayer being responsible for strong post-emission inelastic scattering explains both the unexpected isotropy in the velocity distribution and the excess electron densities observed near zero transverse speed in the VMI distributions in Fig. 5.4b. Upon exposure to low doses of second harmonic 400 nm light ($\sim$1 GW/cm^2 for $\sim$1 s at $\hbar\omega = 3.1$ eV) the peak near zero velocity in the velocity map and radial distribution disappears. The distribution is still fairly isotropic looking on a logarithmic scale but is no longer centralized near zero kinetic energy, indicating that the inelastic scattering effect has been greatly reduced. It should be noted that the resulting radial distribution is still not captured well by the isotropic photoemission model. This will be examined in more detail via full Monte Carlo modeling in Section 3.5.1. Regardless, this "cleaning" effect is highly reproducible over many nanoshells and does not change appreciably upon longer or higher-intensity exposure. This indicates that if surface admolecules are indeed being cleaned off, all or most have been removed at these exposure levels. Interestingly, an observation of Au-thiol bond cleavage and therefore cleaning of ligands from gold nanoparticles with 400 nm exposure has been reported previously by El-Sayed and coworkers and was attributed to hot electron energy transfer into the Au-S ligand bond triggering dissociation.[82] While it is not expected that ligands are being cleaned off here—or if they are, they weren't responsible for scattering in the first place and the removal thus goes unnoticed—a similar hot-electron-mediated cleaning effect may be occurring that requires the high-energy SHG photons. Other sample-cleaning techniques (e.g., chemical rinsing, UV/ozone cleaning, plasma cleaning, and heating on a 200 °C hot plate) have also been attempted prior to loading the nanoshell sample into the vacuum chamber, none of which produced any observable effect on the nanoshell photoemission distributions. This indicates that high densities of hot electrons with sufficiently high energy are essential to the ligand removal process, or possibly that surface cleaning must take place in vacuum due to fast adlayer deposition under ambient conditions.

One final intriguing observation is that this cleaning effect only occurs with 400 nm or higher-energy light (as it has also been observed at 350 nm), with exposure to 2.3 eV OPO photons producing no observable effect. Previous studies have demonstrated strong nanoshell photoemission-dependence on the laser polarization, which was attributed to hot spot effects arising from few- or even sub-nanometer defects on the nanoshell surface.[62] In the interest of eliminating possible contributions from defect hot spots in these initial single-nanoparticle VMI studies, it is noted that all nanoshells described so far were chosen that exhibit less than 10% variations in MPPE signal with laser polarization. By contrast, 90% of the nanoshells display strong polarization dependence due to the presence of defect hot spots, to be discussed in the next section, while more detailed studies of isotropic nanoshells and opportunities for full angular photoemission control will be discussed in Section 6.6 once the notions of volume and surface MPPE have been examined in more detail.

5.2 Directional Photoemission from Nanoshell Defect Hot Spots

The photoemission rate for a typical Au nanoshell is highly sensitive to the laser polarization even for normal-incidence light, as shown in Fig. 5.5b and explored previously in detail.[62] Because the nanoshells observed via TEM and SEM are nominally spherical, the strong polarization dependence indicates the presence of additional structure such as bumps and/or pits on the surface of the Au shell, which break the expected azimuthal symmetry of a supported spherical object. Despite the small individual surface areas of these hot spots relative to the overall nanoshell surface area, it has been shown that plasmonic field enhancements can grow disproportionately relative to a shrinking emitter area with a sharp geometrical feature, thereby enabling even sub-nanometer hot spots to compete with and even dominate the overall photoemissivity.[62] This effect is enhanced even more dramatically in the multiphoton regime, where the photoemission rate is highly nonlinear with respect to the local electric field, scaling as E^{2n} for nPPE. Nanometer-scale surface structure that could potentially produce these effects is evident in the correlated SEM image in the inset of 5.5a, as well as in the TEM images in Fig. 5.1a. The polarization dependence of the photoemission rate shown in Fig. 5.5b is thus fit by a constant term to account for the underlying isotropic behavior expected for a perfectly smooth nanoshell, which becomes the dominant behavior around the minimum photoemissivity polarization angle, θ_{min}, and a localized hot spot term proportional to $\cos^6(\theta - \theta_{\mathrm{max}})$. The latter $2n$th-order cosine term corresponds to the projection of the field along the hot spot axis for a three-photon ($2n = 6$) process. Note that even when polarized along θ_{min}, all of the nanoshells are still orders of magnitude more photoemissive than the ITO substrate.

Photoemission originating from localized hot spots on the nanoshell surface should be leaving the nanoparticle in a well-defined average direction, corresponding approximately to whichever side of the nanoshell the hot spot is located. The measured photoelectron momentum maps for single nanoshells, as in Fig. 5.5a, confirm the expectation of anisotropic photoemission, which is indeed strongly directional. Note that all nanoshells have been SHG-cleaned (see Section 2.5) prior to investigation to eliminate the surface adlayer due to air exposure and the associated inelastic scattering. Contrary to initial expectations, a comparison of the momentum map with the polarization dependence for the same nanoshell (Figs. 5.5a and 5.5b) reveals that the photoemission is actually strongest in the direction orthogonal to the laser polarization at peak photoemissivity angle, θ_{max}. Moreover, orthogonal photoemission is observed for the majority of nanoshells, with only ~10% of the nanoshells exhibiting a nominally parallel photoemission relative to the laser polarization at θ_{max} (Fig. 5.5a). Although initially surprising, the orthogonal emission from these hot spots is consistent with a "nanocrevice"-type defect geometry that can readily form between the crystal domains on the polycrystalline shell. At least one of these nanocrevice defects is evident as a dark spot in the micrograph inset in Fig. 5.5a and is also approximately aligned with the peak photoemission direction. As will be shown in further detail via additional correlated SEM-SPIM studies, along with finite-element simulations, these nanocrevice regions can be-

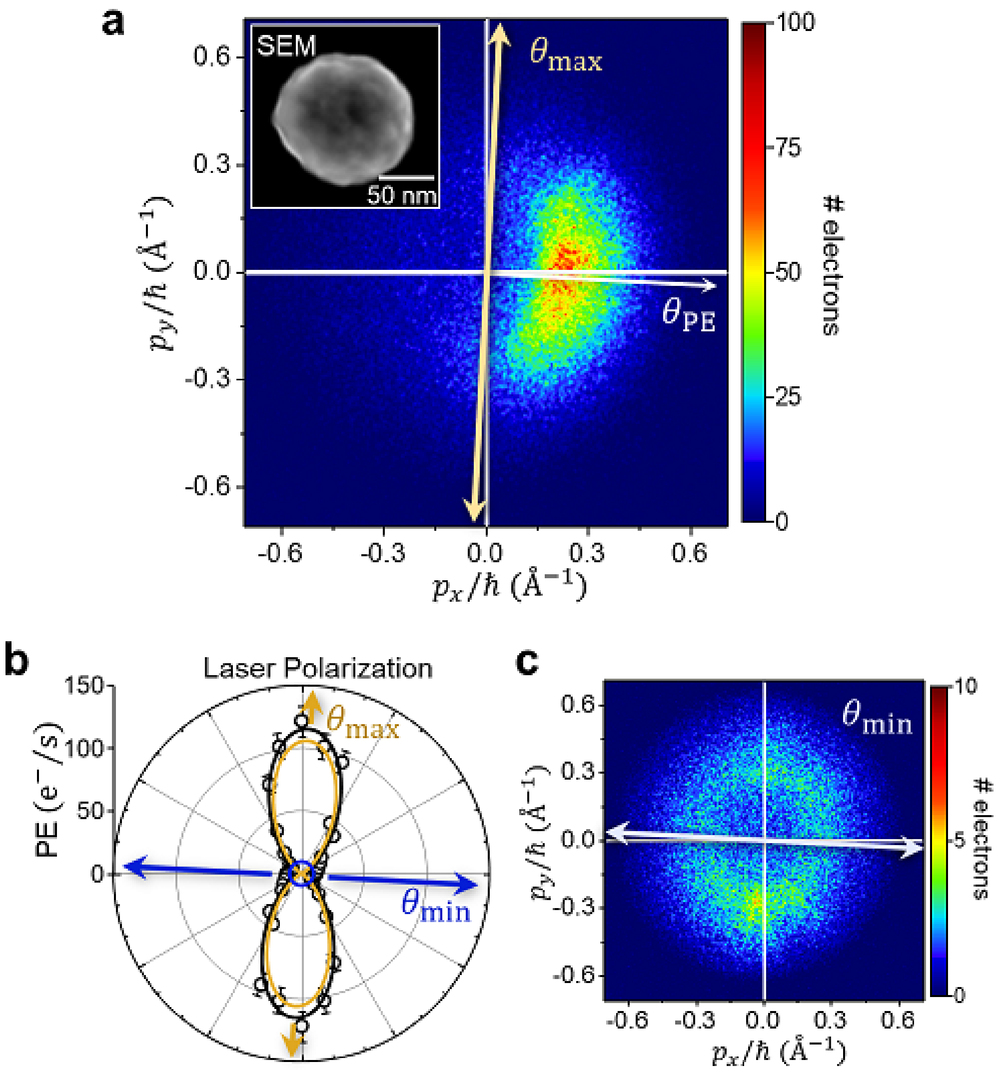

Figure 5.5: Directional photoemission from a single Au nanoshell, with all measurements taken at $\hbar\omega = 1.9$ eV on the dipolar SPR. (a) Photoelectron momentum map for a single nanoshell at the maximum photoemission polarization, $\theta_{\max}$. (Inset: a correlated SEM image.) (b) Polarization dependence for the same nanoshell, fit to $\cos^{2n}(\theta)$ (with $n = 3$) for the hot spot plus a constant term for the isotropic nanoshell contribution. (c) Momentum map for the same nanoshell, but now at the minimum photoemission polarization, $\theta_{\min}$, which demonstrates a more nearly isotropic photoemission behavior.

come strong hot spots when the laser polarization is orthogonal to the nanocrevice spatial axis. If the average photoelectron momentum is approximately radially outward from the nanocrevice hot spot region, then the photoemission direction will also be orthogonal to the laser polarization, as observed.

Additional near-field insight is gained by investigating the statistics of nanoshell photoemissivities, $\sigma_{\mathrm{PE}}^{(n)}(\theta)$ (where $n\mathrm{PPE} = \sigma_{\mathrm{PE}}^{(n)} I^n$), over many nanoshells at polarization angles, $\theta_{\max}$ and $\theta_{\min}$. Photoemissivity statistics for 3PPE at $\hbar\omega = 1.9$ eV are summarized in Fig. 5.6 for 45 individual nanoshells. When combined with correlated momentum maps and SEM images for each nanoshell, these statistics tell a simple story: A given nanoshell surface may contain zero, one, or more nanocrevices, any one of which may become a hot spot when the SPR is driven along the appropriate axis. The maximum nanoshell photoemissivities (at polarization $\theta_{\max}$) are spread out over more than 3 orders of magnitude due to very sensitive dependence on the specific crevice geometry and the corresponding near-field enhancement ($n\mathrm{PPE} \propto (|E|/|E_0|)^{2n}$). By contrast, the minimum photoemissivities are more strongly clustered near the smallest values of $\sigma_{\mathrm{PE}}^{(n)}(\theta_{\min}) \approx 5 \times 10^{-25} \frac{e^-}{\mathrm{s}} / \left(\frac{\mathrm{W}}{\mathrm{cm}^2}\right)^2$. This indicates that the photoemission at polarization $\theta_{\min}$ may be reaching the lower limit of the defect-free dipolar SPR enhancement. This picture is corroborated by momentum maps with polarization at $\theta \approx \theta_{\min}$, as demonstrated in Fig. 5.5c, which in most cases look quite isotropic despite strong anisotropy/directionality observed with polarization at $\theta_{\max}$. It may be noted that even the predominantly isotropic momentum distributions still tend to have a slight preference toward the orthogonal emission relative to the laser polarization, which will be explored in terms of volume photoemission Section 6.6. The total momentum distribution at any laser polarization angle is simply the linear combination of the $\theta_{\min}$ and $\theta_{\max}$ distributions, with the latter strongly peaking due to scaling by $\cos^{2n}(\theta - \theta_{\max})$.

To verify that all directional photoemission observed in these experiments is due to hot spot MPPE enhancement rather than OFE and/or ponderomotive acceleration following emission, photoelectron transverse kinetic energy distributions have been recorded at

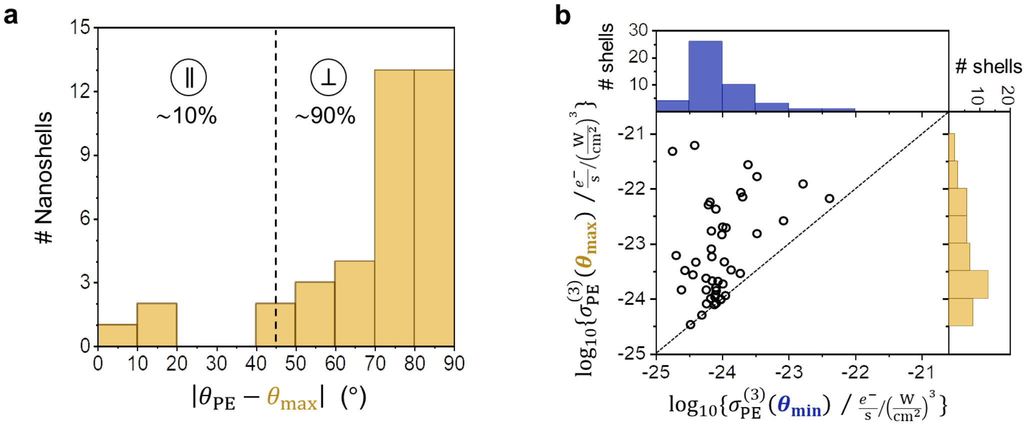

Figure 5.6: (a) Nanoshell statistics on the average photoemission direction (θ_{PE}) relative to θ_{max}, with θ_{PE} determined via Gaussian fit to radially integrated momentum distributions. (b) Nanoshell photoemissivity statistics at the maximum enhancement polarization, θ_{max}, and minimum enhancement polarization, θ_{min}, for each nanoshell.

multiple different laser intensities and frequencies. The results are presented in Fig. 5.7 for a single nanoshell, in this case one displaying the less typical behavior of peak photoemission (with polarization at θ_{max}) parallel to the laser polarization axis (Fig. 5.7a). Even for these uncommon parallel emitters, the intensity- and frequency-dependent behavior demonstrated in Figs. 5.7b and 5.7c is completely consistent with the more commonly observed perpendicular emitters. Specifically, as the intensity is increased in Fig. 5.7b in uniform steps of 0.2 GW/cm^2 at $\hbar\omega = 1.90$ eV, the total photoemission signal increases as I^3 (as expected for 3PPE), but the transverse kinetic energy distributions remain largely unchanged. This strongly supports a three-photon photoemission (3PPE) process. Conversely, although ponderomotive acceleration could in principle be taking place following MPPE in strong hot spot evanescent fields, one would expect the kinetic energy cutoff to increase approximately linearly with laser intensity,[101] whereas no such change is observed in the kinetic energy spectra over a 5-fold change in intensity. Furthermore, the Fermi edge drop-off around 1.5 eV kinetic energy corresponds to the expected value for 3PPE: $3\hbar\omega - \phi = 5.7 - 4.2eV = 1.5$ eV, in which the supported nanoshell work function of ~4.2 eV was also measured previously.[145] Thus, we can be quite certain of these experiments being in the fully perturbative 3PPE regime.

For gain further insight into the photoemission dynamics from nanoshell hot spots, transverse kinetic energy spectra have been measured as a function of laser photon energy, shown in Fig. 5.7c. These results are perfectly consistent with the MPPE mechanism, with the Fermi edge expanding outward by $\Delta n\hbar\omega$ with increasing photon energy and with a clear transition from the 3PPE regime to the 2PPE occurring between $\hbar\omega = 1.90$ and 2.20 eV. This sharp transition is quite strikingly revealed in the inset of Fig. 5.7c, which summarizes the power-law fits to intensity-dependence studies at a series of laser photon energies (nPPE $\propto I^n$) and, as expected, displays a precipitous sigmoidal shift in behavior between $n = 3$ and 2. None of this behavior is expected in an OFE process, nor in a thermionic process.

As a final confirmation of the multiphoton process, the Keldysh parameter (γ, Sec-

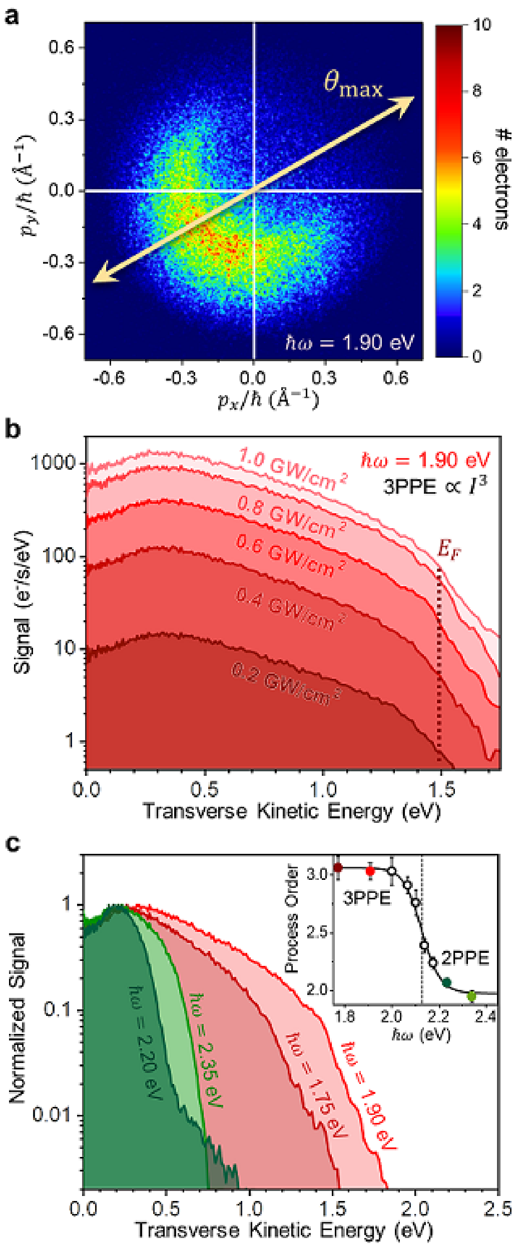

Figure 5.7: Confirmation that all photoemission takes place in the perturbative multiphoton regime. (a) Momentum map for a nanoshell/hot spot exhibiting a nearly parallel emission (but the demonstrated behavior is equally valid for the much more common orthogonal emitters). (b) Angle-integrated transverse kinetic energy spectra as a function of peak pulse intensity. The dashed line represents the kinetic energy of electrons originating from around the Fermi level within the gold. (c) Angle-integrated transverse kinetic energy spectra for different incident photon energies. (Inset: Summary of laser intensity-dependence measurements, with the process order determined via power-law fit, where nPPE ∝ I^n). The tail evident in the $\hbar\omega = 2.20$ eV 2PPE distribution is due to a remaining 3PPE contribution, due to proximity to the 2PPE–3PPE cross-over frequency ($\hbar\omega = 2.15$ eV).

tion 3.4.3) provides a convenient single-parameter indicator for MPPE ($\gamma > 1$) versus OFE ($\gamma < 1$).[91] At the highest peak input intensities at the sample of 1 GW/cm^2 ($E_0 \approx 0.1$ V/nm), for a measured nanoshell work function around 4.2 eV and assuming a large hot spot E-field enhancement of 50 at $\hbar\omega = 1.90$ eV, the Keldysh parameter is $\gamma = \phi/(2U_\mathrm{p} = 4.6$, with a ponderomotive energy $U_\mathrm{p} = e^2E^2/(4m_e\omega^2) \approx 0.1$ eV. These values indicate that photoemission is occurring in the multiphoton regime with minimal post-emission ponderomotive acceleration, even under the most extreme hot spot conditions expected in these experiments. In combination with the laser intensity and frequency studies discussed above, these calculations confirm unambiguously that the directional photoemission occurs from MPPE processes, arising from the specific geometries and nano-localized nature of the nanoshell defect hot spots rather than strong-field acceleration effects.

Unlike surface- or nanotip-based photocathodes, which impose directionality via the macroscopic geometry, the directionality of photoemission from nanoparticles is potentially more subtle, versatile, and tunable in nanoshells by choice of different SPR hot spots. This tunability is clearly demonstrated on a nanoshell that happens to have two hot spots with different θ_max but nearly equal photoemission efficiencies, as shown in Fig. 5.8. For such a system, rotation of the laser polarization between $\theta^{(1)}_\mathrm{max}$ and $\theta^{(2)}_\mathrm{max}$ also rotates the photoemission direction by a nearly equivalent angle (in the present case, approximately 90°). This illustrates the basic concept for an optically-controlled photocurrent switch, which could be operated on femtosecond time scales via ultrafast polarization control. Although the occurrence of nearly equivalent hot spots is not common in these nanoshells due to the variability of defect geometries and the strong $|E/E_0|^6$ photoemission sensitivity to electric field, this photoemission switching behavior is in fact observed for many nanoshells, just with different hot spot photoemissivities. More importantly, this provides a proof-of-concept for how nanoparticles/nanostructures might be specifically synthesized/fabricated for a near-field control of photoemission properties. For example, nanoparticles such as nanostars (to be discussed) or tailored nanolithographic structures[2] could take advantage of this effect in a

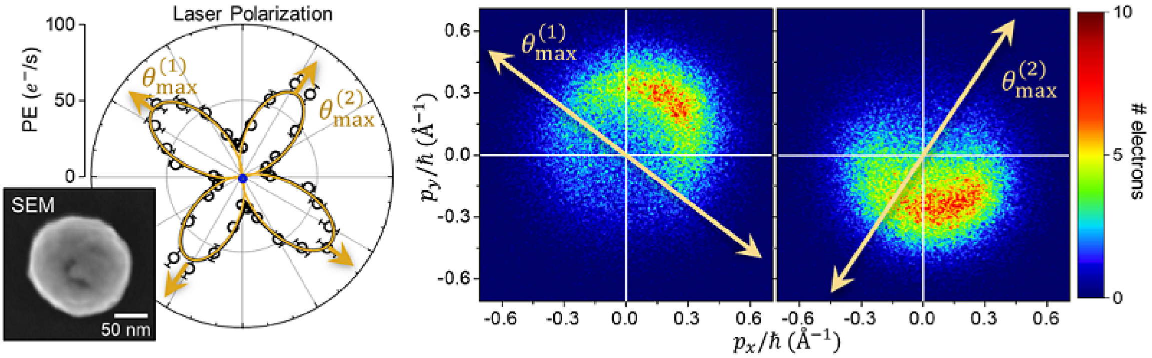

Figure 5.8: Polarization-controlled directional 3PPE from a single nanoshell with multiple hot spots of nearly identical photoemissivity, excited at $\hbar\omega = 1.9$ eV.

far more controlled manner, with multiple strong, tailored hot spots.

As the majority of the nanoshell hot spots exhibit a maximum photoemission orthogonal to the laser polarization direction, we can exploit a combination of SEM and finite element modeling (FEM) to explore which shell topologies might be most likely to produce this behavior. Correlated SEM and VMI images of 45 sample nanoshells reveal a common crevice-type structure corresponding to dark spots on the nanoshell surface (or light spots in TEM), as highlighted in Fig. 5.9. The peak VMI photoemission direction is correlated with one of these crevices in approximately 40% of the nanoshells studied. This 40% correlation is entirely reasonable considering that approximately half of the nanoshells would be expected to have hot spots in the lower hemisphere (not visible in the SEM images), whereas some will have crevices on the sides of the nanoshells that are less evident in the electron beam imaging. It is thus likely that the observed crevices (or sub-features therein) represent a common geometry for a highly photoemissive hot spot.[67] Previous studies have indeed highlighted the nanocrevice geometry as a probable candidate responsible for the extra strong field enhancements observed with nanoshells and rough metal surfaces.[67, 62, 54] It is worth noting that the crevice locations on the nanoshell in Fig. 5.8 are not evidently aligned with the photoemission directionality. This falls into the category of nanoshells that do not display clear directional correlations, possibly due to crevices hidden in the lower hemisphere. It is also possible that the photoemission direction is not perfectly aligned with a crevice evident in SEM/TEM due to a more complex hot spot geometry. Toward this end, more controlled studies of phtooemission from well-defined nanostar tip hot spots are explored next.

Different nanometer-scale features could lead to strong hot spots and photoemission enhancements even within the constraints imposed by these correlated SEM/VMI studies. To help elucidate these features further, FEM simulations have been utilized to explore the electric near-field enhancements for a given nanocrevice defect geometry embedded into the side of a nanoshell. Sample surface field enhancements are calculated in *COMSOL Multiphysics* 5.3 and presented in Figs. 5.10a and 5.10c, where it can be seen that the crevice becomes a strongly enhanced hot spot when the laser is polarized orthogonal to the crevice radial vector (Fig. 5.10a), whereas the hot spot exhibits negligible field enhancement for parallel polarization. If we consider a photoemission model that assumes a local photoemissivity dependent on surface E-field enhancement to the order $2n$, then a 10-fold E-field hot spot enhancement for this sample geometry would correspond to a peak 3PPE enhancement (per unit surface area) of $\sim 10^6$. Using this model as a simple starting point, we integrate the calculated E-field (raised to the appropriate $n = 6$ power for 3PPE) over the entire nanoshell surface. This already predicts an overall 200-fold enhancement of hot spot photoemission for perpendicular ($\theta_{\max}$) vs. parallel ($\theta_{\min}$) polarization. Furthermore, the FEM near-field distributions for orthogonal laser polarization in Fig. 5.10a suggest a very simple physical mechanism for the field enhancements: the crevice behaves like a nanogap or a nanoscale capacitor with the strongest enhancement occurring at the parallel, closely spaced walls near the crevice apex. To avoid unphysically small feature sizes in the model that could lead to singularities in the field enhancements, the smallest radius of curvature in these simulations is limited to the radius of a single gold atom (~1.7 Å). Variation in the crevice parameters (e.g. depth and curvature) changes the exact values of field enhancement, but no essential features of the hot spot behavior. Although such predictions will depend on the precise

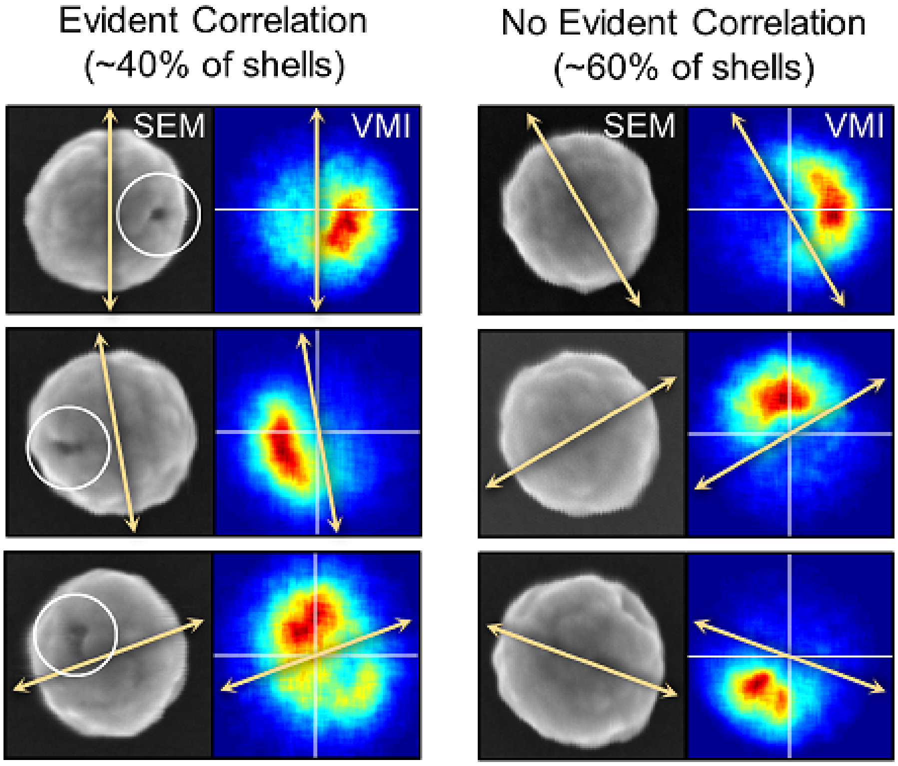

Figure 5.9: Example SEM and VMI images on single nanoshells that show either (left panel) a clear correlation or (right panel) no correlation between the directional photoemission and a nanoshell surface feature.

characterization of the nanocrevice geometry, these model FEM results already rationalize the many orders of magnitude dynamic range in photoemissivity enhancements observed experimentally (see Fig. 5.6b).

To model the hot spot photoelectron momentum distributions for the nanocrevice hot spots without knowledge of the precise crevice geometry, emitted electron trajectories (i.e. bouncing around in the crevice), or surface vs. volume photoexcitation ratio, a simple radial emission model is adopted. The photoelectron fluxes from each surface area element are taken to be proportional to the surface E-field enhancement raised to the $2n = 6$ power appropriate to 3PPE, with these enhancements determined via the previously discussed FEM results and mapped as a fine, uniform mesh over the entire nanoshell surface. The momentum distribution from each surface area element is based on a ballistic three-step model,[17] as discussed in Chapter 4Briefly summarized, a Fermi-Dirac speed distribution is assumed inside the nanoshell, with the emitted photoelectron distribution scaled by a $p\cos(\theta)$ Jacobian transformation from internal to external coordinates, whereby velocity components are treated by the usual conservation of energy (i.e. work function) and parallel momentum at the surface potential barrier. The emission from each nanoshell surface area element is taken to be centered relative to the radial vector (i.e. outward from the center of the nanoshell), which invokes the simple intuitive idea that once the complicated near-field collision dynamics within the defect walls have played out, the photoelectrons will be ejected approximately radially outward from the hot spot region. Such near-field dynamics include diffusion in the gold before emission and the re-absorption or multiple scattering events that may occur for many photoelectron trajectories due to concave crevice geometries. The resulting p_z-integrated (p_x, p_y) momentum maps predicted from this simple physical model are shown in Figs. 5.10b and 5.10d for laser polarization orthogonal ($\theta \approx \theta_{\text{max}}$) and parallel ($\theta \approx \theta_{\text{min}}$) to the nanocrevice axis, respectively. The results for orthogonal polarization in Fig. 5.10a reproduce the essential qualitative behavior observed in the experimental distributions, namely, strong directional photoemission (i) orthogonal to the laser polarization axis and (ii)

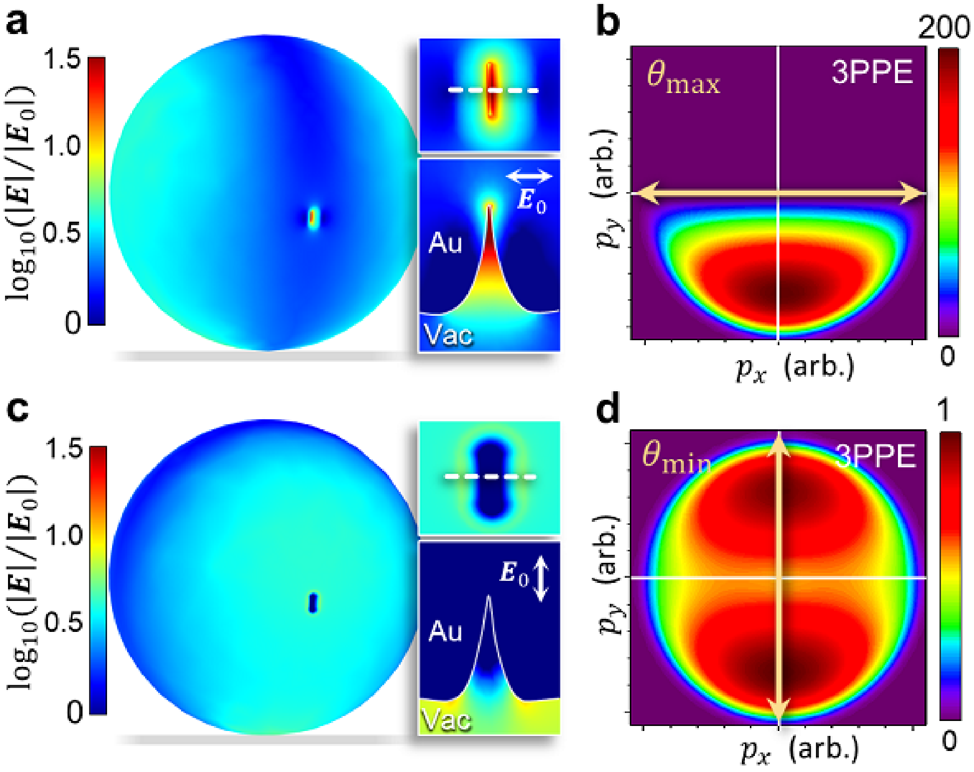

Figure 5.10: Finite-element simulations (a, c) of the near electric field distribution and corresponding model velocity map images (b, d) for the calculated electron flux around a nanoshell with a single nanocrevice are shown for orthogonal (a, b) and parallel (c, d) polarization of the laser relative to the hot spot radial direction. See text for model details.

radially away from the crevice geometry. By contrast, for parallel polarization at $\theta_{\min}$, the crevice exhibits E fields unenhanced by any plasmonic effects, resulting in a much weaker (200-fold less) photoemission characterized by a dipolar SPR near-field distribution and with the peak emission aligned with the laser polarization axis. Interestingly, however, the experimental photoelectron momentum maps at $\theta \approx \theta_{\min}$ often also have a tendency toward orthogonal (but centro-synmmetric) emission (e.g. Fig. 5.5c). Understanding these effects requires an investigation of the internal nanoshell field distributions and volume-mediated photoexcitation/emission mechanisms, to be discussed in Section 6.6.

In summary, transverse (p_x, p_y) photoelectron momentum maps of single Au nanoshells have been explored to reveal highly directional photoemission distributions in the weak-field MPPE regime. Combined evidence from momentum mapping, laser polarization studies, nanoshell photoemissivity statistics, and correlated SEM imaging suggests that small crevices in the nanoshell surface play an important role, leading to directional emission and corroborating previous work revealing the presence of nanoscale hot spots on Au nanoshell surfaces.[67, 185, 62] For the great majority (90%) of the nanoshells, the photoemission direction is orthogonal to the peak laser polarization axis, indicating that the hot spots are due to the nanocrevice-type roughness seen under scanning electron microscopy and simulated via finite-element analysis. Polarization control over the near-field electron photoemission behavior has been demonstrated for a single nanoshell with dual hot spots, providing a proof of concept for the engineering of plasmonic nanostructures with selective directional control of photoemission via laser polarization, which can be rotated on ultrafast time scales.

5.3 Ultrafast Nanostar Photocathodes

With nanostars and other multi-resonant particles, important opportunities for spatiotemporal photocurrent control emerge via frequency- and polarization-selective excitation of different plasmonic hot spots, which are often spatially separated and oriented in different directions.[77, 194, 68, 174, 146] Electric near-field hot spots have been extensively investigated in nanoplasmonic systems, with photoemission electron microscopy (PEEM) studies establishing the correlation between photoemission and plasmonic hot spots with ∼20 nm spatial resolution.[77, 8] Furthermore, these techniques have been combined with optical pulse shaping[21] to achieve coherent control over spatial photoemission distributions on femtosecond timescales.[2] However, direct observation of the corresponding photoelectron momentum-space distributions has remained a challenge, requiring angle-resolved photoelectron mapping from single, resonantly-excited nanoparticles. Such capabilities have only appeared recently[145, 146, 106, 107] as a comprehensive understanding of photocurrent distributions is becoming crucial for the design and implementation of nanocathodes in nascent ultrafast nanoelectronics and electron imaging applications. Full photoelectron momentum and energy characterization has been achieved by Lehr *et al.* on individual gold nanorods and bow-tie nanoantennas using time-of-flight momentum PEEM,[106, 107] which serves to clarify nanoplasmonic angular photoemission distributions and phenomena such as the transition into the optical field emission regime. Angular photoelectron mapping and steering have also been demonstrated for gold[136] and tungsten[204, 11] nanotips, primarily in the field emission regime. Despite these advances, many important aspects of the nanoplasmonic photoelectron emission mechanism and opportunities for angular control remain to be elucidated, particularly in the multiphoton regime.

Here, optically-controlled directional multiphoton photoemission from single gold nanostars is demonstrated using 2D photoelectron velocity mapping and 3D reconstruction for detailed characterization of the angular and energy distributions. These investigations begin with an examination of the plasmonic properties and directional photoemission from single nanostar tips resonantly excited using a pulsed femtosecond laser. Individual tips behave as locally-bright, point-like electron sources with a high degree of spatial coherence. The selective excitation of different tips is then demonstrated on a single nanostar via optical frequency and polarization control, yielding wide angular switching/steering of the tip-aligned photoemission currents. Correlated scanning electron microscopy (SEM) and 3D photoemission modeling clarify the effects of nanostar tip geometry and plasmonic field enhancements. As the overall directional effects are not contingent on laser intensity, the present method for optically controlling photocurrents can be extended from the weak-field (multiphoton) regime into the strong-field (optical field emission) regime. However, weak-field multiphoton photoemission (MPPE) processes are emphasized here due to the minimal nanostar heating, sub-single-electron femtosecond pulses ($\sim 10^{-5}$ photoelectrons from each pulse on average) that preclude space-charge effects, and < 1 eV photoelectron kinetic energy spreads for high temporal coherence. Photocurrent control timescales approaching the attosecond range may be achievable, fundamentally limited only by the nonlinear photoemission decay associated with plasmon dephasing.

5.3.1 Nanostar Plasmon Resonances

(The following synthetic procedures were developed by the Teri W. Odom Group and executed by Priscilla Choo at Northwestern University.)

Nanostars are synthesized via a seedless growth method, in which (4-(2-hydroxyethyl)-1-piperazineethanesulfonic acid) (HEPES) buffer functions both as a nucleation and a shape-directing agent. A 1 M stock HEPES solution is made by dissolving the buffer salt in Millipore water (18.2 MΩ·cm). The pH of the HEPES solution is measured and adjusted to 7.38 using concentrated NaOH solution. Nanostars are synthesized by adding 0.2 mM (final concentration) gold (III) chloride trihydrate ($HAuCl_4$) to 110 mM HEPES buffer and vortexing for one minute after $HAuCl_4$ addition. The growth solution is left in dark for 24 hours to allow for growth and stabilization. To improve size homogeneity and to achieve the desired resonances within the tuning range of Ti:sapphire laser, density gradient centrifugation is carried out to sort the nanostars. A continuous linear sucrose gradient is created by using a custom mixing program of the gradient maker (BioComp Instruments) to mix 50% and 60% weight-to-volume sucrose solutions at an angle. At this point, 500 μL of 8–10 nM concentrated nanostar solutions are layered on the top of the prepared gradient and centrifuged at 4400 g for 4 hours. The samples are fractionated at intervals of 4 mm from the meniscus (BioComp Instruments) and centrifuged at 15000 rpm for 25 minutes to remove excess sucrose. Each fraction is then dialyzed in Thermo Fisher 20K Slide-A-Lyzer Dialysis Cassettes for 24 hours to remove remaining sucrose from the solution. Transmission electron microscopy images are taken of each fraction to choose the population with desired size and aspect ratio of the branches. Fraction 7 out of 23 is selected for the present studies.

The gold nanostars are synthesized with sharp 3.4 ± 0.4 nm radii tips and the sorting selects for simple geometries with an average number of three tips lying in the surface plane (Fig. 5.12). Electron micrographs for a selection of representative nanostars are shown in Fig. 5.11a. Plasmonic properties are readily characterized using normal-incidence laser light for these primarily in-plane geometries, with the nanostars supporting localized surface plasmon resonances across the near-infrared tuning range of the Ti:sapphire oscillator (700–1000 nm). The resonance properties are characterized for three sample nanostars via spectral (Fig. 5.11c) and polarization dependences (Fig. 5.11d), with the peak polarization indicated in the correlated SEM insets aligned along a particular tip for each nanostar. In each case, the n-photon photoemission (nPPE) rate varies as $\Gamma_{n\mathrm{PPE}} \propto \cos^{2n}(\theta - \theta_{\mathrm{tip}})$ as the polarization angle θ is rotated away from the resonant tip, consistent with the field projection onto a single, well-defined hot spot axis. The essential role of the plasmon resonance in driving these behaviors has been established in previous photoemission studies correlated with dark field microscopy for gold nanorods,[64] confirming the direct relation between surface plasmon (Mie) resonances in linear scattering spectra and the peaks observed in MPPE spectra. Due to the $E^{2n} \propto I^n$ electric near-field sensitivity of the n-photon process, nanostars with multiple similar tips may have only one dominant hot spot (e.g. Star 2). Note, for instance, that a mere 10% difference in field enhancement results in a factor of two difference in the 4PPE rate.

Electrons must absorb multiple visible or near-infrared photons (∼1.5 eV) to overcome typical metal work functions (∼5 eV) and escape into the vacuum. The total MPPE rate is

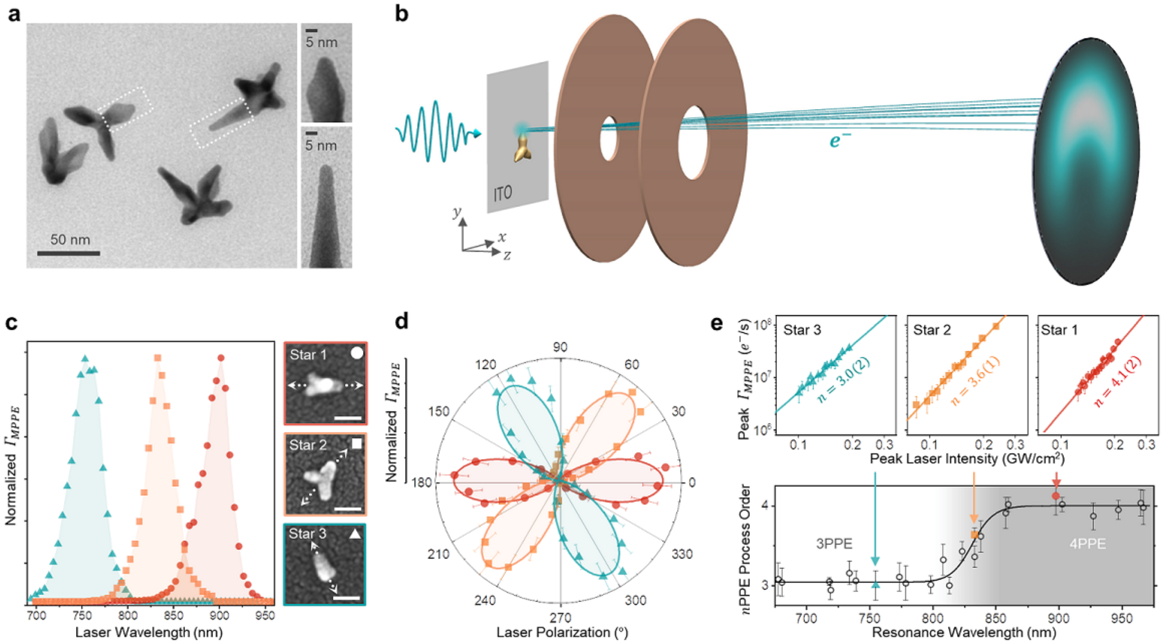

Figure 5.11: Single-nanostar plasmon resonance excitation and photoelectron velocity mapping. (a) Transmission electron micrographs of representative few-arm nanostars (50 nm scale bar) with insets displaying individual tips (5 nm scale bars). (b) Experimental configuration, in which photoelectrons with initial transverse (v_x, v_y) velocity are linearly mapped onto (x, y) position on the MCP detector. (c) Three example nanostars, each with a single dominant plasmon resonance mode excited via polarization aligned along the arm axes, as indicated by the arrows (50 nm scale bars). (d) Polarization-dependent photoemission rate at peak resonance wavelengths for each of the three stars, characterizing the peak polarization settings. Data is fit to $\cos^{2n}(\theta - \theta_{\text{tip}})$ for multiphoton process order n. (e) Summary of multiphoton process orders for plasmon resonance modes on different nanostars, determined via linear intensity-dependence fits on log-log plots (power-law behavior) as demonstrated for the three example stars. The resulting process order data is fit to a sigmoidal curve from $n = 3.01(3)$ to $n = 3.99(4)$, demonstrating the clear transition from the 3-photon to the 4-photon regime with decreasing photon energy. Intermediate values between 3 and 4 are effective process orders representing a weighted average of 3-photon and 4-photon contributions. All reported parenthetical values are standard errors of the variance-weighted nonlinear least squares fits.

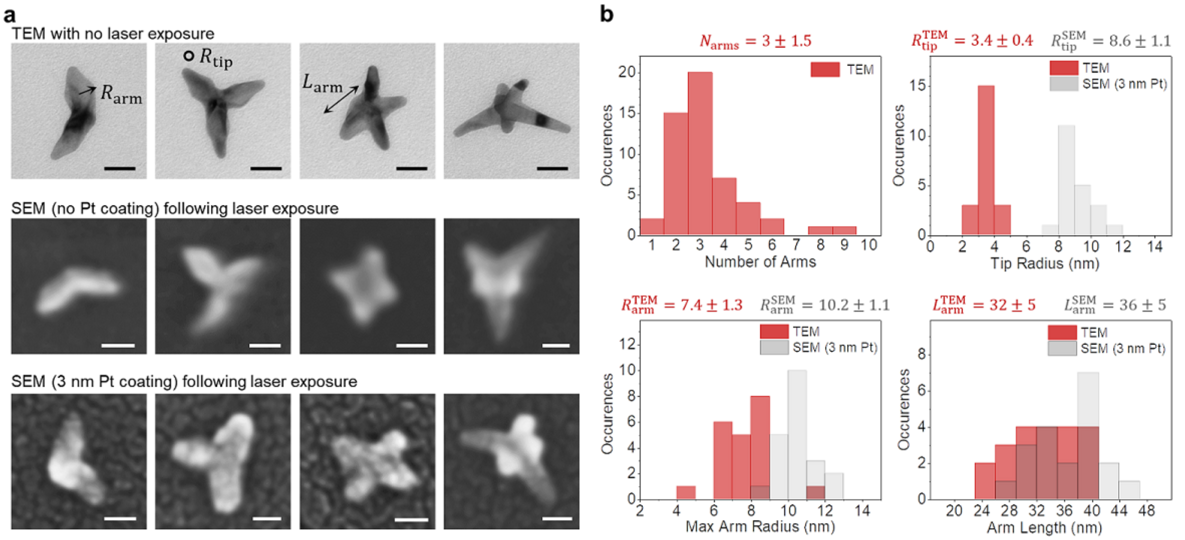

Figure 5.12: Nanostar statistical characterization via electron microscopy. (a) Example transmission electron microscopy (TEM) and scanning electron microscopy (SEM) images of stars with different numbers of arms, N_{arms}. All SEM micrographs are collected following exposure to laser intensities of ∼0.1 GW cm^{-2} or greater in photoemission studies. The lack of observable morphological differences between the unexposed nanostars in TEM images and the laser-exposed nanostars in SEM images (those with no Pt coating, specifically) provides strong evidence that no appreciable particle melting occurs during photoemission studies. For most studies, a 3 nm Pt coating was applied to the nanostars to improve SEM contrast and thereby clarify the nanostar geometries. All scale bars are 25 nm. (b) Statistical characterization of nanostar dimensions in TEM and SEM (3 nm Pt coating) images. An approximate 3 nm broadening is evident in all features due to the Pt coating.

described by a sum over process orders,

$$\begin{aligned}\Gamma_{\mathrm{MPPE}} &= \sum_n \Gamma_{n\mathrm{PPE}} \\ &= \sum_n \sigma_n(\omega,\theta) I_0^n,\end{aligned} \tag{5.1}$$

in which I_0 is the input laser intensity and $\sigma_n(\omega,\theta)$ is the nPPE cross-section as a function of laser frequency and polarization. The plasmonic field enhancement effect is therefore included within $\sigma_n(\omega,\theta)$. Multiphoton process orders are determined for a random selection of resonantly-excited nanostars by measuring photoemission rate as a function of peak laser pulse intensity. The process order summary in Fig. 5.11e reveals a sigmoidal transition from 3PPE to 4PPE centered around 830 nm (1.5 eV), indicating a nanostar tip work function of $\phi \approx 3\hbar\omega_{830} = 4.5$ eV at which 3-photon-excited electrons from the Fermi level begin to overcome the surface potential barrier. Intensity-dependence plots and power-law fits are shown for the three sample nanostars, with the non-integer Star 2 process order ($n = 3.6\pm0.1$) representing weighted contributions from both 3PPE and 4PPE processes. From Eq. 5.1, the log-log slope is

$$\begin{aligned}\frac{\mathrm{dlog}_{10}(\Gamma_{\mathrm{MPPE}})}{\mathrm{dlog}_{10}(I_0)} &= \frac{\sum_n \sigma_n(\omega,\theta) I_0^n n}{\sum_n \sigma_n(\omega,\theta) I_0^n} \\ &= \sum_n w_n n,\end{aligned} \tag{5.2}$$

which is the weighted average over process orders with weight factors $w_n = \sigma_n(\omega,\theta) I_0^n / \sum_n \sigma_n(\omega,\theta) I_0^n$ representing the relative contributions of each process order, such that $\sum_n w_n = 1$. With only 3PPE and 4PPE processes contributing, Eq. 5.2 yields an effective process order of 3.5 when $\sigma_3(\omega,\theta) I_0^3 = \sigma_4(\omega,\theta) I_0^4$, as is the case at 830 nm in Fig. 5.11e. It should be noted that peak photocurrents of 10^8 s^{-1} during the peak laser pulse intensity correspond to an average of only 10^{-5} photoelectrons from each pulse when multiplied by the laser pulse duration ($\sim 10^{-13}$ s). With a laser repetition rate of 75 MHz, photoemission rates greater than 100 s^{-1} are thus achieved with negligible probability of two electron emission events occurring within a single laser pulse, thereby precluding any space-charge effects.

These measurements verify that all signal is predominantly due to MPPE rather than optical field emission or thermionic emission for the range of intensities utilized in these studies. For further verification, the Keldysh parameter, $\gamma = \sqrt{\phi/2U_{\mathrm{p}}}$, is again used to characterize the transition from weak- to strong-field emission,[91] where ϕ is the work function and $U_{\mathrm{p}} = e^2E^2/\left(4m_e\omega^2\right)$ is the ponderomotive energy. For peak input pulse intensities $I_0 < 3 \times 10^8$ W cm^{-2} and simulated field enhancements $|E/E_0| < 100$ described below, Keldysh parameters $\gamma > 3$ fall within the MPPE regime and corroborate the measured intensity dependences.

5.3.2 Single-Tip Photoemission Properties

Selecting Star 1 (Fig. 5.11c and Fig. 5.13a) as a representative single-tip emitter, the characteristic photoelectron velocity distributions were measured and modeled from the resonantly-excited nanostar tip. First, finite element simulations were performed using the nanostar geometry measured via correlated SEM for insight into the plasmonic field enhancements. Nanostar geometries are modeled in *SolidWorks 2017* with a 10 nm diameter core and cylindrically-symmetric arms modeled using dimensions (lengths, widths, and angles) from correlated SEM micrographs, minus the 3 nm Pt coating layer applied prior to SEM imaging for improved contrast (Fig. 5.12). Out-of-plane arms are modeled with shapes/widths determined via TEM statistics (Fig. 5.12) and shorter lengths of ∼25 nm. The tips are modeled with radii of 3.4 nm based on TEM statistical characterization. A 1 nm HEPES ligand layer surrounds the nanostar, with the refractive index set to 1.5 based on typical values for similar organic molecules in the visible range. A small extinction coefficient $k_{\mathrm{lig}} = 0.25$ is included for the ligand layer to account for a consistent red-shift in the experimental versus simulated absorption spectra. This is not expected for the HEPES itself, but is instead attributed to amorphous carbon buildup that commonly occurs in nanotip systems in the regions of strong optical field enhancement.[183] Here the carbon buildup may be attributed to photon- or hot electron-mediated cracking and reorganization of the organic ligands. Consistent application of this small extinction coefficient uniformly improves spectral agreement for all calculations, possibly accounting for other damping effects not considered in the modeling. The complex refractive index of the 10 nm ITO film is determined via ellipsometry and the complex refractive index of gold is taken from the literature.[86] Further details of the finite element modeling are shown in Fig. 5.15 and discussed in Section 3.2. The simulated surface-normal field distribution in Fig. 5.13b highlights all of the tips in the linear case, with a particularly strong peak enhancement of $|E_\perp/E_0| \approx 50$ at the resonantly-excited tip. This tip becomes clearly dominant when the field enhancement is raised to the 8th power for the relevant 4PPE process, with the nonlinear enhancement strongly confined to its apex. Photoemission distributions measured for this hemispherical hot spot geometry may also guide expectations for convex hot spots in other systems, including etched nanotip photocathodes.[126, 192]

The measured 2D (v_z-projected) photoelectron velocity map in Fig. 5.13c shows clear directionality along the resonant tip axis, as would be predicted for electrons emitted outward from the field-enhanced surface region. The 3D velocity distribution (Fig. 5.13e) has been reconstructed using the basis set expansion (BASEX) algorithm,[42] which relies on the approximation of cylindrical symmetry around the resonant x-axis tip to compensate for information lost in the v_z projection (Section 3.6.1). Tip-aligned directional emission is also observed for Stars 2 and 3 (Fig. 5.14), which are resonantly excited in the transition regime and the 3PPE regime, respectively. While both 3PPE and 4PPE processes lead to similarly tip-aligned photoemission distributions, photon energies just above the 3PPE onset may be preferred to reduce the kinetic energy spread (Fig. 5.14) for optimal temporal coherence of the photoelectron waveform.[3]

Photoemission generally proceeds by a combination of volume and surface mechanisms for momentum conservation[189] (Section 3.5). The directional distributions observed here indicate the dominant role of surface scattering, in which case the multiphoton excitation rate depends on the surface-normal electric field,[114, 116, 189] $E_\perp^{2n}$. By contrast, volume excitation mechanisms depend on internal fields as E^{2n} (Fig. 5.15) and produce hot electrons

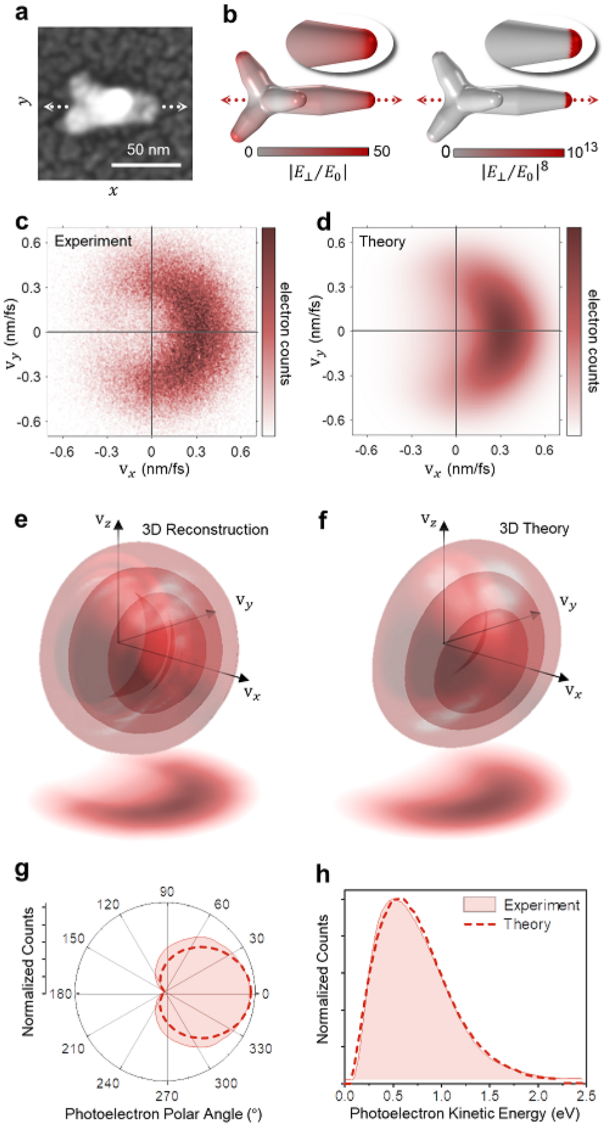

Figure 5.13: Characterization of single-tip multiphoton photoemission. (a) Scanning electron micrograph of a representative single-tip emitter (Star 1). The tips appear broader than in transmission electron micrographs and nanostar statistics due to a 3 nm Pt film deposited prior to electron imaging to improve sample conductivity and image quality. This added thickness is therefore subtracted from the measured nanostar dimensions for modeling and simulation. Scale bar: 50 nm. (b) Modeled nanostar geometry with calculated linear and 8th-order (4-photon) surface-normal electric field enhancements. All measurements and calculations are performed on-resonance at 900 nm and 0° polarization. The ITO-coated substrate and HEPES ligands (not shown) are included in the field calculations. (c) Experimental and (d) theoretical velocity map images of the v_z-projected photoelectron distribution. (e) Reconstructed experimental and (f) theoretical 3D velocity distributions, showing iso-probability surfaces at 75%, 50%, and 25% maximum along with the overall v_z projections. (g) Angular distributions and (h) electron kinetic energy distributions determined from xy slices of the 3D experimental and theoretical distributions.

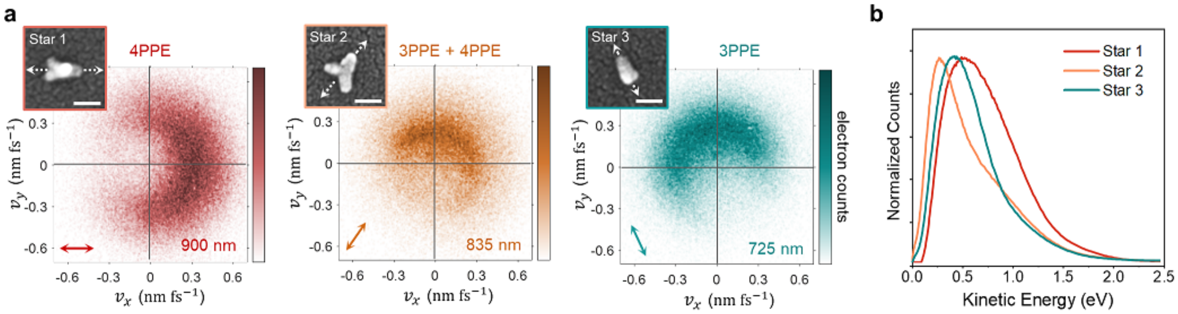

Figure 5.14: Single-tip directional velocity distributions. (a) Velocity maps of the three sample stars in the 4PPE regime (Star 1), transition regime (Star 2), and the 3PPE regime (Star 3). The emission is aligned with the resonant tip in each case. All scale bars are 50 nm. (b) Corresponding electron kinetic energy distributions determined from 3D reconstructions, demonstrating a narrowing in the distribution near the onset of the 3PPE regime (e.g. Star 2).

throughout the nanostar that would escape from various surfaces around the tips and body, leading to largely isotropic rather than directional velocity distributions. The present theoretical investigations are therefore restricted to surface-mediated MPPE, which is further supported by the tip-localized photoemission observed in nanostar PEEM studies.[77]

Calculations based on the coherent surface MPPE theory developed by Yalunin *et al.*[203] were carried out to determine photoemission rates and velocity distributions from each nanostar surface area element, using the full SEM-correlated nanostar geometry and simulated plasmonic fields shown in Fig. 5.13b, with a fine surface mesh shown in Fig. 5.15. To calculate the full 3D photoelectron velocity distribution for a given nanostar, the photoemission contributions from each surface area element are calculated using the surface field enhancements determined via finite element simulation. The photoemission distribution is calculated with respect to each surface normal ($\hat{p}_{z,\mathrm{rel}}$) and rotated into the global frame ($\hat{p}_z$) via Cartesian rotation matrices. Only a single rotation about axis $\hat{p}_z \times \hat{p}_{z,\mathrm{rel}}$ is required for azimuthally-isotropic per-area emission distributions. A sample uniform surface mesh and nonlinear surface-normal field enhancement distribution is shown in Fig. 5.15, along with additional details of the finite element domain. It should be noted that geometries with concave surface regions (including nanostars) may allow for the intersection of emitted electrons with other surfaces of the emitter geometry. These effects are not presently accounted for, although they should be negligible for the tip-like emission described in the present work.

Empirical values are utilized for all surface MPPE model inputs, with the exception of the pulse-averaged Fermi-Dirac electron temperature, which is calculated at 2500 K via a two-temperature model, shown in Fig. 5.16, with a linear nanostar absorption cross-section of 10^4 nm^2 determined via the finite element simulations. The emission process at each nanostar surface area element consists of a heated Fermi gas impinging on the surface barrier and becoming excited via coherent multiphoton absorption into external Volkov (field-dressed) states. The outgoing photocurrent includes direct and surface-rescattered quantum

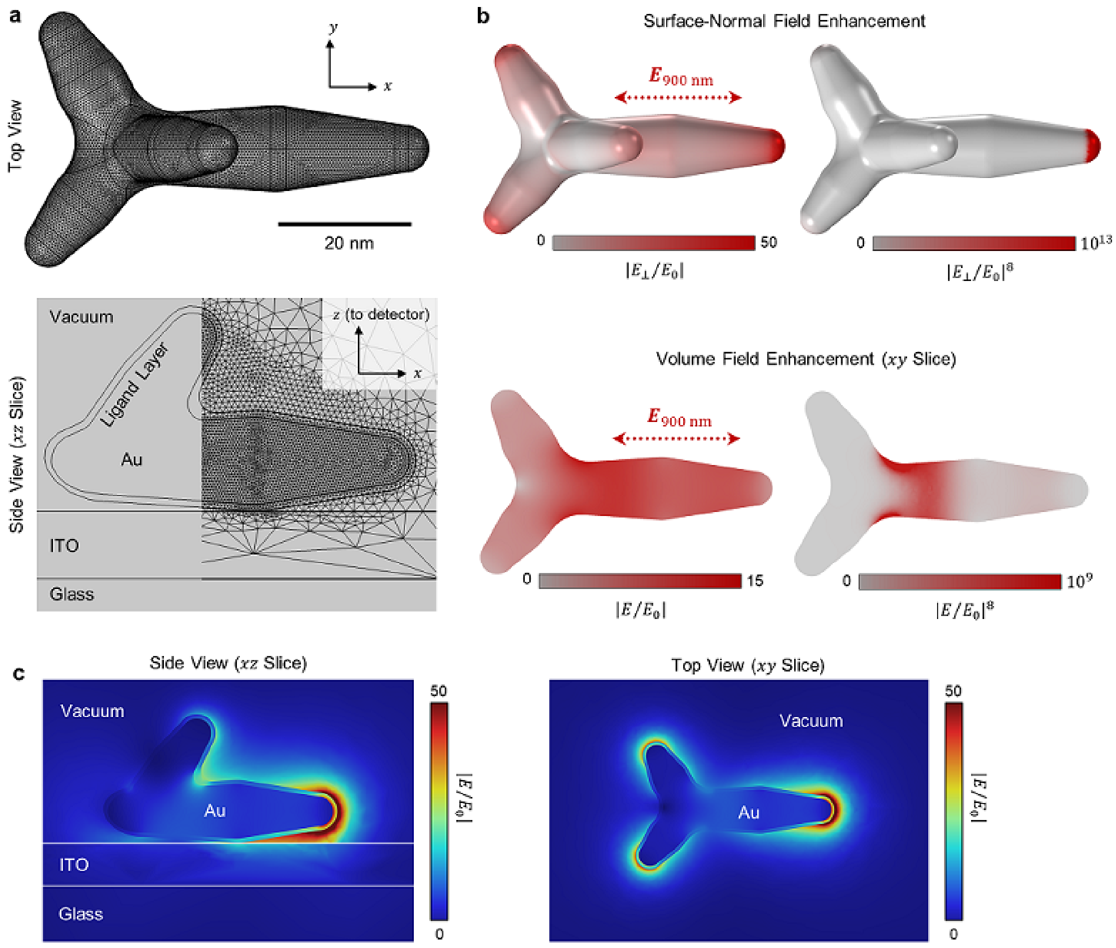

Figure 5.15: Nanostar finite element simulations. (a) Uniform nanostar surface mesh and cross-section demonstrating the typical domain and meshing. (b) Volume and surface field enhancements calculated for the resonantly-excited nanostar (900 nm, 0°). The 8th-order field enhancement for the 4PPE process leads to a highly-localized surface field enhancement at the tip (leading to tip-aligned directional emission), but a more spread-out volume field enhancement that would produce more isotropic emission if volume-mediated MPPE processes were dominant. (c) Domain slices showing the field enhancement with a different color map for additional clarity.

amplitudes. Optical field penetration into the gold is neglected and all excitation therefore occurs from the external evanescent component of the initial free electron wavefunctions, which accounts for momentum non-conservation at the surface barrier. Due to the short decay length of the external electron wavefunction (∼2 Å) and the small quiver amplitude of the emitted electrons (∼1.5 Å) relative to the plasmonic field decay length (∼1.5 nm), the external field is approximated to be uniform in calculating the emission amplitude. The evanescent plasmonic field then ponderomotively accelerates the emitted electrons outward from the surface, uniformly shifting the kinetic energy distribution by U_p. This is simply accounted for in the modeling via the coordinate transformation $p_z^2/2m_e \rightarrow p_z^2/2m_e - U_\mathrm{p}$. The ponderomotive energy $U_\mathrm{p} = E^2e^2/\left(4m_e\omega^2\right) = I_0\left|E/E_0\right|^2 e^2/\left(2c\varepsilon_0 m_e\omega^2\right)$ for the present input intensity ($I_0 = 2\times10^8$ W cm^{-2}) and calculated tip field enhancement ($|E/E_0| = 50$) is only 0.03 eV. Though only a minor contribution in the present studies, the ponderomotive energy scales linearly with the input intensity and quadratically with the field enhancement and thus may become important in other similar systems.

Theoretical 2D (Fig. 5.13d) and 3D (Fig. 5.13f) distributions reiterate and confirm the tip-aligned directionality, with good agreement in the photoelectron angular (Fig. 5.13g) and kinetic energy (Fig. 5.13h) distributions. The slight downward directionality in the theoretical 3D distribution is due to the ITO image charge field, which skews the tip field enhancement toward the substrate (Fig. 5.17). However, the otherwise strong agreement between experimental and theoretical distributions indicates that such substrate symmetry-breaking effects are minor. With regard to substrate effects, it is worth mentioning the possibility of gap resonances occurring in nanoscale junctions between nanoparticles and conducting substrates separated by an organic molecular layer such as the ∼1 nm HEPES ligand layer on the nanostars, as observed previously with Au nanospheres separated from an Au film substrate by an organic spacer layer.[166] While no direct evidence of a gap resonance effect is observed in the present experiments nor in the finite element simulations (Fig. 5.15), due primarily to the in-plane resonance excitation with in-plane polarized light,

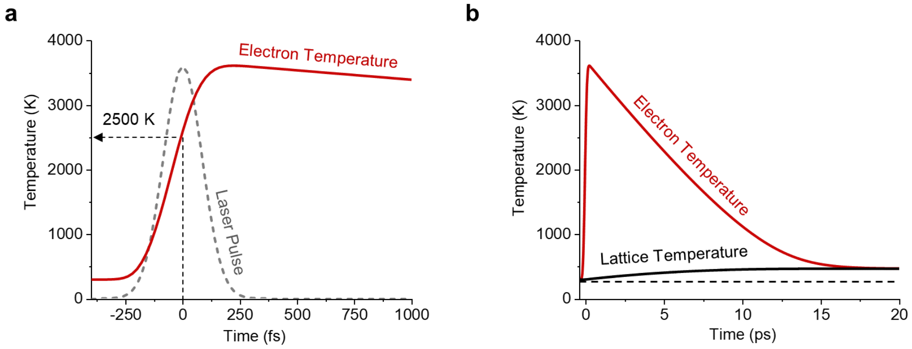

Figure 5.16: Representative nanostar electron sea and lattice heating. (a) Electron temperature calculated via the two-temperature model with the parameters utilized for Star 1 measurements and determined via simulations: peak input intensity 2×10^8 W/cm^{-2}, 200 fs pulse duration, nanostar volume of 10^4 nm^3, and a linear absorption cross-section of 10^4 nm^2. The effective temperature measured in MPPE experiments can be expected to be approximately the temperature at the pulse peak, i.e. ∼2500 K. Due to similar excitation conditions, cross-sections, and volumes for the nanostars studied, this temperature is utilized in all photoemission calculations described in the main text. (b) Evolution of electron and lattice temperatures calculated via the two-temperature model. Peak lattice temperatures less than 500 K are too low to induce nanostar melting.

such effects can be difficult to accurately account for in the simulations as they depend sensitively on the details of the nanostar-substrate interface, which is not directly observe.

Although the near-field contributions to photoemission dynamics and distributions have been investigated in detail in order to gain general insights for arbitrary emitter geometries, the nanostar tips studied here are among the sharpest nanoplasmonic geometries available and for most purposes can be treated as point-like electron sources. Electrons may therefore be emitted into a broad angular distribution (Fig. 5.13g) but still retain a high degree of spatial coherence, determined by the small source radius (3.4 nm) and photoelectron angular uncertainty ($\sim 70^\circ$). The transverse spatial coherence is often characterized via the normalized root-mean-square beam emittance, a conserved phase space quantity in aberration-free systems defined by $\varepsilon_{\text{rms}} = \beta\gamma_L\sigma_r\sigma_\theta$ at the beam waist,[158] in which $\beta = v/c$ for average photoelectron velocity v, γ_L is the Lorentz factor, σ_r is the transverse spatial uncertainty, and σ_θ is the angular uncertainty. Since a beam waist is located at the source, the emittance is approximated via the tip radius ($\sigma_r = 3.4$ nm), angular emission uncertainty ($\sigma_\theta = 70^\circ = 1220$ mrad—Fig. 5.13g), and average velocity ($v/c = 0.0014$), as 5.9 nm·mrad. This serves as an upper limit, as the effective source size is determined by tracing electron trajectories back to the center of the hemispherical tip.[43] Even as an upper limit, this nanostar tip MPPE beam emittance is approaching values achieved on pulsed nanotip sources (around 1.7 nm·mrad) in the linear photoemission regime,[49] which, in turn, are only an order of magnitude higher than the uncertainty limit of $\varepsilon_{\text{rms}} = \hbar/\left(2m_e c\right) = 0.19$ nm·mrad.

Single nanostar tips also remain stable emission sources in the present intensity range during hours of measurements, including at least half an hour of continuous exposure while collecting velocity maps, as demonstrated in Fig. 5.18. Only modest lattice heating of $\Delta T \approx 200$ K is calculated during a laser pulse (Figs. 5.16 and 5.19) with 13 ns between pulses sufficient for equilibration back to room temperature. The high degree of stability and spatial coherence enables ultrafast point-projection[127, 126, 191] and diffractive[66,

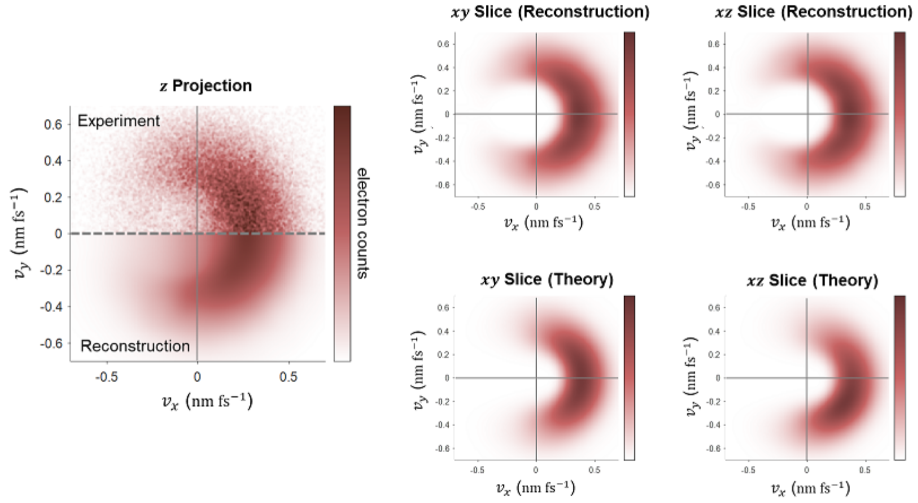

Figure 5.17: Experimental and reconstructed velocity distributions. Comparison between experimental and reconstructed photoelectron velocity projections for Star 1, along with slices through the reconstructed and theoretical 3D distributions. The reconstruction is in good agreement with the experimental velocity map image. The theoretical calculations are also in good agreement with the reconstructed/experimental distributions, aside from a slight skew toward the surface ($-z$ direction) in the xy slice due to the induced ITO substrate image charge oscillation.

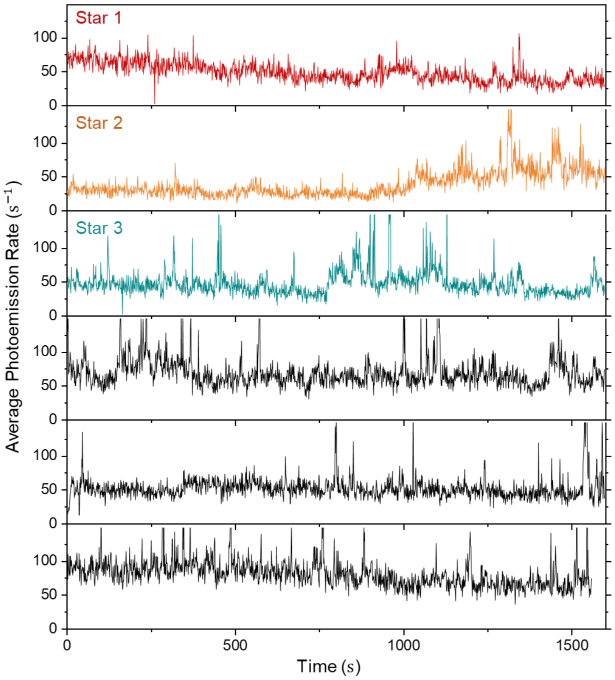

Figure 5.18: Nanostar photoemission time traces. Average photoemission rate (as opposed to peak rate) as a function of time measured for six nanostar emitters. Each star is a single-tip emitter with well-defined photoemission directionality, as has been demonstrated for representative Stars 1–3. Each time trace therefore represents photoemission from a single nanostar tip. Due to the nonlinear process (MPPE $\propto E^6$ or E^8), small fluctuations in the near-electric-field at the tip (±10%) readily lead to the observed signal fluctuations, although the cause of such near-field fluctuations is not currently known. The average laser power is stable to $< 2\%$ during measurements.

127, 191] imaging of nearby nanoscale objects following possible electron beam manipulation such as acceleration or collimation via nanoengineered electron optics.[61] For higher optical intensities, a variety of new physical behaviors emerge in the strong fields and gradients at point-like nanotips,[99] including the onset of tunneling emission and subsequent quiver or sub-cycle dynamics.[72] Such effects are negligible in the present multiphoton photoemission studies, but the theory readily extends into intermediate- and strong-field regimes[203] and the influence of strongly-varying plasmonic fields on the photoelectron trajectories can be included in the manner demonstrated by Dombi *et al.*[39] when necessary.

The temporal coherence is primarily limited by the photoelectron kinetic energy spread, leading to longitudinal dispersion that is most prominent immediately following emission (prior to acceleration in the electrostatic lens), when the average electron kinetic energy is comparable to the spread in the energy distribution. A full width at half maximum kinetic energy spread around 0.8 eV is observed for the characteristic nanostar tip MPPE distribution measured in Fig. 5.13h. This is a substantial improvement over typical kinetic energy spreads > 10 eV in the optical field emission regime[100, 39] and can be improved further by carefully matching the n-photon energy to the work function.[3]

Limits on the achievable photoemission currents from gold nanostars and other plasmonic nanoparticles are imposed either by space-charge effects or by particle melting at high excitation pulse energies. As shown in Fig. 5.19, nanostar melting is expected to occur at photocurrents less than 1 electron/pulse, which precludes any space-charge effects. These melting limits are not approached in the present studies, which are therefore far from the regime in which space-charge effects become important. Photocurrents exceeding 100 electrons emitted in a femtosecond pulse have, however, been demonstrated for patterned gold nanorods10, in which case space-charge limitations do become important. The peak photocurrents reported in Fig. 5.19 are calculated using the surface MPPE theory. The peak nanostar lattice temperatures (see Section 3.3.2) are calculated simply from the bulk heat capacity of gold, a typical nanostar volume of 10^4 nm^3, and simulated linear absorption

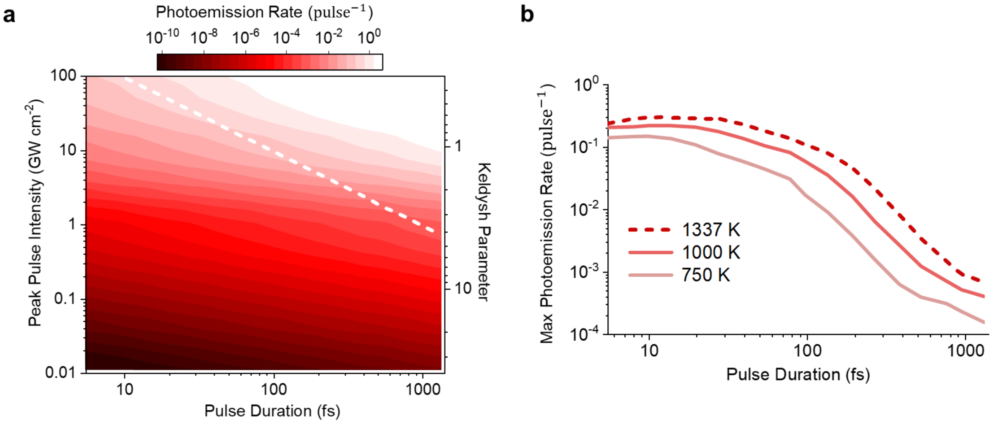

Figure 5.19: Nanostar photoemissivity and limitations due to melting. (a) The photocurrent is calculated using the surface photoemission theory as a function of pulse duration and input pulse intensity, assuming 750 nm excitation (3PPE in weak-field regime), 4.5 eV work function, average nanostar volume of 10^4 nm^3, linear absorption cross-section of 10^4 nm^2 and tip field enhancement factor of 50 from simulations. The dashed line represents the upper limit on pulse energy (intensity × duration) at which the onset of particle melting will occur at or around the melting temperature of bulk gold (1337 K). (b) The corresponding maximum photocurrent is plotted as a function of pulse duration for different possible nanostar melting temperatures, as particle melting typically occurs at lower temperatures due to the high fraction of more weakly-bound surface atoms.

cross-section of 10^4 nm^2. The bulk gold melting temperature (1337 K) serves as an upper limit on the nanostar melting temperature, although nanostar melting is likely to occur at lower temperatures due to the high nanoparticle surface-to-volume ratio and more weakly-bound surface atoms. It is evident that higher intensities can be utilized with shorter pulse durations due to the trade-off between linear absorption and third-order photoemission cross-sections, but the effective photoemission order and the maximum achievable photocurrent begin to level off at shorter pulse durations as the Keldysh parameter drops below unity and into the optical field emission regime.

5.3.3 Polarization- and Frequency-Controlled Directional Photoemission

Building on previous investigations of selective nanostar tip excitation,[77] the excitation of in-plane tips with in-plane polarization control in the present studies provides a particularly clear mapping between optical parameters and tip hot spots. While the presence of many tips and the effect of near-field tip-tip coupling[68] can lead to complicated optical parameter mappings in some cases, the simple, typical nanostar behaviors are emphasized here and selective tip excitation is demonstrated by independently tuning frequency and polarization. Multiple tips are involved in both plasmon resonance modes for the four-tip nanostar in Fig. 5.20a, but simulations in Fig. 5.20b reveal that only one tip hot spot is dominant for each mode. Spectra and polarization plots show two distinct plasmon peaks at nearly-orthogonal peak polarization angles, with the photoemission rate at either peak showing minimal contributions from the other. Entirely frequency-controlled tip selectivity can thus be achieved for an isotropic polarization state (circular or unpolarized) or for a linear polarization state oriented between the two resonance modes. The frequency sensitivity depends on the spectral peak widths, relative amplitudes, and separation.

An intermediate laser frequency setting exists between the spectral peaks at which both plasmon modes are equally excited at their respective linear polarization angles. This is demonstrated by the four-lobed polarization dependence measured between the resonances at

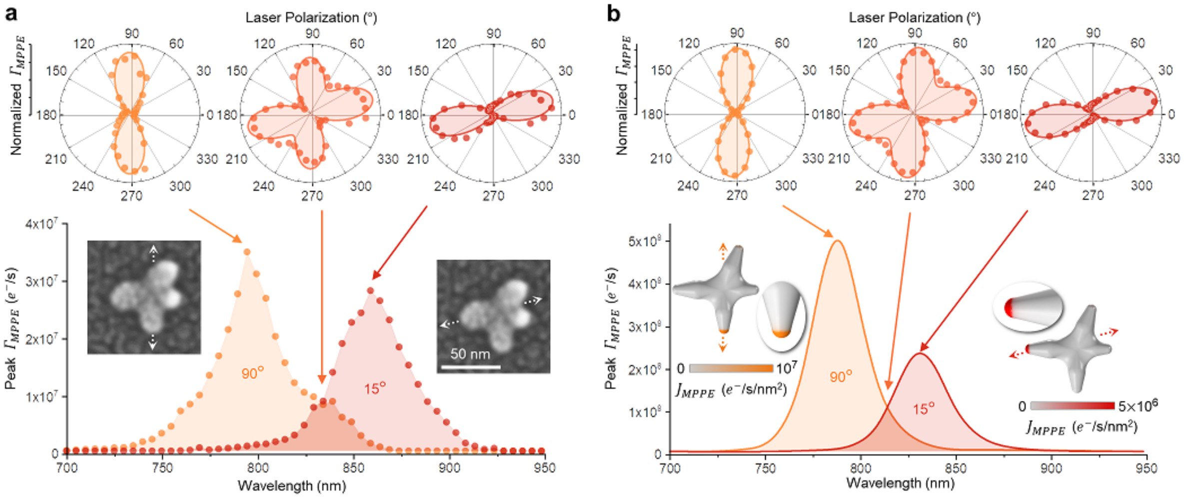

Figure 5.20: Multi-tip excitation and selectivity. (a) Experimental slices through the optical frequency and linear polarization parameter space, with photoemission peaks at (795 nm, 90°) and (860 nm, 15°). At either spectral peak, the laser polarization dependence shows minimal signature of the other resonance, while between resonances (835 nm) the four-lobed behavior shows equal contributions from both resonance modes. The peak polarization axes are indicated in the correlated SEM insets for each resonance, as determined via nonlinear cosine fits shown in the polarization plots (50 nm scale bar). (b) Theoretical surface multi-photon photoemission rates for the correlated nanostar geometry. Aside from a small blue shift, peaks at (785 nm, 90°) and (830 nm, 15°) are in good agreement with the experimental results. All four tips are modeled with the same radius (3.4 nm), but photocurrent density maps demonstrate single-tip excitations at the resonance conditions due to the specific plasmonic mode structure. Measurements and calculations are performed at 1×10^8 W/cm^{-2} peak input intensity.

835 nm in Fig. 5.20a and reiterated by the calculations in Fig. 5.20b for the correlated nanostar geometry. At the intermediate frequency, the linear polarization angle may thus be tuned to select between the two resonance modes and corresponding tip hot spots, demonstrating polarization-controlled selective tip excitation. The relative mode strength (i.e. relative lobe amplitude in the polarization plots) can be continuously adjusted via frequency tuning. Overall, the two-dimensional optical parameter space sampled in Fig. 5.20 is described by the nPPE photoemission cross-section, $\sigma_n\left(\omega,\theta\right)=A_1^{(n)}\left(\omega\right)\cos^{2n}\left(\theta-\theta_1\right)+A_2^{(n)}\left(\omega\right)\cos^{2n}\left(\theta-\theta_2\right)$, in which $A_1^{(n)}\left(\omega\right)$ and $A_2^{(n)}\left(\omega\right)$ are the n-photon spectra of the two plasmon resonance modes. In addition to the strong theoretical agreement with the observed spectral and polarization behaviors (Fig. 5.20b), MPPE rates are calculated to within an order of magnitude of the experimental measurements by integrating the theoretical current density, J_{MPPE}, over the nanostar surface, accounting for both 3PPE and 4PPE contributions. Reserving other aspects of the theory, this level of quantitative agreement corresponds to calculated fields within 50% of the experimental values for a 3PPE process ($\propto E^6$), which is relatively strong agreement considering the sensitivity of the field enhancements to the precise tip radius, the charge distribution during plasmon oscillation (i.e. the overall nanostar geometry), and the surface dielectric environment due to the HEPES surface ligands. Note that while the spectra of the nanostar in Fig. 5.20 happen to coincide with the 3PPE-to-4PPE cross-over around 830 nm (Fig. 5.11e), the observed behaviors are a general feature of multi-resonance geometries and are also demonstrated in the next section with a nanostar studied entirely in the 3PPE regime.

The nanostar in Fig. 5.21a displays simple multi-resonance behavior, with a higher-energy (blue) dipolar resonance mode aligned with the shorter tip and a lower-energy (red) dipolar resonance mode aligned with the longer tip. These two tips are approximately orthogonal and can be individually addressed, as established in the polarization dependence at different excitation frequencies (Fig. 5.21b). By instead maintaining circular polarization, tip selectivity can be achieved with frequency tuning alone, as discussed with the previous nanostar and further demonstrated here via MPPE simulations (Fig. 5.21c). Velocity distributions measured (Fig. 5.21d) and calculated (Fig. 5.21e) at each frequency are directionally aligned with the corresponding resonant tip axis and photoemission directionality is rotated by a full 90° upon frequency-controlled switching between tips. The average electron kinetic energy decreases with excitation frequency by conservation of energy. When both tip modes are excited at intermediate frequencies (e.g. Fig. 5.21c, 775 nm), the resulting velocity distribution is simply a linear combination of the individual tip angular distributions. Thus, this linear combination allows for a continuous steering of the average emission angle, although the total angular distribution is broadened by arising from two separate point-like sources.

Polarization-controlled directional emission is presented in Fig. 5.22 for the same nanostar as in Fig. 5.21, but exclusively at the intermediate frequency setting at which both tips are equally resonantly enhanced. Simulations demonstrate switching of photoemissive regions between the two tip hot spots as the linear polarization is rotated out of alignment with one mode and into alignment with the other (Fig. 5.22a). The photoemission directionality is rotated by 90° (Figs. 5.22b and 5.22c) in the same manner observed via frequency control, due to the same underlying process of selective hot spot excitation. Intermediate polarizations again result in a linear combination of the two tip angular distributions, with the relative weights determined by the polarization dependence (Fig. 5.22a). Although full polarization contrast is demonstrated by complete alignment along either tip mode, the polarization plot indicates that much less angular tuning is necessary to strongly favor one tip over the other due to the $\cos^6(\theta - \theta_{\text{tip}})$ polarization sensitivity for each plasmon mode. Strong tip selectivity can be achieved with a 90:10 emission ratio by only ±10° tuning away from the intermediate polarization, at which the emission ratio is 50:50. Therefore, as a benefit of the MPPE nonlinearity, photoemission directionality can be rotated by 90° with only ∼20° polarization rotation. This fine degree of tip discrimination also indicates possibilities for utilizing higher tip densities for a more continuous control of angular photoemission.

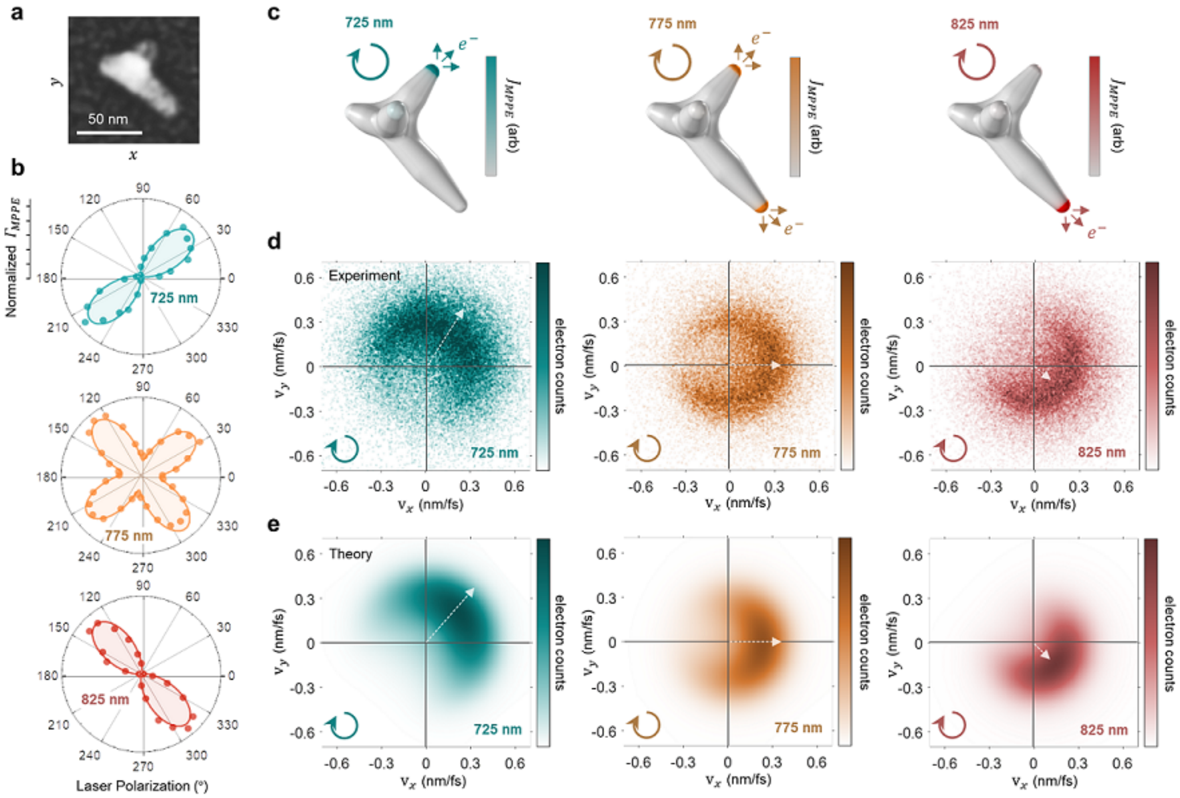

Figure 5.21: Frequency-controlled directional photoemission. (a) Correlated nanostar scanning electron micrograph with the shorter and longer resonant tips at 50° and 315°, respectively (50 nm scale bar). (b) Experimental polarization dependence for frequency at the short-tip resonance (725 nm, blue), between resonances (775 nm, orange), and at the long-tip resonance (825 nm, red) with nonlinear cosine fits for the 3-photon process. (c) Calculated multiphoton surface current distribution at different frequencies, showing the transition from one tip hot spot to the other with circular polarization. (d) Experimental and (e), theoretical v_z-projected velocity maps on and between the two resonances using circular polarization. Vectors indicate the peak directions determined by Gaussian fits around the peaks of the angular distributions. Peak photoemission angles range from 55° (50°) at 725 nm to 325° (315°) at 825 nm for the experimental (theoretical) velocity distributions, i.e. a 90° photoemission rotation. The vector magnitude represents the speed (v_F) of photoelectrons excited from the Fermi level, which decreases with decreasing photon energy by energy conservation, $\frac{1}{2}m_e v_\mathrm{F}^2 = n\hbar\omega - \phi$, with tip work function $\phi = 4.5$ eV and $n = 3$ in this excitation energy range ($\hbar\omega = 1.5$–1.7 eV). The Fermi velocity does not coincide with the apparent edge of the 825 nm (red) distribution due to the velocity dependence of the photoemission amplitude, which leads to deviations from a simple Fermi-Dirac distribution (particularly near zero velocity) and shifts the effective edge outward relative to v_F for near-threshold photon energies.

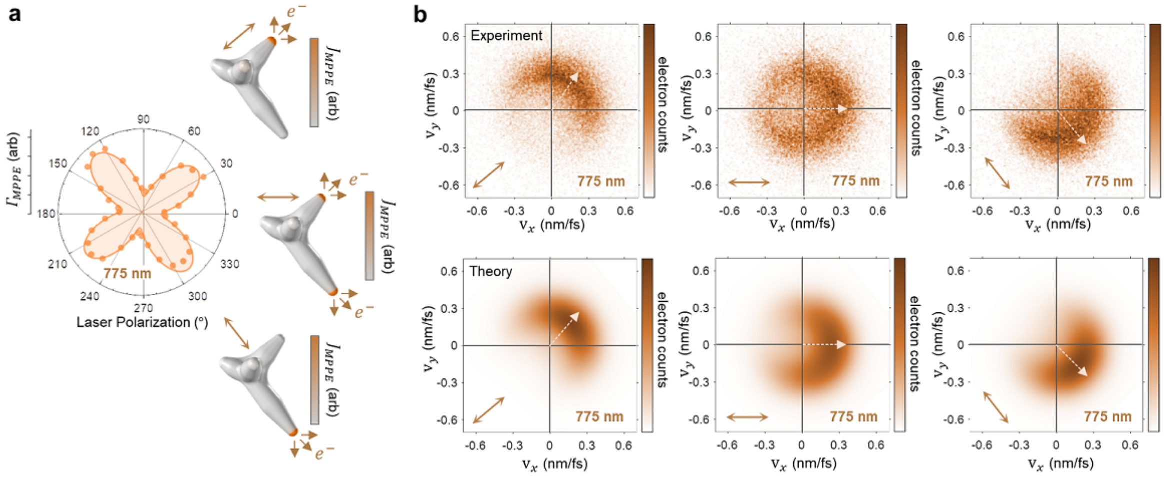

Figure 5.22: Polarization-controlled directional photoemission. (a) Experimental nanostar polarization dependence at 775 nm with nearly equal contributions from both nanostar tip resonances. Tip hot spots are selected by rotating linear polarization while keeping frequency constant, as demonstrated in the calculations on and between the resonances. (b) Experimental and (c) theoretical v_z-projected velocity maps for the different polarizations at constant frequency. Vectors indicate the peak directions determined by Gaussian fits around the peaks of the angular distributions. Peak photoemission angles range from 55° (50°) at 50° linear polarization aligned along the short tip to 310° (315°) at 315° linear polarization aligned along the long tip, for the experimental (theoretical) velocity distributions. The vector magnitude represents the velocity of photoelectrons excited from the Fermi level (v_F), which remains constant for all distributions due to the fixed excitation frequency.

5.3.4 Discussion

Preliminary photoemission directional control capabilities have been demonstrated for gold nanoshells via polarization-sensitive defect hot spot excitation. With gold nanostars, highly versatile photoemission switching/steering has been demonstrated by independently tuning one of two optical degrees of freedom (frequency or linear polarization), leaving the other available for modifying the control characteristics. For example, polarization can be utilized for tip selection and corresponding manipulation of angular currents, while frequency can be simultaneously utilized to control the electron kinetic energy distributions and relative tip photoemission enhancement. Such possibilities illustrate how techniques developed for coherent control over nanoplasmonic hot spots using femtosecond optical amplitude, frequency (phase), and polarization shaping[2, 176] can be directly applied to photocurrent degrees of freedom. The photoemission switching timescale is fundamentally limited by the plasmon dephasing (T_2) time and by the optical cycle of the excitation laser field, which defines the fastest timescale on which polarization and frequency can be manipulated. Due to the E^{2n} process nonlinearity, the nPPE current decays $2n$-times faster than the plasmonic field, which typically dephases in 10 fs or less.[64, 69] Thus, the 3PPE and 4PPE decay times are comparable to the 1–3 fs optical cycles for visible and near-infrared frequencies. This suggests that spatiotemporal control over hot spot excitation and directional current generation may be achieved on timescales approaching the attosecond range, even in the weak-field MPPE intensity regime.

Gold nanostars behave as prototypical nanoplasmonic cathodes, with the multi-tip geometries shown to provide direct maps between laser parameters and excitation of different hot spots. Individual tip hot spots have been extensively characterized for sample nanostars via polarization and spectral studies, correlated SEM imaging, and finite element simulations. Angle-resolved photoelectron velocity measurements demonstrate corresponding frequency and polarization control over photoemission current direction, with all experiments corroborated by 3D surface-mediated photoemission calculations that can be carried out for arbitrary nanoplasmonic geometries. Although volume-mediated excitation processes must also be considered in general, the observed directionality and agreement between experiment and theory strongly underscores the dominant role of surface-mediated MPPE at the sharp nanostar tips. The results presented here highlight opportunities for implementing designer plasmonic nanoparticles and nanostructures as all-optical photocurrent control elements in a variety of applications, including femtosecond electron imaging and diffraction, polarization-sensitive photodetection, site-selective photocatalysis, and terahertz nanoelectronics.

Chapter 6

Volume vs. Surface Multiphoton Photoemission

The relatively low-energy visible resonances and extraordinary optical field concentration in nanoplasmonic systems has served to revitalize the century-old problem[186] of distinguishing between (i) electron excitation throughout the volume of the material, followed by ballistic transport and escape, versus (ii) excitation and emission directly at the surface (Section 1.4).[189] Understanding these mechanisms will unlock opportunities for nanoscale control over hot carriers in emerging plasmonic photocatalytic, photovoltaic, and nanocathode applications (see Section 1.3), among others.

At the heart of this issue is the negligible linear momenta of the incoming photons compared with the outgoing electrons. Momentum conservation thus demands electron scattering with a massive third body during photoexcitation and emission. Photoemission via volume excitation is dominated by scattering with the periodic lattice potential when such a transition is energetically allowed, but visible plasmonic excitation is often below the relevant interband threshold and instead requires scattering with phonons, defects, impurities, or other electrons.[114, 142] These mechanisms depend on the total electric field, $|E|^{2n}$, for n-photon processes. By contrast, surface photoexcitation and emission pathways arise due to the translational symmetry breaking at an interface and thus involve scattering with the surface potential barrier, including contributions from the electromagnetic field variation, localized surface states, and the evanescent external decay of internally-delocalized Bloch wavefunctions.[57] All of these mechanisms depend on the surface-normal electric field,

$|E_\perp|^{2n}$. For nanoscale systems with $\lesssim$ 20 nm dimensions, intraband excitation mediated by geometrical confinement can also become significant.[117, 24, 128] Although ambiguities can arise in categorizing surface vs. volume processes in some systems, the highly-localized surface fields are quite distinct from the diffuse volume fields and corresponding excitation mechanisms/distributions in most nanoplasmonic systems. Further details on the surface vs. volume photoexcitation/emission paradigm, including excitation matrix elements and possible coherent vs. incoherent multiphoton pathways, can be found in Section 1.4.

Given the strong and highly-spatially-varying electric field enhancements in nanoplasmonic systems, volume vs. surface photoexcitation will often lead to disparate spatial and angular photocurrent distributions, which can be harnessed in plasmonic hot carrier devices. Hot carrier catalysts, for instance, already exhibit high reaction efficiencies and product specificity compared with thermally-activated processes,[31, 6] as demonstrated via CO_2 conversion[213] and H_2O splitting[59, 201] for solar fuel production. However, further enhancements in catalytic activity and device functionality can be achieved by controlling the hot carrier spatial and momentum degrees of freedom to compliment anisotropic coatings[96, 125, 201, 25] or even to introduce nanometer site selectivity.[32, 165] Similar opportunities exist in broadband photodetection[95, 22] and solar energy conversion.[30, 202] While internal hot electron emission at metal-molecule[59] or metal-semiconductor[189, 125, 201] interfaces is often classified as either "direct" excitation at the surface or "indirect" transfer following volume excitation,[31, 6, 142, 202] these map directly onto the distinction between surface and volume mechanisms in external (metal-vacuum) photoemission. A deeper understanding and control of volume vs. surface effects is therefore essential to optimizing hot carrier device performance, regardless of the application or collection medium. The majority of this chapter has been taken from recent work on Au nanorods[148] and Au nanoshells.[147]

6.1 Gold Nanorods

The primary focus of this chapter is to distinguish volume vs. surface photoemission pathways in plasmonic nanoparticles by their dramatically different photoelectron momentum distributions. It will first be shown that resonant longitudinal excitation of gold nanorods leads to transverse (orthogonal/side) MPPE distributions due to the dominance of volume excitation mechanisms. A novel transition from volume (transverse/side) to surface (longitudinal/tip) MPPE will then be demonstrated, which occurs with red detuning of the excitation laser as a result of the enhanced metallic screening of internal electric fields at lower frequencies. Detailed modeling of the volume and surface photoemission distributions reproduces all of these effects and allows for the quantitative distinction between the MPPE cross-sections. Most importantly, it is demonstrated that the relative surface vs. volume MPPE depends primarily on plasmonic field enhancements, which can be simulated via classical finite element, finite difference, or other methods. Although measurements are performed in the 2-, 3-, and 4-photon regimes to overcome the ∼4.25 eV gold nanoparticle work function with visible excitation frequencies, the analysis and conclusions are general with respect to process order and should therefore remain valid down to the linear regime for 1-photon applications. Finally, these results allow for the introduction of general design principles for engineering volume and surface processes and thereby controlling hot electron excitation and emission distributions in designer nanoplasmonic systems.

6.1.1 Synthesis

(The following synthetic procedures were developed by the Catherine J. Murphy Group and executed by Sean M. Meyer at the University of Illinois Urbana-Champaign.)

Nanospheres of 70 nm diameter are synthesized based on the method of Perrault *et al.*.[141] A solution of 12 nm spherical gold seeds is prepared by quickly injecting 1 wt% sodium citrate to a boiling aqueous solution of 0.5 mM $HAuCl_4$ under vigorous stirring.

After 5 minutes, a ruby red color is seen, and the heat is turned off and the solution allowed to cool naturally to room temperature on the hot plate. Without any purification, 9.6 mL of water is mixed with 100 μL of 1 wt% $HAuCl_4$ in a 20 mL glass vial and kept under continuous stirring at room temperature with a Teflon-coated stir bar. Quickly, 25 μL of 1 wt% sodium citrate and 115 μL of seed solution were added followed by a rapid injection of 100 μL of 0.03 M hydroquinone. After 20 minutes of stirring, the stir bar is removed, and the particles are centrifuged once at 1000 rcf for 15 minutes and dispersed into 1 mL water. This 1 mL of particle solution is quickly injected into 9 mL of 10 mM CTAB (cetyltrimethylammonium bromide) and mixed gently overnight. The following morning, the particles are subjected to two rounds of centrifugation at 1000 rcf for 15 minutes followed by redispersion in 5 mL of 1 mM CTAB.

Nanorods with aspect ratios (L/D) from 1.5–3 are synthesized using the seed-mediated growth method of Liz-Marzan and coworkers.[58] Small nanorod seeds are prepared in high quality and used as the seeds to grow larger, monodisperse nanorods with the correct size and width. It is recommended, due to the length of the procedure, to refer to the original article for a complete understanding of the synthesis. Briefly, a CTAB and 1-decanol mixture is made and used to prepare small spherical seeds, then carefully in another binary surfactant solution they are introduced with more gold, silver, and acid to grow small nanorods for use in the growth of larger particles. Then, another similar growth solution containing silver, gold, hydrochloric acid, weak reducing agent, and seeds at a precise concentration is mixed and allowed to grow overnight. For the $L/D = 1.5$ nanorods, 45 μL 0.01 M $AgNO_3$ and 55 μL of seeds are used with 500 μL 0.1 M hydroquinone in the absence of any additional acid. For the $L/D = 2.5$ nanorods 200 μL of 0.01 M $AgNO_3$, 50 μL of 1 M HCl, 80 μL if 0.1 M ascorbic acid, and 55 μL seeds were added. The nanorods are then subjected to centrifugation two times at 2000 rcf for 20 minutes and dispersed in 1 mM CTAB after 3+ hours of growth at 27 °C.

Nanorods with $L/D = 3$–5 are prepared, with variations, from the method of Zubarev *et al.*[190] The first step is to make small CTAB-capped gold seeds of 1–2 nm. This is achieved by adding 0.46 mL of a basic sodium borohydride solution (prepared by adding 46 mg of sodium borohydride directly to 10 mL ice-cold 0.01 M sodium hydroxide and diluting this solution 10-fold with 0.01 M sodium hydroxide) under vigorous stirring to a solution of 9.5 mL 0.1 M CTAB and 0.5 mL 0.01 M $HAuCl_4$. After allowing an hour for the excess sodium borohydride to decompose, growth solutions are prepared. Growth solutions are prepared by mixing the following reagents as listed in order of 9.5 mL of 0.1 M CTAB, 0.5 mL of 0.01 M $HAuCl_4$, varying amounts of 0.1 M $AgNO_3$ (10–40 μL), 0.5 mL of 0.1 M hydroquinone, and a varying seed amount (90 μL seeds for L/D = 3–4.5 and 40 μL for larger aspect ratio). The particles are kept at room temperature overnight and grown to completion. The next day, each tube is then subjected to centrifugation two times at 2000 rcf for 20 minutes and the nanorods are dispersed in 1 mM CTAB after 3+ hours of growth at 27 °C.

6.1.2 Nanorod SPR Properties

Strong electric near-field enhancements are generated at the tips of gold nanorods where conduction electrons collectively pile up during longitudinal localized surface plasmon resonance (SPR) oscillations. At the same time, appreciable field enhancements are also generated within the metal volume. High densities of hot carriers may therefore be excited at nanorod tips via surface excitation mechanisms or inside the nanorod via volume excitation mechanisms. The corresponding photoemission pathways are illustrated in Fig. 6.1a, along with the scanning photoelectron imaging microscopy (SPIM) experimental configuration. Different photoemission angular distributions are expected for the two mechanisms,[9] depending upon the nanoparticle geometry and the electric near-field distribution of the excited plasmon mode. This provides a direct means of identifying volume and surface photoemission contributions via single-particle, angle-resolved photoelectron velocity mapping.

Photoemission spectra are shown in Fig. 6.1b for nanorods of similar diameter, D = 21 ± 4 nm (Fig. 6.2), but different lengths and thus aspect ratios (L/D), illustrating

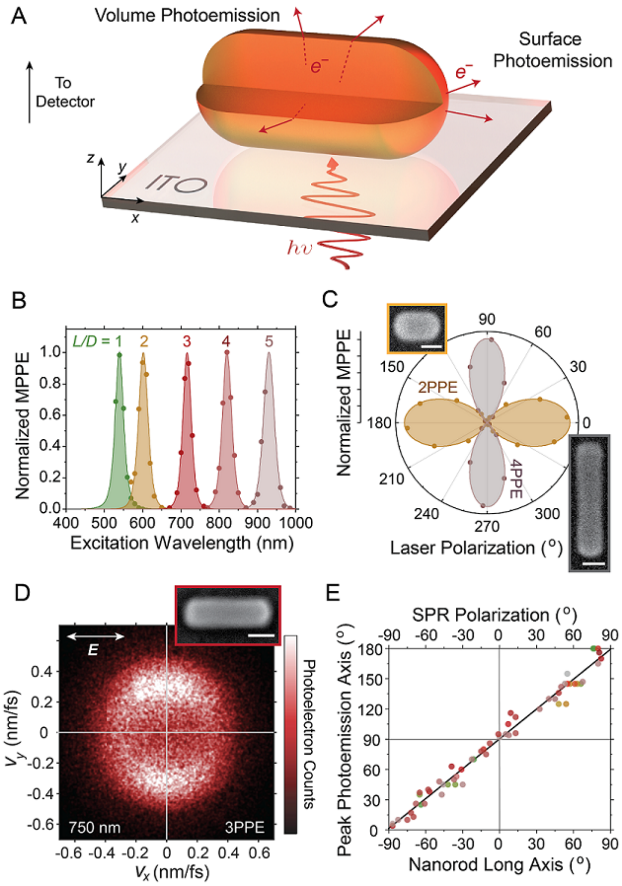

Figure 6.1: Characterization of nanorod surface plasmon resonance photoemission properties. (a) Configuration of scanning photoelectron imaging microscopy experiments, illustrating volume and surface emission from an illuminated gold nanorod (with a quarter section removed to show the volume excitation). (b) Multiphoton photoemission spectra measured for nanorods of various aspect ratios, fit to nonlinear Lorentzian profiles. (c) Signal dependence on linear laser polarization in the azimuthal (xy) plane, fit to $\cos^{2n}(\theta - \theta_{\mathrm{rod}}$ and shown with scanning electron micrographs of the correlated nanorods ($L/D = 1.5$, 2PPE; $L/D = 4.5$, 4PPE), where laser polarization $\theta = 0^\circ$ is along the x axis. (d) Photoelectron velocity map collected at the longitudinal resonance of the correlated $L/D = 3.2$ nanorod in the inset, exhibiting transverse photoemission. (e) Summary of photoemission directionality for all nanorods of various aspect ratios and spatial orientations, with transverse peak photoemission observed in every case. Data colors (here and elsewhere) are mapped to the corresponding wavelength. Scale bars: 20 nm.

the anticipated linear increase of SPR wavelength with nanorod aspect ratio[112, 168] for $L/D \gtrsim 2$ as summarized in Fig. 6.3. For the gold nanorod work function around 4.25 eV, electrons must absorb multiple photons to overcome the surface potential barrier, with nanorod resonances ranging from 950 nm (1.3 eV photon energy, $n = 4$ photons) at $L/D = 5$ down to the spherical limit of 540 nm (2.3 eV photon energy, $n = 2$ photons) at $L/D = 1$. Measurements of the photoemission dependence on linear laser polarization (angle θ) in the azimuthal plane (Fig. 6.1c) show clearly-defined longitudinal resonances along the long nanorod axes, noticeably narrowing in the 4-photon regime ($L/D \approx 4.5$) relative to the 2-photon regime ($L/D \approx 1.5$) due to the nPPE$\propto E^{2n} \cos^{2n}(\theta - \theta_{\text{rod}})$ dependence of the field projection along the nanorod axis. Pulse durations around 150 fs, pulse peak intensities of 10^8 W cm^{-2}, and calculated nanorod extinction cross-sections around 10^{-10} cm^{-2} lead to the excitation of nearly 10^4 plasmons/pulse, which is much larger than the 2–4 quanta occasionally absorbed toward MPPE (one MPPE event every $\sim 10^5$ pulses, with a 75 MHz laser repetition rate), thus justifying a classical treatment of the plasmonic fields.

6.2 Volume-Mediated Nanorod MPPE

While longitudinal electron emission outward from the highly field-enhanced nanorod tips has been observed in the strong-field tunneling[74, 152] and transitional regimes,[106] it is surprisingly observed here that weak-field MPPE is predominantly transverse (orthogonal) to the resonantly-excited longitudinal nanorod axis, as demonstrated in Fig. 6.1d. In other words, electrons are evidently emitted from the sides rather than the tips of the nanorods. This transverse photoemission is observed for every nanorod investigated (Fig. 6.1e), irrespective of aspect ratio ($L/D = 1.5$–5), surface ligands (Fig. 6.4), size ($D = 10$–40 nm, Fig. 6.4), or corresponding size-dependent differences in faceting.[137] Electron thermalization effects during the pulse duration are accounted for via two-temperature modeling[69] as discussed in detail in Section 3.3.3. Intensity-dependence studies (to be discussed further) also demonstrate negligible thermionic or thermally-assisted emission effects. Furthermore,

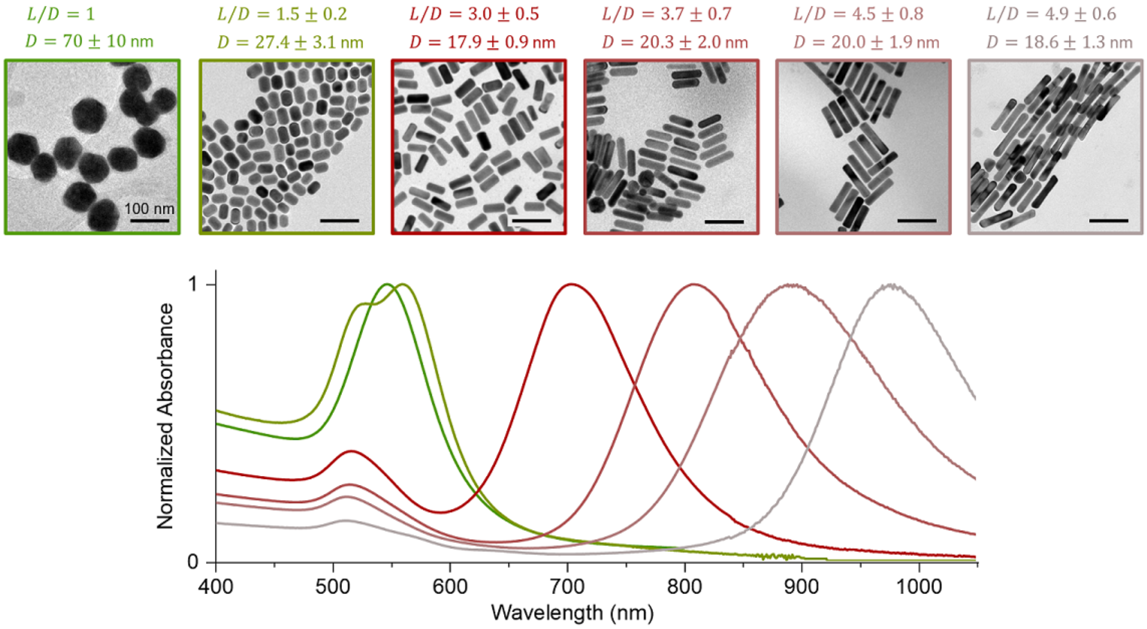

Figure 6.2: Transmission electron micrographs and dimensional statistics of synthesized CTAB-coated nanorod samples, with aspect ratios ranging from 1 (spheres) to 5. The spheres are larger to ensure sufficient signal-to-background in photoemission measurements. Corresponding UV-Vis spectra for aqueous dispersions show longitudinal surface plasmon resonance peaks ranging from 550–980 nm, with transverse surface plasmon resonance peaks at 510 nm.

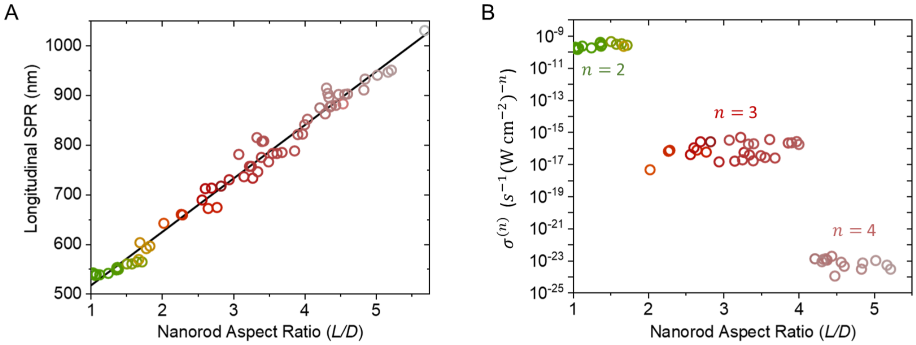

Figure 6.3: Photoemission characteristics of the nanorod samples. (a) Surface plasmon resonances measured via multiphoton photoemission as a function of nanorod aspect ratio. The black line is a linear least squares fit. (b) n-photon photoemission cross-sections determined as a function of nanorod aspect ratio via intensity-dependence studies.

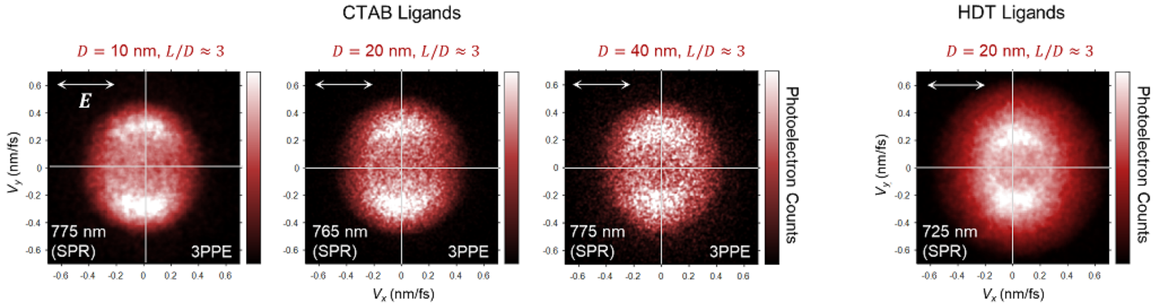

Figure 6.4: Velocity map images collected for CTAB-coated nanorods of 10 nm, 20 nm, 40 nm diameters with similar aspect ratios and longitudinal surface plasmon resonance frequencies. The rightmost panel shows the velocity map for a 20 nm diameter nanorod coated in HDT ligands, which have a covalent Au-thiol bond rather than an ionic CTA-bromide bond.

measurements with dispersion-compensated 40–50 fs pulses yield the same transverse MPPE distributions. Such observations provide a strong initial indication that the transverse photoemission arises due to volume-mediated hot electron MPPE for the nanorod geometry. In such a mechanism, one expects hot electrons excited throughout the nanorod to escape ballistically from the cylindrical body with a predominantly transverse distribution and from the hemispherical tips with a nearly isotropic distribution. As a starting point, if uniform excitation throughout the nanorod volume and a short inelastic mean free path ($\lambda_{\text{inel}} \ll D$) are assumed, the relative side versus tip contributions can be approximately estimated by the ratio of corresponding surface areas, which works out to be $S_{\text{side}}/S_{\text{tip}} = L/D - 1$. It is therefore expected that the photoemission distribution will become isotropic as $L/D \rightarrow 1$ ($S_{\text{side}} \ll S_{\text{tip}}$) or to become increasingly dominated by transverse contributions as $L/D \rightarrow \infty$ ($S_{\text{side}} \gg S_{\text{tip}}$).

To show definitively that the photoemitted electrons primarily originate within the volume of the resonantly-excited nanorods, photoemission distributions are measured as a function of nanorod aspect ratio. As expected, the 2D velocity maps in Fig. 6.5a demonstrate that the photoemission angular distributions become more isotropic with decreasing aspect ratio and completely isotropic in the spherical limit. The radially-integrated angular distributions in Fig. 6.5c can be characterized by an angular contrast, AC, defined as

$$AC = \frac{\langle \| \text{ counts}\rangle - \langle \perp \text{counts}\rangle}{\langle \| \text{ counts}\rangle + \langle \perp \text{counts}\rangle} \tag{6.1}$$

where the brackets denote averaging (within ±2°) over the two longitudinal (0° and 180°) and transverse (90° and 270°) directions on the 2D velocity maps. This definition of the angular contrast provides a model-independent metric of how transverse ($AC \rightarrow -1$) or longitudinal ($AC \rightarrow +1$) a given distribution is. Angular contrast values are summarized as a function of aspect ratio in Fig. 6.5e, where AC clearly becomes more negative (transverse) as the nanorod aspect ratio increases, and goes to 0 in the isotropic spherical limit, as expected for the volume photoemission mechanism. Note that the angular contrast and the photoemission mechanisms described here are not to be confused with molecular photoionization and the corresponding anisotropy parameter, β.[178]

A summary of nonlinear process order, n (where $n\text{PPE} \propto I_0^n$), from intensity-dependence measurements performed on resonance for each nanorod studied is shown in Fig. 6.5d and elaborated in Fig. 6.6. The results show a clear sequential transition from 2PPE to 3PPE to 4PPE with increasing SPR wavelength and linearly-correlated increasing aspect ratio (Fig. 6.1b and Fig. 6.3). The well-defined integer process orders and transitions verify that the present studies are performed in the perturbative MPPE regime rather than the optical field emission or thermionic regimes (Section 3.4). Non-integer process orders in the transition regions arise naturally in the power-law fits and reflect the weighted sum of the two contributing process orders.[144] It is also noted that no sudden changes in photoemission angular distributions or corresponding angular contrast values are observed in the transition regions between process orders. The physics is qualitatively the same at all nonlinear orders studied herein ($n = 2$–4), simply with a different total excitation energy $n\hbar\omega$ and nonlinear absorption cross-sections. It is thus anticipated that the present observations can be extrapolated from the multiphoton regimes down to the linear emission regime for systems with lower hot electron emission barriers, including metal-semiconductor and metal-molecule junctions.

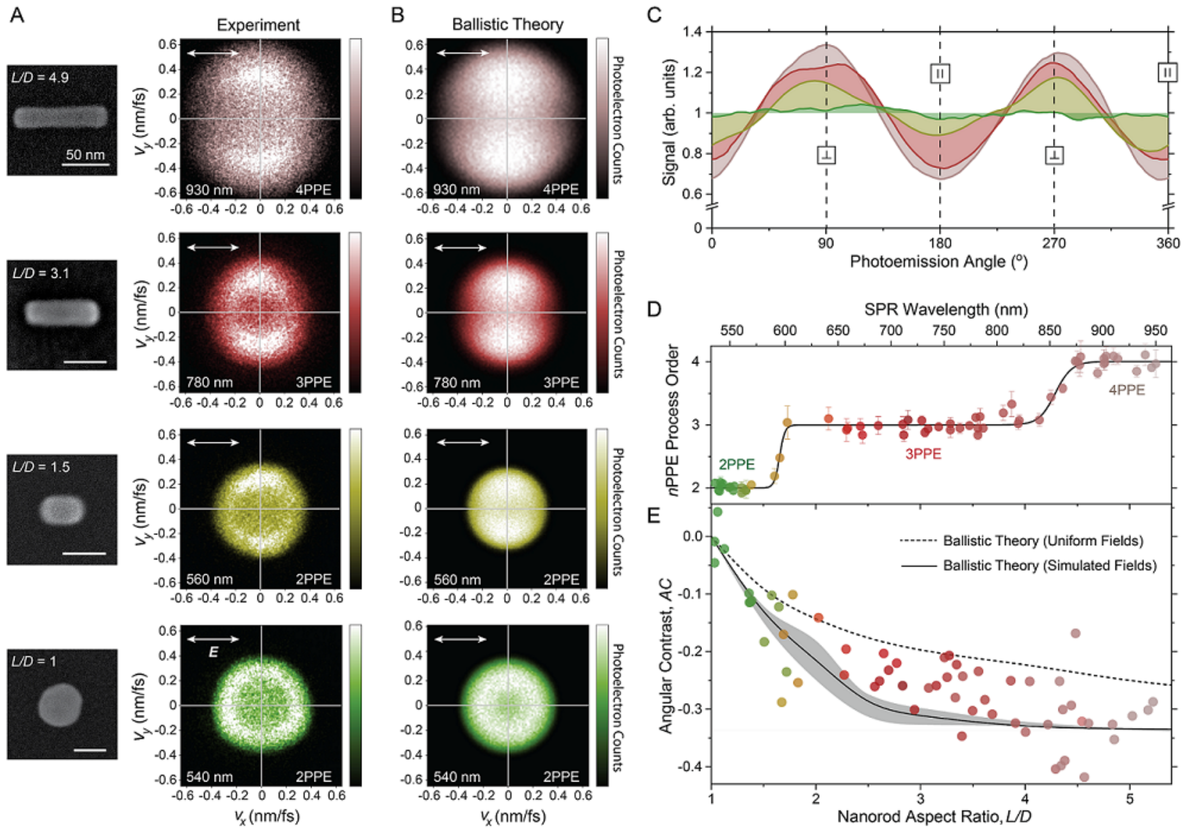

Figure 6.5: Volume photoemission distributions as a function of aspect ratio. (a) Correlated electron micrographs and velocity maps for a series of nanorods excited at their longitudinal surface plasmon resonances (SPRs), down to the spherical limit. Nanospheres of larger $D = 70$ nm were studied compared with nanorods ($D = 20$ nm) for sufficient signal levels, but this is neither expected nor observed to affect their photoemission properties. Scale bars: 50 nm. (b) Velocity distributions for the same nanorods as in (a), modeled using the ballistic (3-step) Monte Carlo theory. (c) Radially-integrated angular distributions from the velocity maps in (a) with transverse ($\perp$) and longitudinal ($\|$) directions indicated and 0° along the x (i.e. v_x) polarization axis. (d) Process order summary of n-photon photoemission measured via power-law intensity-dependence fits (Fig. 6.6—error bars are standard errors of the fits) for all investigated nanorods for longitudinal SPR excitation, shown with overall sigmoidal fits. The SPR wavelength axis is linearly-mapped (except around $L/D = 1$) to the aspect ratio (Fig. 6.3). (e) Photoemission angular contrast of all investigated nanorods for longitudinal SPR excitation, becoming more negative (transverse) with increasing aspect ratio and isotropic in the spherical limit. Ballistic Monte Carlo theory curves shown for uniform and nonuniform (finite-element-simulated) internal fields. The error bounds shown for the simulated fields case assume an inelastic mean free path between 7 nm (top) and 5 nm (bottom), with the primary curve calculated at 6 nm.

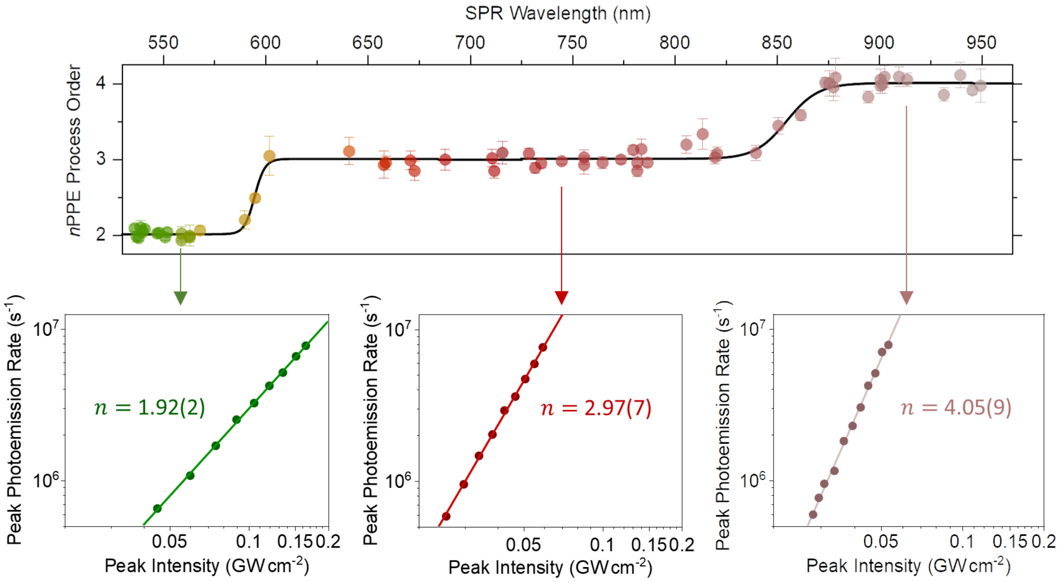

Figure 6.6: Intensity-dependence process order summary with example single-nanorod data and fits for $n = 2$–4. All measurements are performed at the nanorod longitudinal surface plasmon resonance.

To understand the volume MPPE distributions in further detail, a Monte Carlo algorithm is implemented within a ballistic, three-step photoemission model.[17] While this is described in Section 3.5.1, it is presented briefly here. In this model, electrons are first excited to randomly-selected vector momenta (thus approximating isotropic phonon-mediated multiphoton excitation), with Fermi-Dirac weighting, from points selected randomly throughout the nanorod volume. The volume element selection probability is weighted by the nonlinear internal field enhancement ($|E/E_0|^{2n}$) determined via electrodynamic finite element simulations with the ligands and substrate accounted for. For supported nanorod and nanosphere simulations, a 1.5 nm CTAB (cetyltrimethylammonium bromide) ligand layer surrounding the particles is included in the simulations, along with an additional 0.5 nm gap between the ligand layer and the substrate to avoid extra-narrow domain regions. Overall, the rectangular domain consists of the glass substrate with a 10 nm ITO film, the vacuum superstrate, the gold nanoparticle with ligand layer, and a perfectly-matched layer surrounding the domain to prevent field reflection at the domain boundaries. The effect of the transparent conducting substrate image charge oscillation is to enhance the field on the lower half of the nanorod, as accounted for in the Monte Carlo and surface MPPE modeling, respectively. Nanorods are modeled as perfect cylinders with hemispherical end caps, with diameter D and total tip-to-tip length L. Triangular surface and tetrahedral volume meshing were constructed with near-uniform element size across the nanoparticle surface and volume, with the element side length (2 nm) selected to be much smaller than the nanoparticle dimensions and any electric field variation on the surface or within the volume. This is particularly essential, as the same mesh and calculated field values at the vertices are subsequently utilized for both volume and surface photoemission modeling. The optical constants of gold are taken from the literature[86] and determined for the ITO film via ellipsometry. Optical constants $n_{\text{lig}} = 1.5$ and $k_{\text{lig}} = 0.25$ for the CTAB ligand layer, where the small extinction coefficient accounts for the presence of amorphous carbon due to the hot-electron-driven conversion of the organic ligands. Further discussion of this conversion process and nanorod photoemission stability can be found below.

The calculated pulse-averaged electron temperature of 1000 K (via two-temperature modeling; see Section 3.3.3) is utilized for the excited Fermi-Dirac distribution to account for minor effects of electron heating during the pulse duration. The hot electrons then travel ballistically over some distance (d) to the surface with an exponential survival probability for inelastic hot-cold electron-electron scattering, $e^{-d/\lambda_{\text{inel}}}$. The inelastic mean free path, $\lambda_{\text{inel}} \approx$ 6 nm, is approximately constant over the narrow threshold energy range of interest[24, 88] and the possibility of electrons surviving a single inelastic scattering event with sufficient momentum to subsequently escape is accounted for, although this contribution is found to be negligible. Finally, hot electrons that reach the surface are transmitted into the surrounding medium with unity probability if they have sufficient surface-normal momentum to overcome the surface potential barrier and are otherwise reflected and lost. Trajectories following surface reflection could be readily incorporated into the modeling and may be relevant for particle dimensions similar to or less than the inelastic mean free path,[28, 19] but are safely neglected here as $\lambda_{\text{inel}} \ll D$ and L. Quantum barrier reflections corresponding to a sharp barrier (barrier width much smaller than the hot electron wavelength for near-threshold emission[56]) are also modeled in comparison with the smooth barrier limit (e.g. due to image potential and/or ligand effects) and the corresponding transmission unit step function[189, 56], yielding little effect on the resulting distributions. The effect of "refraction" at the surface barrier due to perpendicular momentum loss and parallel momentum conservation is fully accounted for within the simulations. While other integration methods have been used to solve for the spatial distributions of emitted hot electrons,[28, 79] the Monte Carlo method provides a computationally efficient means of integrating over all hot electron trajectories for arbitrary nanoparticle geometries.[31, 19, 84] Further details of the ballistic Monte Carlo method are described in Section 3.5.1.

The calculated Monte Carlo velocity maps in Fig. 6.5b and AC values in Fig. 6.5e recapitulate the experimental angular distributions reasonably well. Simulated AC values for different nanorod diameters are also shown in Fig. 6.7. Small longitudinal surface photoemission contributions are likely the cause of the slightly less negative experimental angular contrast values compared with the calculations, as examined in the next section. Except for near the Fermi edge, which is in good agreement due to the experimental determination of the 4.25 ± 0.1 eV work function from the process order transitions (Fig. 6.5d) and from the velocity maps, the radial dependence of the photoemission distribution is evidently not reproduced as well by the approximation of constant joint density of states and energy-independent excitation matrix elements utilized in the Monte Carlo modeling. Further details of the nascent hot electron distribution could be incorporated into the modeling, but this would require a significantly more detailed *ab initio* treatment of the material band structure and a variety of multiphoton volume excitation channels, including direct versus indirect (phonon-mediated) transitions in coherent and incoherent channels. Such *ab initio* calculations have been demonstrated by Narang and colleagues for two-photon excitation[129] but are beyond the scope of the present work.

6.3 Detuning into the Surface-Mediated Regime

For further insight into the roles of both volume and surface photoemission processes, the electric near-field distributions are simulated as a function of excitation frequency (and thus detuning from SPR) in Fig. 6.8a. Unlike the well-known uniform internal fields for ellipsoids,[177] internal fields for nanorods are stronger near the center due to a hemispherical surface charge distribution at the tips (dipolar in the spherical limit) with field vectors that destructively cancel within the tip regions but add constructively near the nanorod center. Such central concentration of the field distributions leads to more centralized excitation of hot electrons, which subsequently escape predominantly from the sides of the nanorods rather than the tips due to the limiting inelastic mean free path. This results in more negative (transverse) angular contrast values compared with uniform excitation throughout the nanorod body, as seen by comparing the theoretical curves in Fig. 6.5e. This is a

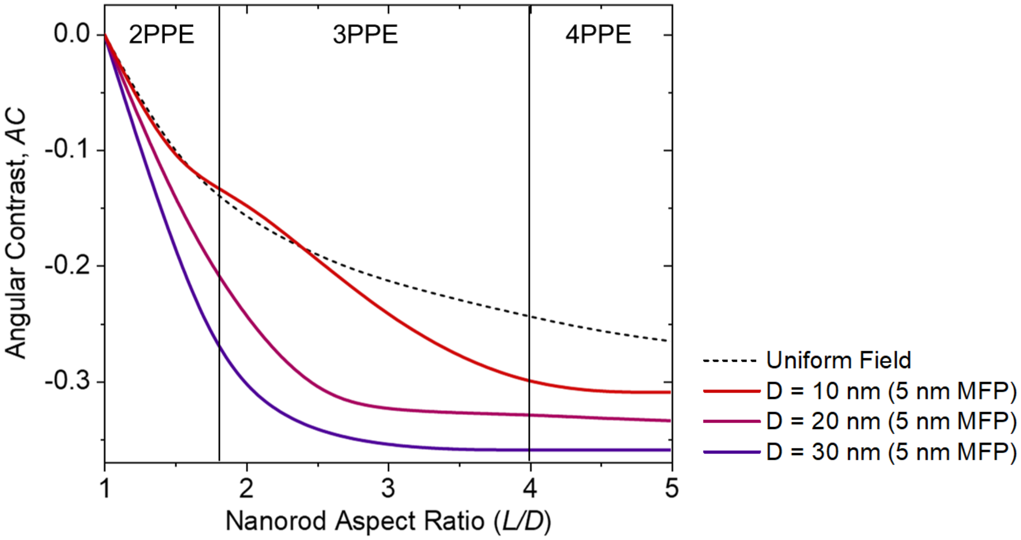

Figure 6.7: Calculated angular contrast (AC) values for nanorods of different diameters and aspect ratios, using the nonlinear field distributions calculated via finite element modeling. As the nanorod radius becomes comparable to the inelastic mean free path (∼5 nm here) more electrons can escape from the entire nanorod surface, including the hemispherical tips. This leads to a more isotropic emission distribution and less negative (less transverse) AC values. The uniform field curve only depends on the relative side vs. tip surface areas, which depends only on the aspect ratio and is constant with diameter.

very different phenomenon from centralized heating effects that have been observed due to higher electron kinetic energy in the center of the nanorod during plasmon oscillations,[74] as thermal effects are negligible in these relatively low-intensity ($I_0 \approx 0.05$–0.1 GW cm^{-2}) perturbative studies.

While the overall field enhancement is strongest on the plasmon resonance, the relative surface field contribution increases with red detuning due to enhanced screening of the internal fields at lower frequencies by the conduction electrons. The ratio of these nonlinear surface and volume field enhancement integrals (proportional to the nonlinear photoemission cross-section ratio, $\sigma_{\mathrm{S}}^{(n\mathrm{PPE})}/\sigma_{\mathrm{V}}^{(n\mathrm{PPE})}$) is summarized for different aspect ratios in Fig. 6.8b. The total multiphoton photoemission rate can be written as

$$\mathrm{MPPE} = \sum_{n} \left(\sigma_{\mathrm{S}}^{n\mathrm{PPE}}(\omega) + \sigma_{\mathrm{S}}^{n\mathrm{PPE}}(\omega)\right) I_0^n, \tag{6.2}$$

where the surface and volume nPPE cross-sections are given by

$$\sigma_{\mathrm{S}}^{n\mathrm{PPE}}(\omega) = c_{\mathrm{S}}^{(n)}(\omega)\eta_{\mathrm{S}}^{(n)}(\omega) \int \left|E_{\perp}(\boldsymbol{r},\omega)/E_0\right|^{2n} dS, \tag{6.3}$$

and

$$\sigma_{\mathrm{V}}^{n\mathrm{PPE}}(\omega) = c_{\mathrm{V}}^{(n)}(\omega)\eta_{\mathrm{V}}^{(n)}(\omega) \int \left|E(\boldsymbol{r},\omega)/E_0\right|^{2n} dV, \tag{6.4}$$

respectively. The $c_{\mathrm{S}}^{(n)}$ and $c_{\mathrm{V}}^{(n)}$ factors are the surface and volume nonlinear absorption densities and $\eta_{\mathrm{S}}^{(n)}$ and $\eta_{\mathrm{V}}^{(n)}$ are the emission quantum yields for a given process order. Strictly speaking, the volume emission quantum yield in Eq. 6.4 is actually a volume-averaged quantity,

$$\eta_{\mathrm{V}}^{(n)}(\omega) = \frac{\int \eta_{\mathrm{V}}^{(n)}(\boldsymbol{r},\omega) \left|E(\boldsymbol{r},\omega)\right|^{2n} dV}{\int \left|E(\boldsymbol{r},\omega)\right|^{2n} dV}, \tag{6.5}$$

which therefore depends on the geometry and can be determined via ballistic Monte Carlo modeling using the simulated fields. Typical values for $\eta_{\mathrm{V}}^{(n)}$ for nanorods are between 0.1% and 1%, as quantified via full nanorod surface maps in Fig. 6.9, although this depends strongly on the frequency[52] and may also be substantially enhanced by surface

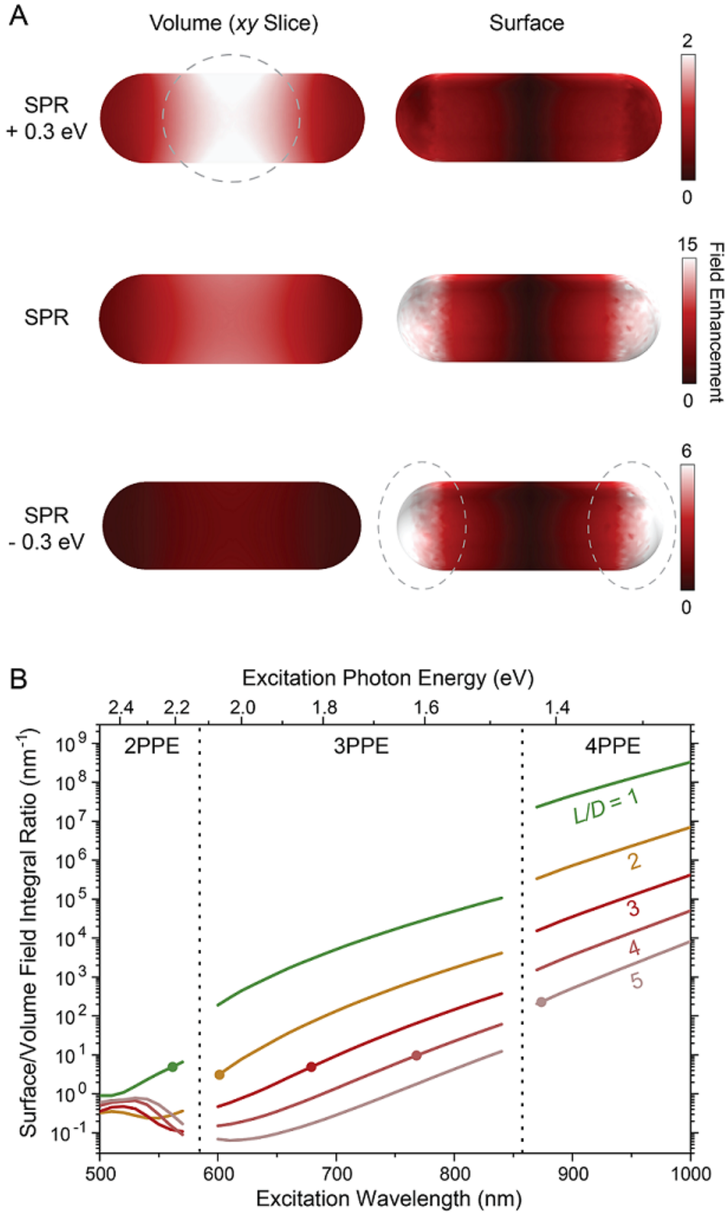

Figure 6.8: Finite element simulations of surface and volume plasmonic field enhancements. (a) Volume ($|E/E_0|$) and surface ($|E_\perp/E_0|$) field enhancement maps for $L/D = 3$ nanorod viewed in the xy plane (ligand layer and ITO substrate accounted for but not shown). Volume fields are dominant at higher excitation energies (e.g. SPR + 0.3 eV) while surface fields are dominant at lower excitation energies (e.g. SPR − 0.3 eV). (b) Ratio of the nonlinear surface field integral to the nonlinear volume field integral for a series of nanorod aspect ratios across the $n = 2$–4 spectral regions. Points indicate the calculated surface plasmon resonance wavelengths. The fluctuations in the 2PPE regime are primarily due to the onset of 5d-band absorption and dispersion.

roughness.[60] By comparison, $\eta_{\mathrm{S}}^{(n)}$ only depends on generic properties of a locally-flat metal-vacuum surface potential barrier and is therefore not geometry-specific. As a result, the only geometry-specific quantities are the field enhancement integrals in Eqs. 6.3 and 6.4 (which encode the plasmonic response of the system) and $\eta_{\mathrm{V}}^{(n)}$, which can be determined via finite element and Monte Carlo modeling, respectively. The remaining $c_{\mathrm{S}}^{(n)}\eta_{\mathrm{S}}^{(n)}$ and $c_{\mathrm{V}}^{(n)}$ values are properties only of the material and/or nanoparticle-vacuum interface. Thus, if these material quantities can be characterized experimentally, then $\sigma_{\mathrm{S}}^{(n)}$ and $\sigma_{\mathrm{V}}^{(n)}$ are fully determined, permitting the surface and volume contributions to be predicted for arbitrary nanoscale or even macroscopic geometries.

Toward the goal of determining $\sigma_{\mathrm{S}}^{(n)}$ and $\sigma_{\mathrm{V}}^{(n)}$ separately, photoelectron velocity mapping is utilized to distinguish the volume and surface distributions. Considering the dramatic change in the relative nonlinear surface vs. volume field enhancements with detuning (see Fig. 6.8b, the photoemission is expected to transition from the transverse volume-dominated distribution ($AC < 0$) always observed around the SPR to a longitudinal surface-dominated distribution ($AC > 0$) with only modest red detuning. This is precisely what is observed in Fig. 6.10a, with the angular contrast summarized in Fig. 6.10c becoming positive around $\Delta\hbar\omega \approx -0.25$ eV detuning. Unlike transverse volume emission, the longitudinal surface emission is often asymmetric due to amplification of any tip field asymmetry (i.e. due to slight tip curvature differences) by the nonlinear process. For example, a 10% difference in the tip fields results in a factor of two difference in 4PPE rates ($\propto |E/E_0|^8$). To take such asymmetry into account, the angular contrast values are obtained by averaging over both longitudinal directions (Eq. 6.1). The measured angular contrast values for 9 sample nanorods resonant between 700–800 nm (L/D = 2.5–3.5) are summarized in Fig. 6.10c, which all display very similar behaviors with detuning. Notably, the range of detuning values crossing $AC = 0$ is about a factor of three narrower than the spread in absolute energies arising from the spread in the SPR energies due to sample heterogeneity, as shown in Fig. 6.11. With respect to detuning from the surface plasmon resonance, all curves in Fig. 6.11a

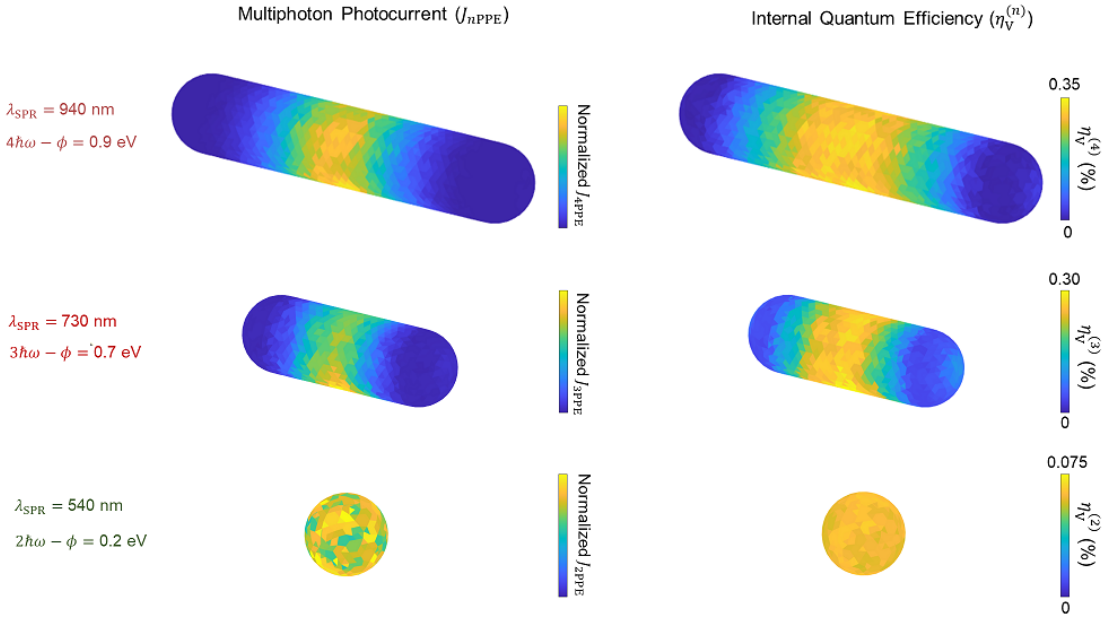

Figure 6.9: Surface photocurrent ($J_{n\text{PPE}}$) and internal quantum efficiency maps for resonantly-excited nanorods with aspect ratio $L/D = 5$ (top), 3 (middle), and 1 (bottom), determined via Monte Carlo volume photoemission simulations. Each rod is resonant in a different nonlinear regime. (Left) The surface current proportional to the total number of escaped electrons from each surface area element, which shows that most electrons are excited near the center of the nanorod in the centralized field-enhanced region, subsequently escaping mostly from the nearby surfaces (as limited by inelastic scattering). (Right) The internal quantum efficiency is taken to be a discrete value for each area element, with the total given by surface-averaged value. The $L/D = 5$ and 3 rods have similar maximum electron kinetic energies ($n\hbar\omega - \phi$) of $\sim$0.8 eV at resonance and therefore have similar quantum efficiencies. The excess electron kinetic energy is much smaller ($\sim$0.2 eV) in the sphere case for the 540 nm resonance and 2-photon photoemission, such that the escape quantum efficiency is about four times smaller. Such frequency dependence is described by Fowler theory (1) (with the frequency dependence trivially extended into the n-photon regime via $\hbar\omega \rightarrow n\hbar\omega$).

are nearly overlapped. However, the spread in the curves with respect to absolute excitation energy (Fig. 6.11b) is as broad as the spread in resonances. Thus, it is clear that the transition is not due to an absolute energy effect such as the transition from 3PPE to 4PPE (with this line indicated in Fig. 6.11b). Furthermore, intensity-dependence measurements verify that the surface emission at -0.4 eV red detuning remains in the multiphoton regime rather than the strong-field regime (Fig. 6.12). Higher input intensities are utilized at -0.4 eV red detuning ($I_0 \approx 2$ GW cm^{-2} versus 0.05 GW cm^{-2} on resonance), but this simply maintains similar signal levels by compensating for the drop in the plasmonic field enhancement off resonance.

Under the present weak-field input intensities, nanorod heating is negligible ($\sim$30 K lattice temperature increase, Fig. 6.13) and thus there is no possibility of melting. To verify that nanorods remain stable emitters during these studies, we demonstrate three typical time traces in Fig. 6.14 for nanorods excited on resonance and at red detuning. The volume emission on resonance is clearly very stable, while surface emission at red detuning can be quite spiky, if fundamentally still fairly stable. The cause of the spikes is unknown, though may be attributed to single-atom displacement (so-called "picocavity") effects, which transiently create a factor of $\sim$4 larger field in a sub-nanometer region.[26] For the 4PPE process, the 4-fold increase in $|E/E_0|$ leads to a 10^5-fold increase in $|E/E_0|^8$, which can thus have noticeable effects despite the miniscule single-atom area. The surface signal fluctuations may alternatively be attributed to ligand rearrangement and corresponding sudden changes in the surface dielectric environment. In any case, the volume emission is insensitive to such effects and thus remains quite stable. Looking with velocity resolution, it is found that while volume photoemission distributions remain quite stable/unchanged after prolonged nanorod exposure, surface distributions tend to change a bit after $\sim$1 hour of continuous exposure (Fig. 6.15). This is attributed to the well-known buildup of amorphous carbon in the strongly field-enhanced tip regions,[183] in this case attributed to the cracking and rearrangement of surface ligands. The nonuniform amorphous carbon leads to varying near-

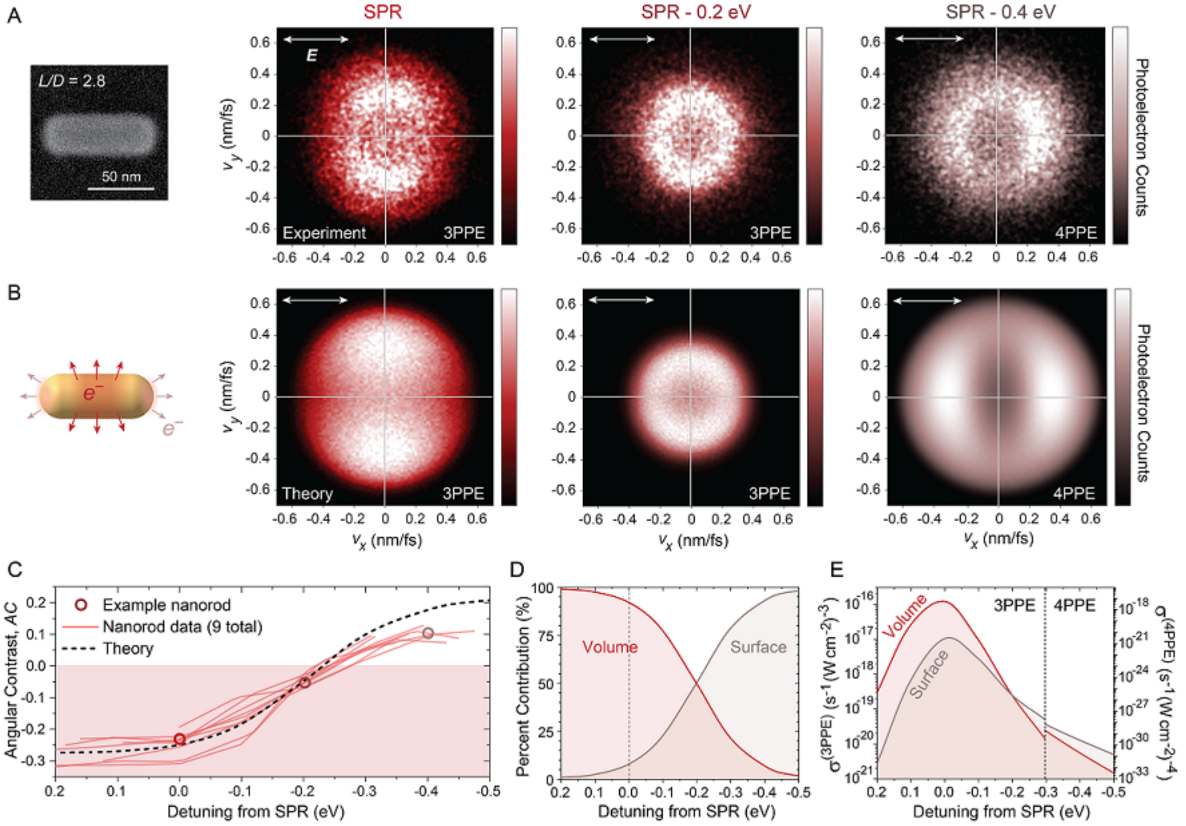

Figure 6.10: Transition from volume to surface photoemission with red detuning. (a) Experimental and (b) theoretical velocity maps at various detunings from the SPR of the correlated example nanorod, showing the transition from volume (transverse) to surface (longitudinal) photoemission. (c) Summary of angular photoemission contrast values for 9 nanorods, with data points for the example rod in (a) and the theoretical curve from (b). All nanorods display consistent behavior and transition from the volume regime (shaded, $AC < 0$) into the surface regime ($AC > 0$) around -0.25 eV detuning. (d) Relative volume and surface contributions determined from the fit of $a^{(n)}$ in (c). (e) Volume and surface nPPE cross-sections for the example nanorod in (a).

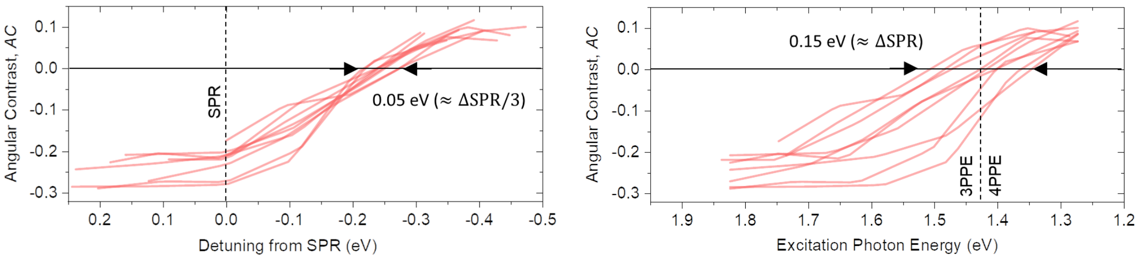

Figure 6.11: Demonstrating that the transition from volume to surface photoemission at lower excitation frequencies is not due to an absolute energy effect, but rather a detuning effect. (Left) Angular contrast versus detuning from the surface plasmon resonance, as also shown in the main text. All curves for 9 nanorods have similar trends and overlap quite well. The spread in detuning values crossing into the surface regime $AC = 0$ is a factor of three smaller than the spread of surface plasmon resonance values. (Right) Angular contrast versus absolute excitation photon energy, showing a much broader spread dictated entirely by the spread in SPRs of the 9 nanorods.

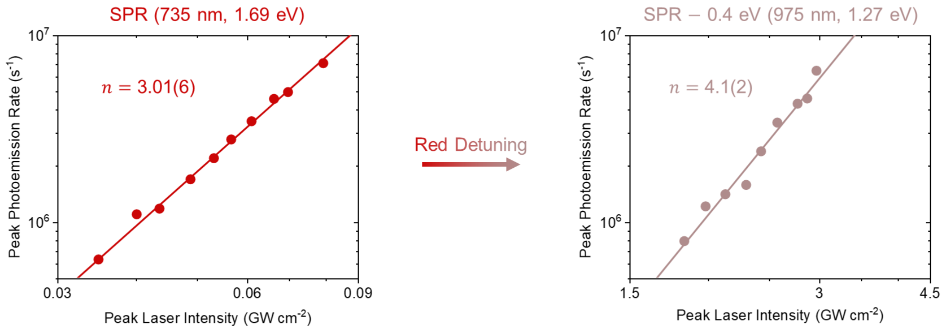

Figure 6.12: (Left) 3PPE intensity dependence for an example nanorod ($L/D \approx 3$) excited on resonance, versus (Right) the 4PPE intensity dependence. Red-detuned emission therefore remains in the multiphoton regime, as expected.

field enhancements and corresponding surface photoemission distributions, while potentially also increasing scattering and therefore leading to more diffuse distributions.

To help theoretically characterize the relative surface and volume contributions to the observed photoelectron distributions, the 3D photoemission distributions (and 2D projections) are modeled for each mechanism, taking the correlated nanorod geometry into account (Fig. 6.10b). Volume photoemission distributions are again modeled via the ballistic Monte Carlo method, while the surface MPPE theory developed by Yalunin and coworkers[203] is implemented to model the surface distributions. The implementation of this surface MPPE theory to arbitrary nanoparticle systems is described in Section 3.5.2. In all experiments and theory, the 3D photoelectron velocity distributions are projected/integrated over the v_z degree of freedom, leading to the 2D (v_x, v_y) velocity maps. The 3D distributions are calculated explicitly, while the experimental 3D distributions could be recovered via inverse Abel transform [42] by assuming cylindrically-symmetric photoemission distributions about the nanorod long axis, as demonstrated in Chapter 5 for gold nanostars but not performed here.

The relative weighting between calculated surface and volume contributions, $\sigma_{\mathrm{S}}^{(n\mathrm{PPE})}/\sigma_{\mathrm{V}}^{(n\mathrm{PPE})}$, depends on the ratio of the field integrals (Fig. 6.8b) as well as the primarily material-specific (geometry-independent) coefficients in Eqs. 6.3 and 6.4. By working in the threshold photoemission regime with excess photoelectron kinetic energies < 2 eV and approximating a constant density of states and excitation matrix elements in this narrow energy range, the frequency dependence of both surface and volume coefficients can be expected to obey Fowler's law,[52] $c_{\mathrm{S}}^{(n)}(\omega)\eta_{\mathrm{S}}^{(n)}(\omega) \propto c_{\mathrm{V}}^{(n)}(\omega)\eta_{\mathrm{V}}^{(n)}(\omega) \propto (n\hbar\omega - \phi)^2$, thus canceling out in the $\sigma_{\mathrm{S}}^{(n\mathrm{PPE})}/\sigma_{\mathrm{V}}^{(n\mathrm{PPE})}$ ratio. As a result, all of the frequency dependence in $\sigma_{\mathrm{S}}^{(n\mathrm{PPE})}/\sigma_{\mathrm{V}}^{(n\mathrm{PPE})}$ is contained within the ratio of the nonlinear field integrals, scaled by a single frequency-independent prefactor

$$a^{(n)} = \frac{c_{\mathrm{S}}^{(n)}(\omega)\eta_{\mathrm{S}}^{(n)}(\omega)}{c_{\mathrm{V}}^{(n)}(\omega)\eta_{\mathrm{V}}^{(n)}(\omega)}. \tag{6.6}$$

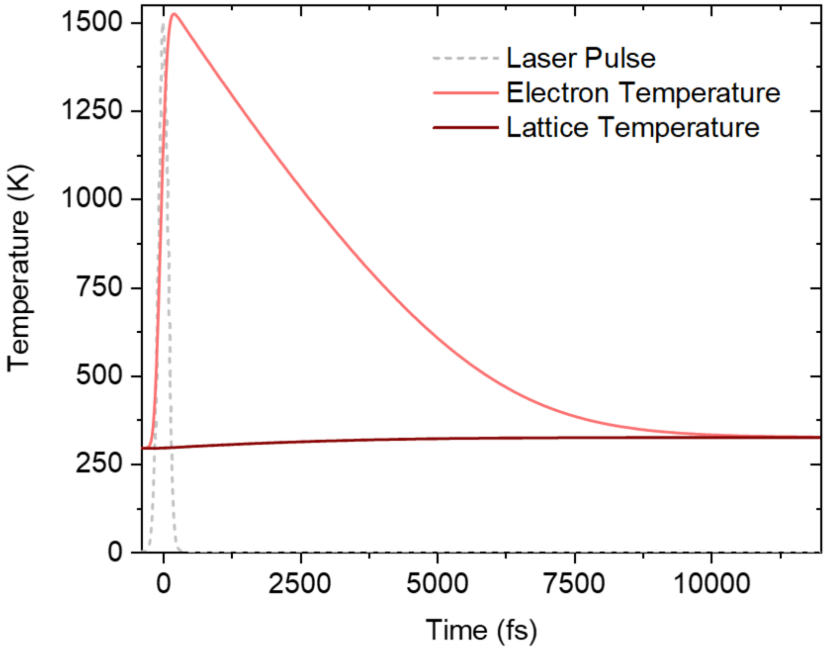

Figure 6.13: Two-temperature model of electron and lattice heating for a D = 20 nm, $L/D = 3$ nanorod. The peak lattice temperature increase is ∼30 K, while the conduction electrons have a pulse-averaged temperature of ∼1000 K (at the pulse peak) and reach an overall peak temperature of 1500 K a couple hundred femtoseconds following excitation, before thermalizing with the lattice on a few-picosecond timescale.

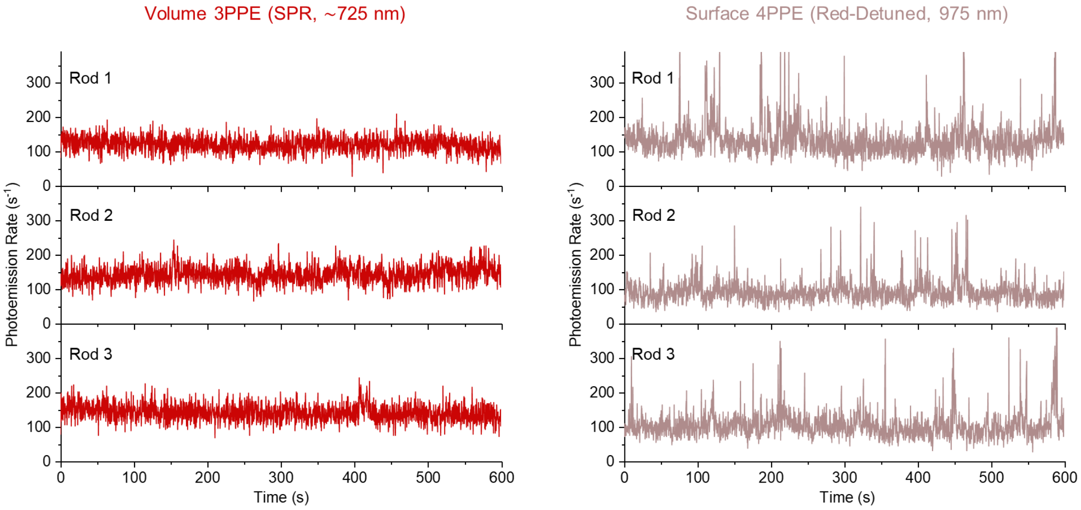

Figure 6.14: Volume (left) and surface (right) MPPE time traces for three typical nanorods.

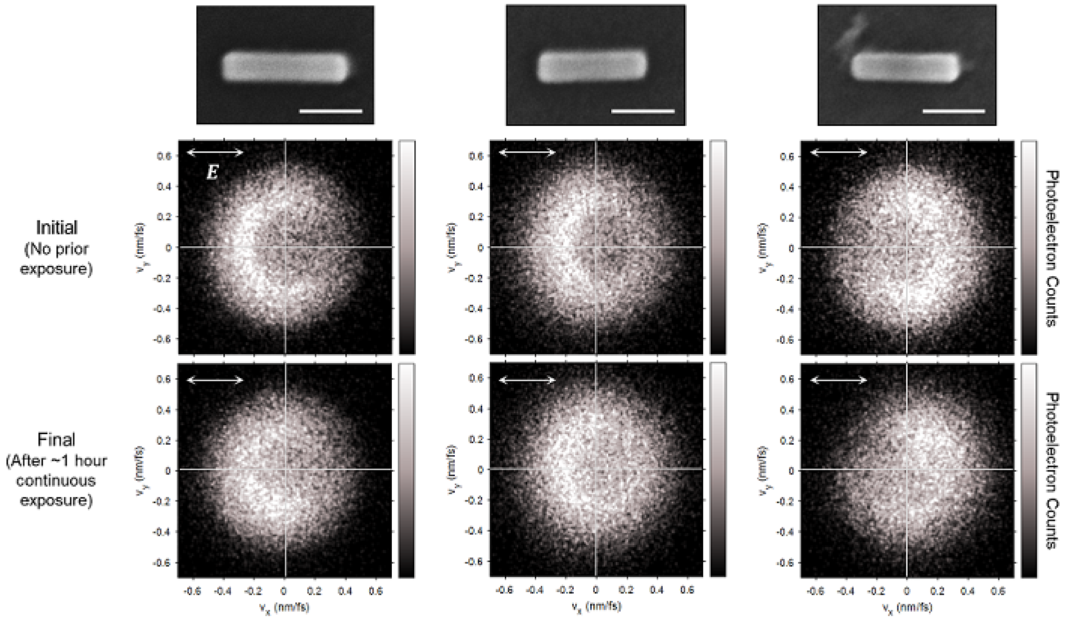

Figure 6.15: Typical changes observed in the surface MPPE velocity distributions following ∼1 hour of continuous laser exposure at typical intensities. All three $L/D \approx 4$ nanorods shown here are excited at 975 nm ($\approx SPR-$ 0.2 eV) in the 4PPE regime, with angular contrast $AC \approx 0$. Due to the limited detuning from resonance (∼0.2 eV), the distributions still have a notable transverse component superposed with the asymmetric longitudinal surface emission.

Thus, the role of experiment in determining the surface and volume photoemission contributions has been reduced to determination of this single $a^{(n)}$ parameter for a given process order, n.

Weighting the modeled surface and volume photoemission distributions by the field integral ratio from Fig. 6.8b, it is found that $a^{(3)} \approx 7.5$ pm ($\pm 50\%$) yields the best agreement with the experimental angular contrast as a function of detuning (Fig. 6.10c). The relative surface and volume contributions are now quantified, as shown in Fig. 6.10d, which indicates that volume processes account for 90% of the total photoemission on resonance. As suggested earlier, the 10% surface contribution on resonance accounts for the slightly less negative (less transverse) experimental angular contrast values in Fig. 6.5e relative to the purely volume Monte Carlo theory. With $\sigma_{\mathrm{S}}^{(n\mathrm{PPE})}/\sigma_{\mathrm{V}}^{(n\mathrm{PPE})}$ now determined and $\sigma_{\mathrm{S}}^{(n\mathrm{PPE})} + \sigma_{\mathrm{V}}^{(n\mathrm{PPE})}$ known directly from the total experimentally-measured photoemission rates (Eq. 6.2), $\sigma_{\mathrm{S}}^{(n\mathrm{PPE})}$ and $\sigma_{\mathrm{V}}^{(n\mathrm{PPE})}$ can be determined independently, as summarized in Fig. 6.10e for the representative nanorod. It is noted that $\sigma_{\mathrm{S}}^{(n\mathrm{PPE})}$ and $\sigma_{\mathrm{V}}^{(n\mathrm{PPE})}$ are only directly determined in the 3PPE range. While explicit $a^{(n)}$ values for other process orders could be determined via additional detuning studies, this investigation instead simply relies on the approximate continuity in experimental $\sigma_{\mathrm{S}}^{(n\mathrm{PPE})}/\sigma_{\mathrm{V}}^{(n\mathrm{PPE})}$ values (i.e. no sudden changes observed with detuning) from the $L/D \approx 3$ nanorod detuning studies in Fig. 6.10 to extend the 3-photon results into the adjacent 2- and 4-photon ranges. With the aid of finite element and Monte Carlo modeling of the geometry-specific quantities (field integrals and escape efficiencies, respectively), this now allows one, in principle, to quantitatively predict the volume vs. surface photoemission behaviors for arbitrary gold nanoparticle geometries.

6.4 General Design Principles

It has been shown that the plasmonic field enhancements are of primary importance in determining the relative surface and volume contributions to electron emission. With $a^{(3)}$ and therefore the material-specific properties in Eqs. 6.3 and 6.4 determined from detuning experiments, the effects of optical parameters and nanoparticle geometry on the relative contributions of surface and volume photoemission can now be quantitatively estimated, including the effects of (i) material screening, (ii) geometric surface-to-volume (S/V) ratio, and (iii) nanoparticle shape/curvature. In particular, it is demonstrated that optical parameters influence the relative surface versus volume contributions primarily via frequency-dependent screening, while the nanoparticle shape controls the plasmonic field distribution at constant excitation frequency. Direct results from the 3PPE range (Fig. 6.10) are again extended into the 2PPE and 4PPE ranges by approximate continuity in $\sigma_{\mathrm{S}}^{(n\mathrm{PPE})}/\sigma_{\mathrm{V}}^{(n\mathrm{PPE})}$, although this will negligibly affect the principles and conclusions discussed.

First, the effects of frequency-dependent screening and the plasmon resonance (Fig. 6.16a) on the surface vs. volume photoemission contributions are considered. Specifically, the plasmonic field enhancements and resulting $\sigma_{\mathrm{S}}^{(n\mathrm{PPE})}/\sigma_{\mathrm{V}}^{(n\mathrm{PPE})}$ ratios are simulated for ligand-free nanorods in vacuum, for a series of aspect ratios (Fig. 6.16a). In this purely vacuum environment, the surface field enhancements are more prominent and longer nanorods are predicted to be surface emitters on resonance, unlike the ligand-coated, ITO-supported nanorods studied experimentally. For nanospheres in the electrostatic approximation and $\boldsymbol{E}_0 = E_0\hat{x}$, the Laplace equation yields a constant internal field (Section 3.1.1)

$$\boldsymbol{E}_{\mathrm{in}} = \frac{3\epsilon_0}{\epsilon(\omega) + 2\epsilon_0} E_0\hat{x}. \tag{6.7}$$

As discussed in Section 3.1.1, the external-to-internal electric field ratio at the tip is given simply by

$$\left|\frac{E_{\mathrm{tip}}(\omega)}{E_{\mathrm{in}}(\omega)}\right| = \left|\frac{\epsilon(\omega)}{\epsilon_0}\right|. \tag{6.8}$$

The crucial result is that the plasmonic resonance term, $\propto \left(\epsilon\left(\omega\right) + 2\epsilon_0\right)^{-1}$, drops out of the field ratio in Eq. 6.8 entirely, leaving only with the screening effects described by the metal dielectric function, $\epsilon\left(\omega\right)$. Furthermore, the same cancellation of the surface and volume plasmonic field enhancements occurs in the full nonlinear field integrals, leading to $\sigma_{\mathrm{S}}^{(n\mathrm{PPE})}/\sigma_{\mathrm{V}}^{(n\mathrm{PPE})} \propto \left|\epsilon\left(\omega\right)/\epsilon_0\right|^{2n}$, as shown in Fig. 6.16a. It is thus concluded that the dramatic increase in surface over volume photoemission at longer wavelengths can be simply attributed to enhanced metallic screening of internal fields. At a constant excitation wavelength, the progressive overall drop in $\sigma_{\mathrm{S}}^{(n\mathrm{PPE})}/\sigma_{\mathrm{V}}^{(n\mathrm{PPE})}$ with increasing nanorod aspect ratio in Fig. 6.16a is due to details of the nanorod geometry and plasmonic field distributions.

Next,the effects of nanoparticle scale (Fig. 6.16b) on the surface vs. volume photoemission contributions are considered. The importance of the geometric S/V ratio has been emphasized in other investigations,[59] but it remained unclear whether this was truly the decisive factor, in general, due to the previous lack of direct mechanistic insight into the surface and volume excitation processes. Here, we effectively isolate the effect of S/V ratio by investigating nanorods with the same aspect ratio but different diameters, as in Fig. 6.16b. By maintaining the same shape, the field enhancement distributions and SPRs remain approximately constant with size, while the S/V ratio changes by three-fold, from 0.44 nm^{-1} ($D = 10$ nm) to 0.15 nm^{-1} ($D = 30$ nm). This factor of three is already relatively minor compared to the orders-of-magnitude changes in $\sigma_{\mathrm{S}}^{(n\mathrm{PPE})}/\sigma_{\mathrm{V}}^{(n\mathrm{PPE})}$ with modest detuning and the similarly strong shape-dependent effects to be discussed next. Moreover, a commensurate change in the volume emission efficiency with nanoparticle size, $1/\eta_{\mathrm{V}}^{(n)} \propto D$, effectively cancels the $S/V \propto D^{-1}$ contribution to $\sigma_{\mathrm{S}}^{(n\mathrm{PPE})}/\sigma_{\mathrm{V}}^{(n\mathrm{PPE})}$. This occurs for larger particles ($D \gg \lambda_{\mathrm{inel}}$) as the fraction of hot electrons excited within the escape depth from the surface ($\sim \lambda_{\mathrm{inel}}$) to the total number of electrons excited throughout the nanoparticle approaches the geometric S/V ratio,[189] such that the escape efficiency scales as S/V (i.e. $\eta_{\mathrm{V}}^{n)} \propto D^{-1}$). Thus, $\sigma_{\mathrm{S}}^{(n\mathrm{PPE})}/\sigma_{\mathrm{V}}^{(n\mathrm{PPE})}$ remains remarkably constant with nanoparticle scale at fixed excitation frequency, as shown in Fig. 6.16b. It is not until particle dimensions become comparable to or smaller than the hot electron inelastic mean free path that the $S/V \propto D^{-1}$ scaling begins to take over.[189] This $\sigma_{\mathrm{S}}^{(n\mathrm{PPE})}/\sigma_{\mathrm{V}}^{(n\mathrm{PPE})} \propto D^{-1}$ regime may nonetheless be relevant for low-energy hot electron catalysis (e.g. $\lambda_{\mathrm{inel}} \approx 40$ nm for gold at ~1.5 eV excitation energy) with small nanoparticles ($D < 30$ nm).

Finally, the effects of nanoparticle shape (Fig. 6.16c) on the surface vs. volume pho-

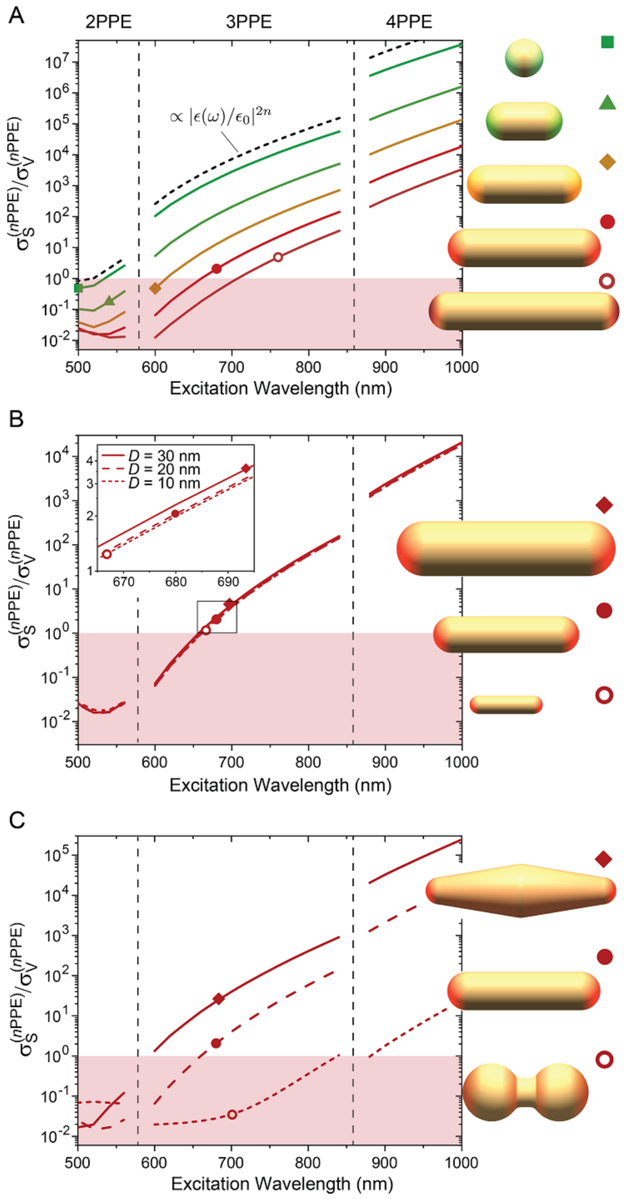

Figure 6.16: Effects of screening, S/V ratio, and nanoparticle geometry (curvature) on surface and volume contributions. This set of simulations is performed in vacuum (no ligands or substrate). Shading indicates the volume-dominated regime. (a) Surface/volume nPPE cross-section ratio determined quantitatively from detuning studies (Fig. 4) for $L/D = 1$–5 nanorods. Points indicate plasmon resonance wavelength. The dashed curve is the scaled dielectric function of gold, which determines the frequency dependence of the surface/volume cross-section ratios. (b) Cross-section ratio for $L/D = 4$ nanorod for $D = 10$–30 nm, with zoomed-in inset. (c) Cross-section ratio for bipyramid, nanorod, and dumbbell, all with similar resonance, S/V ratio (to within 10%), and total V (to within 30%).

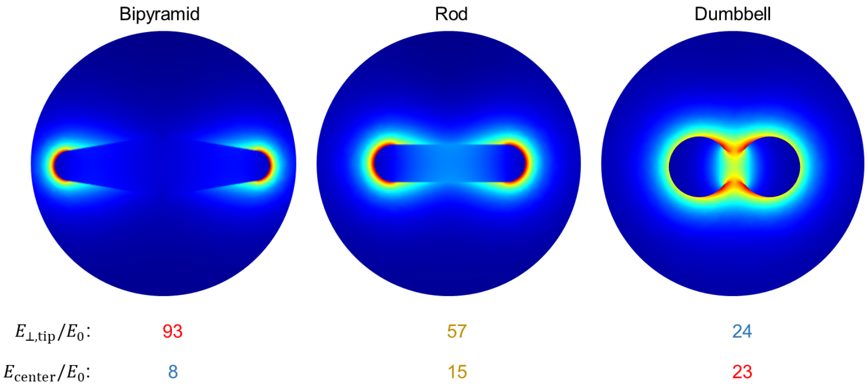

Figure 6.17: Slices of plasmonic field enhancements for bipyramid, nanorod, and dumbbell geometries with the corresponding surface-normal tip enhancements and total volume center enhancements noted. All geometries are simulated in a vacuum environment with no surface ligands.

toemission contributions are considered. While the effect of nanoparticle size/scale has been shown to be generally minor, the nanoparticle shape strongly influences $\sigma_{\mathrm{S}}^{(n\mathrm{PPE})}/\sigma_{\mathrm{V}}^{(n\mathrm{PPE})}$ via the plasmonic field distributions. Sharp convex features, for instance, can lead to more dramatic surface field enhancements due to the lightning rod effect,[108, 99] whereas flat or concave features can shift emphasis to the volume fields. Thus, we attempt to isolate the effects of nanoparticle curvature by comparing particles of different shapes but similar SPR, S/V ratio, and total volume (see Fig. 6.16c). Sharper-tipped geometries, such as bipyramids, have more concentrated surface field enhancements and more diffuse volume enhancements (Fig. 6.17), leading to an enhanced surface photoemission contribution. This is corroborated by observations of tip-localized photoemission from silver bipyramids,[118] and gold nanostars,[144, 77] and etched gold nanotips.[99] Conversely, more concave geometries such as dumbbells display much weaker surface fields and stronger relative interior field enhancements (Fig. 6.17), leading to a dramatically enhanced volume photoemission contribution.

Interestingly, the effect of shape on internal quantum efficiency, $\eta_{\mathrm{V}}^{(n)}$, is typically negligible. For example, $\eta_{\mathrm{V}}^{(3)} = 0.27\%$ for the $L/D = 4$ resonantly-excited nanorod in Fig. 6.16c, while $\eta_{\mathrm{V}}^{(3)} = 0.32\%$ for the dumbbell excited at nearly the same SPR frequency. The strong influence of nanoparticle shape on $\sigma_{\mathrm{S}}^{(n\mathrm{PPE})}/\sigma_{\mathrm{V}}^{(n\mathrm{PPE})}$ therefore arises from the shape-dependent distribution and concentration of plasmonic fields, rather than the volume escape efficiency. This has two significant benefits for designer plasmonic devices: (i) the plasmonic fields can be readily simulated by a variety of classical methods (e.g. finite element simulation), and (ii) a further degree of optical control—beyond frequency-dependent screening—can be readily exerted by coupling to different plasmon resonance modes via laser polarization and frequency. Different plasmon resonance modes will display different volume and surface field distributions, which has been utilized, for instance, to control photocurrents from gold nanostars with multiple tip hot spots associated with different plasmon modes.[144, 77]

In summary, the essential roles of nanoscopic volume vs. surface photoexcitation mechanisms in nanoplasmonic hot electron emission have been demonstrated, along with corresponding opportunities for designing and optically controlling hot electron spatial and momentum distributions. Volume excitation, which is dominant for nanorods excited at their longitudinal resonances, leads to hot electrons excited predominantly near the center of the nanorods in the centralized field-enhanced region, which subsequently escape from the nearby side surfaces in a transverse momentum distribution. However, red detuning of the excitation frequency strongly de-emphasizes the volume fields due to enhanced metallic screening, instead promoting hot electron excitation directly at the tip surfaces. The surface-excited electrons are preferentially emitted longitudinally along the nanorod axis and therefore exhibit completely different spatial and momentum distributions compared with the volume-excited hot electrons. Both processes are shown to be important in nanoplasmonic systems and must be accounted for in general. We have demonstrated that comprehensive volume (ballistic Monte Carlo) and surface (fully quantum) MPPE theory can be used to model these behaviors, but more importantly that the plasmonic field enhancement distributions (rather than the geometric S/V ratio or internal quantum efficiency, $\eta_{\mathrm{V}}^{(n)}$) are critical in controlling the surface vs. volume excitation. After characterizing the material-specific (nonlinear) absorbances, it was shown that the surface vs. volume photoemission properties of arbitrary gold geometries can be predicted simply via classical electrodynamics simulations. This introduces exciting opportunities for the design of hot electron catalysis and nanoelectronic devices, in which the geometry can be optimized to control plasmon mode structure and corresponding surface vs. volume distributions. Hot electron spatiotemporal distributions may then be controlled on nanometer spatial scales and femtosecond timescales via ultrafast optical frequency and polarization manipulation.[2, 144, 146]

6.5 Regulating Photocurrents with Mesoporous Silica Coatings

Another opportunity for controlling both volume and surface photocurrents, or complementing control schemes discussed herein, is to block emission from certain nanoparticle regions via anisotropic SiO_2 coatings. This effort is presently underway and is therefore only mentioned briefly as promising results emerge. While initial indications of insulating silica coatings blocking hot electron emission have been demonstrated,[184] this has now been shown unambiguously via SPIM photoemission studies, with the relevant transmission dynamics characterized. In particular, nanorods have been coated with both dense silica and mesoporous silica. “Mesoporous” silica actually has nanoscale pores of few-nanometer diameters that displace the surface ligands as the stabilizing agent on gold nanorods.[1, 53] Hot electrons excited in the gold nanorods travel through silica with few-nanometer inelastic mean free path, and thus photocurrents are substantially attenuated via dense silica, by orders of magnitude for relatively thin ($\sim$10 nm) silica coatings. Substantial attenuation also occurs through mesoporous silica, although the dynamics do not appear to be single-exponential and drop off much more slowly with coating thickness. This can be interpreted via a simple geometrical model in which hot electrons escape through the nanoscale porous channels that randomly form over the surface. As mesoporous silica can be nonuniformly coated on the nanorod tips, body, or otherwise, this provides an additional method for tailoring hot electron emission distributions, which can compliment nanoparticle geometric and optical control schemes discussed here with nanostars, nanorods, and nanoshells. These studies will illustrate both specific routes for such control, but also general opportunities for applying nonuniform insulating coatings to influence nanoplasmonic hot carrier photocurrents.

6.6 Continuous Angular Control over Nanoshell Photoemission

Emerging capabilities for ultrafast photocurrent control typically rely on tuning optical polarization and/or frequency to selectively excite one or more discrete hot spots defined by the particle geometry. By contrast, a unique case will now be introduced in which hot electron excitation and emission distributions can instead be continuously controlled via linear laser polarization in the azimuthal plane of a gold nanoshell supported on a substrate. In this configuration, it is the laser field that breaks the azimuthal symmetry of the supported nanoshell and determines the plasmonic field distribution. Using angle-resolved photoelectron velocity map imaging, it is found that the hot electrons are predominantly emitted orthogonal to the nanoshell dipolar surface plasmon resonance axis defined by the laser polarization. Furthermore, such anisotropic emission is only observed for nanoshells, while solid gold nanospheres are found to be isotropic emitters. All of these effects are recapitulated via simulation of the plasmonic electric field distributions within the nanoparticle volume and ballistic Monte Carlo modeling of the hot electron dynamics. These results demonstrate a highly predictive level of understanding of the underlying physics and possibilities for ultrafast spatiotemporal control over hot carrier dynamics.

The unique photoemission properties of gold nanoshells are clarified by comparison with gold nanospheres. Gold nanospheres (Fig. 6.18a) are purchased commercially (Nanopartz Inc.) with citrate ligands and average diameter 100 ± 4 nm (1σ standard deviation) characterized via transmission electron microscopy (TEM). Gold nanoshells (Fig. 6.18b) are also purchased commercially (nanoComposix) with lipoic acid ligands, total diameter 147 ± 5 nm, and silica core diameter 118 ± 4 nm characterized via TEM. While the nanosphere dipolar SPR position around 560 nm (Fig. 6.18c) is relatively insensitive to size, a well-known special property of gold nanoshells is the sensitive dependence of the SPR position on core/shell aspect ratio.[133, 93] In this case, the gold nanoshells have a typical dipolar SPR around 675 nm when supported on the ITO-coated glass substrate in vacuum or air, as demonstrated by the single-particle scattering spectrum in Fig. 6.18d. The multiphoton photoemission (MPPE) properties of gold nanoshells have been characterized in detail in Chapter 5, including a work function around 4.3 eV and a corresponding transition between the 2-photon photoemission (2PPE) and 3-photon photoemission (3PPE) regimes occurring around 2.15 eV excitation photon energy (580 nm). The nanospheres and nanoshells are studied on resonance in the 2PPE and 3PPE regimes, respectively, but we shall show that the excitation/emission properties depend primarily on the plasmonic field distributions, such that the angular photoemission behaviors do not fundamentally depend on process order. Therefore, the results presented here should be equally applicable down to the linear (1-photon) regime for lower-threshold-energy metal-semiconductor Schottky barriers or metal-molecule junctions.

While defect hot spots can be present on spherical nanoparticle surfaces and lead to strongly polarization-sensitive signals,[62] directional photoemission,[146] and exceptionally high surface-enhanced Raman scattering,[185, 67] we focus on defect-free nanospheres and nanoshells with minimal MPPE variation as a function of azimuthal linear polarization, demonstrated in Figs. 6.19a and 6.19b for the same particles as in Figs. 6.18c and 6.18d. The particles are therefore highly spherical, as any plasmonic field enhancements variation due to geometric anisotropy would be strongly amplified by the nonlinear photoemission process ($n\text{PPE} \propto |E/E_0|^{2n}$). Any anisotropy to be observed in the hot electron emission distributions can therefore primarily be attributed to symmetry breaking via the linear laser polarization and the corresponding nanosphere and nanoshell plasmonic field enhancement distributions. Furthermore, since the laser polarization only defines an axis rather than a specific direction, the projected (2D) photoelectron velocity distributions are expected to remain centrosymmetric.

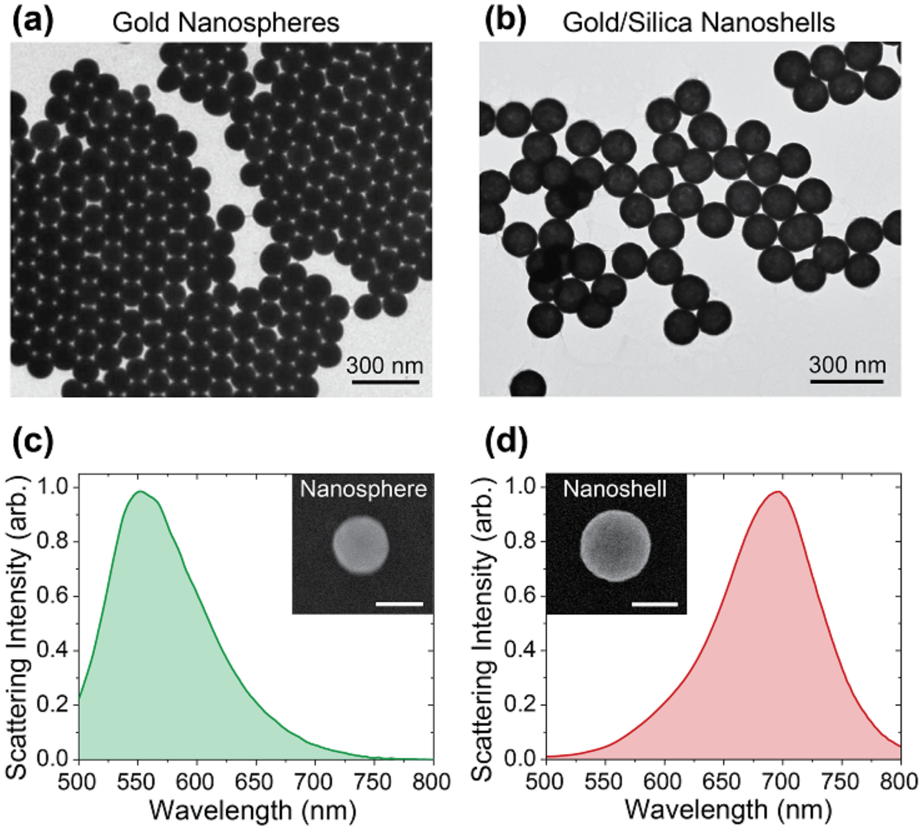

Figure 6.18: Gold nanosphere and nanoshell characterization. (a) Nanosphere and (b) nanoshell transmission electron micrographs. (c) Nanosphere and (d) nanoshell single-particle dark field scattering spectra showing the dipolar surface plasmon resonance peaks, with correlated scanning electron micrographs in the insets (scale bars: 100 nm). These two representative particles are utilized for subsequent correlated photoemission studies and simulations.

Photoelectron velocity maps in Figs. 6.19c and 6.19d for the representative nanosphere and nanoshell, respectively, show distinctly different behaviors. In particular, the nanosphere distribution is azimuthally isotropic while the nanoshell distribution is notably anisotropic with stronger photoemission orthogonal to the laser polarization axis. In both cases, the decrease in photoelectron counts near the center of the distributions is due to a surface-normal velocity weighting factor in the photoemission speed distribution (Section 3.5.2), which leads to a decrease in signal near the center of the 3D distributions that persists in the 2D projections, as will be reproduced in simulations. As expected, the anisotropic nanoshell photoemission distribution remains centrosymmetric.

To quantify the anisotropy, the angular contrast, AC, of the radially-integrated 2D angular distributions is again utilized (Eq. 6.1). Recall that the value of AC approaches $+1$ for highly longitudinal MPPE (parallel to the laser polarization axis) and -1 for highly transverse MPPE (orthogonal to the laser polarization axis). This simple quantification of the anisotropy is agnostic to any particular set of basis functions (e.g. Legendre polynomials) and should not be confused with the anisotropy parameter (β) in molecular photoionization studies,[178] as the nanoparticle photoemission distributions depend on the details of the plasmonic field distributions and hot electron emission dynamics. The nature of such distributions will instead be elucidated via simulations. The isotropic nature of the nanosphere photoemission observed in Fig. 6.19c ($AC \approx 0$), which has also been discussed in detail in Section 6.2, arises from the uniform dipolar field excited within a spherical conductor (Fig. 6.20a) and a volume-mediated photoexcitation/emission mechanism. Such volume MPPE mechanisms, along with the rather more interesting plasmonic field distributions within gold nanoshells that lead to the transverse photoemission observed in Fig. 6.19d ($AC = -0.18$), will now be discussed in detail. By comparing experimental MPPE velocity distributions with simulated surface vs. volume MPPE distributions, it shall be shown that volume mechanisms are unambiguously dominant in these studies.

Volume xy slices are shown in Figs. 6.20a and 6.20b for the two geometries (accounting

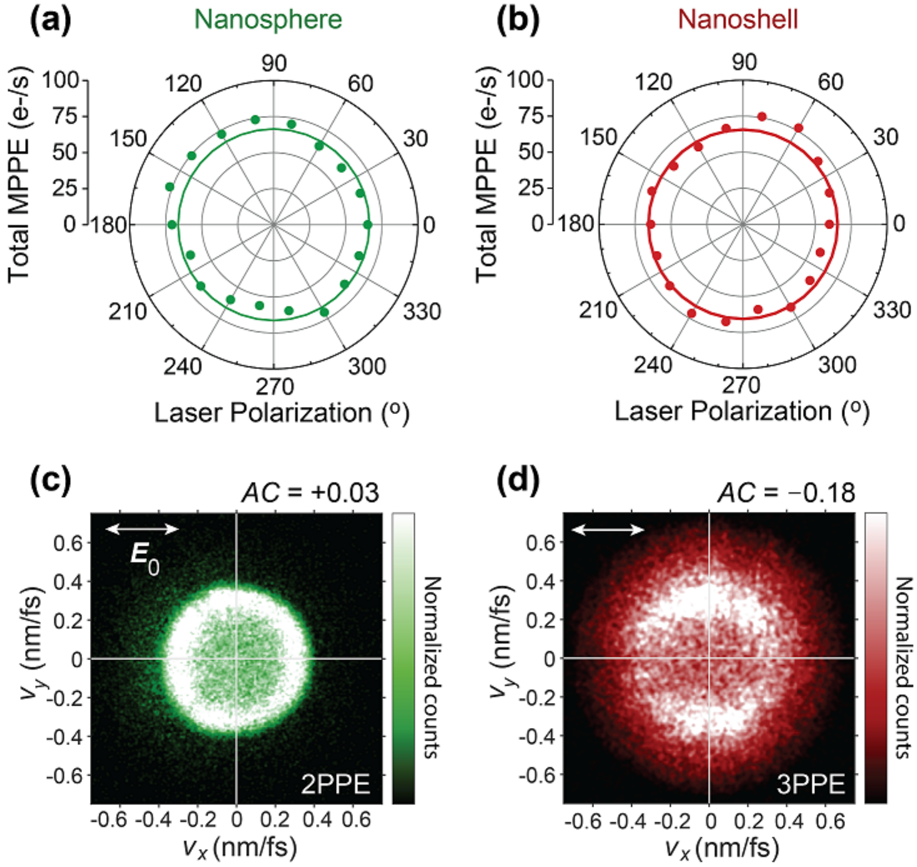

Figure 6.19: Photoemission properties of the representative correlated nanoparticles from Fig. 1. (a) Nanosphere and (b) nanoshell total MPPE rates as a function of linear laser polarization angle at peak input intensity $I_0 = 0.5\ \text{GW/cm}^2$ in both cases. Both particles are highly isotropic, displaying $\lesssim 10\%$ signal variation with laser polarization. The solid lines are the average MPPE rates as a reference. (c) Nanosphere photoelectron velocity map, showing largely isotropic photoemission ($AC \approx 0$) in the 2PPE regime. (d) Nanoshell photoelectron velocity map, showing predominantly transverse photoemission ($AC < 0$) relative to the polarization-defined dipolar SPR oscillation along the x axis.

for the ITO substrate in the simulations). The internal field distribution is highly isotropic for the nanosphere dipolar resonance. By contrast, the nanoshell internal field distribution is anisotropic and favors the shell regions transverse to the laser polarization and corresponding dipolar SPR axis. This is explained by the fact that the excited "bright" nanoshell dipolar mode (Section 3.1.3) consists of the core (i.e. gold void) dipolar oscillation in phase with the shell dipolar oscillation,[93, 151] as illustrated by the charge distribution in Fig. 6.20b. For this oscillation mode, the fields due to like charges destructively cancel for shell regions in close proximity to the polarization axis, while the fields arising from opposite charges further away from this axis around the transverse shell regions add constructively.

Isotropic internal sphere distributions vs. transverse internal shell distributions lead to isotropic vs. transverse hot electron excitation and emission, explaining the observed photoelectron velocity distributions. However, to further elucidate these dynamics, the ballistic Monte Carlo photoemission model is utilized (Section 3.5.1). Briefly, the uniform nanoparticle volume and surface meshes from finite element simulations are utilized to discretize the computational domain. Hot electrons are excited within a randomly-selected (but E^{2n}-weighted) volume element into a randomly selected (Fermi-Dirac-weighted) $\boldsymbol{k}$ vector, based on an assumption of uniform density of states and excitation matrix elements around the gold Fermi level. Hot electrons reach the surface with an exponential survival probability (6 nm inelastic mean free path around 4.5 eV excitation energy[88, 24]) and are transmitted with unit probability if they have sufficient surface-normal momentum to overcome the surface potential barrier, which is a suitable approximation assuming a smooth image potential barrier.[189] All downward-moving photoelectron are neglected by approximating them to be perfectly collected by the ITO substrate. Although the theoretical radial distributions require further modeling beyond the simple approximations of uniform density of states and transition matrix elements employed in this Monte Carlo modeling (i.e. first principles electronic structure theory[24, 129]), many of the essential features are already well reproduced.

The calculated volume-mediated photoemission distributions in Figs. 6.20c and 6.20d

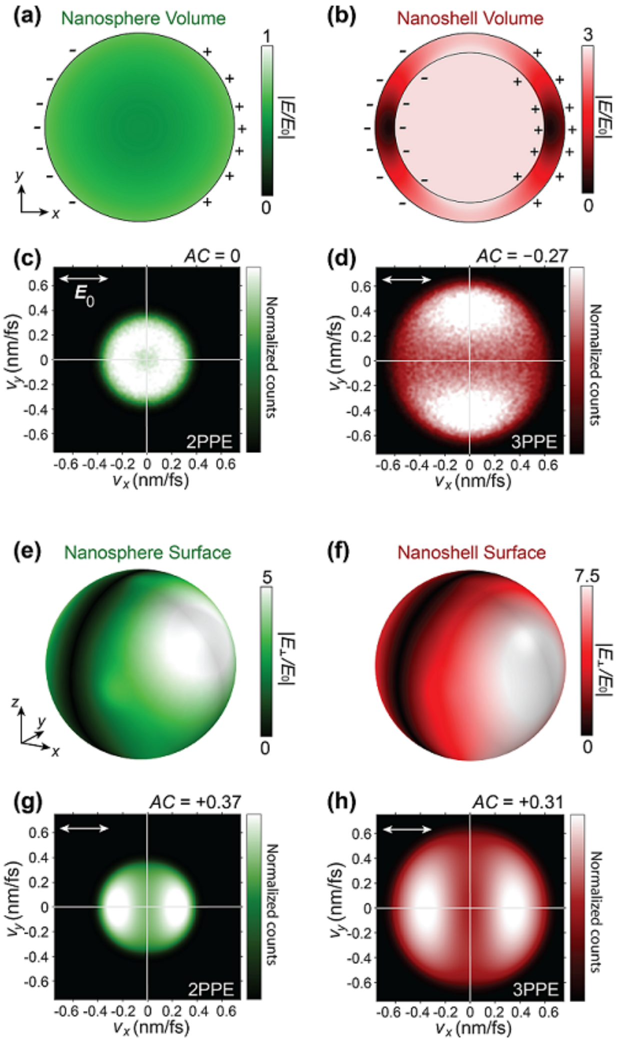

Figure 6.20: Simulated volume and surface plasmonic fields and corresponding photoemission distributions, with the laser polarized along the x axis. (a) Nanosphere and (b) nanoshell xy volume slices showing the simulated field enhancement distributions, with the corresponding volume-mediated photoemission distributions in (c) and (d), respectively, calculated via Monte Carlo MPPE modeling. As observed experimentally, the nanosphere distribution is isotropic ($AC = 0$), while the nanoshell distribution is peaked transverse to the laser polarization axis ($AC < 0$). (e) Nanosphere and (f) nanoshell surface-normal field enhancement distributions, with the corresponding surface-mediated photoemission distributions in (g) and (h), respectively, calculated via quantum MPPE modeling. In both cases, the surface-mediated photoemission is peaked along the laser polarization axis ($AC > 0$).

reiterate the essential behaviors observed in the experimental distributions (Figs. 6.19c and 6.19d)—i.e. isotropic nanosphere emission and transverse nanoshell emission. For comparison, the simulated surface field distributions are shown in Figs. 6.20e and 6.20f along with the corresponding longitudinal dipolar photoemission distributions calculated by implementing the surface-mediated MPPE theory of Yalunin and coworkers[203] for arbitrary nanoscale geometries, as described in Section 3.5.2. Such longitudinal photoemission distributions ($AC \gtrsim +0.3$) are completely different from the observed nanosphere ($AC \approx 0$) and nanoshell ($AC \approx -0.2$) distributions, confirming that volume rather than surface photoemission processes are dominant in these studies.

Now that the transverse nanoshell emission distributions are understood via the internal plasmonic field distributions and ballistic hot electron dynamics, it is shown that the angular distribution can be rotated continuously by the laser polarization. Unlike other demonstrations of photocurrent control where the nanoparticle geometry imposes its anisotropy on the hot electron emission distributions (e.g. nanostars, nanoshell defects, nanorods), the nanoshell emission anisotropy is completely determined by the linear laser polarization axis and can thus be continuously rotated in the azimuthal plane for the normal-incidence light (Fig. 6.21). Setting aside substrate effects, the 3D distributions corresponding to the 2D projections in Fig. 6.21 are approximately cylindrically symmetric about the laser polarization axis, such that the hot electrons are emitted from the top of the nanoshell (and bottom, if reflected rather than collected by the ITO) as well as from the sides, all transverse to the laser polarization. Thus, rather than localized hot spot emission, the photoelectrons originate throughout the gold shell volume. Nonetheless, the plasmonic volume fields and corresponding hot electron distributions can still be controlled to a high degree via the optical excitation parameters, as demonstrated by the continuous polarization-dependent angular control. In general, the spatial resolution for controlling such volume processes is defined by the inelastic mean free path.

These results illustrate new capabilities for continuous photocurrent control as op-

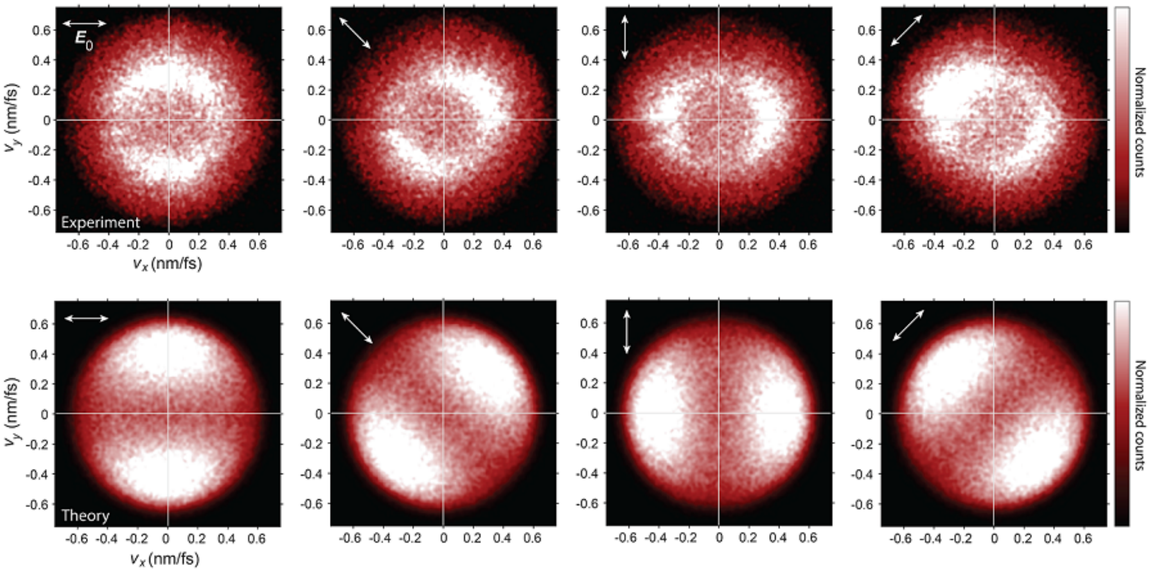

Figure 6.21: Continuous polarization-controlled nanoshell photoemission rotation over the full azimuthal range. Experimental (top) and theoretical (bottom) photoelectron velocity distributions for the representative correlated nanoshell, at a series of linear laser polarizations. The experimental (theoretical) peak photoemission axes are along 87° (90°), 41° (45°), $-3°$ (0°), and $-45°$ ($-45°$), as determined via approximate sinusoidal fits. The peak photoemission is therefore transverse/orthogonal to the laser polarization axis, with constant $AC \approx -0.2$ in each case.

posed to discrete hot spot selectivity, along with the essential role of volume excitation in some nanoplasmonic systems and simple methods for predicting the photoemission distributions via classical plasmonic field simulations and ballistic Monte Carlo modelling. While it has clearly been shown that volume MPPE mechanisms are predominant in the isotropic nanoshell data herein, surface MPPE mechanisms would lead to similar opportunities for continuous angular control over photoemission from nanoshells as well as nanospheres (Fig. 6.20). Furthermore, at higher laser intensities, strong-field processes would yield surface emission along the dipolar SPR axis, similar to demonstrations with gold nanorods[74, 106] and dielectric nanospheres.[181] Furthermore, while we only study the gold nanoshell dipolar SPR here, the quadrupolar resonance mode has a different internal field distribution and will thus produce different hot electron spatial and momentum distributions. This provides both a frequency as well as a polarization "control knob" in these nanoplasmonic systems for ultrafast manipulation of hot electron spatial and momentum distributions.

To summarize this section, it has been shown that gold nanoshells are volume photoemitters when excited at their dipolar SPRs, yielding transverse anisotropic photoemission distributions relative to the linear laser polarization axis. The anisotropic photoemission can be continuously rotated in the azimuthal laser polarization plane due to the spherical symmetry of the nanoshell, demonstrating new opportunities for optical control over hot electron photocurrents and/or charge injection into nearby molecules for plasmonic photocatalysis. These results compliment other emerging capabilities for designing and actively controlling nanoscale hot carrier dynamics via plasmonic hot spot selectivity or anisotropic nanoparticle coatings. In the present case, since polarization can be rotated/shaped on femtosecond timescales, these results represent another step toward coherent photochemistry, spatiotemporal electron waveform control for imaging, and ultrafast nanoelectronics.

Chapter 7

Ultrafast Time-Resolved Velocity Map Imaging

The ultrafast dynamics of nanoplasmonic hot carriers have been previously investigated via optical measurements[69, 10] and by photoemission measurements.[15] Optical measurements may be simultaneously sensitive to both hot carrier and lattice thermalization processes, providing a broad view of dynamics in the nanoparticle following laser excitation. These techniques, however, yield limited information on hot electron-electron thermalization and cannot directly resolve dynamical lifetimes as a function of excitation energy. Without energy resolution, these experiments can only assign a single-exponential decay time to the highly energy-dependent, many-exponential decay dynamics of the hot carriers, with the slowly-decaying hot carriers at the lowest excitation energies therefore disporportionately emphasized. Furthermore, these low-energy ("warm") carriers are of limited importance to hot carrier devices due to their inability to overcome surface barriers or activation energies. Unlike optical measurements, photoemission techniques can readily incorporate energy resolution for a more detailed view of femtosecond hot carrier dynamics.[14] Furthermore, photoemission techniques specifically probe the initial hot carrier thermalization step with limited sensitivity to the subsequent energy cascade, which can be a feature for these studies.

Although optical studies of dynamics in single metal nanoparticles have become more common in the past couple decades,[139, 37, 209, 10, 33] few pump-probe photoemission dynamics studies with single-nanoparticle resolution on femtosecond hot electron dynamics have been performed to date. Single-particle studies are essential to obtaining the most relevant, detailed understanding on nanoparticle properties, and now set the benchmarks that guide nanoparticle design. This not only eliminates inhomogeneous broadening that plagues all ensemble measurements, but also has the potential to reveal new insights that would otherwise be averaged over or concealed. Clearly, single particle studies are also necessary for angle-resolved velocity resolution.

The essential goal is to understand how fast hot electrons in the relevant excitation energy range (for emission/collection/injection/transfer) decay, and by what mechanisms. This will yield fundamental insight into hot carrier dynamics, while also providing practical guiding principles for designing nanoparticle geometries to promote efficient escape in the locations/directions desired. This serves to compliment the angle-resolved photoemission measurements and modeling in previous chapters, now directly resolving the relevant dynamical lifetimes and corresponding energy-dependent inelastic mean free path, rather than relying on bulk gold quantities. To learn as much as possible about the dynamics relevant to all hot carrier applications, therefore, time- and energy-resolved photoemission measurements are performed here on single gold nanorods.

7.1 Femtosecond Pump-Probe

Single gold nanorods ($L/D \approx 4$, $D = 10$ nm) are studied via pump-probe excitation, with the pump-probe time delay controlled with femtosecond resolution by means of a translation stage in the pump beam path (Section 2.9). With a clear pump-probe signal peak observed in the time delay scan, it is first necessary to verify the process taking place during pump-probe illumination of the nanorods, whether a simple two-photon pump-probe process or a more complicated higher-order process. To this end, pump-probe intensity-dependence measurements are performed on an individual nanorod (Fig. 7.1a), in which the pump or probe beam intensity is held fixed while the other is varied. The linear proportionality of signal to intensity obsered in each case indeed describes a simple $1 + 1'$ pump-probe photoemission process, where the prime simply denotes the different photon energy. Linear polarization dependence studies on the same representative nanorod are shown in Fig. 7.1b, demonstrating that the single-color (pump) multiphoton photoemission (MPPE) signal is enhanced by orders of magnitude when the pump polarization is aligned along the resonant longitudinal plasmon axis. Perhaps more suprising is that this is the case for the probe-only (400 nm) polarization dependence as well, despite being closer in energy to the transverse plasmon resonance ($\sim$ 500 nm). The implication is that the pump and probe beams must both be aligned along the longitudinal rod axis for appreciable pump-probe signal, which unfortunately precludes the ability to perform cross-polarized studies to avoid any coherent artifact effects,[143] to be discussed later. Additionally, these polarization behaviors establish that effectively all interactions are plasmon-mediated, with no observable contribution from direct absorption. If direct absorption had any appreciable effect, there would be non-negligible signal for polarization along the transverse plasmon axis.

By varying the time delay between the pump and probe pulses, hot electron dynamics following plasmonic excitation can be temporally resolved. For Gaussian laser pulses, the cross-correlation between the pump and probe pulses will also be Gaussian and represents the instrument response function (IRF), assuming an instantaneous system response. If the response of the system is not effectively instantaneous, due to hot carrier dynamics that persist on timescales approaching or exceeding (i.e. not much less than) the IRF width, then the pump-probe cross-correlation will instead represent the IRF convolved with the impulse response of the system. An example impulse response due to a 30 fs exponential decay process is shown in Fig. 7.2a. So far without energy resolution, this effective exponential decay time represents the average lifetime of hot electrons over the relevant excitation energy range ($\sim$1–2 eV). Furthermore, both the forward process (pump before probe) and reverse process (probe before pump) must be accounted for, which is why any dynamics in a single-color pump-probe experiment result in symmetric broadening of the IRF.[14] In two-color experiments, however, the forward and reverse processes are fundamentally different, and the cross-correlation will generally be asymmetric. It will be shown that the hot electron

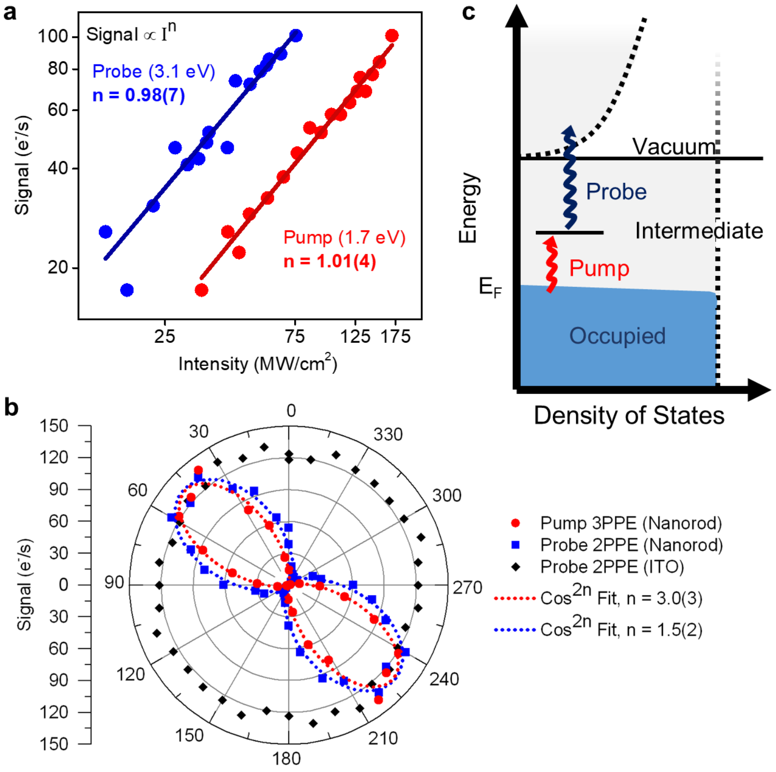

Figure 7.1: (a) Pump-probe intensity-dependence measurements, demonstrating the 1 + 1' excitation. (b) Individual pump and probe azimuthal polarization-dependent MPPE signals. (c) Incoherent pump-probe photoemission pathway through population of intermediate states.

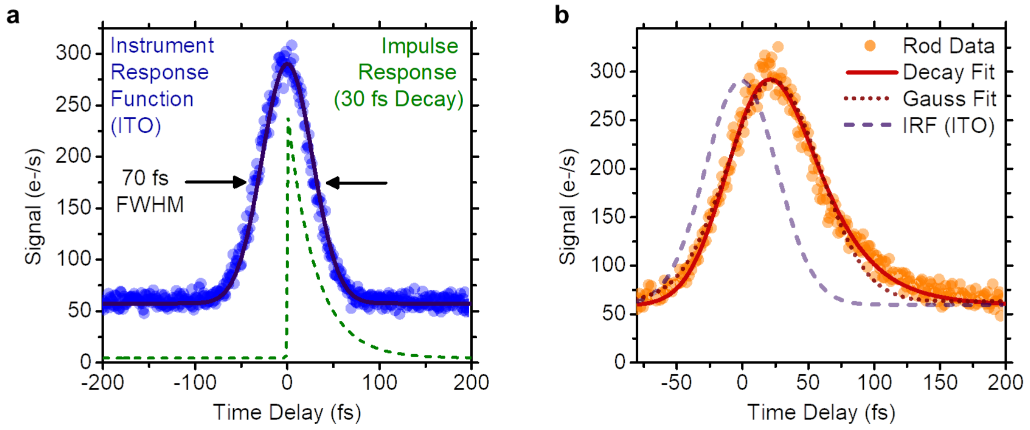

Figure 7.2: Pump-probe time delay scans. (a) Instrument response function measured on the ITO substrate, with an example nanoparticle impulse response (dashed line), the convolution of which yields (b) the nanoparticle delay scan with ∼35 fs forward decay time.

lifetimes drop off precipitously with excitation energy, such that probe-excited hot electrons (3.1 eV) will decay much more quickly than pump-excited hot electrons (1.8 eV) and the reverse decay will be essentially negligible.

The ITO substrate is utilized to measure the system IRF. A cross-correlation measurement on the ITO substrate, shown in Fig. 7.2a, appears highly symmetric and is fit well by a single Gaussian peak. The high degree of symmetry in Fig. 7.2a indicates that either (i) no dynamics are taking place in the ITO on timescales greater than the lower resolvable limit of ∼15 fs, or (ii) dynamics are taking place nearly symmetrically for the forward and reverse processes. It is also possible that (iii) asymmetric pump or probe pulse shapes are effectively compensating for the dynamics and thereby masking them—but it is much less likely that this would happen to be the case. This will be ruled out completely in future studies on Pd films, known to have negligible hot carrier lifetimes.[14] As noted above, case (ii) can be ruled out given the very different photon energies involved: In the reverse process the 3.1 eV probe beam generates a highly-excited hot electron distribution, of which only the hottest can energetically be photoejected by the pump beam. From previous studies in films it is known that highly excited electrons in the 3 eV excitation energy range decay very quickly, on timescales of a few femtoseconds.[88, 102, 24] Although no studies have been performed on ITO, these same studies on various metal films yield lifetimes of ¡ 10 fs even for excitation in the forward-process pump energy range, and therefore case (i) is most likely. In either case, this cross-correlation on ITO sets an upper bound on the width of the IRF, and from the preceding considerations would at most lead to a modest systematic decrease in any decay times measured for hot electrons in gold nanorods.

With the preliminaries established, dynamics are now investigated in gold nanorods. The cross-correlation of a single nanorod shown in Fig. 7.2b deviates notably from the IRF, being both wider and clearly asymmetric, with a tail-off toward positive time delays. As a guide to the eye, the best Gaussian fit is also shown in Fig. 7.2b, which overshoots at negative time delays and undershoots appreciably at positive delays – consistent with a forward exponential decay process. While a Gaussian clearly does not capture the true behavior, the convolution of the two functions in Fig. 7.2a, with the IRF fixed and the exponential decay left floating, fits the data well. The exponential time constant extracted from the fit in Fig. 7.2b is 35 fs. The timescale of this decay is similar to that of hot electron lifetimes measured in gold films for the same 1–2 eV excitation energy range.[14] It should again be noted that this single-exponential fit is merely an approximate average of the energy-dependent (and process-dependent) decay lifetimes. While these measured decay times represent some combination of hot electron lifetimes (T_1) for incoherent pump-probe excitation (i.e. populating intermediate states) and plasmon dephasing times (T_2) for coherent excitation, the measured 35 fs decay times are much longer than the < 10 fs plasmon dephasing times and can therefore be confidently assigned to hot electron lifetimes.

7.2 Time-Resolved Velocity Map Imaging

Combining time and energy resolution for a more complete characterization of the hot electron dynamics, 2D velocity maps are measured as a function of pump-probe time delay. Approximating cylindrically-symmetric photoemission about the nanorod long axis, the 3D

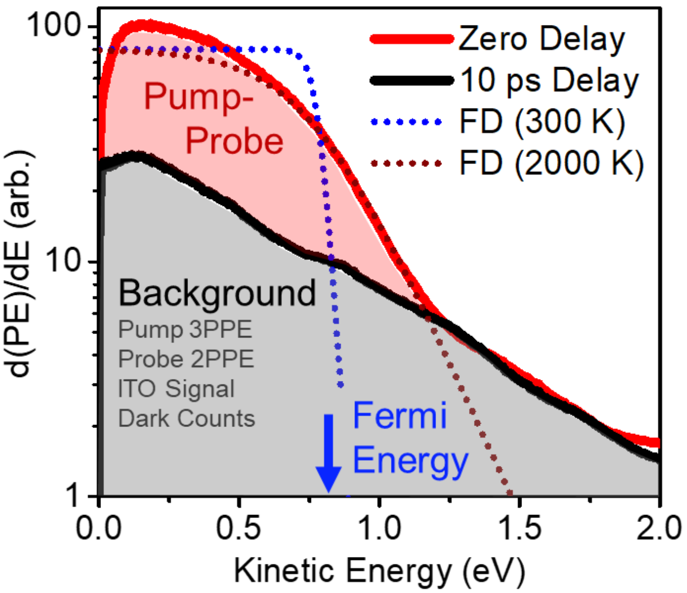

Figure 7.3: Angle-integrated 3D-reconstructed kinetic energy spectrum for a gold nanorod on (red; pump-probe) and off (black; background) the pump-probe delay peak. Pump-probe nanorod 2D velocity distributions are similar to those shown previously in Chapter 6 for single-color MPPE and are thus not shown here. The gradual Fermi edge indicates an elevated electron temperature around 2000 K.

distributions are reconstructed via the BASEX inverse Abel transform algorithm (Section 3.6.1). Kinetic energy distributions are then determined by integrating over the angular distribution, as shown in Figs. 7.3 and 7.4a. The pump-probe signal in Fig. 7.4a is shown decreasing from its optimal value at a +30 fs delay to the non-pump-probe background distribution at large positive time delays. An example energy slice at 0.5 eV above the vacuum level is demonstrated in Fig. 7.4b. By fitting the cross-correlation at each energy bin to an exponential decay, the hot electron lifetimes are determined as a function of excitation energy (Fig. 7.4c). The results appear linear on a log-log scale, indicating a power-law behavior in the probed energy range, where a power-law fit yields an inverse quadratic dependence of the lifetime on the excitation energy in the excitation energy range observed, with good agreement over four different rod measurements. A simple physical model for this behavior, along with the implications for hot electron dynamics, are considered in the next section.

7.2.1 Fermi Liquid Theory Behavior

A simple physical model for the observed inverse-quadratic dependence of the hot electron lifetimes on excitation energy is due to Fermi's Golden Rule. The derivation itself is straightforward, and is discussed in a number of places.[14] The essential idea is illustrated in Fig. 7.5a, in which a hot electron with energy E has a number of states proportional to $E - E_{\mathrm{F}}$ (Fermi level E_{F}) available to decay into during an inelastic electron-electron scattering event. This proportionality relies on the joint density of states (DOS) being approximately constant in this excitation range, and also requires that the number of filled hot electron states is much smaller than the number of available states, or that the filling of hot electron states is also approximately constant in this energy region. These approximations will be examined below. Conversely, the number of cold Fermi sea electrons that can be excited above the Fermi level during the inelastic collision is also proportional to $E - E_{\mathrm{F}}$, under the same assumptions. Therefore, making a final approximation of constant transition dipole

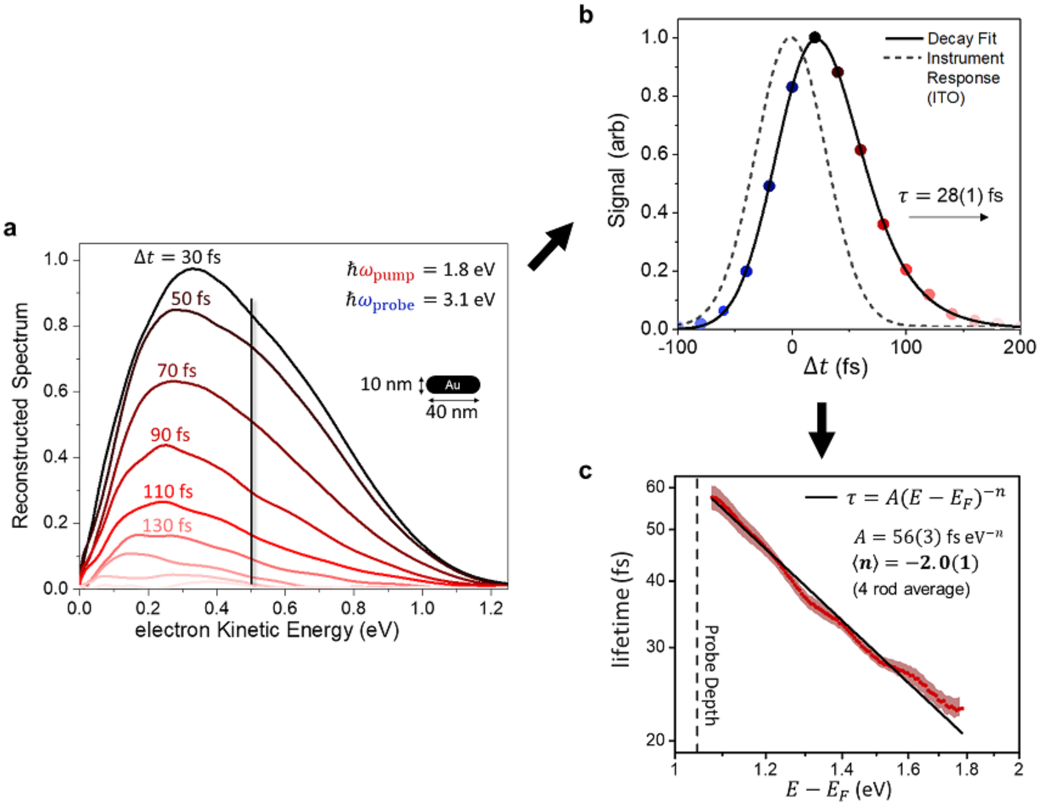

Figure 7.4: Energy-dependent hot electron lifetimes in a single gold nanorod. (a) Background-subtracted kinetic energy spectra as a function of pump-probe delay time. (b) Pump-probe delay scan at energy slice indicated in (a). (c) Summary of fit decay times as a function of excitation energy, shown on a log-log plot with a power-law fit yielding clear inverse quadratic Fermi liquid theory behavior in this excitation energy range.

matrix element for all of the excitations, then Fermi's Golden Rule yields[111]

$$\frac{1}{\tau_{e-e}} \propto (E - E_{\mathrm{F}})^2 . \tag{7.1}$$

The last assumption is known as the random-k approximation, which has been shown to be in good agreement with more detailed calculations.[218] The assumption of a constant DOS within the pump photon energy to either side of the Fermi level is quite reasonable for the gold 6*sp* band.[29]

7.2.2 Hot Electron Decay Processes

While the simple Fermi liquid theory lifetime behavior provides strong evidence for a predominant hot-cold electron-electron scattering decay channel (also well-known to be the predominant hot carrier decay channel in many metal systems [14]), other processes may contribute to the hot electron lifetimes and should be examined. Alternate depopulation channels include inelastic scattering between two hot electrons (Fig. 7.5b), electron-phonon scattering (Fig. 7.5c), and charge transfer to the ITO (Fig. 7.5d). These channels modify the hot electron lifetime in a straightforward manner via Mattheissen's rule:

$$\frac{1}{T_1} = \frac{1}{\tau_{e-e}} + \frac{1}{\tau_{\mathrm{ITO}}} + \frac{1}{\tau_{e-\mathrm{ph}}} + \frac{1}{\tau_{e-e,\mathrm{hot}}}, \tag{7.2}$$

where τ_{ITO} represents a spatially-averaged charge transfer lifetime from nanorod to ITO, $\tau_{e-\mathrm{ph}}$ is the electron-phonon scattering time, and $\tau_{e-e,\mathrm{hot}}$ is the scattering time for two hot electrons, all as a function of energy. If additional population of an excited state occurs subsequent to the pump excitation (i.e. via in-filling from higher excited states), the population dynamics of that energy level can no longer be modeled by such a simple exponential decay and the full kinetics must be accounted for. Auger effects that have previously been observed to affect lifetimes in bulk gold[14] are due to excitation of d-band holes, which does not occur here due to a pump photon energy (1.8 eV) that is just below the d-band threshold energy of gold (Chapter 4). The various population and depopulation processes will now be considered, with additional experimental evidence to indicate the importance of each.

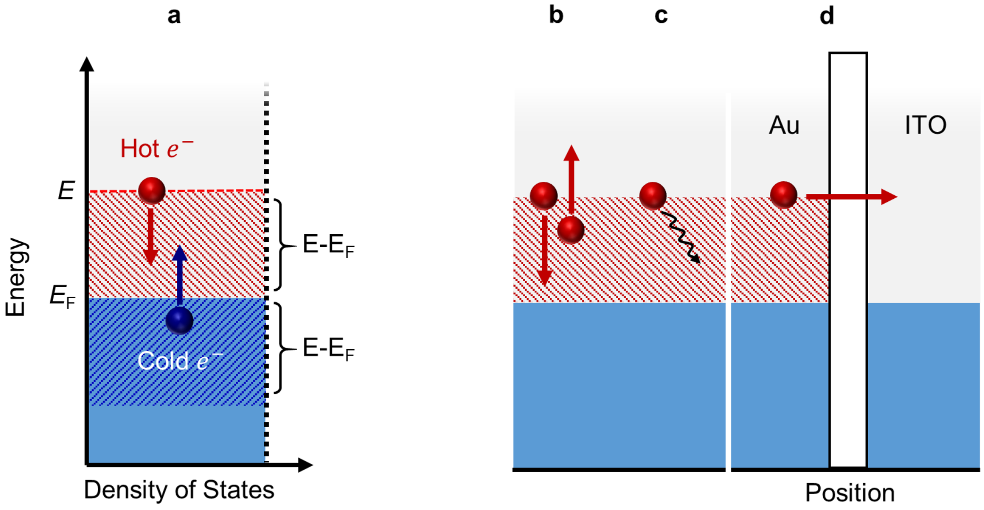

Figure 7.5: Various hot electron decay pathways. (a) Hot-cold electron-electron inelastic scattering, (b) hot-hot electron-electron scattering, (c) electron-phonon scattering, and (d) charge transfer to the ITO substrate.

Scattering between two hot electrons (Fig. 7.5b) is generally not considered due to the low density of hot electrons excited relative to cold electron bath. However, in nanoscale particles with exceedingly high absorption cross-sections due to plasmon-mediated excitation, hot electrons can begin to make up a significant fraction of the relevant conduction band population. In particular, finite element calculations of gold nanorods supported on ITO yield peak absorption cross-sections around 2×10^{-10} cm^2 at the plasmon resonance. For peak pulse intensities around 100 MW/cm^2, corresponding to 2×10^{13} photons/pulse/cm^2 at the pump photon energy, around 4×10^3 hot electrons are excited with each pump pulse. From bulk gold densities and a valency of one electron per atom, the 10×40 nm nanorods have approximately 1.5×10^5 conduction electrons, of which about a third are within a pump photon energy of the Fermi level. With hot electrons therefore approaching 10% of the relevant electron population for scattering, electron-electron scattering between two hot electrons should be taken into consideration. The signature for this second-order kinetic process is a decay rate that depends upon the hot electron population, and the significance of this mechanism is therefore testable by measuring lifetime as a function of pump beam intensity. Such a measurement is shown in Fig. 7.6 for a single nanorod, which reveals that no statistically-significant shift in the average hot electron lifetime occurs with increasing pump intensity. Furthermore, the energy dependence expected of this process would be $(E - E_\mathrm{F})^{-1}$ instead of the observed $(E - E_\mathrm{F})^{-2}$, based on similar considerations as with hot-cold electron-electron scattering, but in this case the second hot electron that gets excited during scattering originates from anywhere between E_F and $(E_\mathrm{F} + h\nu_\mathrm{pump})$ regardless of the other hot electron's energy. Therefore, the second factor of $E - E_\mathrm{F}$ is replaced by a constant factor, $h\nu_\mathrm{pump}$. From both of these experimental observations it is evident that, despite the possibly large densities of hot electrons excited in a nanorod, the inelastic scattering between two hot electrons still does not contribute appreciably to the population dynamics.

Electron-phonon scattering (Fig. 7.5c) occurs on ∼30 fs timescales comparable to electron-electron scattering[4] but is considered quasi-elastic, because on average it only

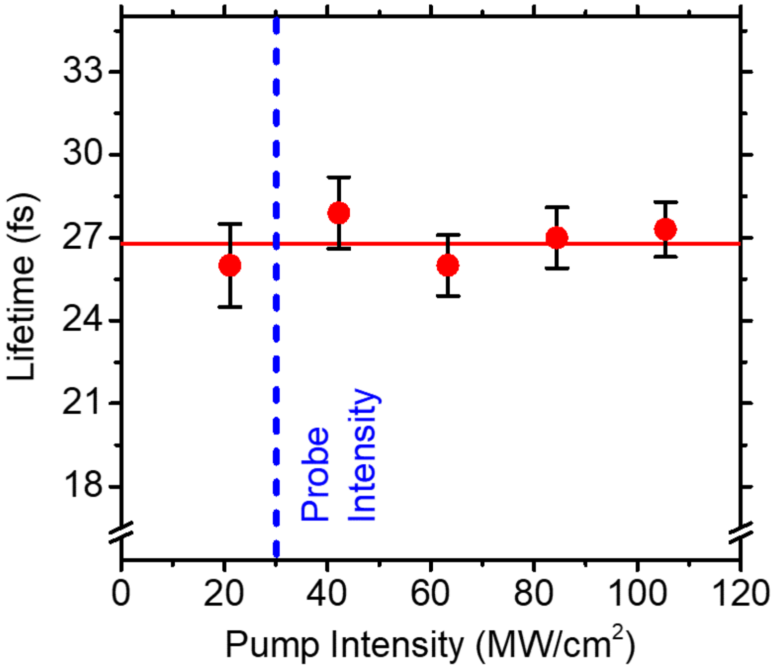

Figure 7.6: Effect of pump beam intensity (and thus hot carrier population and heating) on measured average hot electron decay time. No effect is observed within the experimental uncertainty.

decreases the hot electron excitation energy by 10 meV of so. This is less than the experimental energy resolution and therefore multiple electron-phonon scattering events must occur to constitute an effective change in population for a given energy level. Furthermore, the electron-phonon scattering cross-section depends only weakly on energy, such that all but the highest excited energy levels would be repopulated via electron-phonon cascading at approximately the same rate that they are depopulated, effectively nullifying contributions to the lifetime. The lifetime energy-dependence results in Fig. 7.4c confirm experimentally that electron-phonon scattering has little effect on the lifetimes, else an energy-independent contribution and therefore deviations from the Fermi liquid theory behavior would be expected.

In previous studies of Ag metal nanostructures on graphite,[149] charge transfer between the particle and the substrate (Fig. 7.5d) was found to have a substantial effect on hot electron lifetimes. Charge may either be transferred to or from the substrate, although the much stronger absorption and higher densities of hot electrons in the metal nanoparticles would strongly push the equilibrium in favor of transfer *to* to substrate. The magnitude and energy-dependence of charge transfer is determined by the shape of the tunnel barrier between the nanorods and the ITO, which is due to the organic CTAB spacer layer. Although the shape of the tunnel barrier is not precisely known, there is little expectation that it would yield an $(E - E_{\mathrm{F}})^{-2}$ tunneling probability rather than the exponential tunelling energy dependence for an energy-independent barrier width. Therefore, again invoking the observed inverse-quadratic energy dependence of the lifetimes, it is unlikely that charge transfer is affecting the hot electron dynamics. While this is evidently a negligible effect in the present studies, promoting charge transfer from nanoparticles to a substrate or surrounding semiconductor medium is of substantial interest for photovoltaics and photodetection. Thus, these sorts of studies hold promise for identifying and optimizing such dynamics in systems with stronger transfer characteristics.

Having already discussed the lack of hot electron cascading effects (in-filling of lower energy levels) due to electron-phonon scattering, along with inelastic electron-electron scattering between two hot electrons, any remaining cascading effects are attributed to inelastic electron-electron scattering between hot and cold electrons. Assuming constant DOS and transition dipole matrix element, hot electrons lose half of their excitation energy to an electron-electron scattering event on average,[159] and therefore only states near or less than half of the maximum excitation energy ($h\nu_{\mathrm{pump}}$) will be affected by cascading.[97] Considering the nanorod work function of ∼4.3 eV and the probe photon energy of 3.1 eV, only electrons with $(E - E_{\mathrm{F}}) \gtrsim h\nu_{\mathrm{pump}}/2 = 0.9$ eV are probed in these experiments, and therefore the cascade process should only play a minor role in the measured lifetimes of the lowest-energy hot electrons probed. In the lifetime energy-dependence measurements this would manifest as a small curl-up at lower energies, which is not observed in Fig. 7.4c.

7.3 Discussion

Having excluded all other population and depopulation processes, it would appear that the primary mechanism for hot electron decay in the probed excitation energy range is indeed hot-cold electron-electron scattering, described via Fermi liquid theory. Auger effects are precluded by the fact that the maximum hot carrier energies (i.e. pump photon energies), are insufficient to promote $5d$-band electrons above the Fermi level, which requires ∼2 eV, and indeed full energy transfer in this manner is unlikely. It is also found that little additional excited population is generated in the probed energy range following the pump excitation, and therefore the measured hot electron lifetimes directly reflect τ_{e-e} rather than any additional in-filling kinetics in the energy range of interest. While these studies do not reach all the way down to the Fermi level, the 1–2 eV excitation range studied is particularly relevant for photocatalysis and photovoltaics, in which such energies are required for the hot electrons to overcome the Schottky barrier or transfer into an admolecular energy level. Correspondingly, the hot electron lifetimes have been directly *fit* (rather than compared with models) and shown to have a very precise inverse-quadratic dependence on the excitation energy, which is predicted by simple Fermi's Golden Rule arguments. These results provide enticing indications of opportunities for full time-resolved 3D velocity mapping capabilities for detailed characterization of hot electron dynamics in complicated nanoplasmonic and other nanoscale geometries.

Chapter 8

Summary and Outlook

A new set of experimental and theoretical methods have been built up for studying femtosecond hot electron dynamics in nanoplasmonic systems. A variety of nanoscale geometries have been studied—including thin gold film along, gold nanospheres, nanoshells, nanorods, and nanostars—all revealing new fundamental insights and opportunities for predictively modeling and optically controlling naonscale photocurrents for a wide variety of hot carrier scientific and technological applications. While gold was the primary material investigated, it merely served as a convenient noble metal testbed with negligible oxidation upon air exposure and strong plasmonic resonance properties (along with plentiful options on nanoparticle geometries). The experimental observations and theoretical methods are general with respect to material, and can be readily extended to other plasmonic metals or, some cases, even non-plasmonic systems.

Novel capabilities for angle-resolved photoemission resolution of single, immobilized nanoparticles have led to important insights on volume vs. surface photoemission mechanisms (with plenty of exciting territory remaining to be covered in this realm), photoemission blocking with insulating coatings (e.g. mesoporous silica), and the detailed photoemission distributions from general hot spot geometries (e.g. hemispherical tips), which are applicable to numerous other systems, including etched nanotip photocathodes. Perhaps the most important role of these experiments has been to corroborate and drive the development of a simple, comprehensive theoretical framework both volume and surface photoexcitation/emission dynamics via semi-classical Monte Carlo and fully quantum multiphoton photoemission modeling, respectively. While some developments in the Monte Carlo and other methods were developed "from scratch", much of the theoretical framework was based on the work of others and nearly a century of developments in photoemission theory. The strange and exciting reality is that, even for bulk/film systems, the photoelectric effect is still not completely understood. The unique features of nanoplasmonic systems open up an even richer variety of competing photoemission pathways that sustain the challenge of developing a comprehensive model for all photoemission, particularly when resolved on femtosecond and attosecond timescales. The modest contribution here is to provide a reasonable theoretical framework that (i) captures many of the essential features of these dynamics, (ii) uses methods that are accessible to the typical experimentalist in the field, and (iii) is simple/general enough to allow for ready modification with more detailed *ab initio* theory or experimental phenomenological parameters.

Having just implemented full 3D velocity mapping capabilities and having yet to fully utilize the pump-probe capabilities, many exciting studies lie just ahead on the SPIM world line. A few promising next steps include:

- Either 2D or 3D angle-resolved photoemisison studies of naonparticles (e.g. gold nanorods) with anisotropic insulating coatings (e.g. mesoporous SiO_2), demonstrating new capabilities for photocurrent control. (Work coming out shortly demonstrating the current regulating effects of isotropic coatings, along with initial demonstrations of anisotropy due to coating defects.)

- Studies on nanolithographic structures for detailed geometric control and opportunities for nanoscale electrode engineering, two-slit diffraction demonstrations, or other geometries for nanoelectronics or frequency/polarization-resolved photodetection.

- More detailed time-resolved studies on a variety of nanoparticle geometries, materials, and environments, using 3D VMI to directly determine the radial distributions without relying on symmetry and 3D reconstruction. Detailed investigations of the effects of surface collisions, charge transfer at various interfaces, nonlocality, and the effect of surface-like dielectric function deviations for very small particles.

- Careful 3D velocity-resolved studies on various geometries to refine volume vs. surface photoemission models.
- Pushing into the strong-field regime for novel time- and 3D angle-resolved characterization of these systems.

These and other directions (such as novel alloy, 2D, and quantum materials) all represent exciting and relatively low-barrier future research paths.

Bibliography

[1] N. S. Abadeer, M. R. Brennan, W. L. Wilson, and C. J. Murphy. Distance and plasmon wavelength dependent fluorescence of molecules bound to silica-coated gold nanorods. ACS Nano, 8(8):8392–8406, 2014.

[2] M. Aeschlimann, M. Bauer, D. Bayer, T. Brixner, S. Cunovic, F. Dimler, A. Fischer, W. Pfeiffer, M. Rohmer, C. Schneider, F. Steeb, C. Strüber, and D. V. Voronine. Spatiotemporal control of nanooptical excitations. Proceedings of the National Academy of Sciences of the United States of America, 107(12):5329–5333, 2010.

[3] M. Aidelsburger, F. O. Kirchner, F. Krausz, and P. Baum. Single-electron pulses for ultrafast diffraction. Proceedings of the National Academy of Sciences of the United States of America, 107(46):19714–19719, 2010.

[4] N.W. Ashcroft and N.D. Mermin. Solid State Physics. Saunders College, Philadelphia, 1976.

[5] M. N. R. Ashfold, N. H. Nahler, A. J. Orr-Ewing, O. P. J. Vieuxmaire, R. L. Toomes, T. N. Kitsopoulos, I. A. Garcia, D. A. Chestakov, S. M. Wu, and D. H. Parker. Imaging the dynamics of gas phase reactions. Physical Chemistry Chemical Physics, 8(1):26–53, 2006.

[6] U. Aslam, V. G. Rao, S. Chavez, and S. Linic. Catalytic conversion of solar to chemical energy on plasmonic metal nanostructures. Nature Catalysis, 1(9):656–665, 2018.

[7] H. A. Atwater and A. Polman. Plasmonics for improved photovoltaic devices. Nature Materials, 9(3):205–213, 2010.

[8] C. Awada, T. Popescu, L. Douillard, F. Charra, A. Perron, H. Yockell-Lelievre, A. L. Baudrion, P. M. Adam, and R. Bachelot. Selective excitation of plasmon resonances of single Au triangles by polarization-dependent light excitation. Journal of Physical Chemistry C, 116(27):14591–14598, 2012.

[9] V. E. Babicheva, S. V. Zhukovsky, R. S. Ikhsanov, I. E. Protsenko, I. V. Smetanin, and A. Uskov. Hot electron photoemission from plasmonic nanostructures: The role of surface photoemission and transition absorption. ACS Photonics, 2(8):1039–1048, 2015.

[10] H. Baida, D. Mongin, D. Christofilos, G. Bachelier, A. Crut, P. Maioli, N. Del Fatti, and F. Vallee. Ultrafast nonlinear optical response of a single gold nanorod near its surface plasmon resonance. Physical Review Letters, 107(5):057402, 2011.

[11] A. R. Bainbridge and W. A. Bryan. Velocity map imaging of femtosecond laser induced photoelectron emission from metal nanotips. New Journal of Physics, 16:103031, 2014.

[12] T. A. Baker, A. Grubisic, and D. J. Nesbitt. Plasmon mediated multiphoton photoemission microscopy of Au nanoholes and nanohole dimers. Journal of Physical Chemistry C, 118(13):6959–6971, 2014.

[13] A. Barhoumi, R. Huschka, R. Bardhan, M. W. Knight, and N. J. Halas. Light-induced release of dna from plasmon-resonant nanoparticles: Towards light-controlled gene therapy. Chemical Physics Letters, 482(4-6):171–179, 2009.

[14] M. Bauer, A. Marienfeld, and M. Aeschlimann. Hot electron lifetimes in metals probed by time-resolved two-photon photoemission. Progress in Surface Science, 90(3):319–376, 2015.

[15] D. Bayer, C. Wiemann, O. Gaier, M. Bauer, and M. Aeschlimann. Time-resolved 2ppe and time-resolved peem as a probe of lsp's in silver nanoparticles. Journal of Nanomaterials, 2008.

[16] J. P. Berenger. A perfectly matched layer for the absorption of electromagnetic-waves. Journal of Computational Physics, 114(2):185–200, 1994.

[17] C. N. Berglund and W. E. Spicer. Photoemission studies of copper and silver: Theory. Physical Review A, 136(4a):1030–1044, 1964.

[18] M. G. Blaber, M. D. Arnold, and M. J. Ford. A review of the optical properties of alloys and intermetallics for plasmonics. Journal of Physics-Condensed Matter, 22(14), 2010.

[19] E. Blandre, D. Jalas, A. Y. Petrov, and M. Eich. Limit of efficiency of generation of hot electrons in metals and their injection inside a semiconductor using a semiclassical approach. ACS Photonics, 5(9):3613–3620, 2018.

[20] Craig F. Bohren and Donald R. Huffman. Absorption and scattering of light by small particles. Wiley, New York, 1983.

[21] T. Brixner and G. Gerber. Femtosecond polarization pulse shaping. Optics Letters, 26(8):557–559, 2001.

[22] M. L. Brongersma. Introductory lecture: nanoplasmonics. Faraday Discussions, 178:9–36, 2015.

[23] M. L. Brongersma, N. J. Halas, and P. Nordlander. Plasmon-induced hot carrier science and technology. Nature Nanotechnology, 10(1):25–34, 2015.

[24] A. M. Brown, R. Sundararaman, P. Narang, W. A. Goddard, and H. A. Atwater. Nonradiative plasmon decay and hot carrier dynamics: Effects of phonons, surfaces, and geometry. ACS Nano, 10(1):957–966, 2016.

[25] N. D. Burrows, A. M. Vartanian, N. S. Abadeer, E. M. Grzincic, L. M. Jacob, W. N. Lin, J. Li, J. M. Dennison, J. G. Hinman, and C. J. Murphy. Anisotropic nanoparticles and anisotropic surface chemistry. Journal of Physical Chemistry Letters, 7(4):632–641, 2016.

[26] C. Carnegie, J. Griffiths, B. de Nijs, C. Readman, R. Chikkaraddy, W. M. Deacon, Y. Zhang, I. Szabo, E. Rosta, J. Aizpurua, and J. J. Baumberg. Room-temperature optical picocavities below 1 nm^3 accessing single-atom geometries. Journal of Physical Chemistry Letters, 9(24):7146–7151, 2018.

[27] D. W. Chandler and P. L. Houston. Two-dimensional imaging of state-selected photodissociation products detected by multiphoton ionization. Journal of Chemical Physics, 87(2):1445–1447, 1987.

[28] Q. Y. Chen and C. W. Bates. Geometrical factors in enhanced photoyield from small metal particles. Physical Review Letters, 57(21):2737–2740, 1986.

[29] N. E. Christensen and B. O. Seraphin. Relativistic band calculation and optical properties of gold. Physical Review B-Solid State, 4(10):3321, 1971.

[30] C. Clavero. Plasmon-induced hot-electron generation at nanoparticle/metal-oxide interfaces for photovoltaic and photocatalytic devices. Nature Photonics, 8(2):95–103, 2014.

[31] E. Cortes. Efficiency and bond selectivity in plasmon-induced photochemistry. Advanced Optical Materials, 5(15):1700191, 2017.

[32] E. Cortes, W. Xie, J. Cambiasso, A. S. Jermyn, R. Sundararaman, P. Narang, S. Schlucker, and S. A. Maier. Plasmonic hot electron transport drives nano-localized chemistry. Nature Communications, 8:14880, 2017.

[33] A. Crut, P. Maioli, N. Del Fatti, and F. Vallee. Optical absorption and scattering spectroscopies of single nano-objects. Chemical Society Reviews, 43(11):3921–3956, 2014.

[34] Maciej Dabrowski, Yanan Dai, and Hrvoje Petek. Ultrafast photoemission electron microscopy: Imaging plasmons in space and time. Chemical Reviews, 120(13):6247–6287, 2020.

[35] A. Damascelli. Probing the electronic structure of complex systems by ARPES. Physica Scripta, T109:61–74, 2004.

[36] A. Damm, J. Gudde, P. Feulner, A. Czasch, O. Jagutzki, H. Schmidt-Bocking, and U. Hofer. Application of a time-of-flight spectrometer with delay-line detector for time- and angle-resolved two-photon photoemission. Journal of Electron Spectroscopy and Related Phenomena, 202:74–80, 2015.

[37] N. Del Fatti, D. Christofilos, and F. Vallee. Optical response of a single gold nanoparticle. Gold Bulletin, 41(2):147–158, 2008.

[38] G. N. Derry, M. E. Kern, and E. H. Worth. Recommended values of clean metal surface work functions. Journal of Vacuum Science and Technology A, 33(6):060801, 2015.

[39] P. Dombi, A. Hörl, P. Rácz, I. Márton, A. Trügler, J. R. Krenn, and U. Hohenester. Ultrafast strong-field photoemission from plasmonic nanoparticles. Nano Letters, 13(2):674–678, 2013.

[40] L. Douillard and F. Charra. Photoemission electron microscopy, a tool for plasmonics. Journal of Electron Spectroscopy and Related Phenomena, 189:24–29, 2013.

[41] E. C. Dreaden, A. M. Alkilany, X. H. Huang, C. J. Murphy, and M. A. El-Sayed. The golden age: Gold nanoparticles for biomedicine. Chemical Society Reviews, 41(7):2740–2779, 2012.

[42] V. Dribinski, A. Ossadtchi, V. A. Mandelshtam, and H. Reisler. Reconstruction of abel-transformable images: The gaussian basis-set expansion Abel transform method. Review of Scientific Instruments, 73(7):2634–2642, 2002.

[43] D. Ehberger, J. Hammer, M. Eisele, M. Krüger, J. Noe, A. Högele, and P. Hommelhoff. Highly coherent electron beam from a laser-triggered tungsten needle tip. Physical Review Letters, 114(22):227601, 2015.

[44] A. T. J. B. Eppink and D. H. Parker. Velocity map imaging of ions and electrons using electrostatic lenses: Application in photoelectron and photofragment ion imaging of molecular oxygen. Review of Scientific Instruments, 68(9):3477–3484, 1997.

[45] L. Fan, S. K. Lee, P. Y. Chen, and W. Li. Observation of nanosecond hot carrier decay in graphene. J Phys Chem Lett, pages 1485–1490, 2018.

[46] L. Fan, S. K. Lee, Y. J. Tu, B. Mignolet, D. Couch, K. Dorney, Q. Nguyen, L. Wooldridge, M. Murnane, F. Remacle, H. B. Schlegel, and W. Li. A new electron-ion coincidence 3D momentum-imaging method and its application in probing strong field dynamics of 2-phenylethyl-N, N-dimethylamine. Journal of Chemical Physics, 147(1), 2017.

[47] W. S. Fann, R. Storz, H. W. K. Tom, and J. Bokor. Electron thermalization in gold. Physical Review B, 46(20):13592–13595, 1992.

[48] P. J. Feibelman and D. E. Eastman. Photoemission spectroscopy - correspondence between quantum-theory and experimental phenomenology. Physical Review B, 10(12):4932–4947, 1974.

[49] A. Feist, N. Bach, N. R. da Silva, T. Danz, M. Möller, K. E. Priebe, T. Domröse, J. G. Gatzmann, S. Rost, J. Schauss, S. Strauch, R. Bormann, M. Sivis, S. Schäfer, and C. Ropers. Ultrafast transmission electron microscopy using a laser-driven field emitter: Femtosecond resolution with a high coherence electron beam. Ultramicroscopy, 176:63–73, 2017.

[50] J. M. Fitzgerald, P. Narang, R. V. Craster, S. A. Maier, and V. Giannini. Quantum plasmonics. Proceedings of the Ieee, 104(12):2307–2322, 2016.

[51] V. S. Fomenko and G. V. Samsonov. Handbook of Thermionic Properties: Electronic Work Functions and Richardson Constants of Elements and Compounds. Springer US, Boston, MA, 1966.

[52] R. H. Fowler. The analysis of photoelectric sensitivity curves for clean metals at various temperatures. Physical Review, 38(1):45–56, 1931.

[53] Z. Gao, N. D. Burrows, N. A. Valley, S. Egger, G. C. Schatz, C. J. Murphy, and C. L. Haynes. In solution SERS sensing using mesoporous silica-coated gold nanorods. Analyst, 141(24):6604–6604, 2016.

[54] F. J. García-Vidal and J. B. Pendry. Collective theory for surface enhanced Raman scattering. Physical Review Letters, 77(6):1163–1166, 1996.

[55] J. Gargiulo, R. Berte, Y. Li, S. A. Maier, and E. Cortes. From optical to chemical hot spots in plasmonics. Accounts of Chemical Research, 52(9):2525–2535, 2019.

[56] P. L. Garrido, S. Goldstein, J. Lukkarinen, and R. Tumulka. Paradoxical reflection in quantum mechanics. American Journal of Physics, 79(12):1218–1231, 2011.

[57] M.L. Glasser and A. Bagchi. Theories of photoemission from metal surfaces. Progress in Surface Science, 7(3):113–148, 1976.

[58] G. Gonzalez-Rubio, V. Kumar, P. Llombart, P. Diaz-Nunez, E. Bladt, T. Altantzis, S. Bals, O. Pena-Rodriguez, E. G. Noya, L. G. MacDowell, A. Guerrero-Martinez, and L. M. Liz-Marzan. Disconnecting symmetry breaking from seeded growth for the reproducible synthesis of high quality gold nanorods. ACS Nano, 13(4):4424–4435, 2019.

[59] M. Graf, D. Jalas, J. Weissmuller, A. Y. Petrov, and M. Eich. Surface-to-volume ratio drives photoelelectron injection from nanoscale gold into electrolyte. ACS Catalysis, 9(4):3366–3374, 2019.

[60] M. Grajower, U. Levy, and J. B. Khurgin. The role of surface roughness in plasmonic-assisted internal photoemission schottky photodetectors. ACS Photonics, 5(10):4030–4036, 2018.

[61] W. S. Graves, F. X. Kärtner, D. E. Moncton, and P. Piot. Intense superradiant x rays from a compact source using a nanocathode array and emittance exchange. Physical Review Letters, 108(26):263904, 2012.

[62] A. Grubisic, S. Mukherjee, N. Halas, and D. J. Nesbitt. Anomalously strong electric near-field enhancements at defect sites on Au nanoshells observed by ultrafast scanning photoemission imaging microscopy. Journal of Physical Chemistry C, 117(44):22545–22559, 2013.

[63] A. Grubisic, E. Ringe, C. M. Cobley, Y. N. Xia, L. D. Marks, R. P. Van Duyne, and D. J. Nesbitt. Plasmonic near-electric field enhancement effects in ultrafast photoelectron emission: Correlated spatial and laser polarization microscopy studies of individual Ag nanocubes. Nano Letters, 12(9):4823–4829, 2012.

[64] A. Grubisic, V. Schweikhard, T. A. Baker, and D. J. Nesbitt. Coherent multiphoton photoelectron emission from single Au nanorods: The critical role of plasmonic electric near-field enhancement. ACS Nano, 7(1):87–99, 2013.

[65] A. Grubisic, V. Schweikhard, T. A. Baker, and D. J. Nesbitt. Multiphoton photoelectron emission microscopy of single Au nanorods: Combined experimental and theoretical study of rod morphology and dielectric environment on localized surface plasmon resonances. Physical Chemistry Chemical Physics, 15(26):10616–10627, 2013.

[66] M. Gulde, S. Schweda, G. Storeck, M. Maiti, H. K. Yu, A. M. Wodtke, S. Schäfer, and C. Ropers. Ultrafast low-energy electron diffraction in transmission resolves polymer/graphene superstructure dynamics. Science, 345(6193):200–204, 2014.

[67] E. Hao, S. Y. Li, R. C. Bailey, S. L. Zou, G. C. Schatz, and J. T. Hupp. Optical properties of metal nanoshells. Journal of Physical Chemistry B, 108(4):1224–1229, 2004.

[68] F. Hao, C. L. Nehl, J. H. Hafner, and P. Nordlander. Plasmon resonances of a gold nanostar. Nano Letters, 7(3):729–732, 2007.

[69] G. V. Hartland. Optical studies of dynamics in noble metal nanostructures. Chemical Reviews, 111(6):3858–3887, 2011.

[70] M. Hattass, T. Jalowy, A. Czasch, T. Weber, T. Jahnke, S. Schossler, L. P. Schmidt, O. Jagutzki, R. Dorner, and H. Schmidt-Bocking. A 2 pi spectrometer for electron-electron coincidence studies on surfaces. Review of Scientific Instruments, 75(7):2373–2378, 2004.

[71] C. L. Haynes, A. D. McFarland, and R. P. Van Duyne. Surface-enhanced Raman spectroscopy. Analytical Chemistry, 77(17):338a–346a, 2005.

[72] G. Herink, D. R. Solli, M. Gulde, and C. Ropers. Field-driven photoemission from nanostructures quenches the quiver motion. Nature, 483(7388):190–193, 2012.

[73] T. Higuchi, C. Heide, K. Ullmann, H. B. Weber, and P. Hommelhoff. Light-field-driven currents in graphene. Nature, 550(7675):224, 2017.

[74] R. G. Hobbs, W. P. Putnam, A. Fallahi, Y. Yang, F. X. Kärtner, and K. K. Berggren. Mapping photoemission and hot-electron emission from plasmonic nanoantennas. Nano Letters, 17(10):6069–6076, 2017.

[75] R. G. Hobbs, Y. Yang, A. Fallahi, P. D. Keathley, E. De Leo, F. X. Kärtner, W. S. Graves, and K. K. Berggren. High-yield, ultrafast, surface plasmon-enhanced, Au nanorod optical field electron emitter arrays. ACS Nano, 8(11):11474–11482, 2014.

[76] P. Hommelhoff, C. Kealhofer, and M. A. Kasevich. Ultrafast electron pulses from a tungsten tip triggered by low-power femtosecond laser pulses. Physical Review Letters, 97(24):247402, 2006.

[77] C. Hrelescu, T. K. Sau, A. L. Rogach, F. Jäckel, G. Laurent, L. Douillard, and F. Charra. Selective excitation of individual plasmonic hotspots at the tips of single gold nanostars. Nano Letters, 11(2):402–407, 2011.

[78] S. Hufner. Photoelectron Spectroscopy: Principles and Applications. Springer-Verlag, Berlin, 3 edition, 2003.

[79] R. S. Ikhsanov, A. V. Novitsky, I. E. Protsenko, and A. V. Uskov. Bulk photoemission from plasmonic nanoantennas of different shapes. Journal of Physical Chemistry C, 122(22):11985–11992, 2018.

[80] J. B. Jackson and N. J. Halas. Surface-enhanced Raman scattering on tunable plasmonic nanoparticle substrates. Proceedings of the National Academy of Sciences of the United States of America, 101(52):17930–17935, 2004.

[81] J.D. Jackson. Classical electrodynamics. Wiley, New York, 3rd edition, 1998.

[82] P. K. Jain, W. Qian, and M. A. El-Sayed. Ultrafast cooling of photoexcited electrons in gold nanoparticle-thiolated dna conjugates involves the dissociation of the gold-thiol bond. Journal of the American Chemical Society, 128(7):2426–2433, 2006.

[83] Y. H. Jang, Y. J. Jang, S. Kim, L. N. Quan, K. Chung, and D. H. Kim. Plasmonic solar cells: From rational design to mechanism overview. Chemical Reviews, 116(24):14982–15034, 2016.

[84] A. S. Jermyn, G. Tagliabue, H. A. Atwater, W. A. Goddard, P. Narang, and R. Sundararaman. Transport of hot carriers in plasmonic nanostructures. Physical Review Materials, 3(7):075201, 2019.

[85] J.-M. Jin. Theory and computation of electromagnetic fields. Wiley, Hoboken, N.J., 2010.

[86] P. B. Johnson and R. W. Christy. Optical constants of noble metals. Physical Review B, 6(12):4370–4379, 1972.

[87] A. Kahn. Fermi level, work function and vacuum level. Materials Horizons, 3(1):7–10, 2016.

[88] H. Kanter. Slow-electron mean free paths in aluminum, silver, and gold. Physical Review B-Solid State, 1(2):522–536, 1970.

[89] C. Karnetzky, P. Zimmermann, C. Trummer, C. D. Sierra, M. Wörle, R. Kienberger, and A. Holleitner. Towards femtosecond on-chip electronics based on plasmonic hot electron nano-emitters. Nature Communications, 9:2471, 2018.

[90] P. D. Keathley, W. P. Putnam, P. Vasireddy, R. G. Hobbs, Y. Yang, K. K. Berggren, and F. X. Kartner. Vanishing carrier-envelope-phase-sensitive response in optical-field photoemission from plasmonic nanoantennas. Nature Physics, 15(11):1128, 2019.

[91] L. V. Keldysh. Ionization in the field of a strong electromagnetic wave. Sov. Phys. JETP-USSR, 20(5):1307–1314, 1965.

[92] K. L. Kelly, E. Coronado, L. L. Zhao, and G. C. Schatz. The optical properties of metal nanoparticles: The influence of size, shape, and dielectric environment. Journal of Physical Chemistry B, 107(3):668–677, 2003.

[93] A. S. Kirakosyan, M. I. Stockman, and T. V. Shahbazyan. Surface plasmon lifetime in metal nanoshells. Physical Review B, 94(15):155429, 2016.

[94] C. Kittel. Introduction to Solid State Physics. Wiley, New York, 7th edition, 1996.

[95] M. W. Knight, H. Sobhani, P. Nordlander, and N. J. Halas. Photodetection with active optical antennas. Science, 332(6030):702–704, 2011.

[96] M. W. Knight, Y. M. Wang, A. S. Urban, A. Sobhani, B. Y. Zheng, P. Nordlander, and N. J. Halas. Embedding plasmonic nanostructure diodes enhances hot electron emission. Nano Letters, 13(4):1687–1692, 2013.

[97] E. Knoesel, A. Hotzel, T. Hertel, M. Wolf, and G. Ertl. Dynamics of photoexcited electrons in metals studied with time-resolved two-photon photoemission. Surface Science, 368:76–81, 1996.

[98] B. Kromker, M. Escher, D. Funnemann, D. Hartung, H. Engelhard, and J. Kirschner. Development of a momentum microscope for time resolved band structure imaging. Review of Scientific Instruments, 79(5):053702, 2008.

[99] M. Krüger, C. Lemell, G. Wachter, J. Burgdörfer, and P. Hommelhoff. Attosecond physics phenomena at nanometric tips. Journal of Physics B-Atomic Molecular and Optical Physics, 51(17):172001, 2018.

[100] M. Krüger, M. Schenk, and P. Hommelhoff. Attosecond control of electrons emitted from a nanoscale metal tip. Nature, 475(7354):78–81, 2011.

[101] J. Kupersztych, P. Monchicourt, and M. Raynaud. Ponderomotive acceleration of photoelectrons in surface-plasmon-assisted multiphoton photoelectric emission. Physical Review Letters, 86(22):5180–5183, 2001.

[102] F. Ladstadter, U. Hohenester, P. Puschnig, and C. Ambrosch-Draxl. First-principles calculation of hot-electron scattering in metals. Physical Review B, 70(23):235125, 2004.

[103] J. Langer, S. M. Novikov, and L. M. Liz-Marzan. Sensing using plasmonic nanostructures and nanoparticles. Nanotechnology, 26(32), 2015.

[104] S. K. Lee, F. Cudry, Y. F. Lin, S. Lingenfelter, A. H. Winney, L. Fan, and W. Li. Coincidence ion imaging with a fast frame camera. Review of Scientific Instruments, 85(12):123303, 2014.

[105] S. K. Lee, Y. F. Lin, S. Lingenfelter, L. Fan, A. H. Winney, and W. Li. Communication: Time- and space-sliced velocity map electron imaging. Journal of Chemical Physics, 141(22):221101, 2014.

[106] M. Lehr, B. Foerster, M. Schmitt, K. Krüger, C. Sönnichsen, G. Schönhense, and H. J. Elmers. Momentum distribution of electrons emitted from resonantly excited individual gold nanorods. Nano Letters, 17(11):6606–6612, 2017.

[107] Martin Lehr, Karina Bley, Nicolas Vogel, Bärbel Rethfeld, Gerd Schönhense, and Hans-Joachim Elmers. Evidence of spatially inhomogeneous electron temperature in a resonantly excited array of bow-tie nanoantennas. Journal of Physical Chemistry C, 123(19):12429–12436, 2019.

[108] P. F. Liao and A. Wokaun. Lightning rod effect in surface enhanced Raman scattering. Journal of Chemical Physics, 76(1):751–752, 1982.

[109] Y. F. Lin, S. K. Lee, P. Adhikari, T. Herath, S. Lingenfelter, A. H. Winney, and W. Li. Note: An improved 3D imaging system for electron-electron coincidence measurements. Review of Scientific Instruments, 86(9):096110, 2015.

[110] S. Linic, U. Aslam, C. Boerigter, and M. Morabito. Photochemical transformations on plasmonic metal nanoparticles. Nature Materials, 14(6):567–576, 2015.

[111] S. Link and M. A. El-Sayed. Shape and size dependence of radiative, non-radiative and photothermal properties of gold nanocrystals. International Reviews in Physical Chemistry, 19(3):409–453, 2000.

[112] S. Link, M. B. Mohamed, and M. A. El-Sayed. Simulation of the optical absorption spectra of gold nanorods as a function of their aspect ratio and the effect of the medium dielectric constant. Journal of Physical Chemistry B, 103(16):3073–3077, 1999.

[113] S. E. Lohse and C. J. Murphy. The quest for shape control: A history of gold nanorod synthesis. Chemistry of Materials, 25(8):1250–1261, 2013.

[114] G. D. Mahan. Theory of photoemission in simple metals. Physical Review B, 2(11):4334–4350, 1970.

[115] S.A. Maier. Plasmonics: Fundamentals and Applications. Springer, New York, 1st edition, 2007.

[116] R. E. B. Makinson. The surface photoelectric effect. Physical Review, 75(12):1908–1911, 1949.

[117] A. Manjavacas, J. G. Liu, V. Kulkarni, and P. Nordlander. Plasmon-induced hot carriers in metallic nanoparticles. ACS Nano, 8(8):7630–7638, 2014.

[118] E. Marsell, A. Losquin, R. Svard, M. Miranda, C. Guo, A. Harth, E. Lorek, J. Mauritsson, C. L. Arnold, H. X. Xu, A. L'Huillier, and A. Mikkelsen. Nanoscale imaging of local few-femtosecond near-field dynamics within a single plasmonic nanoantenna. Nano Letters, 15(10):6601–6608, 2015.

[119] J. W. McIver, D. Hsieh, H. Steinberg, P. Jarillo-Herrero, and N. Gedik. Control over topological insulator photocurrents with light polarization. Nature Nanotechnology, 7(2):96–100, 2012.

[120] M. Meier and A. Wokaun. Enhanced fields on large metal particles - dynamic depolarization. Optics Letters, 8(11):581–583, 1983.

[121] M. Merschdorf, W. Pfeiffer, A. Thon, S. Voll, and G. Gerber. Photoemission from multiply excited surface plasmons in Ag nanoparticles. Applied Physics A-Materials Science & Processing, 71(5):547–552, 2000.

[122] H. B. Michaelson. Work function of elements and its periodicity. Journal of Applied Physics, 48(11):4729–4733, 1977.

[123] M. Moskovits. The case for plasmon-derived hot carrier devices. Nature Nanotechnology, 10(1), 2015.

[124] N. E. Motl, A. F. Smith, C. J. DeSantis, and S. E. Skrabalak. Engineering plasmonic metal colloids through composition and structural design. Chemical Society Reviews, 43(11):3823–3834, 2014.

[125] S. Mubeen, J. Lee, N. Singh, S. Kramer, G. D. Stucky, and M. Moskovits. An autonomous photosynthetic device in which all charge carriers derive from surface plasmons. Nature Nanotechnology, 8(4):247–251, 2013.

[126] M. Müller, V. Kravtsov, A. Paarmann, M. B. Raschke, and R. Ernstorfer. Nanofocused plasmon-driven sub-10 fs electron point source. ACS Photonics, 3(4):611–619, 2016.

[127] M. Müller, A. Paarmann, and R. Ernstorfer. Femtosecond electrons probing currents and atomic structure in nanomaterials. Nature Communications, 5:5292, 2014.

[128] P. Narang, R. Sundararaman, and H. A. Atwater. Plasmonic hot carrier dynamics in solid-state and chemical systems for energy conversion. Nanophotonics, 5(1):96–111, 2016.

[129] P. Narang, R. Sundararaman, A. S. Jermyn, W. A. Goddard, and H. A. Atwater. Cubic nonlinearity driven up-conversion in high-field plasmonic hot carrier systems. Journal of Physical Chemistry C, 120(37):21056–21062, 2016.

[130] C. C. Neacsu, S. Berweger, R. L. Olmon, L. V. Saraf, C. Ropers, and M. B. Raschke. Near-field localization in plasmonic superfocusing: A nanoemitter on a tip. Nano Letters, 10(2):592–596, 2010.

[131] C. Ng, J. J. Cadusch, S. Dligatch, A. Roberts, T. J. Davis, P. Mulvaney, and D. E. Gomez. Hot carrier extraction with plasmonic broadband absorbers. ACS Nano, 10(4):4704–4711, 2016.

[132] X. J. Ni, S. Ishii, A. V. Kildishev, and V. M. Shalaev. Ultra-thin, planar, babinet-inverted plasmonic metalenses. Light-Science & Applications, 2, 2013.

[133] S. J. Oldenburg, R. D. Averitt, S. L. Westcott, and N. J. Halas. Nanoengineering of optical resonances. Chemical Physics Letters, 288(2):243–247, 1998.

[134] C. Oubre and P. Nordlander. Optical properties of metallodielectric nanostructures calculated using the finite difference time domain method. Journal of Physical Chemistry B, 108(46):17740–17747, 2004.

[135] M. Pant and L. K. Ang. Ultrafast laser-induced electron emission from multiphoton to optical tunneling. Physical Review B, 86(4), 2012.

[136] D. J. Park, B. Piglosiewicz, S. Schmidt, H. Kollmann, M. Mascheck, and C. Lienau. Strong field acceleration and steering of ultrafast electron pulses from a sharp metallic nanotip. Physical Review Letters, 109(24):244803, 2012.

[137] K. Park, L. F. Drummy, R. C. Wadams, H. Koerner, D. Nepal, L. Fabris, and R. A. Vaia. Growth mechanism of gold nanorods. Chemistry of Materials, 25(4):555–563, 2013.

[138] C. Pellegrini, A. Marinelli, and S. Reiche. The physics of x-ray free-electron lasers. Reviews of Modern Physics, 88(1):015006, 2016.

[139] M. Pelton, M. Z. Liu, S. Park, N. F. Scherer, and P. Guyot-Sionnest. Ultrafast resonant optical scattering from single gold nanorods: Large nonlinearities and plasmon saturation. Physical Review B, 73(15), 2006.

[140] O. Pena and U. Pal. Scattering of electromagnetic radiation by a multilayered sphere. Computer Physics Communications, 180(11):2348–2354, 2009.

[141] S. D. Perrault and W. C. W. Chan. Synthesis and surface modification of highly monodispersed, spherical gold nanoparticles of 50-200 nm. Journal of the American Chemical Society, 131(47):17042–17043, 2009.

[142] H. Petek. Photoexcitation of adsorbates on metal surfaces: One-step or three-step. Journal of Chemical Physics, 137(9):091704, 2012.

[143] H. Petek and S. Ogawa. Femtosecond time-resolved two-photon photoemission studies of electron dynamics in metals. Progress in Surface Science, 56(4):239–310, 1997.

[144] J. Pettine, P. Choo, F. Medeghini, T. W. Odom, and D. J. Nesbitt. Plasmonic nanostar photocathodes for optically-controlled directional currents. Nature Communications, 11:1367, 2020.

[145] J. Pettine, A. Grubisic, and D. J. Nesbitt. Angle- and momentum-resolved photoelectron velocity map imaging studies of thin Au film and single supported Au nanoshells. Journal of Physical Chemistry C, 122(7):3970–3984, 2018.

[146] J. Pettine, A. Grubisic, and D. J. Nesbitt. Polarization-controlled directional multiphoton photoemission from hot spots on single Au nanoshells. Journal of Physical Chemistry C, 122(26):14805–14813, 2018.

[147] J. Pettine, A. Marton Menendez, and D. J. Nesbitt. Continuous angular control over anisotropic photoemission from isotropic gold nanoshells. The Journal of Chemical Physics, 153(10):101101, 2020.

[148] J. Pettine, S.M. Meyer, F. Medeghini, C. J. Murphy, and D. J. Nesbitt. Controlling hot electron spatial and momentum distributions in nanoplasmonic systems: Volume versus surface effects. arXiv:2007.07308, 2020.

[149] W. Pfeiffer, C. Kennerknecht, and M. Merschdorf. Electron dynamics in supported metal nanoparticles: relaxation and charge transfer studied by time-resolved photoemission. Applied Physics a-Materials Science & Processing, 78(7):1011–1028, 2004.

[150] A. Polyakov, C. Senft, K. F. Thompson, J. Feng, S. Cabrini, P. J. Schuck, H. A. Padmore, S. J. Peppernick, and W. P. Hess. Plasmon-enhanced photocathode for high brightness and high repetition rate x-ray sources. Physical Review Letters, 110(7):076802, 2013.

[151] E. Prodan, C. Radloff, N. J. Halas, and P. Nordlander. A hybridization model for the plasmon response of complex nanostructures. Science, 302(5644):419–422, 2003.

[152] W. P. Putnam, R. G. Hobbs, P. D. Keathley, K. K. Berggren, and F. X. Kärtner. Optical-field-controlled photoemission from plasmonic nanoparticles. Nature Physics, 13(4):335–339, 2017.

[153] P. Pyykko and J. P. Desclaux. Relativity and the periodic system of elements. Accounts of Chemical Research, 12(8):276–281, 1979.

[154] E. Quinonez, J. Handali, and B. Barwick. Femtosecond photoelectron point projection microscope. Review of Scientific Instruments, 84(10), 2013.

[155] H. Raether. Surface-plasmons on smooth and rough surfaces and on gratings. Springer Tracts in Modern Physics, 111, 1988.

[156] T. Rangel, D. Kecik, P. E. Trevisanutto, G. M. Rignanese, H. Van Swygenhoven, and V. Olevano. Band structure of gold from many-body perturbation theory. Physical Review B, 86(12):125125, 2012.

[157] A. R. Rastinehad, H. Anastos, E. Wajswol, J. S. Winoker, J. P. Sfakianos, S. K. Doppalapudi, M. R. Carrick, C. J. Knauer, B. Taouli, S. C. Lewis, A. K. Tewari, J. A. Schwartz, S. E. Canfield, A. K. George, J. L. West, and N. J. Halas. Gold nanoshell-localized photothermal ablation of prostate tumors in a clinical pilot device study. Proceedings of the National Academy of Sciences of the United States of America, 116(37):18590–18596, 2019.

[158] M. Reiser. Theory and Design of Charged Particle Beams. WILEY-VCH Verlag GmbH & Co. KGaA, Weinheim, 2008.

[159] R. H. Ritchie and J. C. Ashley. Interaction of hot electrons with a free electron gas. Journal of Physics and Chemistry of Solids, 26(12):1689, 1965.

[160] H. Robatjazi, H. Q. Zhao, D. F. Swearer, N. J. Hogan, L. N. Zhou, A. Alabastri, M. J. McClain, P. Nordlander, and N. J. Halas. Plasmon-induced selective carbon dioxide conversion on earth-abundant aluminum-cuprous oxide antenna-reactor nanoparticles. Nature Communications, 8, 2017.

[161] M. Rohmer, M. Bauer, T. Leissner, C. Schneider, A. Fischer, G. Niedner-Schatteburg, B. von Issendorff, and M. Aeschlimann. Time-resolved photoelectron nano-spectroscopy of individual silver particles: Perspectives and limitations. Physica Status Solidi B: Basic Research, 247(5):1132–1138, 2010.

[162] C. Ropers, D. R. Solli, C. P. Schulz, C. Lienau, and T. Elsaesser. Localized multiphoton emission of femtosecond electron pulses from metal nanotips. Physical Review Letters, 98(4):043907, 2007.

[163] E. Rotenberg and A. Bostwick. microARPES and nanoARPES at diffraction-limited light sources: opportunities and performance gains. Journal of Synchrotron Radiation, 21:1048–1056, 2014.

[164] T. Rybka, M. Ludwig, M. F. Schmalz, V. Knittel, D. Brida, and A. Leitenstorfer. Sub-cycle optical phase control of nanotunnelling in the single-electron regime. Nature Photonics, 10(10):667–670, 2016.

[165] J. B. Sambur, T. Y. Chen, E. Choudhary, G. Q. Chen, E. J. Nissen, E. M. Thomas, N. M. Zou, and P. Chen. Sub-particle reaction and photocurrent mapping to optimize catalyst-modified photoanodes. Nature, 530:77–93, 2016.

[166] F. Schertz, M. Schmelzeisen, M. Kreiter, H. J. Elmers, and G. Schönhense. Field emission of electrons generated by the near field of strongly coupled plasmons. Physical Review Letters, 108(23):237602, 2012.

[167] A. Schiffrin, T. Paasch-Colberg, N. Karpowicz, V. Apalkov, D. Gerster, S. Muhlbrandt, M. Korbman, J. Reichert, M. Schultze, S. Holzner, J. V. Barth, R. Kienberger, R. Ernstorfer, V. S. Yakovlev, M. I. Stockman, and F. Krausz. Optical-field-induced current in dielectrics. Nature, 493(7430):70–74, 2013.

[168] A. L. Schmucker, N. Harris, M. J. Banholzer, M. G. Blaber, K. D. Osberg, G. C. Schatz, and C. A. Mirkin. Correlating nanorod structure with experimentally measured and theoretically predicted surface plasmon resonance. ACS Nano, 4(9):5453–5463, 2010.

[169] G. Schonhense, K. Medjanik, S. Chernov, D. Kutnyakhov, O. Fedchenko, M. Ellguth, D. Vasilyev, A. Zaporozhchenko-Zymakova, D. Panzer, A. Oelsner, C. Tusche, B. Schonhense, J. Braun, J. Minar, H. Ebert, J. Viefhaus, W. Wurth, and H. J. Elmers. Spin-filtered time-of-flight k-space microscopy of Ir - towards the “complete” photoemission experiment. Ultramicroscopy, 183:19–29, 2017.

[170] B. Schröder, M. Sivis, R. Bormann, S. Schäfer, and C. Ropers. An ultrafast nanotip electron gun triggered by grating-coupled surface plasmons. Applied Physics Letters, 107(23):231105, 2015.

[171] V. Schweikhard, A. Grubisic, T. A. Baker, and D. J. Nesbitt. Multiphoton scanning photoionization imaging microscopy for single-particle studies of plasmonic metal nanostructures. Journal of Physical Chemistry C, 115(1):83–91, 2011.

[172] V. Schweikhard, A. Grubisic, T. A. Baker, I. Thomann, and D. J. Nesbitt. Polarization-dependent scanning photoionization microscopy: Ultrafast plasmon-mediated electron ejection dynamics in single Au nanorods. ACS Nano, 5(5):3724–3735, 2011.

[173] K. Sengupta, T. Nagatsuma, and D. M. Mittleman. Terahertz integrated electronic and hybrid electronic-photonic systems. Nature Electronics, 1(12):622–635, 2018.

[174] M. Sivis, N. Pazos-Perez, R. W. Yu, R. Alvarez-Puebla, F. J. García de Abajo, and C. Ropers. Continuous-wave multiphoton photoemission from plasmonic nanostars. Communications Physics, 1, 2018.

[175] N. V. Smith. Photoemission spectra and band structures of *d*-band metals 3 - model band calculations on Rh, Pd, Ag, Ir, Pt, and Au. Physical Review B, 9(4):1365–1376, 1974.

[176] M. I. Stockman. Nanoplasmonics: past, present, and glimpse into future. Optics Express, 19(22):22029–22106, 2011.

[177] J.A. Stratton. Electromagnetic Theory. International Series in Physics. McGraw-Hill, Inc., New York, London, 1st edition, 1941.

[178] A.G. Suits and R.E. Continetti. Imaging in Chemical Dynamics. ACS Symposium Series. American Chemical Society: Distributed by Oxford University Press, Washington, DC, 2001.

[179] D. Sun, C. Divin, J. Rioux, J. E. Sipe, C. Berger, W. A. de Heer, P. N. First, and T. B. Norris. Coherent control of ballistic photocurrents in multilayer epitaxial graphene using quantum interference. Nano Letters, 10(4):1293–1296, 2010.

[180] Q. Sun, H. Yu, K. Ueno, A. Kubo, Y. Matsuo, and H. Misawa. Dissecting the few-femtosecond dephasing time of dipole and quadrupole modes in gold nanoparticles using polarized photoemission electron microscopy. ACS Nano, 10(3):3835–3842, 2016.

[181] F. Sussmann, L. Seiffert, S. Zherebtsov, V. Mondes, J. Stierle, M. Arbeiter, J. Plenge, P. Rupp, C. Peltz, A. Kessel, S. A. Trushin, B. Ahn, D. Kim, C. Graf, E. Rühl, M. F. Kling, and T. Fennel. Field propagation-induced directionality of carrier-envelope phase-controlled photoemission from nanospheres. Nature Communications, 6:7944, 2015.

[182] D. F. Swearer, R. K. Leary, R. Newell, S. Yazdi, H. Robatjazi, Y. Zhang, D. Renard, P. Nordlander, P. A. Midgley, N. J. Halas, and E. Ringe. Transition-metal decorated aluminum nanocrystals. ACS Nano, 11(10):10281–10288, 2017.

[183] J. Szczerbinski, L. Gyr, J. Kaeslin, and R. Zenobi. Plasmon-driven photocatalysis leads to products known from e-beam and x-ray-induced surface chemistry. Nano Letters, 18(11):6740–6749, 2018.

[184] N. Takeyasu, K. Yamaguchi, R. Kagawa, T. Kaneta, F. Benz, M. Fujii, and J. J. Baumberg. Blocking hot electron emission by SiO_2 coating plasmonic nanostructures. Journal of Physical Chemistry C, 121(34):18795–18799, 2017.

[185] C. E. Talley, J. B. Jackson, C. Oubre, N. K. Grady, C. W. Hollars, S. M. Lane, T. R. Huser, P. Nordlander, and N. J. Halas. Surface-enhanced Raman scattering from individual Au nanoparticles and nanoparticle dimer substrates. Nano Letters, 5(8):1569–1574, 2005.

[186] I. Tamm and S. Schubin. On the theory of the photoelectric effect in metals. Zeitschrift Fur Physik, 68(1-2):97–113, 1931.

[187] M. Tanzid, A. Ahmadivand, R. M. Zhang, B. Cerjan, A. Sobhani, S. Yazdi, P. Nordlander, and N. J. Halas. Combining plasmonic hot carrier generation with free carrier absorption for high-performance near-infrared silicon-based photodetection. ACS Photonics, 5(9):3472–3477, 2018.

[188] R. Trebino, K. W. DeLong, D. N. Fittinghoff, J. N. Sweetser, M. A. Krumbugel, B. A. Richman, and D. J. Kane. Measuring ultrashort laser pulses in the time-frequency domain using frequency-resolved optical gating. Review of Scientific Instruments, 68(9):3277–3295, 1997.

[189] A. V. Uskov, I. E. Protsenko, R. S. Ikhsanov, V. E. Babicheva, S. V. Zhukovsky, A. V. Lavrinenko, E. P. O'Reilly, and H. X. Xu. Internal photoemission from plasmonic nanoparticles: Comparison between surface and volume photoelectric effects. Nanoscale, 6(9):4716–4727, 2014.

[190] L. Vigderman and E. R. Zubarev. High-yield synthesis of gold nanorods with longitudinal spr peak greater than 1200 nm using hydroquinone as a reducing agent. Chemistry of Materials, 25(8):1450–1457, 2013.

[191] S. Vogelgesang, G. Storeck, J. G. Horstmann, T. Diekmann, M. Sivis, S. Schramm, K. Rossnagel, S. Schäfer, and C. Ropers. Phase ordering of charge density waves traced by ultrafast low-energy electron diffraction. Nature Physics, 14:184–191, 2017.

[192] J. Vogelsang, J. Robin, B. J. Nagy, P. Dombi, D. Rosenkranz, M. Schiek, P. Groß, and C. Lienau. Ultrafast electron emission from a sharp metal nanotaper driven by adiabatic nanofocusing of surface plasmons. Nano Letters, 15(7):4685–4691, 2015.

[193] A. Vredenborg, W. G. Roeterdink, and M. H. M. Janssen. A photoelectron-photoion coincidence imaging apparatus for femtosecond time-resolved molecular dynamics with electron time-of-flight resolution of σ =18 ps and energy resolution $\delta E/E$ =3.5%. Rev. Sci. Instrum., 79(6):063108, 2008.

[194] D. Q. Wang, A. K. Yang, W. J. Wang, Y. Hua, R. D. Schaller, G. C. Schatz, and T. W. Odom. Band-edge engineering for controlled multi-modal nanolasing in plasmonic superlattices. Nature Nanotechnology, 12(9):889–895, 2017.

[195] J. Z. Wang, K. Yu, Y. Yang, G. V. Hartland, J. E. Sader, and G. P. Wang. Strong vibrational coupling in room temperature plasmonic resonators. Nature Communications, 10, 2019.

[196] B. Wannberg. Electron optics development for photo-electron spectrometers. Nuclear Instruments and Methods in Physics Research Section A, 601(1-2):182–194, 2009.

[197] B.J. Whitaker. Imaging in Molecular Dynamics: Technology and Applications. Cambridge University Press, Cambridge ; New York, 2003.

[198] J. L. White, M. F. Baruch, J. E. Pander, Y. Hu, I. C. Fortmeyer, J. E. Park, T. Zhang, K. Liao, J. Gu, Y. Yan, T. W. Shaw, E. Abelev, and A. B. Bocarsly. Light-driven heterogeneous reduction of carbon dioxide: Photocatalysts and photoelectrodes. Chemical Reviews, 115(23):12888–12935, 2015.

[199] K. A. Willets. Super-resolution imaging of SERS hot spots. Chemical Society Reviews, 43(11):3854–3864, 2014.

[200] D. M. Wood. Classical size dependence of the work function of small metallic spheres. Physical Review Letters, 46(11):749–749, 1981.

[201] B. H. Wu, D. Y. Liu, S. Mubeen, T. T. Chuong, M. Moskovits, and G. D. Stucky. Anisotropic growth of TiO_2 onto gold nanorods for plasmon-enhanced hydrogen production from water reduction. Journal of the American Chemical Society, 138(4):1114–1117, 2016.

[202] K. Wu, J. Chen, J. R. McBride, and T. Lian. Efficient hot-electron transfer by a plasmon-induced interfacial charge-transfer transition. Science, 349(6248):632–635, 2015.

[203] S. V. Yalunin, M. Gulde, and C. Ropers. Strong-field photoemission from surfaces: Theoretical approaches. Physical Review B, 84(19):195426, 2011.

[204] H. Yanagisawa, C. Hafner, P. Doná, M. Klöckner, D. Leuenberger, T. Greber, J. Osterwalder, and M. Hengsberger. Laser-induced field emission from a tungsten tip: Optical control of emission sites and the emission process. Physical Review B, 81(11):115429, 2010.

[205] W. H. Yang, G. C. Schatz, and R. P. Van Duyne. Discrete dipole approximation for calculating extinction and Raman intensities for small particles with arbitrary shapes. Journal of Chemical Physics, 103(3):869–875, 1995.

[206] Y. J. Yang, M. Turchetti, P. Vasireddy, W. P. Putnam, O. Karnbach, A. Nardi, F. X. Kartner, K. K. Berggren, and P. D. Keathley. Light phase detection with on-chip petahertz electronic networks. Nature Communications, 11(1), 2020.

[207] H. Ye, S. Trippel, M. Di Fraia, A. Fallahi, O.D. Mücke, F.X. Kärtner, and J. Küpper. Velocity-map imaging for emittance characterization of multiphoton electron emission from a gold surface. Physical Review Applied, page arXiv:1707.06472 [Physics], 2018.

[208] G. L. Yudin and M. Y. Ivanov. Nonadiabatic tunnel ionization: Looking inside a laser cycle. Physical Review A, 64(1), 2001.

[209] M. Zavelani-Rossi, D. Polli, S. Kochtcheev, A. L. Baudrion, J. Beal, V. Kumar, E. Molotokaite, M. Marangoni, S. Longhi, G. Cerullo, P. M. Adam, and G. Della Valle. Transient optical response of a single gold nanoantenna: The role of plasmon detuning. ACS Photonics, 2(4):521–529, 2015.

[210] Y. S. Zeng, S. W. Qu, B. J. Chen, and C. H. Chan. All-plasmonic optical phased array integrated on a thin-film platform. Scientific Reports, 7, 2017.

[211] A. H. Zewail. 4D ultrafast electron diffraction, crystallography, and microscopy. Annual Review of Physical Chemistry, 57:65–103, 2006.

[212] P. Zhang, T. Wang, and J. L. Gong. Mechanistic understanding of the plasmonic enhancement for solar water splitting. Advanced Materials, 27(36):5328–5342, 2015.

[213] X. Zhang, X. Q. Li, D. Zhang, N. Q. Su, W. T. Yang, H. O. Everitt, and J. Liu. Product selectivity in plasmonic photocatalysis for carbon dioxide hydrogenation. Nature Communications, 8:1–9, 2017.

[214] Y. C. Zhang, S. He, W. X. Guo, Y. Hu, J. W. Huang, J. R. Mulcahy, and W. D. Wei. Surface-plasmon-driven hot electron photochemistry. Chemical Reviews, 118(6):2927–2954, 2018.

[215] Y. J. Zhang, O. Pluchery, L. Caillard, A. F. Lamic-Humblot, S. Casale, Y. J. Chaba, and M. Salmeron. Sensing the charge state of single gold nanoparticles via work function measurements. Nano Letters, 15(1):51–55, 2015.

[216] B. Y. Zheng, H. Q. Zhao, A. Manjavacas, M. McClain, P. Nordlander, and N. J. Halas. Distinguishing between plasmon-induced and photoexcited carriers in a device geometry. Nature Communications, 6, 2015.

[217] S. Zhou, K. Chen, M. T. Cole, Z. Li, J. Chen, C. Li, and Q. Dai. Ultrafast field-emission electron sources based on nanomaterials. Adv Mater, page e1805845, 2019.

[218] V. P. Zhukov and E. V. Chulkov. The femtosecond dynamics of electrons in metals. Physics-Uspekhi, 52(2):105–136, 2009.

[219] P. Zimmermann, A. Hötger, N. Fernandez, A. Nolinder, K. Müller, J. J. Finley, and A. W. Holleitner. Toward plasmonic tunnel gaps for nanoscale photoemission currents by on-chip laser ablation. Nano Letters, 19(2):1172–1178, 2019.

Appendix A

Laser Shutter and Piezo Driver Circuit Diagrams

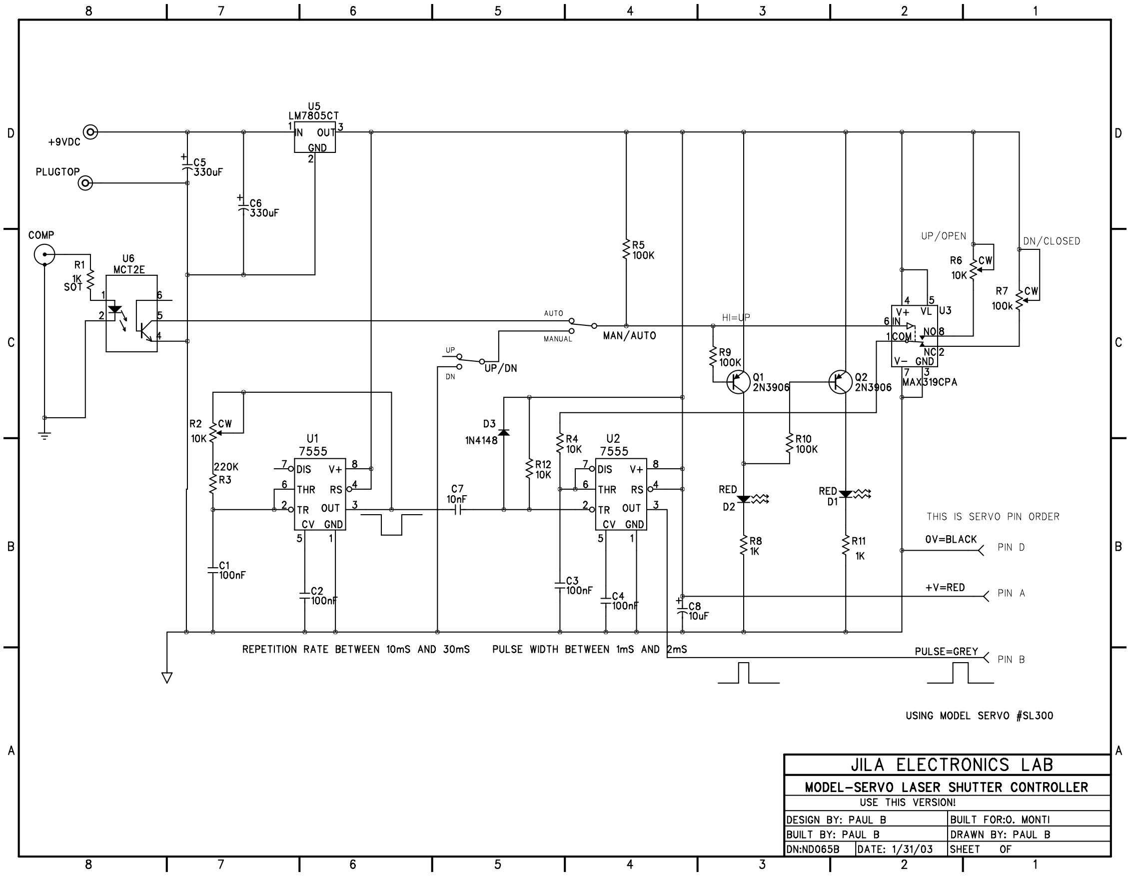
+9VDC
PLUGTOP
COMP
U5
LM7805CT
IN
OUT
GND
C5
330uF
C6
330uF
R1
1K
SOT
U6
MCT2E
R5
100K
AUTO
MANUAL
MAN/AUTO
UP
DN
UP/DN
HI=UP
UP/OPEN
DN/CLOSED
R6
10K
CW
R7
100k
U3
MAX319CPA
V+
VL
IN
COM
NO
NC
V-
GND
R9
100K
Q1
2N3906
Q2
2N3906
R2
10K
220K
R3
C1
100nF
U1
7555
DIS
THR
TR
CV
V+
RS
OUT
GND
C2
100nF
C7
10nF
D3
1N4148
R12
10K
R4
10K
U2
7555
C3
100nF
C4
100nF
C8
10uF
R10
100K
RED
D2
R8
1K
RED
D1
R11
1K
THIS IS SERVO PIN ORDER
0V=BLACK
PIN D
+V=RED
PIN A
PULSE=GREY
PIN B
REPETITION RATE BETWEEN 10mS AND 30mS
PULSE WIDTH BETWEEN 1mS AND 2mS
USING MODEL SERVO #SL300
JILA ELECTRONICS LAB
MODEL-SERVO LASER SHUTTER CONTROLLER
USE THIS VERSION!
DESIGN BY: PAUL B
BUILT FOR:O. MONTI
BUILT BY: PAUL B
DRAWN BY: PAUL B
DN:ND065B
DATE: 1/31/03
SHEET OF
8
7
6
5
4
3
2
1
D
C
B
A

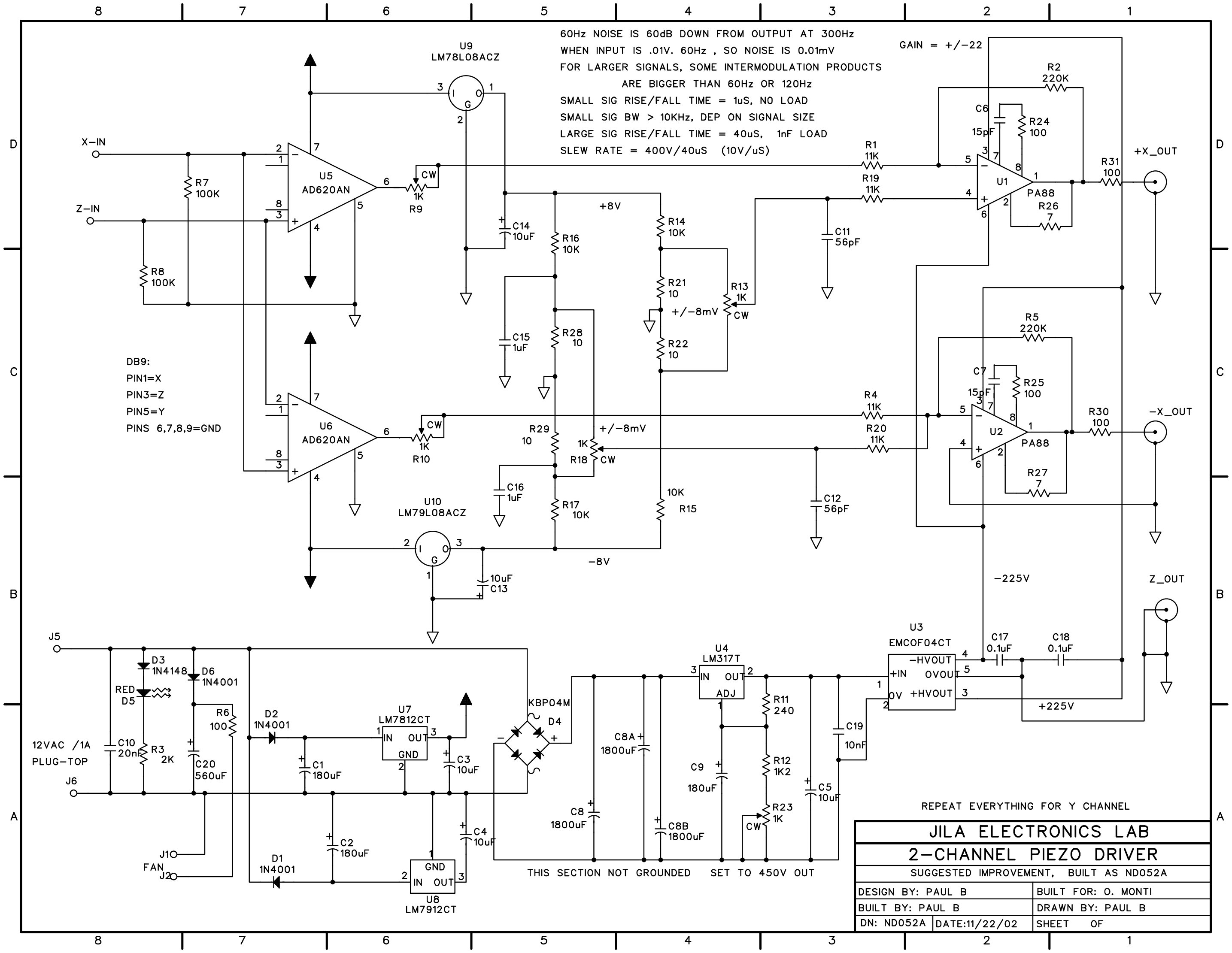

60Hz NOISE IS 60dB DOWN FROM OUTPUT AT 300Hz
WHEN INPUT IS .01V. 60Hz , SO NOISE IS 0.01mV
FOR LARGER SIGNALS, SOME INTERMODULATION PRODUCTS
ARE BIGGER THAN 60Hz OR 120Hz
SMALL SIG RISE/FALL TIME = 1uS, NO LOAD
SMALL SIG BW > 10KHz, DEP ON SIGNAL SIZE
LARGE SIG RISE/FALL TIME = 40uS, 1nF LOAD
SLEW RATE = 400V/40uS (10V/uS)

GAIN = +/-22

DB9:
PIN1=X
PIN3=Z
PIN5=Y
PINS 6,7,8,9=GND

THIS SECTION NOT GROUNDED

SET TO 450V OUT

REPEAT EVERYTHING FOR Y CHANNEL

JILA ELECTRONICS LAB
2-CHANNEL PIEZO DRIVER
SUGGESTED IMPROVEMENT, BUILT AS ND052A

DESIGN BY: PAUL B	BUILT FOR: O. MONTI
BUILT BY: PAUL B	DRAWN BY: PAUL B
DN: ND052A DATE:11/22/02	SHEET OF